

**A Thesis Submitted for the Degree of PhD at the University of Warwick**

**Permanent WRAP URL:**

<http://wrap.warwick.ac.uk/91766>

**Copyright and reuse:**

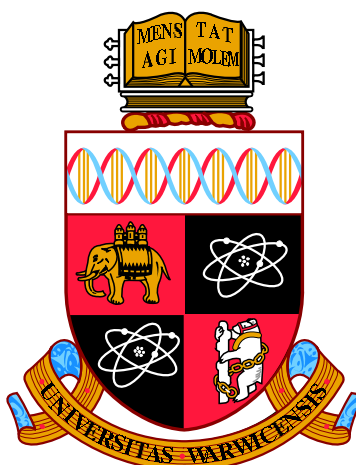
This thesis is made available online and is protected by original copyright.

Please scroll down to view the document itself.

Please refer to the repository record for this item for information to help you to cite it.

Our policy information is available from the repository home page.

For more information, please contact the WRAP Team at: [wrap@warwick.ac.uk](mailto:wrap@warwick.ac.uk)



The design, construction and characterisation of  
self-assembled biomimetic multi-chromophoric  
photosystems

by

Wen-Dong Quan

Thesis

Submitted to the University of Warwick

for the degree of

Doctor of Philosophy

MOAC DTC & Department of Chemistry

September 2016

THE UNIVERSITY OF  
WARWICK

# Contents

<b>List of Tables</b>	<b>v</b>
<b>List of Figures</b>	<b>vi</b>
<b>Acknowledgements</b>	<b>x</b>
<b>Declarations</b>	<b>xi</b>
<b>Abstract</b>	<b>xiii</b>
<b>Abbreviations</b>	<b>xv</b>
<b>Chapter 1 Introduction</b>	<b>1</b>
1.1 A brief dialogue on the energy landscape . . . . .	2
1.2 Basic photochemistry . . . . .	5
1.2.1 Basic overview of molecular orbitals and excited states . . . .	6
1.2.2 Photophysical processes of excited states . . . . .	10
1.2.3 The road towards ‘seeing’ electronic movement - a brief history of ultrafast laser technologies . . . . .	12
1.2.4 Basic interpretations of ultrafast pump-probe spectroscopy ex- periments . . . . .	14
1.3 Biological light harvesting complexes (LHCs) . . . . .	17
1.3.1 Structure of LHCs . . . . .	19
1.3.2 Excited energy transfer mechanisms in natural LHCs . . . . .	20
1.4 Photovoltaic cells and state of the art synthetic mimics . . . . .	24
1.4.1 Basic functional principle of photovoltaic cells . . . . .	24
1.4.2 Porphyrins . . . . .	26
1.4.3 Ligand directed arrangement of porphyrin . . . . .	29
1.4.4 Direct conjugation of porphyrin . . . . .	30
1.5 Concept and aim of present project . . . . .	33

1.5.1	Polymer nano assemblies . . . . .	33
1.5.2	Maleimide - a potential photosensitiser . . . . .	35
1.5.3	The ultimate aim . . . . .	36
1.5.4	The scope of the current thesis . . . . .	37
	References . . . . .	38
<b>Chapter 2 General experimental techniques and instruments</b>		<b>46</b>
2.1	General materials . . . . .	46
2.2	General instrumentation . . . . .	47
2.3	Assembly method . . . . .	47
2.4	Multi-angle laser light scattering measurements . . . . .	48
2.5	Electron microscopy . . . . .	48
2.6	Static fluorescence spectroscopy . . . . .	48
2.6.1	Fluorescence quantum yield measurements . . . . .	48
2.6.2	Extension of the instrument <i>CFM</i> . . . . .	49
2.7	Time resolved transient electronic absorption spectroscopy (TEAS) .	51
2.7.1	Laser generation and beam paths . . . . .	51
2.7.2	Sample delivery system . . . . .	54
2.7.3	Global fitting procedures . . . . .	55
2.7.4	Global fitting error analysis . . . . .	56
2.8	<i>Ab initio</i> quantum mechanical calculations (QMC) . . . . .	57
2.8.1	Hartree-Fock self-consistent field (HF-SCF) theory . . . . .	58
2.8.2	Higher level QMC methods developed on HF-SCF . . . . .	61
2.8.3	Density functional theory (DFT) . . . . .	65
	References . . . . .	66
<b>Chapter 3 Unravelling the photodynamics of a mono-amino-maleimide (MAM) fluorophore</b>		<b>70</b>
3.1	Introduction . . . . .	70
3.2	Maleimide modifications . . . . .	72
3.3	Static spectroscopy characterisation of NM-MAM . . . . .	76
3.4	TEAS of NM-MAM in various solvents . . . . .	78
3.5	QMC of NM-MAM . . . . .	81
3.6	Overall interpretation of photodynamics of MAM . . . . .	85
3.7	Conclusion . . . . .	88
3.8	Experimental data . . . . .	90
3.8.1	NM-MAM synthesis . . . . .	90
3.8.2	Global fitting . . . . .	91

References . . . . .	92
----------------------	----

**Chapter 4 The construction and photophysical characterisation of self-ordering porphyrin assemblies 96**

4.1 Introduction . . . . .	96
4.2 Choice and synthesis of components . . . . .	97
4.2.1 Azide functionalised polymer . . . . .	98
4.2.2 Alkyne functionalised porphyrin . . . . .	100
4.2.3 Conjugation of pDMA to Zn-dPP . . . . .	103
4.3 Macro-assembly morphology characterisation of Zn-dPP-pDMA in aqueous media . . . . .	106
4.3.1 Multi-angle laser light scattering characterisations . . . . .	107
4.3.2 UV-Vis absorption of filtrated samples . . . . .	107
4.3.3 Transmission electron microscopy (TEM) studies . . . . .	108
4.3.4 Overall interpretation . . . . .	110
4.4 Static spectroscopic characteristics . . . . .	111
4.5 Effects of assembly on the ultrafast photodynamics of Zn-dPP-pDMA	114
4.6 Conclusion . . . . .	116
4.7 Experimental . . . . .	116
4.7.1 Synthetic procedures and characterisation data . . . . .	116
4.7.2 Global fitting of TAS . . . . .	121
References . . . . .	122

**Chapter 5 Construction of the push-pull self-assembled multichromophoric system 128**

5.1 Introduction . . . . .	128
5.2 Assembly conditions determination and characterisation . . . . .	129
5.2.1 T:Zn-dPP-pDMA molar ratio . . . . .	129
5.2.2 UV-Vis spectra analysis . . . . .	132
5.2.3 Dry-state transmission electron microscopy observations and overall assembly interpretation . . . . .	134
5.3 TEAS experiments . . . . .	136
5.4 QMCs on the T-N $\cdots$ Zn-dPP-pDMA coordinated complex . . . . .	139
5.4.1 Individual components . . . . .	140
5.4.2 T-N $\cdots$ Zn-dPP-pDMA coordinated complex . . . . .	141
5.5 Photorelaxation pathways of systems under study . . . . .	142
5.6 Conclusion . . . . .	145
5.7 Experimental . . . . .	146

5.7.1 Global fitting . . . . .	147
References . . . . .	149
<b>Chapter 6 Summary and future prospect</b>	<b>155</b>
6.1 Exploitation of maleimide based chromophore for water splitting ap- plications . . . . .	156
6.2 Introduction of true RC to Zn-dPP-pDMA assemblies . . . . .	158
References . . . . .	160

# List of Tables

3.1	Fluorescence quantum yields and global fitted time constants of NM-MAM in various solvents . . . . .	81
4.1	Fitted radii of filtrated Zn-dPP-pDMA assemblies . . . . .	107
4.2	Fitted time constants for Zn-dPP and Zn-dPP-pDMA systems . . . .	116
5.1	Quantity of T and Zn-dPP-pDMA in the preliminary molar ratio screening measurements . . . . .	130
5.2	Global fitted time constants of each system studied in Section 5.3 . .	137
5.3	Oscillator strengths of excited states of interest for T-N...Zn-dPP-pDMA . . . . .	142

# List of Figures

1.1	Solar energy spectrum on Earth's surface . . . . .	3
1.2	Highest PV efficiencies under research . . . . .	5
1.3	Molecular orbitals of benzene . . . . .	9
1.4	Schematic of photodynamic processes . . . . .	10
1.5	Simple illustration of time resolved observation techniques . . . . .	13
1.6	Typical observations of difference spectra from TEAS experiments . . . . .	15
1.7	Schematic of light reaction pathway . . . . .	18
1.8	Photosystem I complex structure . . . . .	20
1.9	Schematic of excited energy transfer in LHCs . . . . .	21
1.10	Pictorial description of EET mechanisms . . . . .	22
1.11	Illustrations of biological EET pathways . . . . .	23
1.12	Schematic of main components in a PVC . . . . .	24
1.13	Schematic of working principle of a DSC . . . . .	25
1.14	Chemical structures of chlorophyll a/b and porphyrin . . . . .	26
1.15	Basic Lindsay synthesis conditions . . . . .	27
1.16	Reaction mechanism of Lindsay synthesis . . . . .	27
1.17	Example of a porphyrin UV-Vis spectrum and its frontier molecular orbitals . . . . .	28
1.18	Ligand directed assembly of large porphyrin arrays . . . . .	29
1.19	Insertion of a 'guest' molecule into the porhyrin arrays . . . . .	30
1.20	Schematic of linear poly-porphyrin synthesis . . . . .	31
1.21	Poly-porphyin to template interaction . . . . .	31
1.22	State-of-the-art poly-porphyrin rings . . . . .	32
1.23	Examples of assemblies by block copolymers . . . . .	34
1.24	Emmission of amino-maleimide in mixed sovlent . . . . .	36
1.25	Illustrated concept of the current project . . . . .	37

2.1	Red extension of the fluorometer spectral responsivity correction factor matrix. . . . .	51
2.2	Table schematic for transient electronic absorption spectroscopy experiments. . . . .	53
2.3	Schematic and photo of sample reservoir for TEAS experiments. . . .	54
3.1	Chemical structures of basic maleimide viriants . . . . .	72
3.2	Synthesis steps of MBM . . . . .	72
3.3	Typical modification of MBM . . . . .	73
3.4	SN <sub>1</sub> reaction mechanism of MBM . . . . .	74
3.5	Ring-opening-ring-closing reaction mechanism of MBM . . . . .	74
3.6	Synthetic scheme of 1-methyl-3-(methylamino)-1 <i>H</i> -pyrrole-2,5-dione (NM-MAM) . . . . .	75
3.7	Normalised UV-Vis spectra of NM-MAM . . . . .	76
3.8	Normalised fluorescence spectra of NM-MAM . . . . .	77
3.9	TAS of NM-MAM in cyclohexane and acetonitrile . . . . .	78
3.10	TAS of NM-MAM in methanol and deuterated methanol . . . . .	79
3.11	DAS extracted from TAS of NM-MAM . . . . .	80
3.12	Representative geometry of NM-MAM over the course of QMMD simulations . . . . .	82
3.13	Populations decay of NM-MAM over QMMD simulations . . . . .	83
3.14	Potential energy cuts of NM-MAM along OH (MeOH) coordinate . .	84
3.15	Illustration of electron driven proton transfer mechanism for NM-MAM solvated in MeOH . . . . .	85
3.16	Schematic of photodynamical processes of NM-MAM . . . . .	88
3.17	<sup>1</sup> H NMR spectrum of NM-MAM . . . . .	90
3.18	Representative fits over the TAS of NM-MAM in methanol . . . . .	91
3.19	$\frac{\chi^2}{\chi_{min}^2}$ for time constraints extracted from TAS of NM-MAM . . . . .	92
4.1	General polymerisation with RAFT using a CTA . . . . .	98
4.2	Synthetic scheme of azide functionalised pDMA . . . . .	99
4.3	Synthetic scheme of Zn-dPP . . . . .	101
4.4	Reaction scheme of Zn-dPP to pDMA conjugation . . . . .	103
4.5	SEC of polymers in DMF with LiBr . . . . .	104
4.6	IR spectra of relevant compounds for the synthesis of Zn-dPP-pDMA	105
4.7	UV-Vis absorption spectrum of filtrated Zn-dPP-pDMA assemblies .	108
4.8	TEM of Zn-dPP-pDMA assemblies post 0.22 $\mu$ m filtration . . . . .	109
4.9	TEM of Zn-dPP-pDMA assemblies post 0.45 $\mu$ m filtration . . . . .	109

4.10	Cryo-TEM of unfiltered Zn-dPP-pDMA assemblies . . . . .	109
4.11	Cartoon representation of the Zn-dPP-pDMA assembly . . . . .	110
4.12	Normalised UV-Vis spectrum of Zn-dPP and Zn-dPP-pDMA systems	111
4.13	Static fluorescence heat map of Zn-dPP and Zn-dPP-pDMA systems	112
4.14	TAS of Zn-dPP and Zn-dPP-pDMA systems . . . . .	114
4.15	DAS of Zn-dPP and Zn-dPP-pDMA systems . . . . .	115
4.16	$^1\text{H}$ NMR spectrum of 2 (Section 4.2) . . . . .	117
4.17	$^1\text{H}$ NMR spectrum of 3 (??) . . . . .	118
4.18	$^1\text{H}$ NMR spectrum of 3a (Section 4.2) . . . . .	119
4.19	$^1\text{H}$ NMR of Zn-dPP . . . . .	120
4.20	Representative fit of Zn-dPP-pDMA in different solvents . . . . .	121
4.21	$\frac{\chi^2}{\chi_{min}^2}$ for life times of Zn-dPP and Zn-dPP-pDMA systems . . . . .	122
5.1	Chemical structure of hexadentate T . . . . .	129
5.2	Normalised UV-Vis spectra of different ratios between Zn-dPP-pDMA:T upon assembly . . . . .	131
5.3	Normalised UV-Vis spectra of assembled Zn-dPP-pDMA+T and other system of interest . . . . .	132
5.4	Normalised UV-Vis spectra of assembled system using control T-Phe HAB . . . . .	133
5.5	Schematic of the solvent switch assembly method, TEM and illustra- tion of Zn-dPP-pDMA+T assemblies . . . . .	135
5.6	TAS of all systems studied in Chapter 5 . . . . .	136
5.7	Decay associated spectra of all systems studied in Chapter5 . . . . .	138
5.8	Frontier molecular orbitals of Zn-dPP and T . . . . .	140
5.9	Frontier MOs of interest for the T-N $\cdots$ Zn-dPP-pDMA coordinated complexes . . . . .	141
5.10	Illustration of proposed relaxation dynamics of Zn-dPP-pDMA+T as- semblies . . . . .	145
5.11	MALDI/TOF spectrum of T-Phe . . . . .	147
5.12	Representative traces of global fits of the TAS of assembled Zn-dPP- pDMA+T upon photoexcitation at 320 nm . . . . .	148
5.13	Representative traces of global fits of the TAS of assembled Zn-dPP- pDMA+T upon photoexcitation at 420 nm . . . . .	148
5.14	$\frac{\chi^2}{\chi_{min}^2}$ for all time constants for systems studied in Chapter5 . . . . .	149
6.1	Proposed approach for exploited EDPT pathway of maleimide chro- mophores . . . . .	157

6.2	General structure of HAB variants demonstrated by Jux <i>et al.</i> . . . .	158
6.3	Proposed approach expanding on the T-N $\cdots$ Zn-dPP-pDMA assembled system. . . . .	159

# Acknowledgements

First and foremost, I would like to thank Prof. Alison Roger for giving me the opportunity to undertake a Ph.D. with the Molecular Organisation and Assembly in Cells DTC; my project supervisors, Prof. Rachel O'Reilly, Dr. Vasilios Stavros and Prof. Richard Napier, who, despite my many short comings, never gave up on my work and provided constant support. Without all these amazing people, none of the work presented would be possible. I'm also extremely grateful to all of my supervisors for not only guiding me through my adventure into scientific research, but also taught me a great number of important lessons in life.

Secondly, I would like to thank the members of the O'Reilly and the Stavros groups, whose expertise and insights in their respective field prevented me from wondering into the wrong direction time after time. In particular, Dr. Helen Willcock and Dr. Mathew Robin who taught me the synthetic chemistry techniques; Dr. Michael Horbury and Dr. Simon Ed Greenough who taught me the ultrafast spectroscopic techniques. I also greatly appreciate the help with proof reading by Dr. Kay Doncom and Mr. Lewis Baker, whose keen eyes and suggestions helped me complete this thesis.

Thirdly, I must thank my parents, for their understanding of my infrequent visits for the duration of the Ph.D. work. My gratitude also extend to other family members encompassing all of my cousins, nephews and nieces for keeping my parents company and providing them with care in my stead. Last, but certainly not least, I would like to thank my partner Sofia, for her moral support, care and being the main reason for my diet to consist of more than noodles.

# Declarations

This thesis is submitted to the University of Warwick in support of my application for the degree of Doctor of Philosophy. It has been composed by myself and has not been submitted in any previous application for any degree. The work presented (including data generated and data analysis) was carried out by the author except in the cases outlined below:

- Transient electronic absorption spectroscopy experiments discussed in Section 3.4 were performed in collaboration with Dr. Michael Staniforth at the University of Warwick.
- *Ab initio* quantum mechanical calculations discussed in Section 3.5 were performed by Dr. Tolga Kasili at the Technische Universität München.
- Transmission electron microscopy images discussed in Sections 4.3.3 and 5.2.3 were taken by Dr. Anaïs Pitto-Barry at the University of Warwick.
- Cryogenic transmission electron microscopy images discussed in Section 4.3.4 were taken by Mr. Ian Hands-Portman at the University of Warwick.
- *Ab initio* quantum mechanical calculations discussed in Section 5.4 were performed by Mr. Lewis Baker at the University of Warwick.
- All mass spectrometry measurements were conducted by Dr. Lijiang Song at the University of Warwick.

Parts of this thesis have been published in or submitted to scientific journals by the author:

## **Chapter 3**

Towards a Universal Fluorescent Probe: Unravelling the Photodynamics of an Amino-Maleimide Fluorophore, M. Staniforth, W-D Quan, T. N. V. Karsili, R. K. O'Reilly, and V. G. Stavros, **submitted**.

## **Chapter 4**

Retaining Individualities: the Photodynamics of Porphyrin Aggregates, W.-D. Quan, A. Pitto-Barry, L. A. Baker, E. Stulz, R. Napier, R. K. O'Reilly and V. G. Stavros, *Chem.*

*Commun.*, 2016, **52**, 1938–1941.

# Abstract

The potential of a maleimide based fluorophore as well as the utilisation of simple methodologies to produce synthetic mimics of natural light harvesting complex (LHC) were explored.

In Chapter 1, the inspiration for the current work is discussed, followed by a brief guide for the interpretation of the work presented in subsequent chapters. Finally, the ultimate aim and concept for the thesis is detailed. The general instruments and methodologies applicable to all experiments conducted are then described in Chapter 2.

Chapter 3 presents the first set of results from the thesis work. This work focused on unravelling the previously unexplained fluorescence quenching observed in maleimide based fluorophores in protic solvent. This was achieved through the use of computational chemistry, ultrafast spectroscopy and synthetic chemistry. The work identified a photochemical process, in the form of electron driven proton transfer, as the fluorescence quenching mechanism. Such understandings should provide a much needed insight towards future designs of maleimide based fluorophores that fully realise the potential of this class of photoactive pigments.

This was then followed by the attempt to produce the platform for which inter-chromophoric assemblies could occur in aqueous media, documented in Chapter 4. The main body of the work involved the selection of the most effective synthetic method readily reported in the literature: the synthesis of functionalised porphyrin through the condensation reaction between dipyrrolemethane and functionalised aldehyde; and the conjugation between porphyrin and polymers with the cop-

per catalysed alkyne-azide cyclo addition click reaction. The resulting platform was successfully demonstrated to be capable of self-assembly, without the need of covalently linking the chromophores to one another. Furthermore, and most importantly, the photophysical properties of these chromophores were largely retained in the assembled structure. The results presented could lead to a new class of photoactive nanostructures that closely mimic natural LHCs, in which the properties of individual chromophores could be fully exploited and assembled without the need of covalent linkage.

The potential of using the platform documented in Chapter 4 to produce functional natural LHC mimics was then explored in the final results chapter, Chapter 5, where a pseudo reaction centre (RC) was introduced. The spectroscopic experiments demonstrated that the photodynamics of the assembly was significantly altered in the presence of the RC. This was proposed to be based on a push-pull mechanism facilitated by the presence of metal to N donor coordinated complex. Furthermore, the N donor in the chosen RC proved to be instrumental for the assembly and spectral differences observed. Therefore, these presented properties of the platform described could likely produce much more complex, functional multi-chromophoric assemblies.

The thesis then closed with a brief overview and an outlook which discussed two multi-chromophoric assemblies, based on the work presented in Chapter 3–5.

# Abbreviations

<b>ADC(<math>N</math>)</b> – algebraic diagrammatic construction to the $N^{th}$ order	microscopy
<b>AO</b> – atomic orbital	<b>Cyt bf</b> – cytochrome bf
<b>APS</b> – active pixel sensor	<b>DAS</b> – decay associated spectra
<b>ASE</b> – asymptotic standard error	<b>DDQ</b> –
<b>ATP</b> – adenosine triphosphate	2,3-dichloro-5,6-dicyano-1,4-benzoquinone
<b>B3LYP</b> – Becke 3-parameter Lee-Yang-Parr functional	<b>DFT</b> – density functional theory
<b>BBO</b> – $\beta$ -barium borate	<b>DLS</b> – dynamic light scattering
<b>c-hexane</b> – cyclohexane	<b>DMA</b> – $N,N$ -dimethylacrylamide
<b>C102</b> – Coumarin 102	<b>DMF</b> – $N,N$ -dimethylformamide
<b>CASSCF</b> – complete-active space self-consistent field method	<b>DNA</b> – deoxyribonucleic acid
<b>CFM</b> – spectral responsivity correction factor matrix	<b>EDPT</b> – electron driven proton transfer
<b>CLA</b> – chlorophyll A	<b>EET</b> – excited energy transfer
<b>CLB</b> – chlorophyll B	<b>ES</b> – excited state
<b>CPIR</b> – coherent phonon-induced relaxation	<b>ESA</b> – excited state absorption
<b>CT</b> – charge transfer	<b>FC</b> – Franck-Condon
<b>CuAAC</b> – copper(I)-catalysed azide-alkyne cycloaddition	<b>FCAM</b> – Franck-Condon active vibrational mode
<b>cryo-TEM</b> – cryogenic transmission electron	<b>FIET</b> – Förster type incoherent energy transfer
	<b>FMO</b> – Fenna-Matthews-Olson
	<b>FT-IR</b> – Fourier transform infra-red
	<b>FWHM</b> – full width at half maximum
	<b>GFP</b> – green fluorescence proteins

<b>GS</b> – ground state	<b>MCSCF</b> – multiconfiguration self-consistent field method
<b>GSB</b> – ground state bleach	<b>MD</b> – molecular dynamics
<b>GTO</b> – Gaussian type orbitals	<b>MeOH</b> – methanol
<b>HAB</b> – hexaarylbenzene	<b>MO</b> – molecular orbitals
<b>HF</b> – Hartree-Fock	<b>MPN</b> – Møller-Plesset perturbation theory to the $N^{th}$ order
<b>HF-SCF</b> – Hartree-Fock self-consistent field	<b>MPPT</b> – Møller-Plesset perturbation theory
<b>HK</b> – Hohenberg-Kohn	<b>MWCO</b> – molecular weight cut off
<b>HKS</b> –Hohenberg-Kohn-Sham	<b>NADP<sup>+</sup></b> – nicotinamide adenine dinucleotide phosphate
<b>HOMO</b> – highest occupied molecular orbital	<b>ncAA</b> – non-canonical amino acids
<b>HPLC</b> – high performance liquid chromatography	<b>NIPAM</b> – <i>N</i> -isopropylacrylamide
<b>HR-MS</b> – high resolution mass spectrometry	<b>NM-MAM</b> – 1-methyl-3-(methylamino)-1 <i>H</i> -pyrrole-2,5-dione ( <i>n</i> -methyl monoamino maleimide)
<b>IC</b> – internal conversion	<b>PAA</b> – poly-acrylic acid
<b>IET</b> – intermolecular vibrational energy transfer	<b>PC</b> – plastocyanin
<b>IRF</b> – instrument response function	<b>PE</b> – potential energy
<b>IR</b> – infrared	<b>PEC</b> – potential energy cut
<b>ISC</b> – intersystem crossing	<b>PES</b> – potential energy surface
<b>IVR</b> – intramolecular vibrational redistribution	<b>PFP</b> – pentafluorophenyl acetate
<b>KIE</b> – kinetic isotope effect	<b>PR</b> – proton recombination
<b>KS</b> – Kohn-Sham	<b>prep-SEC</b> – preparatory size exclusion chromatography
<b>LCAO-MO</b> – linear combination of atomic orbitals for expressing molecular orbitals	<b>PS</b> – photosystem
<b>LE</b> – locally excited	<b>PS-I</b> – photosystem I
<b>LH1</b> – light harvesting complex I	<b>PS-II</b> – photosystem II
<b>LH2</b> – light harvesting complex II	<b>PT</b> – proton transfer
<b>LHC</b> – light harvesting complex	<b>PTFE</b> – polytetrafluoroethylene
<b>LUMO</b> – lowest unoccupied molecular orbital	
<b>MAM</b> – monoamino maleimide	
<b>MBM</b> – monobromo maleimide	

<b>PVs</b> – photovoltaics	<b>T</b> – hexadentate template
<b>Q</b> –plastoquinone	<b>TAS</b> – transient absorption spectra
<b>QH<sub>2</sub></b> – plastoquinonol	<b>TD-DFT</b> – time dependent density functional theory
<b>QMC</b> – <i>ab initio</i> quantum mechanical calculations	<b>TEAS</b> – transient electronic absorption spectroscopy
<b>QMMD</b> – non-adiabatic surface hopping molecular dynamics	<b>TEM</b> – dry-state transmission electron microscopy
<b>QS</b> – quinine sulfate dihydrate	<b>THF</b> – tetrahydrofuran
<b>RAFT</b> – reversible addition-fragmentation chain transfer	<b>Ti-sapp</b> – Ti:Sapphire
<b>RC</b> – reaction centre	<b>TLC</b> – thin layer chromatography
<b>SB</b> – shutter block	<b>TMS</b> – tetramethysilane
<b>SCF</b> – self-consistent field	<b>UV</b> – ultraviolet
<b>SE</b> – stimulated emission	<b>UV-Vis</b> – ultraviolet-visible
<b>SLS</b> – static light scattering	<b>Vis</b> – visible
<b>SEC</b> – size exclusion chromatography	<b>VMI</b> – velocity map imaging
<b>SPA</b> – support plane analysis	<b>WLG</b> – white light generator
<b>STO</b> – Slater type orbitals	

# Chapter 1

## Introduction

Through the aeons from abiogenesis to date, nature has produced some of the most efficient organic machineries in the form of biological organisms. These range from the efficient movements of various animals, the aerodynamic optimised shapes of birds, down to the molecular complexes facilitating all the above-mentioned processes. Humans, with their perceptive and analytical abilities, have long drawn inspirations from these marvels for their own betterment. Examples range from aircrafts which often mimic the shape of birds, to computational algorithms inspired by the neural-networks found in brain and nervous systems.

Owing to the growing concerns over the adverse effects of heavy reliance on fossil fuels as energy sources, much attention and research has been placed on alternative, sustainable sources of energy since the early 2000s. Of all the candidates being explored, solar power energy could be considered analogous to the photosynthesis performed by plants, and would therefore benefit most from biomimetic designs.<sup>1-3</sup> Indeed, impressive gains in efficiency have been achieved over the span of a decade, especially in emerging technologies such as organic photovoltaics and dye sensitised solar cells.<sup>1-6</sup>

However, there is still potential for improvements over the current technologies, especially when it comes to creating a close-to-life synthetic biomimics ranging from robotics to molecular machines. The present project therefore explored the possibility of generating a biomimetic photoactive system using simple synthetic and assembly methods. The present chapter opens with a brief discussion on the current energy landscape and a simple overview of photophysical processes; then proceeds to identify the key characteristics of the natural light harvesting complexes and current state-of-the-art synthetic mimics; finally leading to the design concept and thus the ultimate goal of the current project.

## 1.1 A brief dialogue on the energy landscape

One of the defining chapters for human civilisation was arguably the utilisation of fire during the stone age. Its importance was perhaps best embodied in the mythical tales recounting the event, told across most modern cultures, the most well known being the ancient Greek Titan Prometheus stealing fire from the gods for the benefits of mankind. Since then, mastery over fire led to the development of era defining technologies such as metallurgy, pottery and steam power *etc.*, ushering in the advent of the bronze age, iron age and more recently, the industrial revolution. Development of civilisations were further boosted by the discovery and utilisation of petroleum as a major energy source for post-industrial societies. This, along with the advancements in agriculture and medical care, facilitated the rapid improvement in quality of life and expansion of human population since the early 1900s. Thanks to the development of oil extraction infrastructures as well as the wide adoption of petroleum fuelled transportation technologies over the past century, fossil fuels are now the most economically competitive and convenient form of energy source.

However, at the turn of millennium, the detrimental consequences of the relentless usage of oil reserves became apparent. One of the more concerning consequences was climate change, likely attributed the sudden injection of greenhouse gasses into the atmosphere, causing increasingly extreme weather conditions across the globe, the result of which were large-scale damage to local infrastructure, economy and human lives.<sup>7;8</sup> Furthermore, advancements in modern technologies could be considered a ‘double-edged sword’: on the one hand, great conveniences and production efficiencies have arisen from these advancements; on the other hand, if the technologies cease to function, most modern societies would follow. As the majority of technologies currently employed rely on a supply of energy to perform their tasks, it is therefore in the interest of human societies to reduce their reliance on energy sources that would inevitably deplete over time, and migrate to other, renewable sources, as an alternative to fossil fuels.

The question is therefore, *what is the best alternative?*. To answer the question, there are a number of options worthy of discussion. Considering first, nuclear fission power. Not only is the infrastructure highly developed and efficient, it is also a relatively clean solution with little, if any, associated greenhouse gas emissions. However, the risks of a meltdown, as seen in Chernobyl in 1986 and most recently Tōhoku in 2011, raised serious safety concerns over large scale deployment of such technology. Furthermore, geopolitical tension involving their potential weaponisation render their worldwide adoption a sensitive and complicated process. Secondly,

geothermal power, one of the most environmentally friendly sources of energy. A prime example of geothermal energy utilisation has been demonstrated in Iceland, where 25% of their domestic electricity needs are provided with geothermal power.<sup>9</sup> However, as the name suggests, this source of energy is heavily dependent on local geology, where only communities near volcanic vents could be sustained with this method. Thirdly, the state-of-the-art, fusion power generation, which could provide an almost endless supply of energy with no greenhouse gas emission and essentially none of the risks posed by nuclear fission power generation. As such, fusion power is an extremely enticing solution to the human energy needs. However, the technologies involved are still extremely expensive. For example, the most promising fusion reactor, International Thermonuclear Experimental Reactor (ITER), capable of producing net energy gain, recently started construction in France costing an expected minimum of \$18 billion, and is not scheduled to begin operation until at least 2025.<sup>10</sup> Thus, construction of reactors with similar or greater scale to that of ITER may remain financially prohibitive, making their wider deployment unlikely for at least another generation.

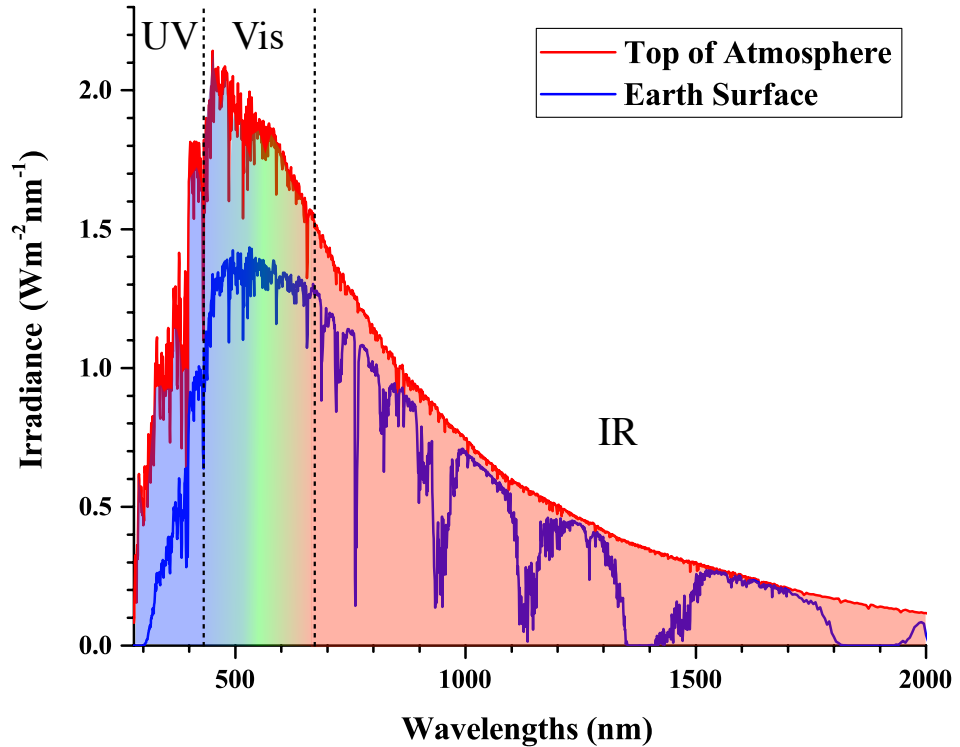


Figure 1.1: Solar energy spectrum on Earth's surface. Spectral regions corresponding to UV (ultraviolet), Vis (visible); and IR (infrared) radiations are separated by dotted vertical lines and are labelled accordingly. Numerical data derived from National Renewable Energy Laboratory (NREL), US.<sup>11</sup>

This then brings us to largest fusion reactor readily available, the sun, responsible for a number of other energy sources such as wind, hydropower and biomass. It is estimated that the Earth's surface receives *ca.* 100,000 TW of power directly from the sun, enough to provide humanity's annual electricity need in less than an hour.<sup>12</sup> To put such a number into perspective, with the 2005 estimation of urban area covering *ca.* 1% of the Earth's surface (3% of land area),<sup>13</sup> a 22% coverage of urban area with photovoltaics (PVs) at 5% efficiency would be required to meet the total electricity need of humanity. The coverage of urban area required drops to a more manageable 2.5% if the most efficient experimental PVs were utilised (46% efficiency).<sup>4</sup> The solar energy spectrum on the Earth's surface is shown in Figure 1.1. Unfortunately, the aforementioned estimate of area requirement overlooked a few key factors limiting the usability of solar power. Firstly, population density, hence energy needs, are usually unevenly distributed amongst urban areas, thus, some cities may require redistribution from neighbouring areas to meet their energy demand. Secondly, the seasonal nature of sunlight means that a complex set of energy storage/distribution infrastructures would be required to provide consistent power through out the year. Thirdly, vehicles for transportation (cars, planes, ships *etc.*) are still heavily reliant on fossil fuels. As such, the transition towards a society sustained by electricity alone is a challenge that requires the combined effort of a large range of industries. Last, and perhaps most importantly, the cost effectiveness of PVs is still uncompetitive against energy production from fossil fuels, making its wider adoption a costly investment.

From the options listed, all options exhibit advantages and limitations over each other. However, generation of electricity *via* solar energy harvesting offers the most flexibility in terms of installation scales and modularity. Furthermore, even small improvements in their efficiency and cost could lead to a significant reduction in installation size requirement and adoption cost respectively. Thus, research into the improvements in efficiency along with reduction in production costs of PVs may be the most cost effective investment to address the current energy needs in the near future. Indeed, research in PVs technology since its inception during 1970s has significantly improved the cost and efficiency of PVs.<sup>14</sup> The improvement over the years is best illustrated in the chart provided by National Center for Photovoltaics (Figure 1.2).<sup>4</sup> In particular, efficiencies of up to 22% and 46% have been demonstrated in crystalline and multi-junction cells respectively, and organic based PVs have shown a rapid increase from *ca.* 2% to 12% in merely a decade. To further improve the light harvesting capabilities of PVs, researchers are starting to look to biological processes for inspiration. More specifically, the highly efficient light harvesting com-

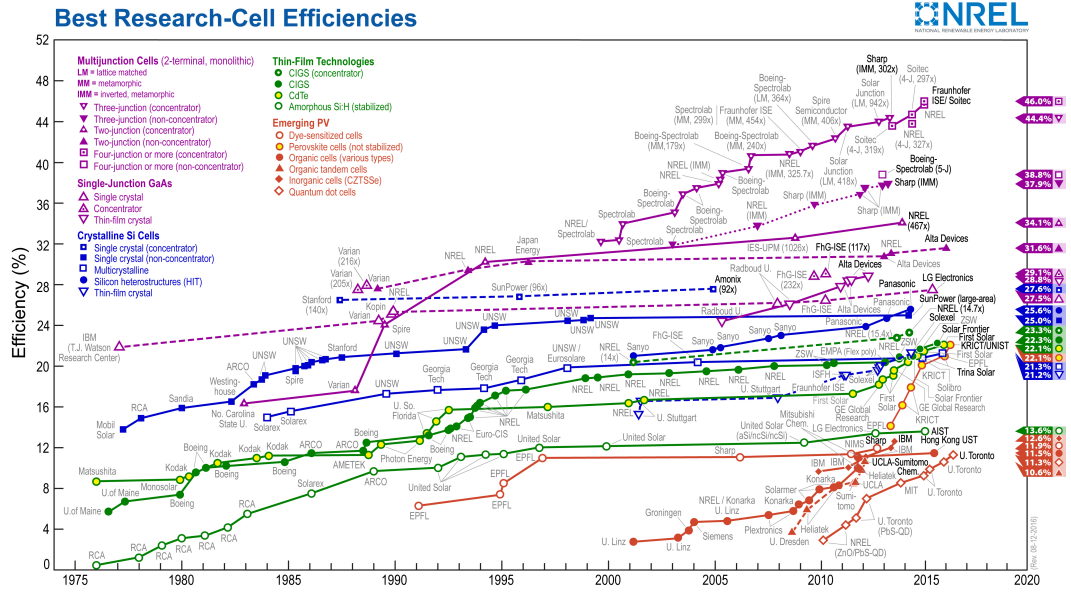


Figure 1.2: Highest PVs efficiencies currently under research. Data obtained from the National Center for Photovoltaics (a subsidiary of the NREL),<sup>4</sup> showing the progress in light harvesting efficiencies of PVs over the years.

plexes (LHCs), found in high plants and other light harvesting organisms. As a result of the insights contributed by the biochemical and biophysical research communities, the qualities of the reverse engineered blueprints have improved dramatically since the early 1900s. Together, with the advancements in chemical engineering and manufacturing capabilities, a boom in the production of elegant synthetic mimics of natural LHCs had occurred since the early 2000s. Both the biological LHCs and their mimics are discussed in detail in subsequent sections, with the latter forming the central and underlying theme of the present thesis.

## 1.2 Basic photochemistry

Before exploring the multi-chromophoric biological and biomimetic complexes described herein, one should acquire some basic appreciation of the photodynamics of light harvesting pigments. Therefore, a simplified overview of the processes that a photoactive molecule could undertake upon photoexcitation is presented in the current chapter. It is worth noting that, the aim of this section is merely to provide the reader sufficient familiarity with the processes and terminologies involved in the current thesis. Readers are encouraged to seek comprehensive details from other source of literature.<sup>15;16</sup>

### 1.2.1 Basic overview of molecular orbitals and excited states

At the turn of the 20<sup>th</sup> century, the understanding of the physical world was divided into two main categories, matter and light (or electromagnetic radiations), due to the relatively accurate description by two models, particles and waves respectively. However, the localised particulate description of matter breaks down when applied to atomic scale systems. This prompted a new wave of physicists to come up with an more unified theory, thus leading to the development of what is now considered one of the most successful theories to date, quantum mechanics, a theory that provides an accurate, unified description of the two previously separate entities. The staple of quantum mechanics is the well-known time-dependent Schrödinger equation,<sup>17</sup> with the following general form:

$$i\hbar\frac{\partial\Psi(\mathbf{r},t)}{\partial t} = \hat{H}\Psi(\mathbf{r},t) \quad (1.1)$$

where  $i = \sqrt{-1}$ ;  $\hbar$  is the reduced Planck constant ( $\frac{h}{2\pi}$ );  $\Psi(\mathbf{r},t)$  is the wave function dependent on position vector ( $\mathbf{r}$ ) and time ( $t$ ); and  $\hat{H}$  is the Hamiltonian operator, a function that describes all the inter/intramolecular interactions of the quantum system. While the time-dependent form of the Schrödinger’s equation could provide a description of all the molecular properties of a quantum body, the calculations of these are usually limited to systems with a small number of quantum bodies. Therefore, it is more viable to obtain a qualitative description of systems under investigation, namely the visualisation of electron waves as atomic and molecular orbitals (AOs and MOs, respectively) and the static potential energy (PE) of a given electronic configuration, which could be obtained by solving the time-independent form of the Schrödinger’s equation:

$$\hat{H}\Psi(\mathbf{r},\mathbf{R}) = E\Psi(\mathbf{r},\mathbf{R}) \quad (1.2)$$

where  $\Psi(\mathbf{r},\mathbf{R})$  is the wavefunction dependent on the electronic ( $\mathbf{r}$ ) and nuclear ( $\mathbf{R}$ ) coordinates; and  $E$  is the total energy eigenvalue of the system, given by the operator  $\hat{H}$  acting on  $\Psi(\mathbf{r},\mathbf{R})$ . However, this equation can only be solved analytically on systems consisting of no more than one electron. Therefore, for all systems studied in chemistry, the solution to these equations can only be approximated. The method adopted is the Born-Oppenheimer approximation, which takes advantage of the significant differences between the masses of electrons and nuclei. As such, electron reconfiguration (*i.e.* transition or movements) inside a molecule is considered instantaneous compared to those of the nuclei. Therefore, one could solve the electronic kinetic energy along a set of fixed coordinates of the nuclei. A more in-

formative description is perhaps best illustrated with an example of a simple system  $\text{H}_2^+$  ion, consisting of 2 nuclei and 1 electron. The full Hamiltonian ( $\hat{H}$ ) for this particular system is therefore:

$$\hat{H} = -\frac{\hbar^2}{2m_e} \cdot \frac{\partial^2}{\partial \mathbf{r}^2} - \sum_{i=1}^2 \frac{\hbar^2}{2m_i} \cdot \frac{\partial^2}{\partial \mathbf{R}_i^2} + V(\mathbf{r}, \mathbf{R}_1, \mathbf{R}_2) \quad (1.3)$$

where  $m_e$  and  $m_{i=1,2}$  are the masses of the electron and nucleus 1 and 2 respectively;  $\mathbf{r}$  and  $\mathbf{R}_{i=1,2}$  are the coordinates of the electron and two nuclei respectively.  $\hat{H}$  is further simplified into the following form:

$$\hat{H} = T_e + T_N + V \quad (1.4)$$

where  $T_e = -\frac{\hbar^2}{2m_e} \cdot \frac{\partial^2}{\partial \mathbf{r}^2}$ ,  $T_N = -\sum_{i=1}^2 \frac{\hbar^2}{2m_i} \cdot \frac{\partial^2}{\partial \mathbf{R}_i^2}$  and  $V = V(\mathbf{r}, \mathbf{R}_1, \mathbf{R}_2)$  are the electron kinetic energy, nuclear kinetic energy and the system's potential energy respectively. The time-independent Schrödinger equation then takes the following form:

$$\hat{H}\Psi(\mathbf{r}, \mathbf{R}_1, \mathbf{R}_2) = E\Psi(\mathbf{r}, \mathbf{R}_1, \mathbf{R}_2) \quad (1.5)$$

As mentioned, the nuclei coordination is fixed for each calculation, thus the complete wavefunction ( $\Psi$ ) of Equation (1.5) can be separated into the electronic and nuclear wavefunctions:

$$\Psi(\mathbf{r}, \mathbf{R}_1, \mathbf{R}_2) = \psi_e(\mathbf{r}; \mathbf{R}_1, \mathbf{R}_2)\psi_N(\mathbf{R}_1, \mathbf{R}_2) \quad (1.6)$$

where  $\psi_N$  is the nuclear wavefunction for nuclei at positions  $\mathbf{R}_1$  and  $\mathbf{R}_2$ ; and  $\psi_e$  is the electronic wavefunction dependent on both the electron position,  $\mathbf{r}$ , and nuclei positions. Thus, when substituting a trial solution into Equation (1.6), we get:

$$\hat{H}\psi_e\psi_N = \psi_N T_e \psi_e + \psi_e T_N \psi_N + V\psi_e\psi_N + W = E\psi_e\psi_N \quad (1.7)$$

where  $W = -\sum_{i=1}^2 \frac{\hbar^2}{2m_i} (2\frac{\partial \psi_e}{\partial \mathbf{R}_i} \cdot \frac{\partial \psi_N}{\partial \mathbf{R}_i} + \frac{\partial^2 \psi_e}{\partial \mathbf{R}_i^2} \cdot \psi_N)$ , which is usually neglected due to the presence of nuclear mass in the denominator. With some rearrangement of Equation (1.7), it becomes:

$$\psi_e T_N \psi_N + (T_e \psi_e + V\psi_e)\psi_N = E\psi_e\psi_N \quad (1.8)$$

The total energy can now be approximated by first solving the electronic wavefunction  $\psi_e$ :

$$T_e\psi_e + V\psi_e = E_e\psi_e \quad (1.9)$$

where the eigenvalue  $E_e$  is the electronic contribution to the total energy of the system, and the solution gives the electronic wavefunction ( $\psi_e$ ). By multiplying both sides with the complex conjugate of  $\psi_e$  and integration, the remaining, nuclear part of the equation is then:

$$T_N\psi_N + E_e\psi_N = E\psi_N \quad (1.10)$$

The solution to Equation (1.10) then gives the nuclear wavefunction ( $\psi_N$ ), and the eigenvalue  $E$  is the total energy of the system. This is a simple demonstration of the power of the Born-Oppenheimer approximation, the multicomponent system can now be solved by invoking this approximation, which allows the electronic component and nuclear components to be solved separately.

As mentioned, MOs are essentially the visualisation of the probability of the electron ‘existing’ within the position interval  $d\mathbf{r}$  ( $P_{\mathbf{r}}$ ), which is given by the Born rule:

$$P_{\mathbf{r}} = |\psi_e(\mathbf{r})|^2 d\mathbf{r} \quad (1.11)$$

where  $|\psi_e(\mathbf{r})|^2$  can be interpreted as the probability density electronic distribution with respect to a fixed nuclear geometry. The total integral of  $P_{\mathbf{r}}$  ( $P_T$ ) is normalised to 1:

$$P_T = \int_{-\infty}^{+\infty} |\psi_e(\mathbf{r})|^2 d\mathbf{r} = 1 \quad (1.12)$$

which is simply a statement of a fundamental law of probability statistics, in that over all space, the electron must exist, thus  $P_T = 1$ . Based on these, MOs can now be intuitively presented as probability density of electrons. Key considerations of the MOs will be discussed with reference to the model molecule benzene, visualised in Figure 1.3.<sup>15</sup>

As shown in Figure 1.3, chemical bonds may be considered as the interactions of the electrons of a set of atoms, or AOs. The AOs interfere either constructively or destructively (like waves) to generate a set of MOs. These MOs are shown for benzene as an example. In particular, when the waves are in phase, constructive interference (or addition of two positive waves) is observed between AOs (as seen between C atoms in  $\pi_1$ ); when out of phase, destructive interference (or addition of two positive and negative waves) is observed (as seen between C atoms in  $\pi_2$ ). When

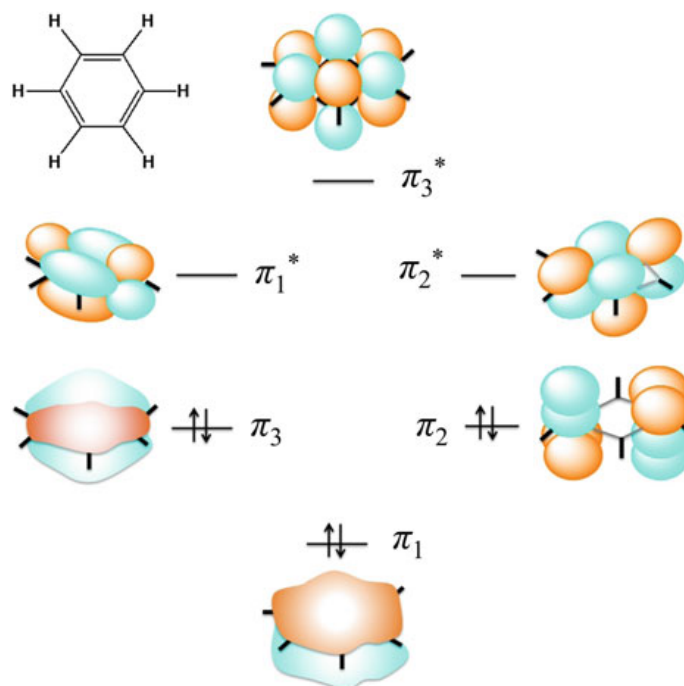


Figure 1.3: Visualised MOs of the model molecule benzene. Occupancy of orbitals are indicated by the up or down arrows and anti-bonding orbitals are denoted by  $*$ .<sup>15</sup>

undergoing photoexcitation, an electron absorbs energy, resulting in an exchange of orbital occupation. In most cases, these exchanges occur in the frontier orbitals, *i.e.* the highest occupied MO (HOMO) and lowest unoccupied MO (LUMO), of the unexcited molecule. In the case of benzene, the HOMO and LUMO are the  $\pi_2$  and  $\pi_3$  (degenerate) and  $\pi_1^*$  and  $\pi_2^*$  (degenerate) orbitals; the photoexcited state corresponding to the movement of an electron from a  $\pi$  to  $\pi^*$  orbital is denoted as a  $\pi\pi^*$  state. In addition, the spin of the electron needs to be considered, indicated by ' $\uparrow$ ' and ' $\downarrow$ ' in Figure 1.3. All photoexcitations require the preservation of the overall spin multiplicity of the molecule. This is one of the selection rules governed by the transition dipole moment of a molecule. Such an excited state is called a singlet state when the spin of both electrons are antiparallel, and is indicated by the superscript '1'; for example  $^1\pi\pi^*$  in the case of benzene. While the change of spin *via* direct photoexcitation can be considered forbidden, as in the probability of transition,  $p = 0$ , it could occur from a singlet excited state through other relaxation processes from the singlet states, such an excited state is called a triplet state with the denotation  $^3\pi\pi^*$ . In molecules, there exists, a large number of singlet and triplet excited states, and are usually referred to as  $S_n$  and  $T_n$  respectively, where  $n=1,2,3\cdots$  indicates the energy levels above the ground state

( $S_0$ ).

### 1.2.2 Photophysical processes of excited states

The photodynamics of a chromophore is perhaps best described with the visual aid of a generalised Jablonski diagram depicting all the major processes, presented in Figure 1.4.

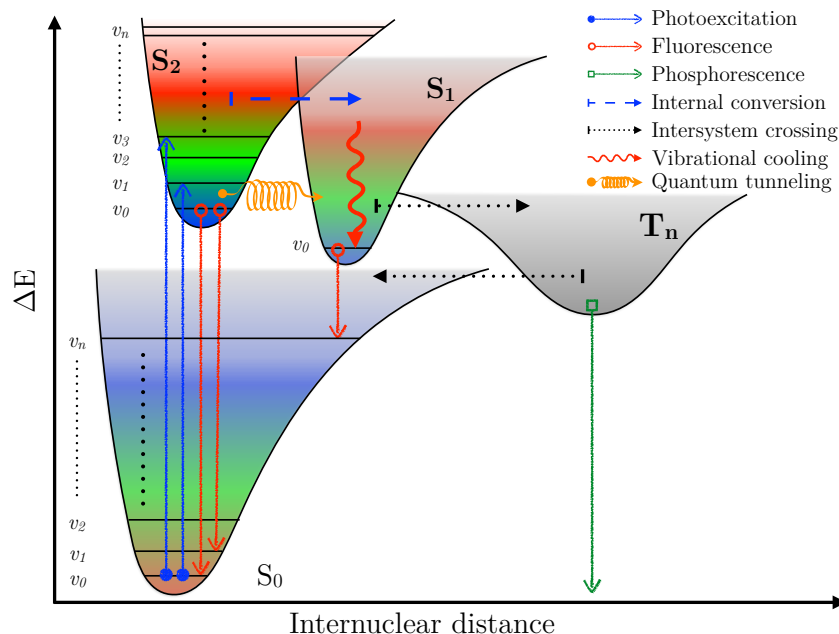


Figure 1.4: Schematic of possible photodynamic processes an excited state chromophore might undergo. Each possible relaxation pathway is associated with a different arrow type, with the details given in the legend. Vibrational modes within each state are represented as horizontal lines and are labelled  $v_{0,1,2\cdots n}$ .

As shown in Figure 1.4, there are a number of very well established photophysical processes for a chromophore. Firstly, photoexcitation, or absorption (blue solid arrows), as depicted in the scheme, are shown as vertical excitations. This could be considered a pictorial description of the Born-Oppenheimer approximation, which, in essence, states that due to the much greater mass of an atom's nucleus compared to its electrons, the nucleus would appear stationary during electronic movements/transitions. Thus, during photoexcitation, changes only occur along the energy axis of Figure 1.4, and are usually referred to as vertical transitions. The likelihood of a vibronic transition is determined by the overlap between the vibrational components of the respective electronic state's wavefunctions (from Equation (1.2)), which encompasses the Franck-Condon principle. Therefore, these transitions occur between vibrational modes of different MOs. However, as the number of vibrational

modes within each electronic state could be cumbersome to follow, they are often generalised to the collective states involved. Therefore, electronic transitions are usually denoted as  $S_n \leftarrow S_0$  ( $S_2 \leftarrow S_0$  in Figure 1.4).

Once the molecule is in its excited state, there are a number of processes for the molecule to dissipate this acquired energy. These are separated into two groups: radiative and non-radiative pathways, classified based on whether the process involves the emission of a photon. Again, with reference to Figure 1.4, the  $S_2$  state could either relax into  $S_1$  (denoted as  $S_2 \rightarrow S_1$ ) *via* the non-radiative pathways called internal conversion (IC, blue dashed arrows) or quantum tunnelling (orange cyclic arrows); or directly back to the ground state ( $S_2 \rightarrow S_0$ ) *via* the radiative process of fluorescence (red solid arrows). The likelihood of IC is determined similar to the vibronic transitions (wavefunction overlap), but with an additional principle known as the Fermi’s golden rule. This, in essence, states that the probability of a transition between two states is dependent on the density of vibronic modes of the destination state (number of vibrational modes per unit energy) denoted  $\rho$ . At the same energy level,  $\rho$  is generally higher for the lower energy state ( $S_1$  in this case). Thus, IC, when available, is usually one of the faster pathways and hence preferred in most systems. Fluorescence from the highest lying states are therefore usually relatively weak due to the rapid relaxation in to lower energy states *via* IC. Finally, quantum tunnelling is often slower given that it is an energetically barriered process and is usually out-competed by other processes in solvated systems, hence is not considered in the current thesis.

After these initial relaxation processes, the molecule is now in the  $S_1$  excited state (*via* IC of  $S_2 \rightarrow S_1$ ). In addition to the two aforementioned processes, namely IC and fluorescence, both resulting in  $S_1 \rightarrow S_0$ , three additional non-radiative pathways are available. The first two processes involve the relaxation within the molecule’s vibrational modes: i) intramolecular vibrational-energy redistribution (IVR), in which the average vibrational quantum number for a specific mode reduces; and ii) intermolecular vibrational energy transfer (IET), where  $v_0$  is reached by dissipating the energy to the surrounding molecules. Of the two processes, IET only occurs in the presence of a molecular bath, which could be in the form of solvent molecules. As IVR and IET are both related to the vibrational modes of the excited state, they are sometimes considered concurrently, especially in solvated systems and are referred to as vibrational cooling (red curly arrow). The third process is the transition from the singlet state into triplet states ( $S_1 \rightarrow T_n$ ), called intersystem crossing (ISC, black dotted arrows). As mentioned in Section 1.2.1, the transition between singlet and triplet states involves the ‘flipping’ of the spin of the electrons involved, which re-

duces their probability significantly. Therefore, ISC is usually the slowest process, and is generally the major contributor for photophysical observations beyond ns time scales. It is important to note that all the discussed relaxation pathways (IC, quantum tunnelling, IET, IVR, ISC and fluorescence) are available to all singlet excited states, but are discussed with regard to  $S_2$  and  $S_1$  separately for clarity.

Finally, the remaining molecules relaxed to their triplet states could return to  $S_0$  along three potential pathways. The first is the aforementioned non-radiative ISC, but in the reversed order  $T_n \rightarrow S_0$ . The second is the non-radiative process collisional cooling. As the name suggests, this process involves the molecule dissipating its excited energy by simply colliding into another molecule, which could only take place in solvated system and is facilitated by the long life time of triplet states ( $\mu\text{s}$ – $\text{ms}$ ). The last process, is the radiative pathway known as phosphorescence. This process is usually quenched by collisional cooling in solution as they take place in similar time frame at ambient temperatures, thus are usually only observed in solutions below the freezing temperature of the solvent, or in bulk solids of the chromophores.

Based on the discussion so far, one could summarise that the photodynamics of a chromophore could be viewed as the movements of electrons. One of the corner stones of modern science is the ability to observe the phenomenon under study. As such, researchers have strived to develop instruments capable of directly observing how a molecule relaxes from a higher energy state to a lower energy state. We will now have a brief look at the events that led to the developments of ultrafast spectroscopy.

### 1.2.3 The road towards ‘seeing’ electronic movement - a brief history of ultrafast laser technologies

Two major factors which limit human’s awareness of their surroundings are space and time. In the spatial domain, observable resolutions had been the limit of what our eyes could see, until the invention of optics. The first compound microscope developed by Robert Hooke in 1665 facilitated the observations of microbial organisms.<sup>18</sup> Over time light microscopy technologies have evolved to sub-cellular resolutions with techniques such as confocal microscopy. In conjunction with fluorescence-tags, localisation of protein could be identified with confidence.<sup>19</sup> Alternative techniques such as electron microscopy, atomic force microscopy and scanning probe microscopy *etc.* further pushed the spatial observation into atomic scales.

On the other hand, the concept of observing an event in a time-resolved fashion was first demonstrated by Eadweard Muybridge with his motion picture of the galloping horse in 1878. This was achieved by taking 24 consecutive pictures

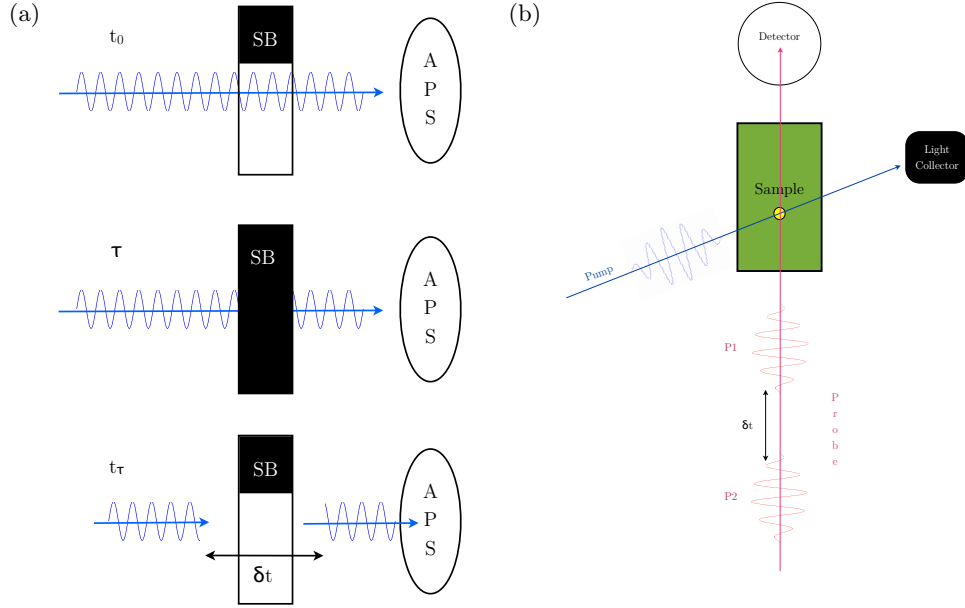


Figure 1.5: Two methods of making time resolved observations. (a) The most basic method, a continuous train of light passes through the open shutter block (SB) at  $t_0$ . The shutter (or optical chopper in some cases) closes the SB for a short time ( $\tau$ ) then opens again. Thus, this method artificially generates pulses of light by ‘chopping’ the light into small fragments where time resolution, ( $\delta t$ ) is determined by the speed of the ‘chopper’. The sensor, an active pixel sensor (APS) in this example, then captures information as a series of events. Time resolution afforded by this method is sufficient for observing some sub-cellular events. (b) The method utilising short pulses of lights, enabled by laser technology. Time delay,  $\Delta t$ , is introduced by varying the light path. The optical density (OD) of the first probe pulse, P1 ( $OD_{t_0}$ ), is synchronised to hit the sample with the incident pump pulse, as well as that of the second probe pulse, P2 ( $OD_{t_\tau}$ ), arriving after  $\Delta t$ , are recorded by the detector. The difference between the two readings provides information on the events taking place at this time scale. Time resolution of this method is largely limited by the pulse width of light generated.

over the distance the galloping horse travels in one second, which set the standard of 24 frames per second (*ca.* 42 ms between each frame) for the filming and television industries, still implemented in present days. Developments of technology subsequently matured and the standard method is illustrated in Figure 1.5a, where a shutter or optical chopper blocks a continuous train of light, introducing a time delay ( $\Delta t$ ), which then opens again to observe the event after  $\Delta t$ . The time delay is therefore directly determined by the speed at which the shutter can physically open and close. The modern digital cameras perform all of the processes with microprocessors, improving the temporal resolution by moving the speed bottleneck to photon detector processing speeds. These developments facilitated the technologies capable of capturing events at up to 1 ms resolution (1000 frames per second). In conjunction with microscopy technology development, scientists can now observe sub-cellular events within living organisms.<sup>20</sup>

However, photodynamics of a molecular system, which, as discussed in the preceding section, could be considered the motion of atoms and electrons, take place on a much shorter time scale than those of cellular processes (ms scale). To put this in perspective, the speed of atomic motion at ambient temperature is *ca.*  $1 \text{ km}\cdot\text{s}^{-1}$  and the typical distance of an atomic bond is  $1 \text{ \AA}$  ( $10^{-10} \text{ m}$ ). To observe this motion, a time resolution of  $\frac{1 \times 10^{-10} \text{ m}}{1000 \text{ ms}^{-1}} = 1 \times 10^{-13} \text{ s}$ , or 100 femtoseconds (fs,  $1 \times 10^{-15} \text{ s}$ ) is required.<sup>21</sup> This was made possible by the advent of laser technology in 1960.<sup>22</sup> Based on this invention, picosecond (ps,  $1 \times 10^{-12} \text{ s}$ ) to sub-ps pulses of light could be produced, with the method referred to as ‘mode-locking’. The most commonly practised method for the generation of sub-ps light pulses at the time employed saturable dyes as the mode-locker to produce intense short pulses of light.<sup>23;24</sup> A simple schematic is shown in Figure 1.5b to illustrates the basic principle of such time-resolved spectroscopy experiments. The development of dye-lasers continued and eventually generated pulses as short as 6 fs,<sup>25</sup> and served as the work horse of time-resolved spectroscopy studies. However, they were gradually replaced upon the demonstration of 60 fs pulses being generated by solid-state Ti:Sapphire (Ti-sapp) lasers in 1991,<sup>26</sup> eventually reaching *ca.* 4 fs.<sup>27;28</sup> While the ability of Ti-sapp to generate such short pulses of light in the absence of a saturable absorber surprised researchers of the time, the mechanism of operation was soon explained by what is now referred to as ‘Kerr Lens Mode-locking’.<sup>29–31</sup> These breakthroughs thus paved the way for revealing the photophysical processes for a multitude of chromophores. For further details into the operation of lasers, the reader is directed towards references elsewhere.<sup>21;32</sup>

This then leads us to the discussion on the experiments observing the aforementioned photophysical processes facilitated by the advancements in ultrafast laser technologies.

#### 1.2.4 Basic interpretations of ultrafast pump-probe spectroscopy experiments

With the tools of observing molecular photorelaxation processes available, a brief description of these experiments, namely ultrafast pump-probe spectroscopy facilitated by sub-ps light pulses is warranted. There are two major techniques of ultrafast spectroscopy experiments, in the gas phase or condensed phase. For the gas phase experiment, the molecule is first vaporised, and subsequent observations are conducted under vacuum. This type of experiment allows the complete isolation of the molecules of interest, away from environmental perturbations. Thus the complete photophysical processes could be identified when combined with sufficient quantum

mechanical calculations. As such, this is an extremely powerful technique for obtaining a thorough understanding of the photochemistry and photophysics undergone by the molecule, especially with the utilisation of time of flight mass spectroscopy and velocity map imaging (VMI). However, the current thesis is focused purely on the condensed phase experiments, therefore, the details of VMI are not discussed further. Readers are instead directed towards comprehensive literature reviews of this powerful technique.<sup>33–36</sup>

We shall now briefly describe the observations obtained by the pump-probe experiments conducted in the condensed phase. In this type of experiment, the molecule or system of interests could take the form of solid, liquid or solvated in a solvent of choice. However, for the current thesis, the systems under study were all in the solution. The experiments utilising the pump-probe spectroscopy techniques described in Section 1.2.3 are referred to as transient electronic absorption spectroscopy (TEAS), the interpretation of the resulting observations will be discussed with reference to Figure 1.6.

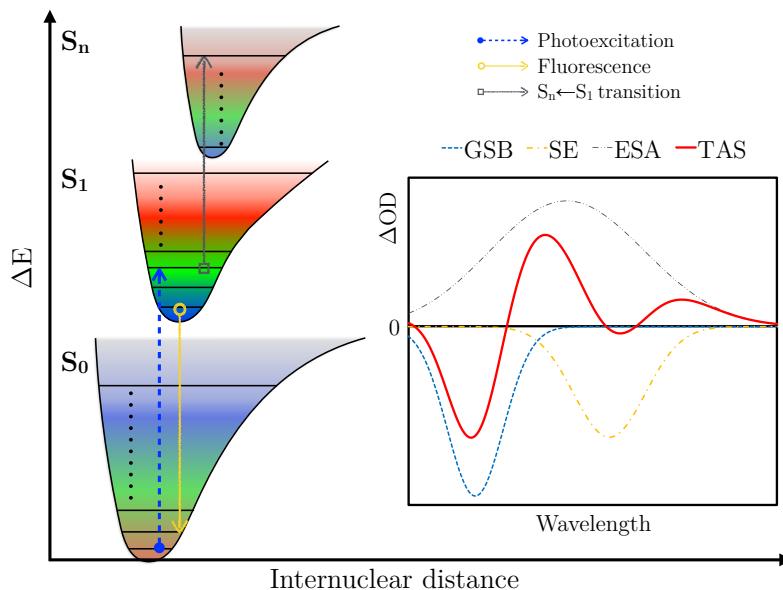


Figure 1.6: Typical observations of difference spectra from TEAS experiments, as well as the photophysical processes corresponding to the features demonstrated. Where: GSB–ground state bleaching; SE–stimulated emission; ESA–excited state absorption; and TAS–transient absorption spectrum.

Briefly, in a TEAS experiment, a difference spectrum is generated by subtracting the UV-Vis spectrum of sample prior to photoexcitation by the pump pulse from the spectrum collected at a chosen time delay post photoexcitation. By varying the time delay for each spectrum, a set of difference spectra are collected in an

experiment. These collective spectra are referred to as transient absorption spectra (TAS). Each spectral trace of TAS could be considered the absorption spectrum of the molecule under study at that particular time post-photoexcitation. As mentioned in Section 1.2.2, there are a few photophysical processes that a molecule can undergo. First, is the photoexcitation (dashed blue arrow, Figure 1.6), in this process, certain fraction of molecules that are populated in the ground state is transitioned into their excited state ( $S_1$  in the case shown in Figure 1.6). This in turn depletes some of the population in the ground state,  $S_0$ , and as a result, the absorption of the corresponding  $S_1 \leftarrow S_0$  transition is reduced. This reduction is manifested in the form of a negative feature similar to the molecule’s static UV-Vis absorptions (blue dashed trace in Figure 1.6), and is usually referred to as ground state bleach (GSB). The dashed arrow in Figure 1.6 therefore indicates this loss of absorption.

The newly generated  $S_1$  population can now undergo further photoexcitation into the  $S_n$  excited states, such processes are referred to as excited state absorption (ESA). These transitions are usually different in energy compared to the  $S_1 \leftarrow S_0$  transition, hence often manifest as a positive feature in the TAS, shown as the grey dashed trace in Figure 1.6.

Lastly, all radiative processes are usually observed as stimulated emissions (SE). This is caused by the probe pulse inducing the photoexcited molecule to emit a photon in the identical direction of propagation of the probe pulse. As a result, the extra photons detected from this process are observed as negative features in the TAS, shown as the yellow dashed trace in Figure 1.6. It is important to note that, SE only occurs for optically allowed transitions and therefore, shares similar spectral features as the static fluorescence emission spectrum of the system under study. The combination of these aforementioned components then give rise to the observed spectral features in a TAS, shown as the solid red trace in Figure 1.6.

These then provide the time constants at which potential photodynamic processes can take place. The data fitting can be performed either on individual traces or globally. In the former case, the analysis can be completed in a very rapid manner as each time trace could be treated independently. However, the information obtained may not be representative of the overall dynamics. In contrast, global fitting procedures are generally more computationally expensive and can be time consuming. However, these expenses are justified as the information obtained with global fitting is much more descriptive and provides a much greater degree of insight into the observed dynamics. Therefore, the global fitting procedure was chosen for the analysis of TAS presented in the current thesis. Through the procedures described in Section 2.7.3, the decay associated spectra (DAS) can be obtained for each time

constant, hence the photophysical process associated with the time constant. In particular, the shapes of the DAS are highly informative in guiding the interpretation of the TAS. As a general rule, any negative components correspond to an exponential rise in that population whilst any positive components correspond to an exponential decay in population. The flow of excited state populations can be visualised in the DAS when a positive and a negative features appear concomitantly. This can be interpreted as either a change in electronic state (IC or ISC), or relaxation within a single electronically excited state (IET).<sup>37;38</sup>

With the basic appreciations on photodynamic processes and the technique involved in their observations, a brief discussion on the key properties of biological photosynthetic systems is presented in the following section.

### 1.3 Biological light harvesting complexes (LHCs)

Photosynthetic organisms could be considered one of the foundations of the ecosystems on the Earth's surface, providing the oxygen and food required for sustaining most, if not all, of the animal kingdom. As such, photosynthesis is one of the most important biochemical processes for life on Earth. A simplistic view of photosynthesis could be in the form of a device combining PVs and a battery, where energy from the sun is harvested (similar to PVs) and stored in the form of carbohydrates (similar to a battery), using CO<sub>2</sub> and water as raw materials and releasing oxygen as a by-product. Animals and other forms of life lacking photosynthetic capability then consume both the oxygen and carbohydrates (and other nutrients subsequently produced using carbohydrates) during their daily activities, while releasing CO<sub>2</sub> as their by-product. The two organelles in eukaryotic organisms responsible for these processes are chloroplast in plants and mitochondria in animals, analogous to a solar powered battery pack and a transformer in common electronics. Therefore, macroscopically speaking, the biosphere on Earth's surface could be considered a large sophisticated device that cycles CO<sub>2</sub> and oxygen, sustained by the sun and water.

Thanks to their significance in agricultural yield, the photosynthesis process has been extensively studied over the years. As such, the biochemical reactions involved are relatively well understood, with the key elements mostly identified. The overview of the reactions found in light harvesting plants is presented in Figure 1.7.

Briefly, the two major pathways involved in photosynthesis found in plants are the light dependent pathway (light reaction) and the light independent pathway (dark reaction). The light reaction, as the name suggests, collects energy from sunlight to split water, which initiates the overall process and generates a bank of

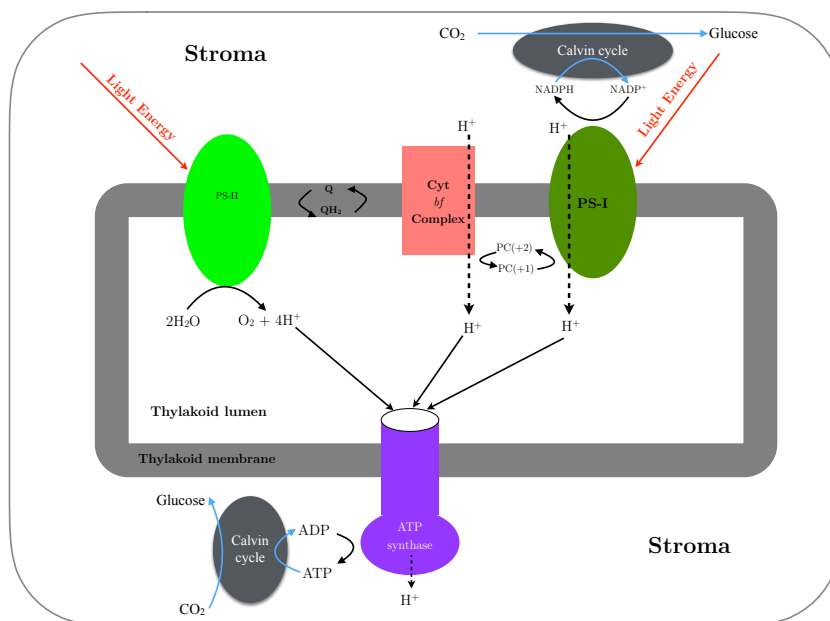


Figure 1.7: Schematic of light reaction pathway, recreated based on the illustration by F.M. Harold.<sup>39</sup> Light energy is first absorbed by PS-II, splitting water into protons and atomic oxygen, with plastoquinone (Q) as the electron acceptor, reduced to plastoquinol ( $Q \rightarrow QH_2$ ). The electron from  $QH_2$  is then transferred to plastocyanin (PC) by the cytochrome *bf* (Cyt *bf*) complex, transporting a proton from the stroma into the thylakoid lumen. PS-I then completes this energy transfer with the aid of additional light energy to reduce nicotinamide adenine dinucleotide phosphate (NADP<sup>+</sup>) into NADPH, as well as transporting another proton into the thylakoid lumen. The 6 protons generated in these processes give rise to a proton gradient across the thylakoid membrane, driving the adenosine triphosphate (ATP) synthase and storing all the energy in the form of ATP, the bio-energy unit utilised in most biochemical processes. The ATP and NADPH generated are then used in the dark reaction, or Calvin cycle, to produce glucose from CO<sub>2</sub>, without the need of light.

small reactive intermediates (ATP and NADPH). The dark reactions, also known as the Calvin cycle, then converts these energetic intermediates into more stable molecules, in the form of glucose and eventually fatty acids as the long term energy storage. Of the two processes, the light dependent pathway is of particular interest to synthetic light harvesting applications, thanks to their extremely high light to chemical energy transfer efficiencies, reaching 80% in photosystem II (PS-II) and 100% in photosystem I (PS-I),<sup>40</sup> surpassing even the most efficient experimental PVs (*ca.* 46%).<sup>4</sup> However, the efficiency at converting light into energy forms usable by humans (firewood and food) drops to a mere 1%, due to processes required for supporting the plant's own survival. Therefore, mimics of PS-I and PS-II may improve the efficiencies of current and future synthetic light harvesting devices, hence their competitiveness against fossil fuel based energy sources, as discussed in Section 1.1.

### 1.3.1 Structure of LHCs

Although the determinations of molecular structures of crystals has progressed rapidly since the first demonstration with NaCl by William and Lawrence Bragg in 1913,<sup>41</sup> the first protein structure, of myoglobin, was not solved until 45 years later by Kendrew and co-workers.<sup>42</sup> This was largely due to the difficulties entailed in obtaining a diffraction grade protein crystal. In comparison, the photosystems (PSs) from higher plants are much greater not only in size, but also in complexity, making their crystallisation even more challenging. Furthermore the vast quantity of purified PS complexes required, along with the lack of a rapid expression system of plant PSs, added further complications to obtaining the molecular structure of PS complexes. Thus, somewhat unsurprisingly, the progress towards solving the molecular structure of PSs was relatively slow, limited by technologies available to both fields of crystallography and biochemistry. These challenges were rapidly overcome with the discovery of photosynthetic cyanobacteria. The first crystal structure of a PS-I complex at 4 Å resolution, of the cyanobacterium *Synechococcus elongatus*, was reported nearly 3 decades after the publication of the crystal structure of myoglobin.<sup>43</sup> Subsequent to this report, tremendous progress has been made in the biochemical and crystallography technologies, leading to an exponential growth in the number of PS structures solved. We will now briefly discuss the general chromophoric arrangements of PSs, with reference to the recently reported structure of PS-I from the pea plants, resolved to the impressive resolution of 2.8 Å, presented in Figure 1.8.<sup>44</sup>

As shown in Figure 1.8, the arrangement of pigment molecules is highly complex within PS-I from pea plant. However, such complexity also comes with surprisingly minimalistic design principles. Firstly, carotenoids ( $\beta$ -carotene, violaxanthin and lutein) are scattered between the two main light absorbing units: chlorophyll A (CLA) and chlorophyll B (CLB). These carotenoids are considered the ‘wires’ of the LHCs, both structurally and photophysically. Secondly, upon close inspection, one could clearly see a concentric circle of CLAs (cyan in Figure 1.8b) around the so called ‘special pair’ of CLAs, which connect to the primary electron acceptor phyloquinone (magenta in Figure 1.8b) and the three  $\text{Fe}_4\text{S}_4$  clusters. Thirdly, one could observe an outer ring of pigments, built up with a mixture of CLAs and CLBs (purple in Figure 1.8b). Interestingly, CLBs reside almost exclusively on positions furthest from the inner ring, with the connection between the two rings made up of exclusively CLAs. In essence, the design principle could be viewed as the search for the optimal stacking of rings consisting of pigment molecules, centered around the special CLA pair.

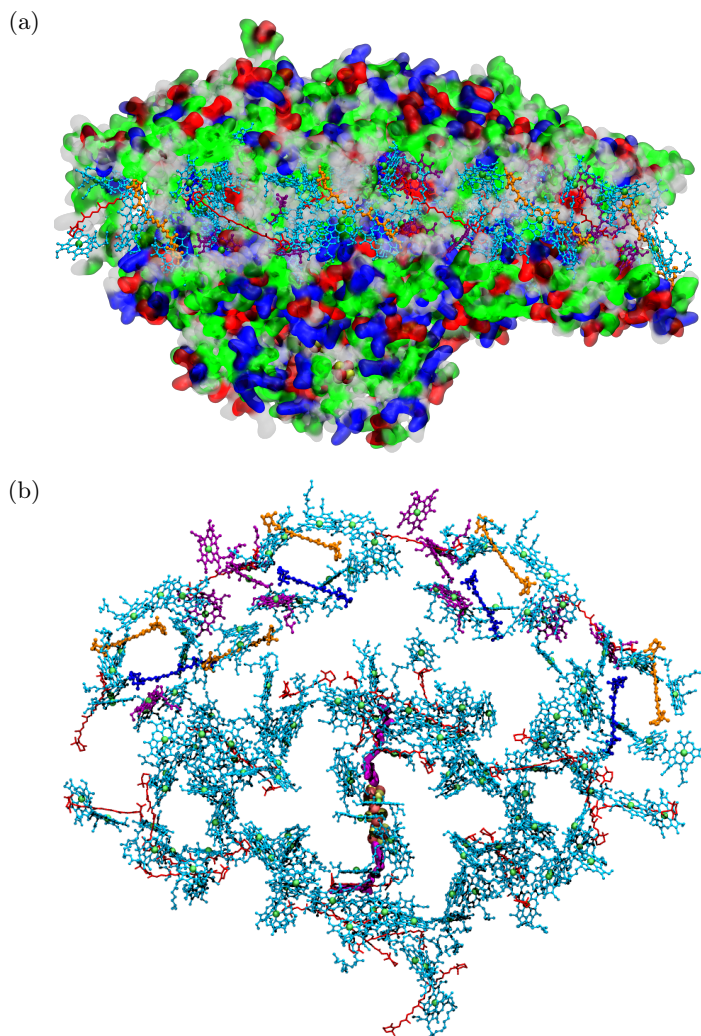


Figure 1.8: Crystal structure of PS-I from the pea plant, (a) from the side and, (b) top views (protein backbone is removed for clarity).<sup>44</sup> Rendered with the software package VMD.<sup>45–47</sup> The protein chains are presented as surfaces from the side view only for clarity, and are coloured by residue type: acidic–red; basic–blue; non-polar (hydrophobic)–grey; polar (hydrophilic)–green. Pigment molecules are coloured by type: chlorophyll A–cyan; chlorophyll B–purple; phylloquinone–magenta;  $\beta$ -carotene–red; violaxanthin–violet; lutein–orange. Elements of special interest are represented as spheres, where: Mg–green; S–yellow; and Fe–red.

### 1.3.2 Excited energy transfer mechanisms in natural LHCs

While the structural biology field enjoyed much limelight with their revelation of LHC structures, the biophysical communities did not stay stagnant and made significant contributions towards solving the secret of the LHCs' extraordinary efficiencies. This was largely thanks to the advent of ultrafast (sub 100 fs) solid-state Ti-sapp laser technologies, as chronicled in Section 1.2.3. Indeed, thanks to the coherent collabo-

rative efforts of biochemical and biophysical communities, a torrent of experimental and theoretical investigation on the ultrafast (fs–ps time scales) photodynamics of LHCs are now available.<sup>44;48–59</sup> With these works, scientists now have a good grasp of the time frame at which most energy transfer pathways take place in biological LHCs, recently summarised in an extensive review by Scholes and co-workers, with the time frame illustrated in Figure 1.9.<sup>60</sup>

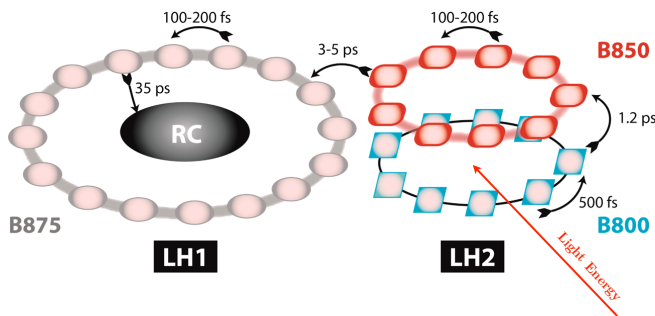


Figure 1.9: Schematic of excited energy transfer in LHCs found in purple bacteria, rate time constants are indicated on arrows corresponding to each processes.<sup>60;61</sup> LH1–light harvesting complex I; LH2–light harvesting complex II; RC–reaction centre. Labels B800, B850 and B875 are colloquial names for the individual components of LHCs.

As shown in Figure 1.9, the excited energy transfer (EET) between chromophores are extremely rapid, with time constants averaging  $\sim 300$  fs. The inter-complex EET is completed within the time scale of  $\sim 1.2$ – $5$  ps. Finally, the harvested photoexcited energy is transferred into the reaction centre (RC), with the time constant of  $\sim 35$  ps. Such rapid rate of EET into the RC has been widely considered the key to achieving their quantum efficiency. The secret for these impressive rates of EET is now relatively well-deciphered, with the state-of-the-art two-dimensional Fourier transform electronic spectroscopy experiments. These experiments, first applied with great success by Fleming and co-workers,<sup>62</sup> revealed evidence of quantum coherence within the Fenna–Matthews–Olson (FMO) bacteriochlorophyll complex from *Chlorobium tepidum*.<sup>57</sup> Furthermore, these experiments were conducted with the FMO complex solvated in water, at ambient temperature. Such a feat had been considered close to impossible due to the significant noise in condensed-phase systems. This in turn gave rise to the observed rapid rate of photoexcited energy from collective pigment molecules funnelling into the RC of the LHCs. This ability of rapid inter-chromophore and inter-complex EET then became one of the most prized properties that the synthetic community seek to reproduce in synthetic complexes. Thus, a brief discussion on the established EET mechanism in these complex assemblies is warranted. Together with the basic processes discussed in Section 1.2, a simplistic

overview of potential photophysical pathways could be established. We first consider the three candidate mechanisms for EET to occur: the classical downhill pathway, Förster type incoherent energy transfer (FIET), and coherent phonon-induced relaxation (CPIR).

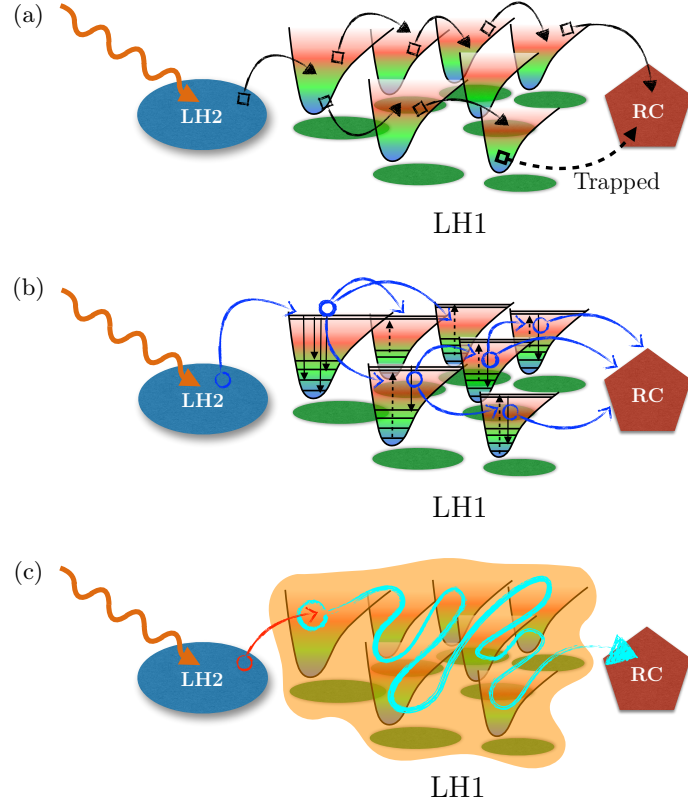


Figure 1.10: Pictorial description of potential EET mechanisms. LH2–light harvesting complex II; LH1–light harvesting complex I; RC–reaction centre. (a) Classical downhill energy transfer. Solid arrows indicate energy transfer and dashed arrow indicate restricted transfer due to a trapping site. (b) Förster type incoherent energy transfer. Transfer of excited energy is possible as long as a ‘matching’ excitation (upward dashed arrows) is available for the relaxation (downward solid arrows). Blue arrows indicate possible energy hopping routes. (c) Coherent phonon-induced relaxation. The collective chromophores essentially become a single ‘superstate’, as such, energy could ‘travel’ anywhere within the ensemble until being transfer to the RC. Cyan arrow indicate possible EET paths within collective chromophores.

With reference to Figure 1.10, of the three EET mechanisms, the classical mechanism (Figure 1.10a), where the excited energy moves progressively downwards until reaching the lowest potential energy well, is the most ineffective for EET due to the potential trapping of excited energy by a local minima amongst the collective chromophores. In comparison, photoexcited energy can ‘hop’ between ‘donors’ and ‘acceptors’ with the FIET mechanism (Figure 1.10b).<sup>63;64</sup> This could occur as long as matching relaxation and excitation, *i.e.* of identical energy difference, are available

within the effective FIET range (aptly coined the ‘Förster distance’), thus minimising the probability of being trapped. Finally, CPIR (Figure 1.10c) can be considered as an exploitation of the quantum mechanical concept of superpositions of quantum states, where with sufficient coupling between chromophores, a collective superstate could exist until the excess electronic energy is transferred to the destination.<sup>65;66</sup> Therefore, the concept of a trap is simply not applicable to CPIR. While the two mechanisms transport electronic energy through different properties of the chromophores: the hopping of emissive transitions in the case of FIET and the direct coupling and extension of the chromophores’ molecular orbitals in the case of CPIR, they can both overcome the limitation of a classical trap. However, CPIR is generally harder to achieve, due to the strong chromophoric coupling (hence precise spatial arrangement between chromophores) required as well as the interference introduced by the surrounding bath of the chromophores. With the wide range of arrangements and time scales for all EET processes observed within biological LHCs, it is generally accepted that both FIET and CPIR are utilised in LHCs, with FIET being, in general, the dominant mechanism between weakly coupled pigments and *vice versa*. The pictorial summary of the EET mechanisms in biological LHCs, namely FIET and CPIR, is presented in Figure 1.11.

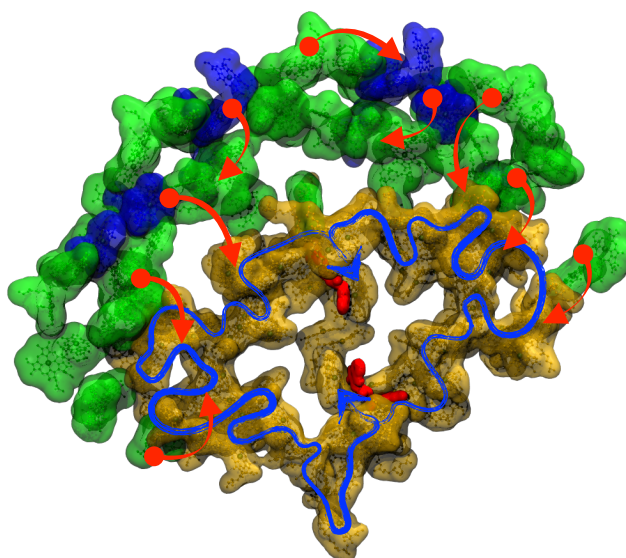


Figure 1.11: Illustrations of biological EET pathways using the structure of PS-I from the pea plant as a template.<sup>44</sup> CLA and CLB from the antenna complex are coloured green and blue respectively, CLA of the reaction centre are coloured light brown. Red arrows indicate FIET hopping of the energy, and the blue lines indicate the random path of energy for the CPIR mechanism, before reaching the special pair of CLA indicated by the two arrow heads.

## 1.4 Photovoltaic cells and state of the art synthetic mimics

With the impressive properties discussed in Section 1.3, biological LHCs have naturally inspired the scientific community to attempt the creation of synthetic systems that mimic and ultimately exceed the achievements of evolution. Indeed, numerous multi-chromophoric arrays with increasing complexity and elegance have been reported in the past 2 decades since the report of the PS-I structure. In the present section, a brief description of the functional mechanism of photovoltaic cells is presented; followed by the introduction of the basic synthetic pigment analogue, porphyrins; and exemplar state-of-the-art arrays created using these sub-units.

### 1.4.1 Basic functional principle of photovoltaic cells

As stated previously, photovoltaic cells (PVCs) could be considered the direct analogue to the light reactions utilised in light harvesting organisms of modern day technologies. On the one hand, PVCs exploit photoactive components to harvest light energy provided by the sun in similar fashion to LHCs. On the other hand, unlike the process of photosynthesis, which stores the excitation energy into chemical intermediates (as discussed in Section 1.3), PVCs generally convert these energy into electronic movements, resulting in the generation of electricity. While there are a number of different types of PVCs,<sup>1;5;6;67;68</sup> they tend to follow similar construction and functional principles. A simple overview of the main components involved is illustrated in Figure 1.12

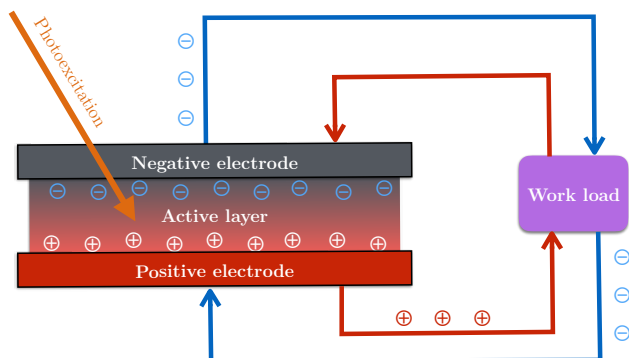


Figure 1.12: A schematic of the main functional components of a typical PVC. Recreated from the work by Cheng *et al.*<sup>1</sup>

With reference to Figure 1.12, a typical PVC device consists of four major components, with the photoactive material residing in the active layer. These ma-

materials are generally semiconductors or composites of electron donors and acceptors. For devices built with semiconductors, the electrons are simply photoexcited into the conduction band, generating an electron flow into the negative electrode, through the circuitry, and back into the positive electrode. For the composite materials, electrons within the donor material is promoted higher energy levels (referred to as excitons). The excitons generated then migrate over the bulk donor materials until being transferred to the acceptor materials. These excess electrons in the acceptor layers are then collected by the negative electrode; while the depleted electrons (referred to as holes) in the donor materials are replenished from the positive electrode. Therefore, the current flow could be visualised as the movement of either excitons or holes. The electricity generated through these processes are applied to a work load. Of the many types of PVC technologies, the dye-sensitised solar cells (DSC) bear the most similarity to the biological LHCs.<sup>2;3;5</sup> A schematic of the working principle of DSCs is shown in Figure 1.13.

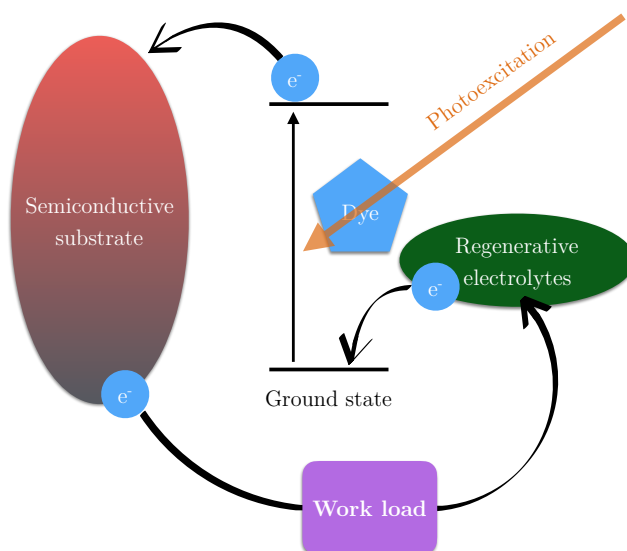


Figure 1.13: A schematic of a typical DSC device. Adapted from the work by Grätzel and co-workers.<sup>3</sup>

Briefly, upon photoexcitation of the dye molecule, the promoted electron is directly injected into the semiconductive substrate. This then generates an exciton excess, which gives rise to the current flow in identical manner as previously described. However, as the dye molecule is now oxidised, electrolytes (usually solubilised in organic solvents) are required to regenerate the dye molecule at the positive electrode. The electrolytes usually perform this duty by first capturing the electron from the positive electrode, which is then donated to the dye molecule. This approach

offers the reduction in cost by allowing the selection of cheaper semiconductive materials while improving their efficiencies by introducing a chromophore that extend the spectral coverage of the DSC. As suggested by Grätzel,<sup>3</sup> the ideal photosensitiser should exhibit close to unity photoexcitation energy transfer to the semiconducting layer. Therefore, a synthetic complex capable of achieving similar efficiency to those found in biological LHCs could be highly beneficial towards the development of DSC technologies.

### 1.4.2 Porphyrins

One of the most commonly-used synthetic analogues to chlorophylls are by far the porphyrin variations. These are used in multiple applications such as, and not limited to, a photosensitiser extending the absorption range of PVs, or as a pseudo reaction core for other sensitiser chromophores.<sup>69–71</sup> The structures of the two main chlorophyll variants,<sup>72</sup> and the basic (unmodified) porphyrin is shown in Figure 1.14.

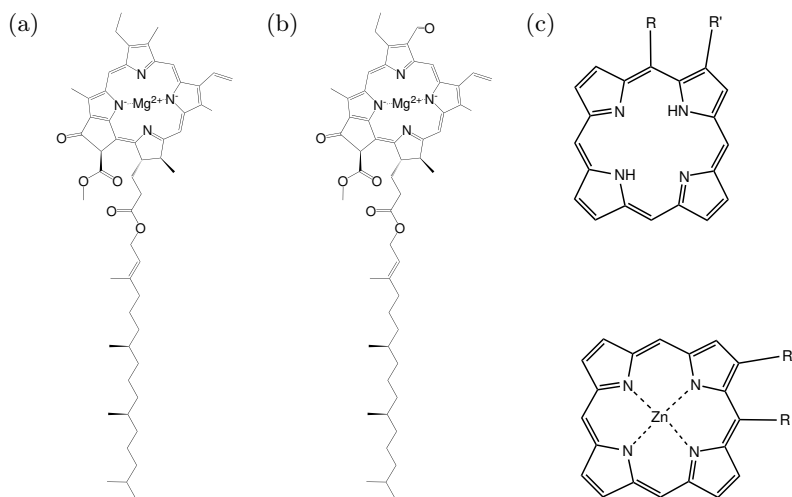


Figure 1.14: Chemical structures of (a) CLA; (b) CLB; and (c), (top) freebase and (bottom) Zn-porphyrin, the two main sites for possible functionalisation, *meso* and  $\beta$ , are labelled R and R' respectively.

As shown in Figure 1.14, the basic structure of porphyrins closely resembles the aromatic core of the two chlorophyll variants. In addition to their resemblance, the main reason for the wide adoption of porphyrins by the synthetic communities is their facile modifications. In particular, a total of 12 sites, grouped as two general positions are available for modification. The first is the 4 sites at the *meso* positions, and the second being the 8 sites at the  $\beta$  position, an example site of each are labelled R and R' in Figure 1.14c respectively. Of the two modification sites, the *meso* position is the most easily modified. This is thanks to the efforts by the syn-

thetic chemistry communities, most notably the Lindsay group, whose introduction of the porphyrin synthesis technique, coined the ‘Lindsay method’, gave way to the large bank of *meso*-modified porphyrins in the literature.<sup>73–77</sup> The general Lindsay synthesis of a porphyrin is shown in Figure 1.15.

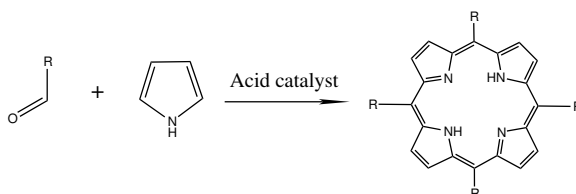


Figure 1.15: Basic Lindsay synthesis conditions.

As shown in Figure 1.15, the most basic Lindsay reaction involves a functionalised aldehyde and a pyrrole molecule, catalysed by acid. The reaction could be considered a series of condensation reactions between the functionalised aldehyde and pyrrole molecules. Upon the final macro-ring closure of an oligomer consisting of 4 pyrrole monomers, the cyclic intermediate is then oxidised, yielding the desired porphyrin product. The brief summary of the reaction mechanism is shown in Figure 1.16.

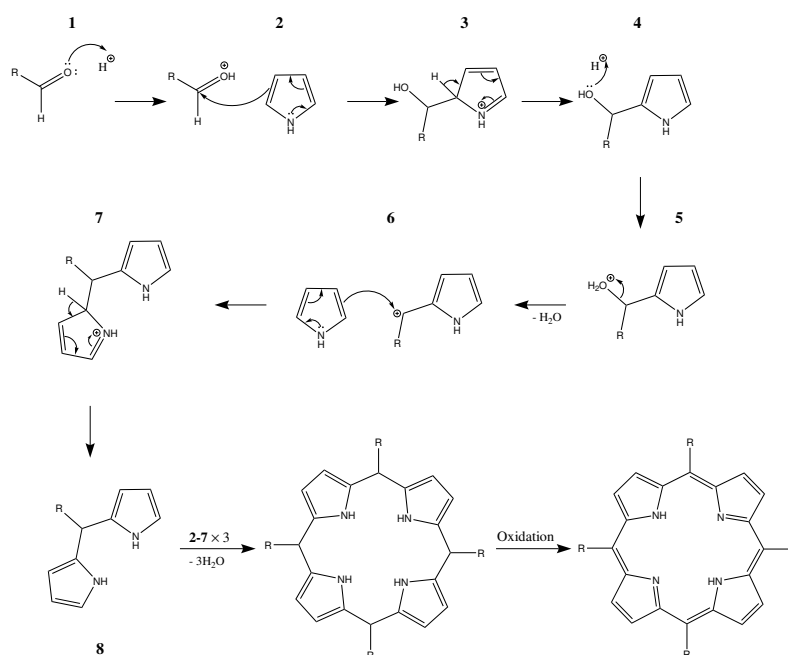


Figure 1.16: Basic overview of the reaction mechanisms in the Lindsay synthesis of porphyrin. Steps 1–7 are then repeated until a macro-cyclic pyrrole oligomer is formed, which is subsequently oxidised to produce the desired porphyrin.

Furthermore, different functional groups could be introduced to the 4 available sites by mixing variants of the aldehyde in the reaction. However, precise functionalisations of desired sites tend to require stepwise synthesis of individual building blocks. The synthetic steps employed for the current thesis will be discussed in detail in Section 4.2.2. Due to their role as a popular LHC mimic component, the photophysical properties of porphyrins are also very well studied. A typical UV-Vis spectrum and the four frontier MOs of a porphyrin molecule are shown in Figure 1.17.

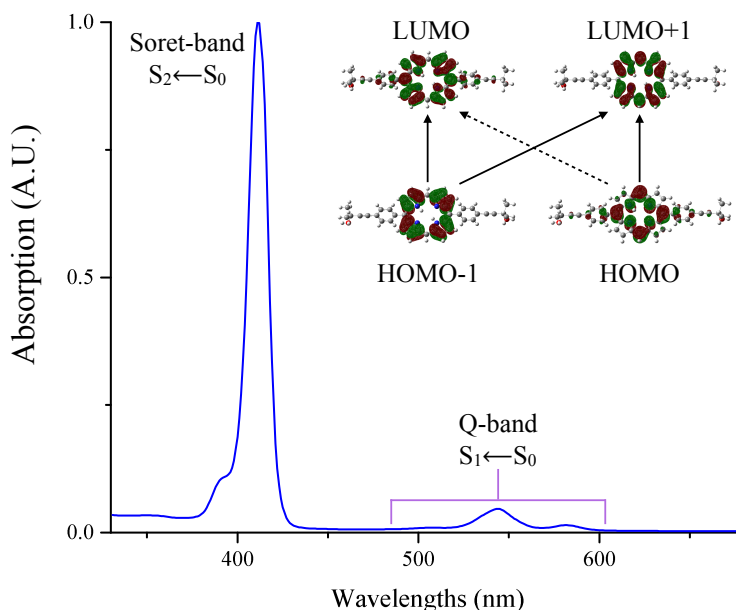


Figure 1.17: An example of the UV-Vis spectrum of porphyrin, the absorption peaks corresponding to the excited states are labelled accordingly. Inset shows the four frontier molecular orbitals, highest occupied (HOMO and HOMO-1) and lowest unoccupied (LUMO and LUMO+1), described by Gouterman,<sup>78</sup> with arrows indicating possible transitions between the MOs presented.

Briefly, most porphyrin species exhibit an intense absorption band corresponding to the  $S_2 \leftarrow S_0$  transition, traditionally known as the ‘Soret-band’; the absorptions corresponding to  $S_1 \leftarrow S_0$ , known as the ‘Q-band’, are generally weaker and show various degrees of splitting, depending on the degree of degeneracy between the excited state electronic configurations. The nature of these transitions has been well described by the Gouterman’s four-orbital model.<sup>78</sup> As shown in Figure 1.17, the strong absorption at the Soret-band makes porphyrin a very good candidate for light harvesting pigments. While porphyrins are relatively well utilised as sensitisers for PVs,<sup>69–71</sup> one of the most impressive advancements in their utilisations is arguably the constructions of sophisticated multi-porphyrin arrays. As the full scope of the research area has been very well documented in the literatures elsewhere,<sup>79–83</sup>

subsequent discussions will focus on a few select examples of particular relevance to the present thesis.

### 1.4.3 Ligand directed arrangement of porphyrin

Ligand directed arrangements of porphyrin can be considered a relatively flexible construction method that rely mainly on metal to ligand interactions, and are also more similar to how chlorophylls are arranged within biological LHCs, as discussed in Section 1.3.1. While there are a multitude of reported systems of arrays produced using this method, we will focus on the system demonstrated by Kobuke and co-workers, capable of intermolecular EET at the time scales of *ca.* 13–21 ps.<sup>84;85</sup> The structural arrangement and building blocks are shown in Figure 1.18.<sup>84;85</sup>

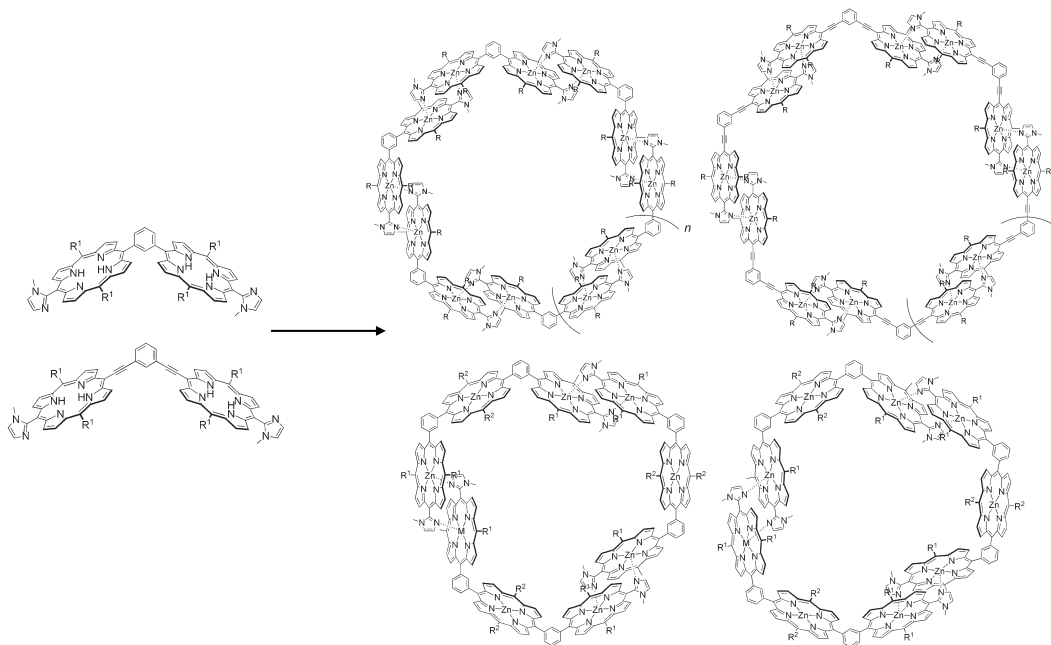


Figure 1.18: An example of a large cyclic array of porphyrin arranged by N donor (from ligand) to Zn metal (from porphyrins) interactions. Demonstrated by Kobuke and co-workers.<sup>84;85</sup>

As shown in the example in Figure 1.18, the ligand directed assemblies of porphyrin arrays largely exploit the interaction between the metal centre of the porphyrin and the N-donor ligand, giving rise to a few specific design rules. First, metallated porphyrins are required. Second, a non-bonding ( $n$ ) molecular orbital (N-donor) is usually required for stable interactions between the porphyrin metal centre and ligand, in most cases amine or carbonyl groups are utilised. Third, initial building blocks are usually oligomers of  $n$ -porphyrins ( $n=2-3$ ). In the case shown in Figure 1.18, two porphyrins are conjugated to a phenyl at the 1 and 3 positions to

create the angles needed to establish a ring-like final assembly pattern. The versatility of this particular method is further demonstrated by the insertion of a ‘guest’ molecule into the cavity of the macro porphyrin ring, as shown in Figure 1.19.<sup>85</sup>

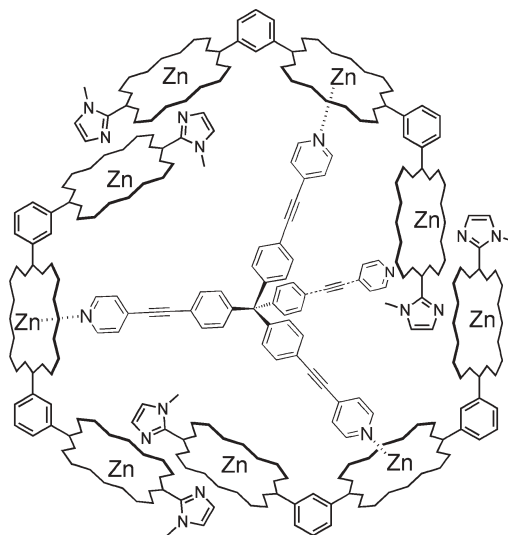


Figure 1.19: The insertion of a ‘guest’ molecule into macro-molecular porphyrin ring assembly, demonstrated by Kobuke and co-workers.<sup>85</sup>

As a result of the ligand directed nature of these assemblies, they are highly versatile, as individual components could be designed and produced separately. However, their sensitivity towards disruptions from their environment such as changes in solvents are also increased due to the delicate nature of the metal to N-donor interactions. In some cases, conjugations between building blocks are performed post assembly to improve their stability. This then leads onto the second method in creating multi-porphyrin arrays.

#### 1.4.4 Direct conjugation of porphyrin

At the other end of the spectrum, the direct conjugation of  $n$ -porphyrins ( $n \geq 4$ ) may be considered less flexible method of producing multi-porphyrin arrays, however, the arrays are much more structurally stable as a result of the direct conjugation between porphyrin sub-units. As such, they are much more robust and are very resilient towards environmental disruptions, when compared to the ligand directed macro-assemblies. The general method in making such an array involves two main steps, first, by creating a set of linear poly-porphyrins, as shown in Figure 1.20. Traditionally, the porphyrin polymer then undergoes a final coupling step to join the two ‘open ends’ to give the final cyclic poly-porphyrin array. However, such

syntheses are usually very low yielding and required highly dilute solutions, due to the inability to prevent coupling between separate polymers chains.

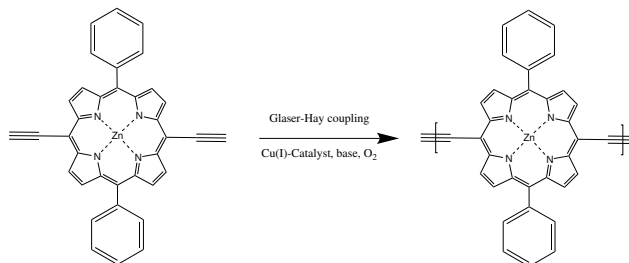


Figure 1.20: The synthesis of basic linear porphyrin polymers by Glaser-Hay coupling.

This limitation was overcome with the introduction of a structural template to the final ‘closing’ step. This was mainly pioneered by the Anderson group, who demonstrated a number of highly elegant porphyrin rings constructed using such methods.<sup>86–89</sup> Of particular interest to the author is the hexadentate template, a hexaarylbenzene (HAB) variant, first reported by Anderson and co-worker in 2008.<sup>90</sup> The template to poly-porphyrin interaction is shown in Figure 1.21.

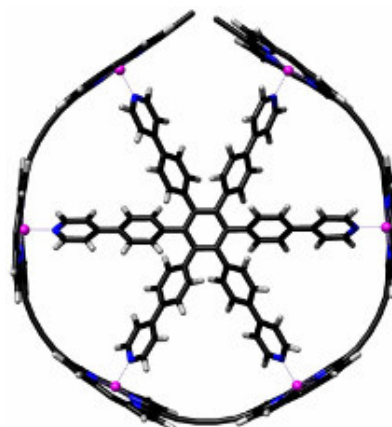


Figure 1.21: The demonstration of hexadentate template to poly-porphyrin interaction by Anderson and co-workers.<sup>90</sup>

As shown in Figure 1.21, the presence of a template introduces additional metal (Zn from porphyrin) to ligand (N donor from the template) interactions. These interactions then mould the linear poly-porphyrin around the shape of the template molecule. As such, by holding the polymer at the desired configuration prior to the final coupling step, the yield of cyclic final products could be significantly improved. With this powerful synthetic tool, a number of impressive macro assemblies between cyclic arrays of poly-porphyrin were demonstrated. A selected few of these state-of-

the-art poly-porphyrin rings are shown in Figure 1.22.<sup>87;91;92</sup>

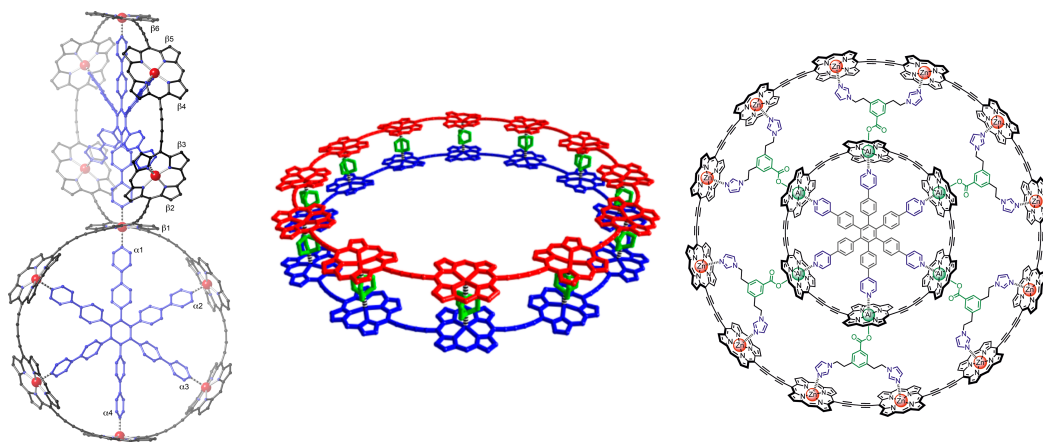


Figure 1.22: Selected examples of multi-ring assemblies demonstrated by Anderson and co-workers. From left to right, spiro-fused nano-rings;<sup>91</sup> coordinated double-deck assembly in the presence of 1,4-diazabicyclo[2.2.2]octane;<sup>87</sup> and the Russian doll-like multi-component assembly with the hexadentate template and two porphyrin nano-rings of different sizes.<sup>92</sup>

In addition to their impressively elegant structural arrangements, these nanostructures also demonstrated photophysical properties that mimics the biological LHCs. In particular, upon closure of the poly-porphyrin ring shown in Figure 1.21, the completed assembled system demonstrated the corporative enhancements between porphyrin monomers. This resulted in the strong two photon absorption cross section (*i.e.* the potential to be photoexcited to a higher energy state by two photons of lower energy) of  $\sim 10^5$  GM (Goeppert-Mayer units,  $1 \text{ GM} = 10^{-50} \text{ cm}^{-4} \cdot \text{s-photon}^{-1}$ ) per porphyrin unit, a remarkable 5000 fold enhancement compared to the monomers (20 GM) employed.<sup>93;94</sup> Furthermore, excited energy from the inner ring of the Russian doll complex (Figure 1.22, right) had been demonstrated to migrate into the outer ring within the time frame of  $\sim 40$  ps.<sup>92</sup> As such, this 9-component complex not only closely resembled the multi-concentric rings structure of the PS-I described in Section 1.3.1, but also the capability of inter-ring EET at ps times scales, as discussed in Section 1.3.2.

As demonstrated by all the examples described in this section, the synthetic chemistry community has produced a number of porphyrin arrays with structural elegance and complexity approaching those found in biological LHCs. However, as mentioned in the opening of the chapter, there is still scope for improvements to be made in the production of biomimetic photoactive systems. This will be discussed in the final section of this chapter.

## 1.5 Concept and aim of present project

As impressive as the brilliant display of porphyrin nano-arrays showcased in Section 1.4 were, they are still limited by a few factors. Firstly, these assemblies are rarely soluble in aqueous media, hence usually constructed in organic solutions. While these are of little concern to a lot of applications such as traditional PVs and organic photonics, they are in contrast to the aqueous media where most biology thrives. Secondly, the extensive stacking of the porphyrin molecules could lead to significantly altered photophysical properties. Although these properties could be employed by natural LHCs through precise arrangements, the synthetic systems still lack such specificity, thus coordinating solvents are usually required to prevent uncontrolled stacking of chromophores. Thirdly, all the aforementioned nano-arrays required, to some degree, the direct conjugation between chromophores, which is in contrast to the lack of direct inter-chromophore conjugations found in biological light harvesting complexes. Last, but certainly not least, is that all the discussed systems require highly complex procedures, often involving a large number of synthetic steps. While they are achievable for the experts in the fields and skilled chemists on laboratory scales, industrial scale synthesis of these systems may be prohibitively expensive. Thus the wider adoption of these nano-arrays into industrial applications remains challenging. Therefore, the author's aims at the start of the thesis work was to contribute to the field by attempting to address the following questions:

- Can we create a self-assembled system containing porphyrin and other photosensitisers in aqueous media – thus a closer mimic to biological LHCs?
- Can such a system prevent the extensive stacking of porphyrins without the use of coordinating solvent, even upon assembly – which could improve modularity and ease of their productions?
- Can such a system be produced with minimal and approachable synthetic methods – potentially paving the way towards industrial adoption?

The most important question is perhaps the first one, which will allow the investigation of the subsequent two. We will therefore, begin with a brief look at the choice of methods for tackling this challenge.

### 1.5.1 Polymer nano assemblies

For the first question, namely the creation of self-assembled system containing porphyrin, examples already exist in the literature, but not in the field of biomimetic

light harvesting applications. Instead, they are largely utilised in the field of bio-imaging research or photodynamic therapies, which incorporate porphyrins into some amphiphilic systems with small water soluble functional groups forming self-reporting nano particles in aqueous media.<sup>95–98</sup> However, due to their application-oriented design, which only exploited the chromophores’ static photophysical properties, there has been an apparent paucity of investigations into their ultrafast dynamics. Furthermore, the nanostructure of these assemblies appear relatively limited in variation and tunability. We have therefore chosen to explore the potential of polymer chemistry, which, in recent years, researchers have produced well-defined polymer-based self-assembled structures with relatively simple synthetic methods that are easily scaled up.<sup>99–103</sup>

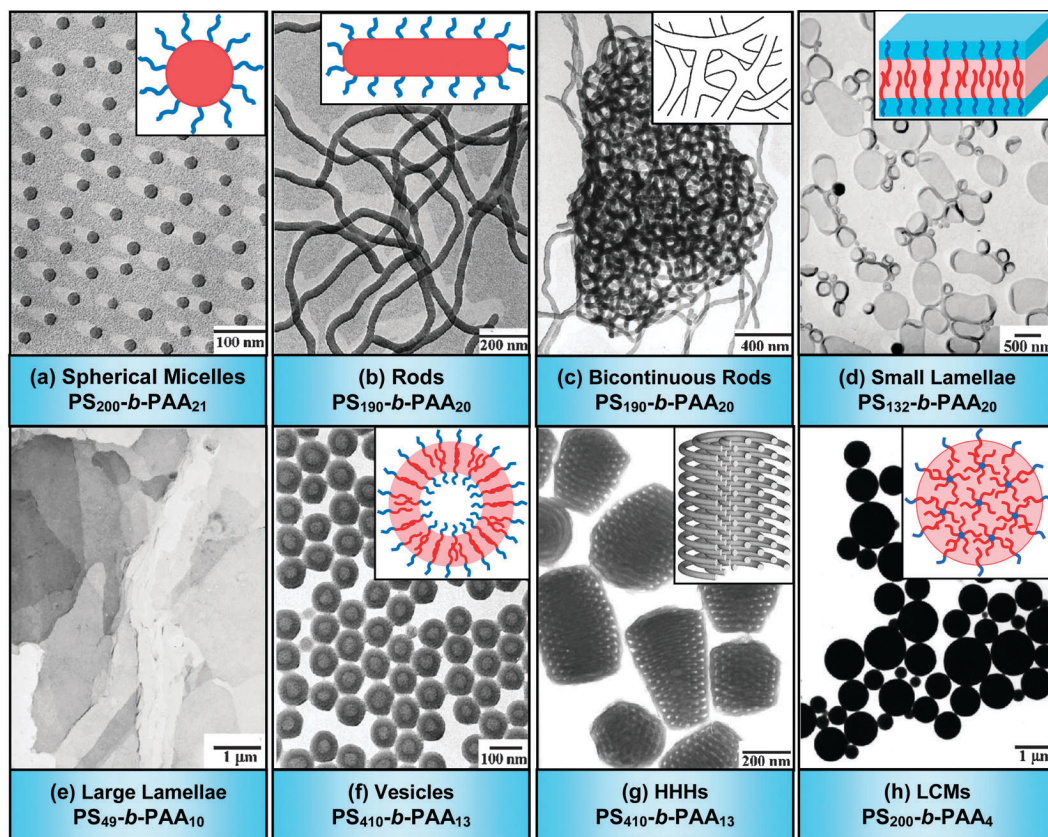


Figure 1.23: Examples of the range of nanostructures possible with block copolymers.<sup>99;104</sup> PS–poly-styrene; PAA–poly-acrylic acid; HHHs–hexagonally packed hollow hoops; LCMs–large compound micelles.

The resultant self-assembled structures formed from block copolymers are determined by the volume ratio between the solvophilic and solvophobic blocks.<sup>101</sup> As such, the resultant assembly could be tuned by simply varying the lengths of the am-

phiphilic chains, making them highly versatile systems. The range of morphologies available are illustrated in Figure 1.23.<sup>99</sup> With the maturing techniques in precision polymer synthesis,<sup>105;106</sup> even more complex morphologies will be easily accessible in time. In addition, it was recently reported that self-assembly could be achieved by simply blending two types of polymer prior to direct dissolution into water, further boosting its simplicity.<sup>107</sup>

With these benefits discussed, polymers were chosen as the assembly vehicle for the current thesis. This leads to the discussion of a potential sensitiser in conjunction with porphyrin.

### 1.5.2 Maleimide - a potential photosensitiser

Although the Soret-band absorptions of porphyrin variants are very strong as mentioned in Section 1.4.2, they are limited to a relatively small spectral range. In comparison, chlorophylls from natural LHC cover a much broader spectral range, with two intense absorption bands of *ca.* 375–525 nm and 625–700 nm.<sup>108;109</sup> Therefore, it would benefit a light harvesting system by introducing a photosensitiser, a secondary chromophore covering a different region of the UV-Vis spectrum. As discussed in Section 1.2, the FIET hopping between chromophores relies on the presence of excitation and relaxation transitions with identical/similar energy levels. These are generally perceived as overlaps between the donor’s emission spectrum and the acceptor’s absorption spectrum. As such, fluorescence close to the Soret-band absorption of porphyrin (see Figure 1.17) is a requirement for potential sensitisers.

It was recently reported that maleimide, a common handle for protein tagging through thiol-ene coupling,<sup>110–112</sup> exhibited high fluorescent emissions upon amino or thiol functionalisations on the 2 and/or 3 positions.<sup>113;114</sup> The emissions in these reports show very strong spectral overlap with the porphyrin Soret-band. Other reports also suggested that aggregation induced emission could be introduced with certain *N*-modifications.<sup>115–117</sup> The former case is especially enticing for the purpose of the current thesis as no aggregation is required, thus simplifying the design processes. Furthermore, functionalisation of maleimides often involve very simple synthetic techniques and relatively inexpensive reagents,<sup>113;114</sup> making them highly versatile. However, the fluorescence of the maleimides have been reported to be universally quenched upon solvation in protic solvent, illustrated in Figure 1.24.

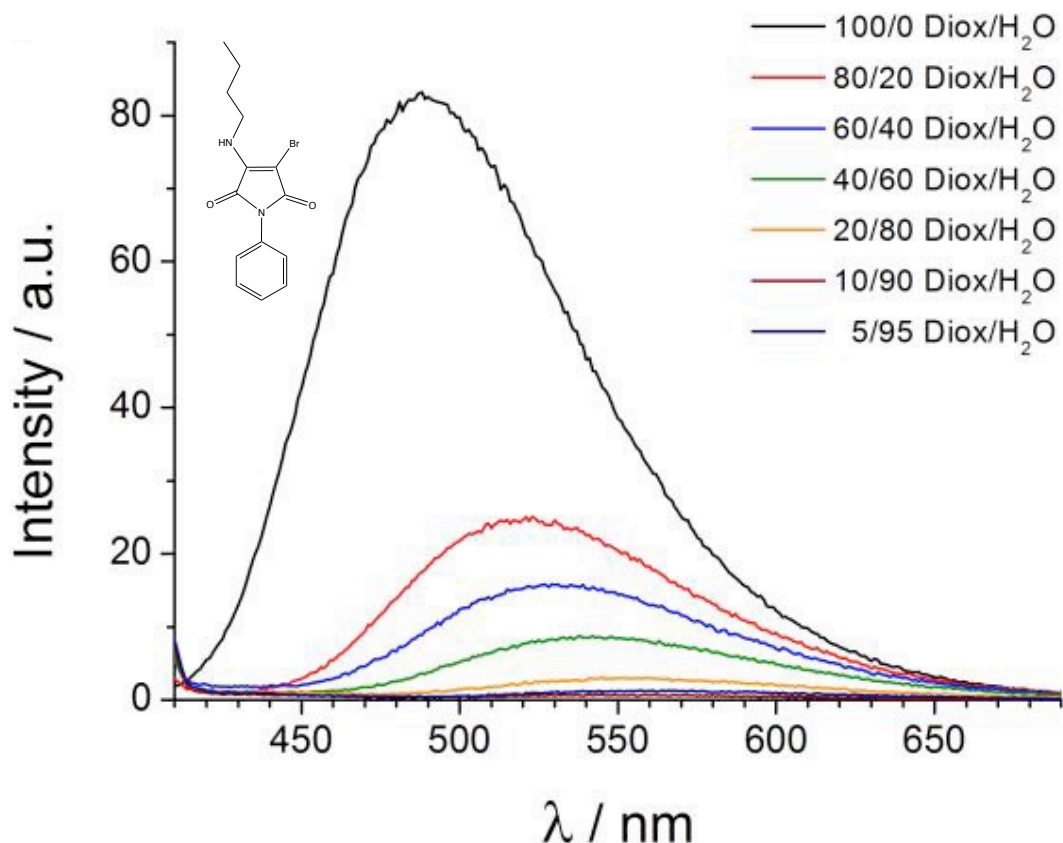


Figure 1.24: The fluorescence spectra of a model amino-maleimide (structure shown in the inset), Diox=dioxane, reported by Mabire *et al.*<sup>113</sup> The intensity of the fluorescence suffers clear reduction as water content increases.

As shown in Figure 1.24, the fluorescence of the model amino-maleimide is almost fully quenched in a mixed solvent of 95% water in dioxane. In the field of bio-imaging, this environment sensing property was utilised to identify disassembly of micelles by the fluorescence life time imaging (FLIM) technique.<sup>114</sup> However, for the remit of the current thesis, the fluorescence intensity of this system in water is a key consideration. Therefore, the nature of such quenching needs to be investigated to determine their viability as a sensitiser pigment.

### 1.5.3 The ultimate aim

With decisions for the assembly vehicle and sensitiser made, the concept of the current thesis is therefore to establish the feasibility of constructing a polymer-porphyrin conjugate that could self assemble. The ultimate goal is illustrated in Figure 1.25.

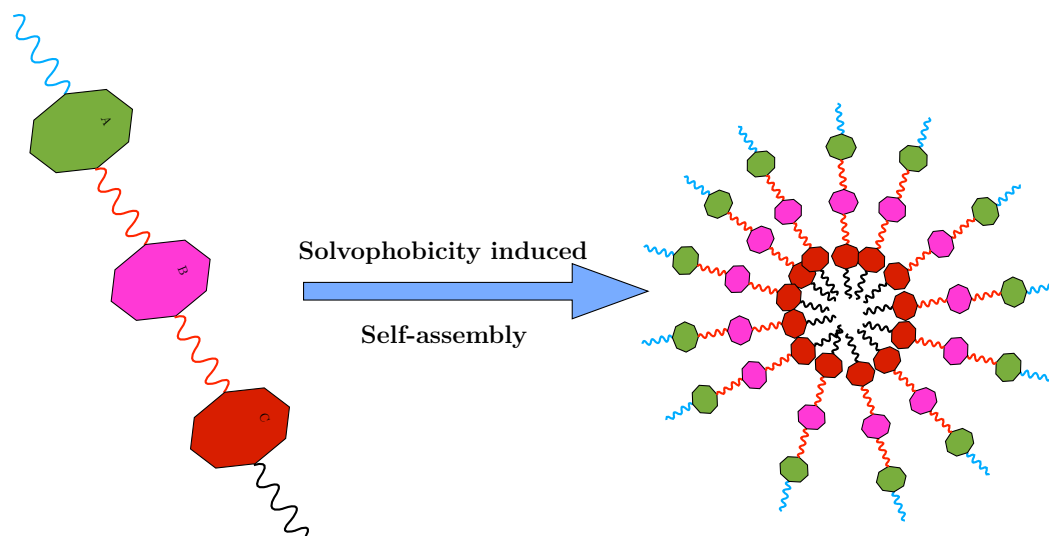


Figure 1.25: A schematic illustrating the current project design concept. Blocks labelled in different colours and letters represent the different chromophores that harvest light collaboratively. Curly lines of different colours represent polymers with differing properties. The collection of all the polymer-chromophore conjugates then assemble by solvophobic interactions.

With reference to Figure 1.25, the ultimate goal of the project was to create a system with multiple chromophores covering a large spectral range complimenting each other. These chromophores are interlinked with polymers or functional groups, for purposes such as photo-protection, energy transfer enhancements and an artificial reaction core etc. These conjugates would then be assembled into a macro-reactor capable of performing the light driven reactions, which could be designed based on the desired application by varying the individual components of the conjugate.

#### 1.5.4 The scope of the current thesis

While the ultimate goal for the overall project is the production of a multi-chromophoric system that could perform a wide range of photo-induced reaction in aqueous environments, as illustrated in Section 1.5.3, such an endeavour is beyond the scope of the current thesis. As will be revealed in the ensuing chapters, the current thesis can contribute to the creation of such a system. This has been made possible through the following fundamental and proof-of-concept experiments:

- Determination of the mechanism behind the fluorescence quenching of amino-maleimide in protic solvent and thus its feasibility as an upstream sensitiser.
- Screening for the simplest synthetic method for producing polymer-porphyrin conjugates in sufficient quantities.

- Assemble polymer-porphyrin conjugates and upon assembly, determine if the degree of stacking is controlled.
- Determine the feasibility of applying such an assembly method for producing multi-chromophoric biomimetic nanostructures.

With these insights, more complex systems could be built in the future, which would help generate a potentially economically viable system in-line with the one envisioned in Section 1.5.3.

## References

- [1] Y.-J. Cheng, S.-H. Yang and C.-S. Hsu, *Chem. Rev.*, 2009, **109**, 5868–5923.
- [2] U. Bach, D. Lupo, P. Comte, J. Moser, F. Weissörtel, J. Salbeck, H. Spreitzer and M. Grätzel, *Nature*, 1998, **395**, 583–585.
- [3] M. Grätzel, *Acc. Chem. Res.*, 2009, **42**, 1788–1798.
- [4] National Renewable Energy Laboratory, U.S. Department of Energy, *Efficiency chart*, [http://www.nrel.gov/ncpv/images/efficiency\\_chart.jpg](http://www.nrel.gov/ncpv/images/efficiency_chart.jpg), 2015.
- [5] M. Grätzel, *J. Photochem. Photobiol., B*, 2003, **4**, 145–153.
- [6] S. Günes, H. Neugebauer and N. S. Sariciftci, *Chem. Rev.*, 2007, **107**, 1324–1338.
- [7] R. J. Francey, C. M. Trudinger, M. van der Schoot, R. M. Law, P. B. Krummel, R. L. Langenfelds, L. P. Steele, C. E. Allison, A. R. Stavert, R. J. Andres and C. Roedenbeck, *Nat. Clim. Change*, 2013, **3**, 520–524.
- [8] C. Le Quéré, C. Rödenbeck, E. T. Buitenhuis, T. J. Conway, R. Langenfelds, A. Gomez, C. Labuschagne, M. Ramonet, T. Nakazawa, N. Metzl *et al.*, *science*, 2007, **316**, 1735–1738.
- [9] Orkustofnun–National Energy Authority of Iceland, *Geothermal*, <http://www.nea.is/geothermal/>, 2016.
- [10] D. Clery, *Science*, 2015, **348**, 854–856.
- [11] National Renewable Energy Laboratory, U.S. Department of Energy., *Simple Model of the Atmospheric Radiative Transfer of Sunshine (SMARTS)*, [http://www.nrel.gov/rredc/smarts/smarts\\_files.html](http://www.nrel.gov/rredc/smarts/smarts_files.html), 2010.

- [12] Q. Schiermeier, J. Tollefson, T. Scully, A. Witze and O. Morton, *Nature*, 2008, **454**, 816–823.
- [13] Center for International Earth Science Information Network. Columbia University, Palisades, *Global Rural–Urban mapping project: urban/rural extents*, <http://sedac.ciesin.columbia.edu/data/collection/gpw-v4>, 2008.
- [14] C. Zheng and D. M. Kammen, *Energy Policy*, 2014, **67**, 159–169.
- [15] P. Evans, Rachel C. and Douglas and H. D. Burrow, *Applied Photochemistry*, Springer Netherlands, 1st edn., 2013.
- [16] P. W. Atkins and R. S. Friedman, *Molecular Quantum Mechanics*, Oxford University Press, 5th edn., 2011.
- [17] E. Schrödinger, *Phys. Rev.*, 1926, **28**, 1049–1070.
- [18] R. Hooke, *Micrographia, Some Physiological Descriptions of Minute Bodies Made by Magnifying Glasses with Observations and Inquiries Thereupon*, Public Domain, 1665.
- [19] L. Alanko, T. Porkka-Heiskanen and S. Soinila, *J. Chem. Neuroanat.*, 2006, **31**, 162–168.
- [20] R. Davies, J. Graham and M. Canepari, *J. Microsc.*, 2013, **251**, 5–13.
- [21] A. H. Zewail, *J. Phys. Chem. A*, 2000, **104**, 5660–5694.
- [22] T. H. Maiman, *Nature*, 1960, **187**, 493–494.
- [23] F. P. Schafer, W. Schmidt and J. Volze, *Appl. Phys. Lett.*, 1966, **9**, 306–309.
- [24] A. J. DeMaria, D. A. Stetser and H. Heynau, *Appl. Phys. Lett.*, 1966, **8**, 174–176.
- [25] R. L. Fork, C. H. B. Cruz, P. C. Becker and C. V. Shank, *Opt. Lett.*, 1987, **12**, 483–485.
- [26] D. E. Spence, P. N. Kean and W. Sibbett, *Opt. Lett.*, 1991, **16**, 42–44.
- [27] I. P. Christov, M. M. Murnane, H. C. Kapteyn, J. Zhou and C. Huang, *Opt. Lett.*, 1994, **19**, 1465–1467.
- [28] J. K. Ranka, A. L. Gaeta, A. Baltuska, M. S. Pshenichnikov and D. A. Wiersma, *Opt. Lett.*, 1997, **22**, 1344–1346.

- [29] U. Keller, G. W. 'tHooft, W. H. Knox and J. E. Cunningham, *Opt. Lett.*, 1991, **16**, 1022–1024.
- [30] F. Salin, J. Squier and M. Piché, *Opt. Lett.*, 1991, **16**, 1674–1676.
- [31] D. K. Negus, L. Spinelli, N. Goldblatt and G. Feugnet, in *Sub-100 femtosecond pulse generation by Kerr lens modelocking in Ti:sapphire*, Optical Society of America, Washington D.C., 1991, pp. 120–124.
- [32] U. Keller, *Nature*, 2003, **424**, 831–838.
- [33] M. N. Ashfold, N. H. Nahler, A. J. Orr-Ewing, O. P. Vieuxmaire, R. L. Toomes, T. N. Kitsopoulos, I. A. Garcia, D. A. Chestakov, S.-M. Wu and D. H. Parker, *Phys. Chem. Chem. Phys.*, 2006, **8**, 26–53.
- [34] S. J. Greaves, R. A. Rose and A. J. Orr-Ewing, *Phys. Chem. Chem. Phys.*, 2010, **12**, 9129–9143.
- [35] T. Suzuki and B. J. Whitaker, *Int. Rev. Phys. Chem.*, 2001, **20**, 313–356.
- [36] B. J. Whitaker, *Imaging in molecular dynamics: Technology and applications*, Cambridge University Press, 2003.
- [37] A. S. Chatterley, C. W. West, V. G. Stavros and J. R. R. Verlet, *Chem. Sci.*, 2014, **5**, 3963–3975.
- [38] C. R. S. Mooney, D. A. Horke, A. S. Chatterley, A. Simperler, H. H. Fielding and J. R. R. Verlet, *Chem. Sci.*, 2013, **4**, 921–927.
- [39] F. M. Harold, *The Vital Force: A study of Bioenergetics*, W.H. Freeman, 1987.
- [40] A. V. Ruban, M. P. Johnson and C. D. P. Duffy, *Energy Environ. Sci.*, 2011, **4**, 1643–1650.
- [41] W. H. Bragg and W. L. Bragg, *Proc. R. Soc. A*, 1913, **88**, 428–438.
- [42] J. C. Kendrew, G. Bodo, H. M. Dintzis, R. Parrish, H. Wyckoff and D. C. Phillips, *Nature*, 1958, **181**, 662–666.
- [43] N. Krauß, W.-D. Schubert, O. Klukas, P. Fromme, H. T. Witt and W. Saenger, *Nat. Struct. Mol. Biol.*, 1996, **3**, 965–973.
- [44] X. Qin, M. Suga, T. Kuang and J.-R. Shen, *Science*, 2015, **348**, 989–995.

- [45] W. Humphrey, A. Dalke and K. Schulten, *J. Mol. Graphics*, 1996, **14**, 33–38.
- [46] J. Stone, *M.Sc. thesis*, Computer Science Department, University of Missouri-Rolla, 1998.
- [47] M. Sanner, A. Olsen and J.-C. Spehner, Proceedings of the 11th ACM Symposium on Computational Geometry, New York, 1995, pp. C6–C7.
- [48] B. F. Milne, C. Kjær, J. Houmøller, M. H. Stockett, Y. Toker, A. Rubio and S. B. Nielsen, *Angew. Chem. Int. Ed.*, 2016, **55**, 6248–6251.
- [49] J. Martiskainen, R. Kananavičius, J. Linnanto, H. Lehtivuori, M. Keränen, V. Aumanen, N. Tkachenko and J. Korppi-Tommola, *Photosyn. Res.*, 2011, **107**, 195–207.
- [50] N. Nelson and W. Junge, *Annu. Rev. Biochem.*, 2015, **84**, 659–683.
- [51] J. M. Anna, G. D. Scholes and R. van Grondelle, *BioScience*, 2014, **64**, 14–25.
- [52] R. Moca, S. R. Meech and I. A. Heisler, *J. Phys. Chem. B*, 2015, **119**, 8623–8630.
- [53] D. I. G. Bennett, K. Amarnath and G. R. Fleming, *J. Am. Chem. Soc.*, 2013, **135**, 9164–9173.
- [54] H. Liu, H. Zhang, D. M. Niedzwiedzki, M. Prado, G. He, M. L. Gross and R. E. Blankenship, *Science*, 2013, **342**, 1104–1107.
- [55] G. Schlau-Cohen, J. M. Dawlaty and G. Fleming, *IEEE J. Sel. Top. Quantum Electron.*, 2012, **18**, 283–295.
- [56] M. Ballottari, M. J. P. Alcocer, C. D’Andrea, D. Viola, T. K. Ahn, A. Petrozza, D. Polli, G. R. Fleming, G. Cerullo and R. Bassi, *Proc. Natl. Acad. Sci. U.S.A.*, 2014, **111**, E2431–E2438.
- [57] G. S. Engel, T. R. Calhoun, E. L. Read, T.-K. Ahn, T. Mancal, Y.-C. Cheng, R. E. Blankenship and G. R. Fleming, *Nature*, 2007, **446**, 782–786.
- [58] E. Collini, C. Y. Wong, K. E. Wilk, P. M. G. Curmi, P. Brumer and G. D. Scholes, *Nature*, 2010, **463**, 644–647.
- [59] G. Trinkunas, J. L. Herek, T. Polívka, V. Sundström and T. Pullerits, *Phys. Rev. Lett.*, 2001, **86**, 4167–4170.

- [60] T. Mirkovic, E. E. Ostroumov, J. M. Anna, R. van Grondelle, Govindjee and G. D. Scholes, *Chem. Rev.*, 2016.
- [61] G. R. Fleming and R. van Grondelle, *Curr. Opin. Struct. Biol.*, 1997, **7**, 738–748.
- [62] T. Brixner, J. Stenger, H. M. Vaswani, M. Cho, R. E. Blankenship and G. R. Fleming, *Nature*, 2005, **434**, 625–628.
- [63] T. Förster, *Discuss. Faraday Soc.*, 1959, **27**, 7–17.
- [64] B. W. van der Meer, in *Förster Theory*, Wiley-VCH Verlag GmbH & Co. KGaA, 2013, pp. 23–62.
- [65] N. Lambert, Y.-N. Chen, Y.-C. Cheng, C.-M. Li, G.-Y. Chen and F. Nori, *Nat. Phys.*, 2013, **9**, 10–18.
- [66] *Quantum Effects in Biology*, ed. M. Mohseni, Y. Omar, G. S. Engel and M. B. Plenio, Cambridge University Press, 2014.
- [67] H. Hoppe and N. Sariciftci, *J. Mater. Res.*, 2004, **19**, 1924–1945.
- [68] B. C. Thompson and J. M. Fréchet, *Angew. Chem. Int. Ed.*, 2008, **47**, 58–77.
- [69] Y. Xie, Y. Tang, W. Wu, Y. Wang, J. Liu, X. Li, H. Tian and W.-H. Zhu, *J. Am. Chem. Soc.*, 2015, **137**, 14055–14058.
- [70] A. Yella, H.-W. Lee, H. N. Tsao, C. Yi, A. K. Chandiran, M. Nazeeruddin, E. W.-G. Diau, C.-Y. Yeh, S. M. Zakeeruddin and M. Grätzel, *Science*, 2011, **334**, 629–634.
- [71] Y. Terazono, G. Kodis, K. Bhushan, J. Zaks, C. Madden, A. L. Moore, T. A. Moore, G. R. Fleming and D. Gust, *J. Am. Chem. Soc.*, 2011, **133**, 2916–2922.
- [72] I. Fleming, *Nature*, 1967, **216**, 151–152.
- [73] B. J. Littler, M. A. Miller, C.-H. Hung, R. W. Wagner, D. F. O’Shea, P. D. Boyle and J. S. Lindsey, *J. Org. Chem.*, 1999, **64**, 1391–1396.
- [74] J. K. Laha, S. Dhanalekshmi, M. Taniguchi, A. Ambroise and J. S. Lindsey, *Org. Process Res. Dev.*, 2003, **7**, 799–812.
- [75] E. Stulz, S. M. Scott, Y.-F. Ng, A. D. Bond, S. J. Teat, S. L. Darling, N. Feeder and J. K. M. Sanders, *Inorg. Chem.*, 2003, **42**, 6564–6574.

- [76] P. D. Rao, S. Dhanalekshmi, B. J. Littler and J. S. Lindsey, *J. Org. Chem.*, 2000, **65**, 7323–7344.
- [77] M. O. Senge, *Chem. Commun.*, 2011, **47**, 1943–1960.
- [78] M. Gouterman, *J. Mol. Spectrosc.*, 1961, **6**, 138–163.
- [79] S.-P. Wang, Y.-F. Shen, B.-Y. Zhu, J. Wu and S. Li, *Chem. Commun.*, 2016, **52**, 10205–10216.
- [80] J. Yang, M.-C. Yoon, H. Yoo, P. Kim and D. Kim, *Chem. Soc. Rev.*, 2012, **41**, 4808–4826.
- [81] N. Aratani, D. Kim and A. Osuka, *Acc. Chem. Res.*, 2009, **42**, 1922–1934.
- [82] F. Durola, V. Heitz, F. Reviriego, C. Roche, J.-P. Sauvage, A. Sour and Y. Trolez, *Acc. Chem. Res.*, 2014, **47**, 633–645.
- [83] Y. Nakamura, N. Aratani and A. Osuka, *Chem. Soc. Rev.*, 2007, **36**, 831–845.
- [84] F. Hajjaj, Z. S. Yoon, M.-C. Yoon, J. Park, A. Satake, D. Kim and Y. Kobuke, *J. Am. Chem. Soc.*, 2006, **128**, 4612–4623.
- [85] Y. Kuramochi, A. Satake and Y. Kobuke, *J. Am. Chem. Soc.*, 2004, **126**, 8668–8669.
- [86] M. C. O’Sullivan, J. K. Sprafke, D. V. Kondratuk, C. Rinfray, T. D. W. Claridge, A. Saywell, M. O. Blunt, J. N. O’Shea, P. H. Beton, M. Malfois and H. L. Anderson, *Nature*, 2011, **469**, 72–75.
- [87] J. K. Sprafke, B. Odell, T. D. W. Claridge and H. L. Anderson, *Angew. Chem. Int. Ed.*, 2011, **50**, 5572–5575.
- [88] S. Liu, D. V. Kondratuk, S. A. L. Rousseaux, G. Gil-Ramírez, M. C. O’Sullivan, J. Cremers, T. D. W. Claridge and H. L. Anderson, *Angew. Chem. Int. Ed.*, 2015, **54**, 5355–5359.
- [89] D. V. Kondratuk, L. M. Perdigão, A. M. Esmail, J. N. O’Shea, P. H. Beton and H. L. Anderson, *Nat. Chem.*, 2015, **7**, 317–322.
- [90] M. Hoffmann, J. Kärnbratt, M.-H. Chang, L. M. Herz, B. Albinsson and H. L. Anderson, *Angew. Chem. Int. Ed.*, 2008, **47**, 4993–4996.
- [91] L. Favereau, A. Cnossen, J. B. Kelber, J. Q. Gong, R. M. Oetterli, J. Cremers, L. M. Herz and H. L. Anderson, *J. Am. Chem. Soc.*, 2015, **137**, 14256–14259.

- [92] S. A. Rousseaux, J. Q. Gong, R. Haver, B. Odell, T. D. Claridge, L. M. Herz and H. L. Anderson, *J. Am. Chem. Soc.*, 2015, **137**, 12713–12718.
- [93] A. Mikhaylov, D. V. Kondratuk, A. Cnossen, H. L. Anderson, M. Drobizhev and A. Rebane, *J. Phys. Chem. C*, 2016, **120**, 11663–11670.
- [94] M. Drobizhev, Y. Stepanenko, Y. Dzenis, A. Karotki, A. Rebane, P. N. Taylor and H. L. Anderson, *J. Am. Chem. Soc.*, 2004, **126**, 15352–15353.
- [95] E. Huynh, L. Y. C., B. L. Helfield, M. Shakiba, J.-A. Gandier, C. S. Jin, E. R. Master, B. C. Wilson, D. E. Goertz and G. Zheng, *Nat. Nanotechnol.*, 2015, **10**, 325–332.
- [96] J. F. Lovell, C. S. Jin, E. Huynh, H. Jin, C. Kim, J. L. Rubinstein, W. C. W. Chan, W. Cao, L. V. Wang and G. Zheng, *Nat. Mater.*, 2011, **10**, 324–332.
- [97] T. V. Duncan, P. P. Ghoroghchian, I. V. Rubtsov, D. A. Hammer and M. J. Therien, *J. Am. Chem. Soc.*, 2008, **130**, 9773–9784.
- [98] Y. Liu, S. Li, K. Li, Y. Zheng, M. Zhang, C. Cai, C. Yu, Y. Zhou and D. Yan, *Chem. Commun.*, 2016, **52**, 9394–9397.
- [99] Y. Mai and A. Eisenberg, *Chem. Soc. Rev.*, 2012, **41**, 5969–5985.
- [100] H.-A. Klok and S. Lecommandoux, *Adv. Mater.*, 2001, **13**, 1217–1229.
- [101] A. Blanazs, S. P. Armes and A. J. Ryan, *Macromol. Rapid Commun.*, 2009, **30**, 267–277.
- [102] M. Stefik, S. Guldin, S. Vignolini, U. Wiesner and U. Steiner, *Chem. Soc. Rev.*, 2015, **44**, 5076–5091.
- [103] R. K. O'Reilly, C. J. Hawker and K. L. Wooley, *Chem. Soc. Rev.*, 2006, **35**, 1068–1083.
- [104] N. S. Cameron, M. K. Corbierre and A. Eisenberg, *Can. J. Chem.*, 1999, **77**, 1311–1326.
- [105] K. A. Parker and N. S. Sampson, *Acc. Chem. Res.*, 2016, **49**, 408–417.
- [106] S. Yamago, *Chem. Rev.*, 2009, **109**, 5051–5068.
- [107] D. B. Wright, J. P. Patterson, N. C. Gianneschi, C. Chassenieux, O. Colombani and R. K. O'Reilly, *Polym. Chem.*, 2016, **7**, 1577–1583.

- [108] M. Chen and R. E. Blankenship, *Trends Plant Sci.*, 2011, **16**, 427–431.
- [109] R. Croce and H. Van Amerongen, *Nature Chem. Biol.*, 2014, **10**, 492–501.
- [110] M. Moser, T. Behnke, C. Hamers-Allin, K. Klein-Hartwig, J. Falkenhagen and U. Resch-Genger, *Anal. Chem.*, 2015, **87**, 9376–9383.
- [111] K. Ortmayr, M. Schwaiger, S. Hann and G. Koellensperger, *Analyst*, 2015, **140**, 7687–7695.
- [112] S. Waichman, C. You, O. Beutel, M. Bhagawati and J. Piehler, *Anal. Chem.*, 2011, **83**, 501–508.
- [113] A. B. Mabire, M. P. Robin, W.-D. Quan, H. Willcock, V. G. Stavros and R. K. O'Reilly, *Chem. Commun.*, 2015, **51**, 9733–9736.
- [114] M. P. Robin, P. Wilson, A. B. Mabire, J. K. Kiviaho, J. E. Raymond, D. M. Haddleton and R. K. O'Reilly, *J. Am. Chem. Soc.*, 2013, **135**, 2875–2878.
- [115] H. Imoto, K. Kizaki, S. Watase, K. Matsukawa and K. Naka, *Chem.-Eur. J.*, 2015, **21**, 12105–12111.
- [116] K. Kizaki, H. Imoto, T. Kato and K. Naka, *Tetrahedron*, 2015, **71**, 643–647.
- [117] T. Kato and K. Naka, *Chem. Lett.*, 2012, **41**, 1445–1447.

## Chapter 2

# General experimental techniques and instruments

In this chapter, materials and their preparations, instrumentation, calculations and characterisation techniques applicable to all chapters are described briefly. Methodologies specific to each chapter will be given therein.

### 2.1 General materials

Spectroscopic grade 1,4-dioxane (dioxane), tetrahydrofuran (THF), cyclohexane (c-hexane) and methanol (MeOH) were purchased from VWR. HPLC grade solvents (acetonitrile, THF, dioxane, MeOH) were purchased from Fisher Scientific. Pyrrole was purchased from Aldrich and distilled over calcium hydride ( $\text{CaH}_2$ ) under vacuum (0.5 mBar) and stored under  $\text{N}_2$  protected from light prior to use. Water for synthesis, spectroscopy and self assembly was purified to a resistivity of  $18.2 \text{ M}\Omega\cdot\text{cm}$  using a Millipore Simplicity Ultrapure water system. All other chemicals and solvents were purchased from Sigma, Aldrich, Fluka, Photonic Solutions or Acros and used as received unless stated otherwise. Silica gel (43-60 micron) for column chromatography was purchased from Apollo Scientific Limited. Dialysis was performed using Spectra/Por<sup>®</sup> of appropriate molecular weight cut off (MWCO), purchased from VWR or Fisher Scientific. Preparatory size exclusion chromatography (prep-SEC) was performed with Bio-Beads<sup>™</sup> S-X Resin in appropriate solvents, purchased from Bio-Rad.

## 2.2 General instrumentation

$^1\text{H}$  and  $^{13}\text{C}$  NMR spectra were recorded on a Bruker DPX-300, DPX-400, or AV-250 spectrometer at room temperature. Chemical shifts are given in ppm downfield from the internal standard tetramethylsilane (TMS) in subsequent chapters where appropriate. Infrared spectra were recorded on a Perkin Elmer, spectrum 100 FT-IR spectrometer. Fluorescence spectra were recorded using an Agilent Cary Eclipse Fluorescence spectrophotometer. High resolution mass spectrometry (HR-MS) was conducted on a Bruker UHR-Q-ToF MaXis with electrospray ionisation. Matrix-assisted laser desorption/ionization time-of-flight (MALDI/TOF) was performed with Bruker Ultraflex Extreme MALDI-TOF/TOF MS. UV-Vis absorption spectroscopy measurements were carried out on a Perkin Elmer Lambda 35 UV/Vis spectrometer or Agilent Cary 60 UV-Vis spectrometer. Quartz cells with screw caps and four polished sides (Starna) were used for fluorescence and UV-Vis measurements. The specific refractive index increment ( $dn/dc$ ) of the polymers were measured on a refractometer (Bischoff RI detector) operating at  $\lambda_0 = 632\text{ nm}$ .

## 2.3 Assembly method

For all assembled systems studied, the solvent switch method was applied. Briefly, all materials required for the final concentration and volume (stated within respective chapters) were dissolved in half of the final volume of a water miscible organic solvent capable of fully solubilising the materials. This initial solution was then sonicated for at least 20 minutes. An equal volume of  $18.2\text{ M}\Omega\cdot\text{cm}$  water was then slowly (flow rate at  $0.6\text{ mL}\cdot\text{min}^{-1}$ ) added to the solution with stirring *via* peristaltic pump overnight. The final mixture was then transferred to dialysis tubing with  $3.5\text{ kDa}$  molecular weight cut off (MWCO), and dialysed against  $18.2\text{ M}\Omega\cdot\text{cm}$  water to remove the organic solvent over a minimum of 6 water changes. As an example, for  $25\text{ mL}$  of sample with a final desired concentration of  $3\text{ mg}\cdot\text{mL}^{-1}$ ,  $75\text{ mg}$  of material was dissolved in  $12.5\text{ mL}$  of the organic solvent and sonicated for 30 minutes.  $12.5\text{ mL}$  of  $18.2\text{ M}\Omega\cdot\text{cm}$  water was then added to the stirring solution drop wise *via* peristaltic pump and the solution was left to stir overnight. The resulting mixture was dialysed against  $18.2\text{ M}\Omega\cdot\text{cm}$  water using dialysis tubing with  $3.5\text{ kDa}$  MWCO over 6 water changes. The final solution was diluted with  $18.2\text{ M}\Omega\cdot\text{cm}$  water when required for subsequent characterisation or analysis.

## 2.4 Multi-angle laser light scattering measurements

Multi-angle laser light scattering measurements were performed at angles of observation ranging from  $15^\circ$  up to  $150^\circ$  with an ALV CGS3 setup operating at  $\lambda_0 = 632$  nm and at  $20^\circ\text{C}$ . Data were collected in duplicate with 150–300 s run times. Calibration was achieved with filtered toluene and the background was measured with filtered  $18.2\text{ M}\Omega\cdot\text{cm}$  water.

## 2.5 Electron microscopy

For dry-state transmission electron microscopy (TEM), samples were prepared on graphene oxide (GO)-coated carbon grids (Quantifoil R2/2).<sup>1</sup> Generally, a drop of sample (20  $\mu\text{L}$ ) was pipetted on a grid, blotted immediately and left to air dry. TEM observations were performed on a JEOL 2000FX electron microscope at an acceleration voltage of 200 kV. For cryogenic electron microscopy (cryo-TEM), the samples were prepared at ambient temperature by placing a 10  $\mu\text{L}$  droplet on a TEM grid. The extra liquid was then blotted with filter paper and the sample was vitrified by plunging into liquid ethane at its freezing point. The frozen samples were subsequently kept under liquid nitrogen. Cryo-TEM was performed with a JEOL 2010F TEM, operated at 200 kV with images recorded on a Gatan UltraScan 4000 camera.

## 2.6 Static fluorescence spectroscopy

### 2.6.1 Fluorescence quantum yield measurements

The fluorescence quantum yields ( $\phi_f$ ) discussed in Chapter 3 were measured according to reported protocols,<sup>2</sup> relative to quinine sulfate dihydrate (QS) standards (freshly prepared in 105 mM perchloric acid aqueous solutions), chosen due to its relative insensitivity towards oxygen quenching.<sup>3;4</sup> The samples under study were diluted from fresh 100  $\mu\text{M}$  stock solutions. All solvents and stock solutions used for the measurements were not degassed to better represent conditions in most applications. All uncorrected spectra were collected with the following instrument settings: photomultiplier tube at 800 V; excitation and emission slit width at 2.5 nm; 1 nm data increment; and 1 s integration time with no emission filter. The spectra were subsequently corrected with the red-extended spectral responsivity correction factor matrix (*CFM*, see Section 2.6.2). The intensities centered at *ca.* double the excitation wavelength ( $\lambda_{\text{ex}}$ ) were discounted as they arise from scattering. The final spectra

were integrated with the trapezoidal numerical integration method (MATLAB®), which estimates the areas under the previously discounted wavelength range arising from scattering.

### 2.6.2 Extension of the instrument *CFM*

The *CFM* provided by the manufacturer of the fluorometer utilised for all fluorescence measurements was limited to 600 nm. Therefore, the  $\phi_f$  obtained with the relative measurement protocols,<sup>2</sup> may be inaccurate for chromophores whose emission covers a spectral range longer than 600 nm. As such, red extension of the *CFM* was required. The standard method is the utilisation of a calibrated light-source.<sup>5</sup> However, this method requires a specialised light-source, and is performed within facilities of the manufacturer, leading to excessive cost in both time and money. The extension was therefore performed using an alternative, previously reported method with fluorescein and oxazine 101 as standards.<sup>6</sup> Briefly, uncorrected spectra of the dye standards, fluorescein (Sigma) in ethanol and oxazine 101 (Photonic Solutions) in methanol, at 100 nM concentration, were collected in a cuvette with three clear quartz walls. The data were collected with 1 nm data increments and 2 s integration time, the slit-widths for both excitation and emission were set to 2.5 nm. The wavelength-dependent correction factor ( $CF_{\lambda_m}$ ) at  $\lambda_m$  was then calculated according to Equation (2.1):

$$CF_{\lambda_m} = \frac{Std_{\lambda_m}}{Acq_{\lambda_m}} \quad (2.1)$$

where,  $Std_{\lambda_m}$  is the normalised corrected emission spectrum, with  $\lambda_m$  denoting the wavelength of the spectrum (applicable to all subsequent expressions), of the dye standard, available from the PhotochemCAD software package (see reference for measurement conditions),<sup>7-9</sup> and  $Acq_{\lambda_m}$  is the normalised uncorrected emission spectrum collected by the spectrometer. The final *CFM* continuum was then generated by applying a normalisation factor,  $\alpha_j$ , to each  $CF_{\lambda_m}$  continuum from each dye, calculated using the overlapping regions of the adjacent  $CF_{\lambda_{mi}}$  and  $CF_{\lambda_{mj}}$  with:

$$\alpha_j = \frac{\sum_{\lambda} \left[ \frac{CF_{\lambda_{mi}}}{CF_{\lambda_{mj}}} \right] / \sigma_{\lambda_{mi},j}^2}{\sum_{\lambda} 1 / \sigma_{\lambda_{mi},j}^2} \quad (2.2)$$

the variance,  $\sigma_{\lambda_{mi},j}^2$ , assuming zero error from the standard spectrum, was given by:<sup>10</sup>

$$\sigma_{\lambda_m i, j}^2 = \left[ \frac{1}{J_{\lambda_m i}} + \frac{1}{J_{\lambda_m j}} \right] \left[ \frac{CF_{\lambda_m i}}{CF_{\lambda_m j}} \right]^2 \quad (2.3)$$

where  $J_{\lambda_m i/j}$  are the un-normalised intensities of the acquired spectrum. Finally, a single continuum was produced by applying the ‘cumulative’ normalisation factor,  $\beta_i$ , as the product of  $\alpha_1 \dots j$  to respective  $CF_{\lambda_m i}$  continua:

$$\beta_i = \prod_{i=1}^j \alpha_i \quad (2.4)$$

where the normalisation factor for the first set of  $CF_{\lambda_m}$ ,  $\alpha_1$ , was set to 1. The *CFM* provided by the manufacturer was used as  $CF_{\lambda_m 1}$  (220–600 nm),  $CF_{\lambda_m 2}$  and  $CF_{\lambda_m 3}$  were obtained with fluorescein (555–700 nm) and oxazine 101 (655–800 nm) respectively. The overlapping regions were simply replaced by the subsequent  $CF_{\lambda_m i}$ , instead of the weighted-average of the normalised  $CF_{\lambda_m i}$  demonstrated in the reference,<sup>6</sup> due to the significant noise associated with the overlapping regions in the measurements (see Figure 2.1). The region at 555–800 nm of the new *CFM* was then smoothed using the Savitzky-Golay filter with the MATLAB<sup>®</sup> software package. The spectral responsivity corrected emission spectrum,  $F_{\lambda_m}$  was then obtained by:

$$F_{\lambda_m} = Acq_{\lambda_m}^S \cdot CF_{\lambda_m} \quad (2.5)$$

where  $Acq_{\lambda_m}^S$  is the uncorrected fluorescence emission spectrum of the sample under study. The final *CFM*, respective  $CF_{\lambda_m}$  from the two standard dyes as well as their  $Acq_{\lambda_m}$  are shown in Figure 2.1, which shows the significant noise associated with unprocessed *CFM* for spectral regions beyond 750 nm. Therefore, in practice, although the new *CFM* covers a range of up to 800 nm, it should only be utilised for measurements of up to 750 nm. As such, all corrected spectra in the current thesis did not exceed 750 nm.

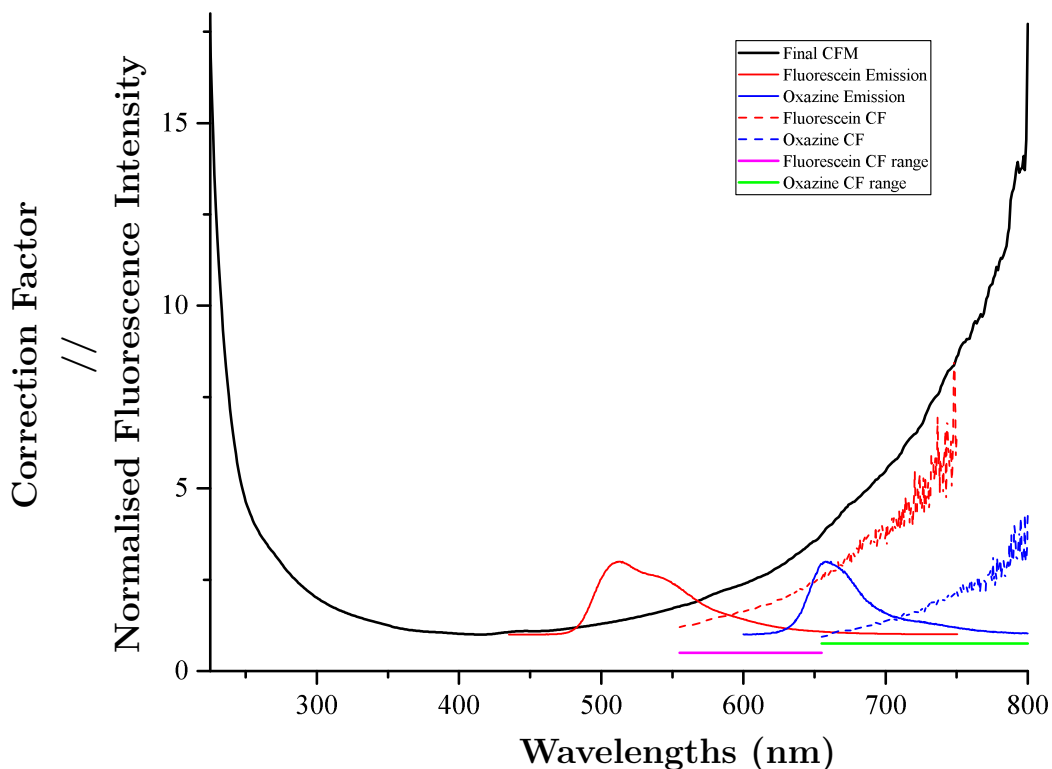


Figure 2.1: The red-extended *CFM* (black); the emission profile of standard dyes (solid colour coded lines) used for generating the new *CFM*; their unnormalised correction factor (CF, dashed colour coded lines); and their respective correction factor range (solid horizontal lines). The fluorescence emission spectra are offset vertically for visual clarity.

## 2.7 Time resolved transient electronic absorption spectroscopy (TEAS)

### 2.7.1 Laser generation and beam paths

The experimental procedures for the time resolved transient electronic absorption spectroscopy (TEAS) are detailed in previously reported works.<sup>11–13</sup> Briefly, a commercially available Ti:sapphire oscillator and amplifier system (Spectra-Physics) produces 3 mJ laser pulses of  $\sim 40$  fs duration centered around 800 nm with a repetition rate of 1 kHz. For TEAS, pump pulses ( $\lambda_{\text{pu}}$ ) were generated from the 800 nm fundamental using a Spectra-Physics TOPAS-C optical parametric amplifier, to produce  $\lambda_{\text{pu}}$  of either 320, 345, 360 or 365 or 420 nm (specified within each of the subsequent chapters) with powers of between 1-2 mJ·cm<sup>-2</sup> and a pulse duration of  $\sim 80$  fs. Of the 1 mJ per pulse 800 nm laser beam, 5% (50  $\mu$ J/pulse) was focused into a CaF<sub>2</sub> window to generate probe pulses drawn from a white light super continuum (330–

700 nm). The remaining 95% was either blocked (with a laser beam block) or used to generate the pump pulse centered around 400 nm ( $1\text{--}2\text{ mJ}\cdot\text{cm}^{-2}$ ) through second harmonic generation using a  $\beta$ -barium borate crystal where applicable. Pump-probe polarisations were held at the magic angle ( $54.7^\circ$ ) relative to one another to avoid anisotropic effects. Changes in optical density ( $\Delta\text{OD}$ ) of the sample were calculated from probe intensities, collected using a spectrometer (Avantes, AvaSpec-ULS1650F). A delay stage was positioned in the probe path which introduced a time delay  $\Delta t$ , between the arrival of the probe pulses relative to pump pulses, up to a maximum of  $\Delta t = 2\text{ ns}$ . Chirp-correction of all resultant transient absorption spectra (TAS) were performed using the KOALA package.<sup>14</sup> The delivery system for the samples was a flow-through cell (Demountable Liquid Cell by Harrick Scientific Products, Inc.), henceforth referred to as a Harrick Cell. The sample was circulated using a peristaltic pump (Masterflex) with polytetrafluoroethylene (PTFE) tubing, recirculating sample from a 50 mL reservoir (with minimum sample volume of *ca.* 20 mL), in order to provide each pump-probe pulse pair with fresh sample. The laser table setup is shown in Figure 2.2.

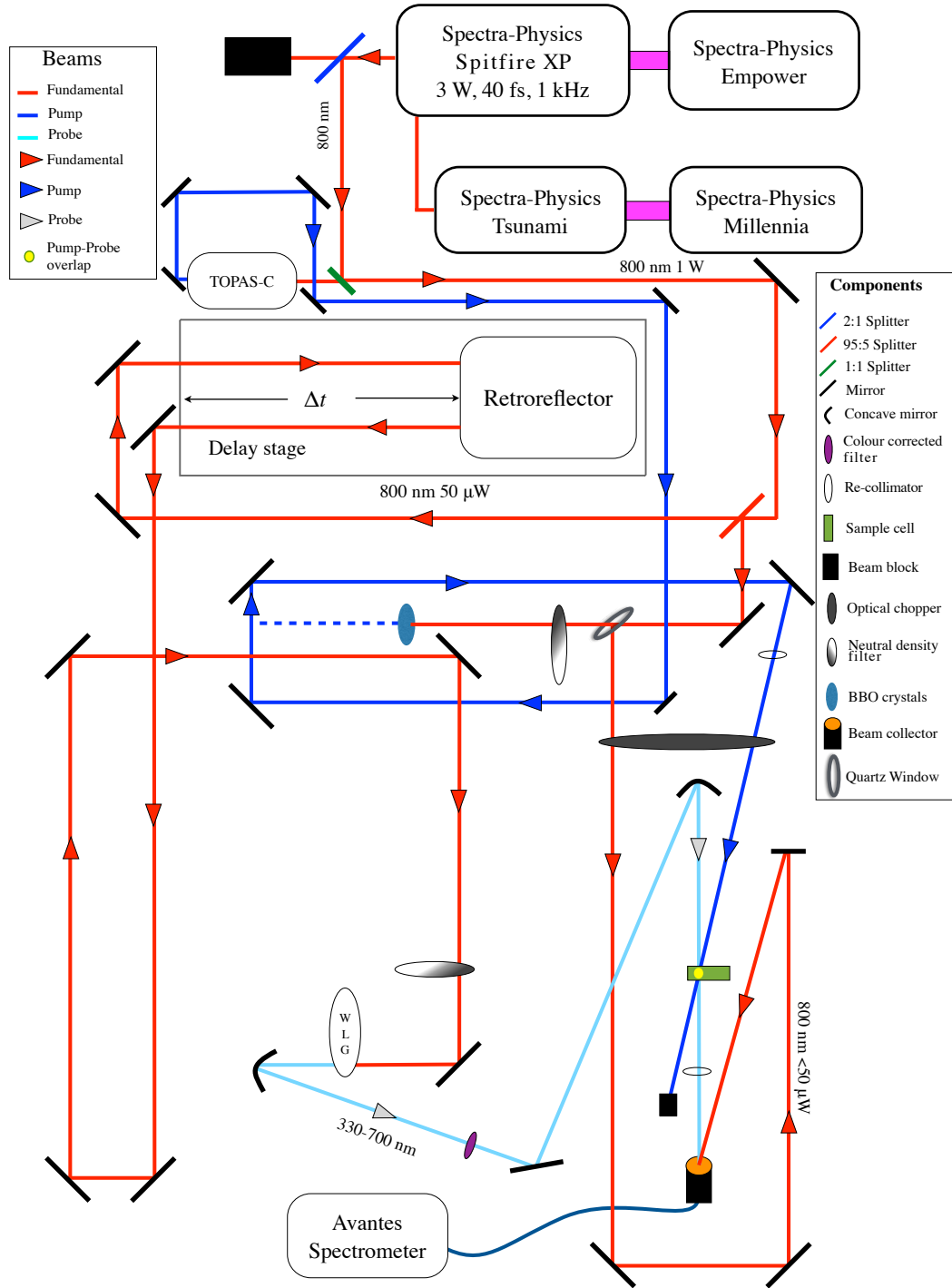


Figure 2.2: Schematic of the beam paths of the laser table used for the TEAS experiments. Components are labelled in the legend. WLG, white light generator ( $\text{CaF}_2$  window); BBO crystals,  $\beta$ -barium borate crystals. The laser beams are colour coded, and their direction of propagations are indicated by colour coded arrows and detailed in the legend. The dashed blue line indicates frequency doubled pulse produced from the fundamental 800 nm seed, in TEAS experiments with 400 nm photoexcitation, instead of pump pulses produced from TOPAS-C.

### 2.7.2 Sample delivery system

One of the most useful tools for elucidating the mechanism for a photochemical observation is the kinetic isotope effect (KIE).<sup>15–17</sup> In the case of a proton movement, KIE could be induced by deuterating the molecule of interest, the solvent, or both. However, for systems involving protons that could be easily exchanged with water, extreme care is usually required in sample preparation. Furthermore, for the TEAS experiments, a pool of sample is used for the duration of a series of experiments, which could last between 5–14 hours. Therefore, if the sample solution were exposed to air, small amounts of exchange between the atmospheric water content could occur. Although the effect of such exchange may not be apparent for individual measurements, multiple experiments over an extended period of duration (as is the case for most TEAS measurements) could result in the loss of observable KIE due to the accumulation of protonated samples.

To counter these exchanges without needing to prepare an unnecessarily large amount of sample for each measurement, a sample delivery system was developed. The schematic and a photo of the reservoir are shown in Figure 2.3.

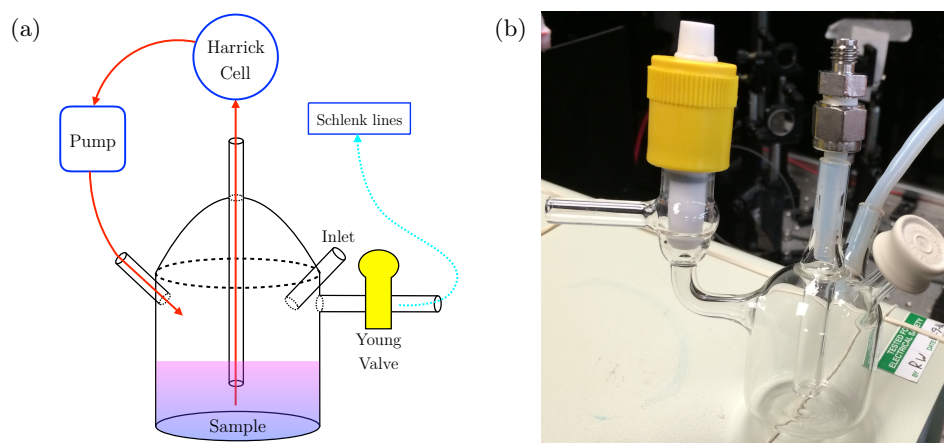


Figure 2.3: (a) Schematic of the custom designed reservoir, where: red arrows indicate flow of sample during TEAS experiment; cyan dotted arrow indicates potential air extraction, which could be isolated with the Young high-vacuum valve. (b) Photo of reservoir with all external components on the glassware.

In short, the set-up consists of a Schlenk line connected to a custom reservoir designed in-house. The Schlenk line followed the previously established design.<sup>18</sup> The reservoir was built upon a sealed glass ‘bottle’ with 4 separate inlet/outlets: the first outlet is a vertical glass tube extending from the top of the glassware to *ca.* 1 cm over the bottom; the second outlet is connected to the side of the glassware, with a Young PTFE high-vacuum valve between it and the Schlenk line; the two

inlets are short glass tubes extended from the side of the glassware, with one being connected to the sample pump *via* PTFE tubing and the other sealed with septum after the reservoir is filled with sample.

As shown in Figure 2.3, a close to complete isolation of the sample from atmospheric contact can be facilitated by this design once assembled. Furthermore, the septum seal in conjunction with the Young valve allows sample transfer between another sealed flask equipped with Young valve and the reservoir *via* cannula transfer. Therefore, with standard air sensitive practices, the samples under study can be kept under an inert, water-free atmosphere, for the entire duration of the TEAS experiment. The first showcase of using such setup was demonstrated with a study on 4-*tert*-butylcatechol,<sup>19</sup> and were used in all experiments performed in the current thesis, with the KIE measurements being a crucial experiments for the results presented in Chapter 3.

### 2.7.3 Global fitting procedures

All TAS obtained were first chirp corrected with the KOALA package.<sup>14</sup> A global fitting procedure, based on a previously reported method,<sup>20;21</sup> was then used to determine the set of lifetimes which characterise a function of  $n$  exponential decays convoluted with a Gaussian instrument response function (IRF),  $\mathcal{G}(\Delta t)$ , with the basic functional form:

$$\mathcal{F}(\lambda, \Delta t) = \sum_i^n \mathcal{G}(\Delta t) \otimes A_i(\lambda) e^{\frac{-(\Delta t - t_0)}{\tau_i}}, \quad (2.6)$$

where  $A_i(\lambda)$  is the decay associated spectrum (DAS) of the  $i^{\text{th}}$  exponential decay component with lifetime  $\tau_i$ ,  $t_0$  describes time zero of pump-probe overlap, and the convolution procedure is denoted by  $\otimes$ . This basic form was applied to fit the TAS of processes that did not show dynamics with  $\tau \leq 500$  fs in the current thesis. In these cases, if the signal associated with the IRF (likely multicomponent in nature and attributed to linear and non-linear solvent-, glass-, and solute- only responses) were significantly stronger than those arising from dynamics of the studied system, delay times less than 150 fs were omitted from the fitting process. It is important to note that, in most cases, *i.e.* where IRF signals were not significantly stronger than those arising from dynamics of interest, IRF signals should not be removed as these can be captured by a time constant similar to that of the full width at half maximum (FWHM) of the IRF, which would appear as a rapid process occurring at the temporal resolution of the instrument.

In cases where the dynamics with  $\tau \leq 500$  fs were present, coupled with sig-

nificantly strong signals attributed to the IRF, the aforementioned additional time constants can affect the other time constants extracted. Furthermore, omission of data prior to 150 fs would obscure the time constant extracted for these fast dynamics. Therefore, a different method of capturing these IRF associated signals was devised. Briefly, as these signals closely resembled the sum of a positive and negative Gaussian functions, the TAS were fitted with a modified functional form:

$$\mathcal{F}(\lambda, \Delta t) = \mathcal{G}(\Delta t)_{IRF} + \sum_i^n \mathcal{G}(\Delta t) \otimes A_i(\lambda) e^{\frac{-(\Delta t - t_0)}{\tau_i}}, \quad (2.7)$$

where  $\mathcal{G}(\Delta t)_{IRF}$  is the sum of a positive and negative Gaussian function:

$$\mathcal{G}(\Delta t)_{IRF} = A_a(\lambda) e^{-\frac{(\Delta t - t_0)^2}{2\left(\frac{FWHM}{2k\sqrt{2\ln 2}}\right)^2}} - A_b(\lambda) e^{-\frac{(\Delta t - t_0)^2}{2\left(\frac{FWHM}{2\sqrt{2\ln 2}}\right)^2}} \quad (2.8)$$

where  $A_{a,b}(\lambda)$  captures the amplitude of each of the Gaussian functions,  $k$  ( $\sim 1.25$ - $2$ ) is a constant introduced to account for the narrower FWHM of the positive component of  $\mathcal{G}(\Delta t)_{IRF}$ . The same FWHM and  $t_0$  from  $\mathcal{G}(\Delta t)_{IRF}$  were applied for the convolution and fitting of the photodynamic processes (second term of Equation (2.7)). The Levenberg-Marquardt algorithm was then used to minimise the sum of squares between  $\mathcal{F}(\lambda, \Delta t)$  and the experimental TAS. While this method is significantly more computationally expensive and time consuming due to the two additional parameters, dynamics with time constants close to the FWHM of the IRF could be extracted with more confidence. This form of global fitting function was applied for the analysis of TEAS experimental data from Chapter 3 and 5, with both exhibiting dynamics occurring at close to 500 fs time scales.

#### 2.7.4 Global fitting error analysis

For systems whose processes of interest are sufficiently described by two exponential decays, support plane analysis (SPA) was used to determine a 95% confidence interval on the lifetimes determined from global fitting.<sup>22</sup> Briefly, the goodness of fit,  $\chi^2$ , for the globally fitted lifetimes was  $\chi_{min}^2$ . The values of  $\tau_1$  and  $\tau_2$  extracted with procedures described in Section 2.7.3 were systematically varied, and for each pair of values,  $\tau_1$  and  $\tau_2$  remain fixed whilst the fitting procedure reoptimises all other parameters, and returns a goodness of fit  $\chi^2(\tau_1, \tau_2)$ . The ratio  $\frac{\chi^2(\tau_1, \tau_2)}{\chi_{min}^2}$  was calculated, and a 95% confidence interval for the lifetimes is defined as:<sup>23</sup>

$$\frac{\chi^2(\tau_1, \tau_2)}{\chi_{min}^2} = 1 + \frac{p}{\nu} F^{-1}(0.95, p, \nu), \quad (2.9)$$

where  $p$  is the number of parameters used in the global fitting procedure,  $\nu$  is the number of degrees of freedom and  $F^{-1}$  is the inverse-F cumulative distribution function. An upper bound on the uncertainty for the lifetimes is taken to be the value which satisfies the following two conditions: i) is the largest deviation from the global lifetimes; and ii) satisfies equation 2.9. While this method is considered a more accurate determination of errors of the fitting procedure, practically, it is only applicable to fittings with exactly two exponentials of interest, which, in most cases, also requires the addition of one or more exponentials to account for processes outside the temporal resolution or ‘window’ of the TEAS experiments. In the case where only one  $\tau$  is varied at a time, uncertainties at the 95% level were assigned to the determined lifetimes using an asymptotic standard error (ASE) technique.<sup>21;23</sup> SPA is better because it accounts for dependancy between time constants, whereas ASE does not, but is tractable for systems with many processes. For  $n=1$ , there cannot be dependancy, therefore SPA is equivalent to ASE.

Briefly, for each TAS the goodness of fit for the set of optimised parameters determined by the global fit was calculated ( $\chi_{min}^2$ ). Subsequently, the value of one lifetime  $\tau$  was varied in a systematic manner whilst keeping all other lifetimes fixed (including constants obtained for the IRF). The global fit optimisation proceeds as before and a new goodness of fit was calculated, denoted by  $\chi^2(\tau)$ . A 95% confidence interval for the value of the lifetime  $\tau$  is then defined by:

$$\frac{\chi^2(\tau)}{\chi_{min}^2} = 1 + \frac{p}{\nu} F^{-1}(0.95, p, \nu), \quad (2.10)$$

Thus, for each fixed value of  $\tau$ , the goodness of fit ratio  $\frac{\chi^2(\tau)}{\chi_{min}^2}$  was calculated until Equation (2.10) was no longer satisfied. The uncertainty reported was that which deviates maximally from the globally fitted lifetime and satisfies Equation (2.10). This procedure was repeated for all lifetimes which correspond to dynamical processes.

For both methods described, some errors of  $\tau$  could be ‘unbounded’ on one side (longer or shorter time) of the global minimum, *i.e.* unable to reach the 95% confidence interval within reasonable range (*e.g.* non-negative  $\tau$ ). In such instances, deviations to the ‘bounded’ sides were quoted as the error instead of the largest deviation obtained.

## 2.8 *Ab initio* quantum mechanical calculations (QMC)

In the current thesis, *ab initio* quantum mechanical calculations (QMC) at various level of theory were performed to aid the qualitative analysis of the experimental

data. The basic principles underlying these methods are briefly described herein. However it is important to stress this brevity in description, which is only provided for the methods applicable to the current thesis work. Each method is linked to the appropriate results chapters (3 and 5).

### 2.8.1 Hartree-Fock self-consistent field (HF-SCF) theory

As discussed briefly in Section 1.2, the electronic configuration of a system under study can be predicted by solving the electronic part of the time-independent Schrödinger equation, in the following form:

$$\hat{H}\Psi(\mathbf{r}; \mathbf{R}) = E(\mathbf{R})\Psi(\mathbf{r}; \mathbf{R}) \quad (2.11)$$

where  $\Psi(\mathbf{r}; \mathbf{R})$  is the electronic wavefunction, which depends on the electronic coordinate  $\mathbf{r}$ , and depends parametrically on the fixed nuclear coordinate  $\mathbf{R}$ ; and  $E(\mathbf{R})$  is the electronic energy. As the nuclear coordinate  $\mathbf{R}$  is fixed for a particular solution, it is henceforth assumed to be included in all notations of wavefunction, *e.g.*  $\Psi(i) = \Psi(i; \mathbf{R})$  for all subsequent expressions unless otherwise stated. The Hamiltonian operator  $\hat{H}$  described in Section 1.2.1, for the case of a hydrogen atom with one electron and one nucleus, is the sum of two terms (neglecting the nuclear repulsion term):

$$T = -\frac{\hbar^2}{2m_e} \cdot \frac{\partial^2}{\partial \mathbf{r}^2}; \quad V = -\frac{eZ}{4\pi\epsilon_0 r} \quad (2.12)$$

where  $T$  and  $V$  are the kinetic and potential energy of the electron respectively;  $\hbar$  is the reduced Planck's constant;  $m_e$  is the mass of the electron;  $r$  is the distance between the electron and nuclei;  $e$  is the elementary charge;  $Z$  is the electronic charge of the nucleus (*e.g.* number of protons  $\times e$ ); and  $\epsilon_0$  is the vacuum permittivity. However, this form is not applicable to the systems under investigation, *i.e.* systems with multiple electrons such as the maleimide and porphyrin based systems studied in Chapter 3 and 5. In these cases,  $T$  and  $V$  are:

$$T = -\frac{\hbar^2}{2m_e} \cdot \sum_i^N \frac{\partial^2}{\partial \mathbf{r}^2}; \quad V_{ee} = \frac{1}{2}j_0 \sum_{i \neq j}^N \frac{1}{r_{ij}}; \quad V_{ne} = -j_0 \sum_i^{N_e} \sum_l^{N_n} \frac{Z_l}{e_i} \cdot \frac{1}{r_{il}} \quad (2.13)$$

where  $V_{ee}$  and  $V_{ne}$  are the electron-electron Coulomb repulsion energy and electron-nuclear Coulombic potential energy respectively;  $N_e$  and  $N_n$  are the number of electrons and nuclei in the system respectively;  $r_{ij}$  is the inter-electronic distance be-

tween electrons  $i$  and  $j$ ;  $r_{il}$  is the distance between electron  $i$  and nucleus  $l$ ;  $Z_l$  nuclear charge of nucleus  $l$ ; and  $j_0 = \frac{e^2}{4\pi\epsilon_0}$ . As mentioned in Section 1.2.1, analytical solutions to the time-independent Schrödinger equation is only obtainable for some systems with a single electron due to the difficulty in dealing with the electron-electron repulsion, where  $V$  is now dependent on  $r_{ij}$ . As such, simplification or approximation methods are required. The foundation for most of these methods is the Hartree-Fock self-consistent field (HF-SCF) theory. First, we simplify the solution to ignore (for now)  $r_{ij}$  by assuming that an electron moves within a spherical average of potential, arising from the other electrons and the nucleus within the system. Therefore, the multi-electron zero-order wavefunction  $\Psi_0$  could be sufficiently described by the collective wavefunction of all single electronic wavefunctions  $\psi$ . Thus:

$$\hat{H}_{hf}\Psi_0 = E_{hf}\Psi_0; \quad \hat{H}_{hf} = \sum_i^N \hat{h}_i \quad (2.14)$$

where  $\hat{h}_i$  is the Hamiltonian of the wavefunction (or orbital) of the single electron  $i$ ,  $\psi_{eo,i}(i)$ , depending on the coordinate of the electron  $\mathbf{r}_i$  and parametrically on the nuclear coordinate  $\mathbf{R}$ .  $\psi_{eo,i}(i)$  is then the solution of:

$$\hat{h}_i\psi_{eo,i}(i) = E_{eo,i}\psi_{eo,i}(i) \quad (2.15)$$

where  $E_{eo}$  is the energy of an electron in the electronic orbital  $eo$ . By finding the solution for  $E_{eo}$  for each electron in the system individually, the approximation of the zero-order wavefunction is then the cumulative product of all single-electron wavefunctions:

$$\Psi_0 = \prod_{i=1}^N \psi_{eo,i}(i) \quad (2.16)$$

In summary, the zero-order wavefunction  $\Psi_0$  depends on all the possible electronic coordinates, and the electronic energy  $E$  is the sum of all the electron energies in the  $i^{th}$  electronic orbitals ( $E_{eo,i}$ ). However, as mentioned in Section 1.2.1, one must take into account of the spins of the electrons, and in accordance to the Pauli principle, electrons occupying the same spatial orbital must have the opposite spin. Therefore, a spin function is introduced, and the product between it and the orbital wavefunction  $\psi_{eo,i}(i)$  gives the spin orbital  $\phi_{eo,i}(i)$ , which depends on the spin-space coordinates of electron  $i$ . To comply with the Pauli principle, the overall wavefunction is written as the Slater determinant of the spin orbitals:

$$\Psi_0 = \frac{1}{\sqrt{N!}} \det \begin{vmatrix} \phi_a(1) & \phi_b(1) & \cdots & \phi_z(1) \\ \phi_a(2) & \phi_b(2) & \cdots & \phi_z(2) \\ \vdots & \vdots & \ddots & \vdots \\ \phi_a(N) & \phi_b(N) & \cdots & \phi_z(N) \end{vmatrix} \quad (2.17)$$

where  $\frac{1}{\sqrt{N!}}$  is the normalisation factor, and the determinant is an  $N$  by  $N$  matrix, accounting for all the spin orbitals ( $N$ ) for each electron ( $N$ ). The formulation is usually written in the simplified form by only writing the principle diagonal:

$$\Psi_0 = \|\phi_a(1)\phi_b(2)\cdots\phi_z(N)\| \quad (2.18)$$

with normalisation factor implied.

Unfortunately, one cannot simply ignore the electron-electron repulsion as it is critical for accurate computation of the electronic structures. Therefore, to account for these interactions, the Fock operator is introduced. As mentioned, this assumes that each electron moves in the electrostatic field of the nucleus and the average field of the other  $N - 1$  electrons. For closed-shell systems with doubly occupied orbitals, the ‘restricted’ Hartree-Fock (HF) equation is then:

$$\left\{ h_i + \sum_{eo'} (2J_{eo'} - K_{eo'}) \right\} \psi_{eo}(i) = \epsilon_{eo} \psi_{eo}(i) \quad (2.19)$$

where  $\epsilon_{eo}$  is the one-electron orbital energy; the expression in  $\{\}$  is the Fock operator, henceforth expressed as  $f_i$ ;  $J_{eo'}$  and  $K_{eo'}$  are the Coulomb and exchange operators respectively. In particular,  $J_{eo'}$  accounts for the Coulombic repulsion between electrons occupying orbitals  $eo'$ . The exchange operator,  $K_{eo'}$ , represents the modification of the Coulombic energies arising from the effects of spin correlation (the antisymmetry of the total wavefunction). It is worth stressing that, the derivations of these functions are not presented in this thesis, but only an overview, in order to aid the readers understanding of the origin of some of the theoretical results presented in Chapters 3 and 5. Full derivations can be found elsewhere.<sup>24</sup>

Finally, this method assumes that the wavefunctions of all other electrons are known. However, this is, in general, never the case for systems under study. Therefore, the calculations first start with an approximation of the collective wavefunctions, which is then used to numerically solve the electronic HF equation. This new solution is then used as the new, improved, approximation to start a new iteration of computation. This cycle is repeated until a predetermined criterion, *e.g.* the variation between total energies obtained from consecutive iterations,  $\Delta E \leq 1 \times 10^{-5}$

eV, is reached for example, which forms the basis of the self-consistent field (SCF) algorithms.

The complete numeric approximation of a single atomic orbital using the HF-SCF is usually straightforward. However, for a molecule with multiple atoms, the numerical solution is extremely complex and must be treated by a different technique. The commonly accepted method is the linear combination of atomic orbitals for expressing molecular orbitals (LCAO-MO). This method, in essence, introduces a set of  $N_p$  basis functions  $\chi_p$ , which can be considered as the atomic orbitals for each electron in the molecule. These basis functions are typically Slater type orbitals (STO) or Gaussian type orbitals (GTO). Each spatial wavefunction,  $\psi_{eo}$ , can be expressed as a linear combinations of this set of basis functions:

$$\psi_{eo} = \sum_{p=1}^{N_p} c_{eo,p} \chi_p \quad (2.20)$$

where  $c_{eo,p}$  is a coefficient describing the contribution of basis function  $\chi_p$  towards describing the spatial wavefunction  $\psi_{eo}$ . The aforementioned numerical computation of  $\Psi_0$  is now simply the computations of the  $c_{eo,p}$  for a set of  $N_p$  linearly independent spatial wavefunctions. Therefore, the accuracy of the approximation is dependent on the choice of these ‘basis sets’. Generally speaking, the larger the number of functions in the basis set utilised, the more accurate the approximation, however, the computation cost also increases. As such, most QMCs are performed with a minimum basis set that provide sufficient accuracy. Due to the vast amount of basis sets available, they are not listed herein. Instead, the reader is directed to the in-depth review of available basis sets by Hill.<sup>25</sup>

While the current thesis utilised higher level QMC methods (Chapters 3 and 5), LCAO-MO is implemented by all of the quantum computation packages. Therefore, thanks to the low computation cost of HF-SCF, this was performed in all calculations as the first step in generating the initial approximation for subsequent higher level calculations. A brief discussion of some higher level methods will be presented in the ensuing sections.

### 2.8.2 Higher level QMC methods developed on HF-SCF

Although the HF-SCF theory provides a good initial approximation for computing the wavefunctions, the averaged interactions nature renders it incapable of accounting for electron correlations. Furthermore, the restricted HF equation stated (Equation (2.19)) is only applicable to closed-shell systems with doubly occupied orbitals,

*i.e.* ground state (GS) of most molecules. Although excited states could be computed using the unrestricted HF method, it is vulnerable to spin contaminations. Hence, to compute the excited state (ES) electronic structure, as well as to take electron correlations into account, improvements over the HF-SCF were developed.

### Configuration interaction

Firstly, the configuration interaction method, which is built on the initial HF wavefunction, consists of  $N_{so}$  of spin orbitals, with  $N_e$  electrons. At the GS configuration, the system would have the lowest  $N_e$  orbitals occupied by electrons, hence occupied orbitals, and  $N_{so} - N_e$  virtual or unoccupied orbitals. This configuration could be expressed as the Slater determinant:

$$\Psi_0 = \|\phi_a \phi_b \cdots \phi_l \phi_m \phi_n \cdots \phi_z\| \quad (2.21)$$

where  $\Psi_0$  is the GS HF wavefunction, and  $\phi_a, \phi_b \cdots \phi_z$  are the spin orbitals. A configuration state (or ES) determinant then moves an electron from a lower energy occupied orbital to a higher energy unoccupied orbital. For example, if the electron at  $\phi_n$  is promoted to  $\phi_p$ , the configuration determinant then has the following expression:

$$\Psi_n^p = \|\phi_a \phi_b \cdots \phi_l \phi_m \phi_o \cdots \phi_p \cdots \phi_z\| \quad (2.22)$$

where  $\Psi_n^p$  is the singly excited determinant. If two electrons are promoted, it would be the doubly excited determinant, *e.g.* if electrons from  $\phi_l$  and  $\phi_n$  are moved to  $\phi_p$  and  $\phi_q$  respectively, then the doubly excited determinant is:

$$\Psi_{l,n}^{p,q} = \|\phi_a \phi_b \cdots \phi_m \phi_o \psi_r \cdots \phi_p \cdots \phi_q \cdots \phi_z\| \quad (2.23)$$

Excited determinants with increasing number of electron promotions can be formed until all possible electronic configurations are exhausted. The configuration interaction method then expresses the overall wavefunction and accounts for the electron correlation as the linear combination of the possible excited determinants:

$$\Psi = c_0 \Psi_0 + \sum_{a,p} c_a^p \Psi_a^p + \sum_{\substack{a < b \\ p < q}} c_{a,b}^{p,q} \Psi_{a,b}^{p,q} + \sum_{\substack{a < b < c \\ p < q < r}} c_{a,b,c}^{p,q,r} \Psi_{a,b,c}^{p,q,r} + \cdots \quad (2.24)$$

In a configuration interaction calculation,  $c_{eo,p}$  from the initial computation of Equation (2.20) is held constant and the coefficient in Equation (2.24) ( $c_0, c_{a,b}^{p,q}$  *etc.*) are computed. While this gives good approximations for the GS energy, it

is not sufficient for accurate calculations of ES energies. Thus the multiconfiguration self-consistent field method (MCSCF) improves on the configuration interaction method by optimising both  $c_{eo,p}$  (from Equation (2.20)) and  $c_0, c_{a,b}^{p,q} \dots$  (from Equation (2.24)) in the computations. However, this can lead to unrealistic computation cost. The complete-active space self-consistent field method (CASSCF) goes some way to alleviate this cost by allowing the user to identify relevant orbitals of interest. Therefore, CASSCF requires good chemical intuitions for accurate approximations. In theory, these two types of methods could provide an exact approximation of the energies, if all possible configurations are included. However, the computation cost increases exponentially with the number of configurations included. Therefore, it is usually only computed by including, at most, up to the triply excited determinants.

### Møller-Plesset perturbation theory (MPPT)

The second method for correcting the electron correlation errors is the Møller-Plesset perturbation theory (MPPT), described in the work by Møller and Plesset in 1934.<sup>26</sup> This method takes into consideration that the HF wavefunction is not the eigenfunction of Hamiltonian for the overall wavefunction:

$$\hat{H}\Psi_0 \neq E_{hf}\Psi_0 \quad (2.25)$$

where  $E_{hf}$  is the HF energy, and  $\hat{H}$  is the Hamiltonian of the overall wavefunction (as in Equations (2.11) and (2.14)). However,  $\Psi_0$  can be considered the eigenfunction of the zero-order (Hartree-Fock, Equation (2.19)) Hamiltonian,  $\hat{H}_{hf}$ , which is the sum of all the Fock operators,  $f_i$ , from Equation (2.19):

$$\hat{H}_{hf} = \sum_{i=1}^{N_e} f_i; \quad \hat{H}_{hf}\Psi_0 = E_{hf}\Psi_0 \quad (2.26)$$

The difference between the two Hamiltonians is then considered the perturbation,  $\lambda\hat{V}$  which accounts for the electron correlations:

$$\lambda\hat{V} = \hat{H} - \hat{H}_{hf} \quad (2.27)$$

the perturbed wavefunctions and energy are then expressed in power series of  $\lambda$ :

$$\Psi_{pert} = \lambda\Psi_1 + \lambda^2\Psi_2 + \lambda^3\Psi_3 + \dots \quad (2.28)$$

$$E_{pert} = \lambda E_1 + \lambda^2 E_2 + \lambda^3 E_3 + \dots \quad (2.29)$$

these are then added to the zero-order (HF) wavefunctions and energy to approximate the overall wavefunction and energy:

$$\Psi = \Psi_0 + \lambda\Psi_1 + \lambda^2\Psi_2 + \lambda^3\Psi_3 + \dots \quad (2.30)$$

$$E = E_{hf} + \lambda E_1 + \lambda^2 E_2 + \lambda^3 E_3 + \dots \quad (2.31)$$

where  $\Psi_{1,2,\dots}$  and  $E_{1,2,\dots}$  are the perturbations of the overall wavefunction and energy, respectively, from the HF approximation; and  $\lambda$  is just a constant that keeps track of the order of the perturbation terms, and is set to 1 at the end of the calculations. The calculation methods are abbreviated by the order of perturbation at which the expansions are truncated. For example,  $E$  given by MP0 is simply the HF energy, MP1 is truncated at  $\lambda^1$  terms, MP2 includes the  $\lambda^2$  terms, and so on. MP2 is one of the most widely used methods for approximating GS electronic energies, and the energy correction,  $E_{\text{MP2}}$ , is:

$$E_{\text{MP2}} = \sum_{J \neq O} \frac{\langle \Psi_J | \hat{V} | \Psi_O \rangle \langle \Psi_O | \hat{V} | \Psi_J \rangle}{E_O - E_J} \quad (2.32)$$

where  $\Psi_O$  are the occupied orbitals;  $\Psi_J$  are the virtual (unoccupied) orbitals;  $\hat{V}$  is defined in Equation (2.27); and  $E_{O,J}$  are the corresponding orbital energies. The total energy ( $E_{\text{tot}}$ ) of the molecule is therefore the sum of  $E_{hf}$  and  $E_{\text{MP2}}$ . These methods are usually referred to ‘MPN’, where  $N$  denotes the order at which the perturbation is truncated and  $E_{\text{tot}}$  is obtained in similar manner:

$$E_{\text{tot}} \approx E_{hf} + E_{\text{MP1}} + E_{\text{MP2}} + \dots + E_{\text{MPN}} \quad (2.33)$$

While the MP method may not be as accurate as the aforementioned configuration interaction or MCSCF methods, it is less computationally expensive to achieve often quantitatively useful results. Furthermore, similar to the configuration interaction method, it is only used for computing the GS energy. However, the perturbation energy obtained from MPN methods was applied to approximate the Green’s many-body function in the algebraic diagrammatic construction (ADC) scheme, first demonstrated by Schirmer in 1985.<sup>27;28</sup> Similar to the MPN methods, the ADC methods are denoted according to the perturbation order, *i.e.*, ADC( $N$ ). In the original work by Shirmer, the approximation was performed to the second order of perturbation, or ADC(2), and was recently extended to ADC(3) by Dreuw and co-workers in 2014.<sup>29</sup> The ADC(2) method for many-body problems strikes a

good balance between quantitatively useful results and computational costs. In conjunction with being implemented in the Turbomole computation package,<sup>30–32</sup> it is an increasingly popular method for computing excited state dynamics, and was instrumental for generating the potential energy surface cuts presented in Chapter 3. However, the method of ADC is highly complex and its derivation is beyond the scope of the current work. The readers are instead directed to the in depth review by Drew and Wormit and the references therein for details of this computational method.<sup>33</sup>

### 2.8.3 Density functional theory (DFT)

Although the methods based on the HF-SCF approximation could provide a close to full description of the systems under study, they are also relatively expensive, which, at minimum, scale as  $N^4$  for a system of  $N$  atoms.<sup>34</sup> As such, the computations become excessively expensive as the number of atoms in a molecule increases. Therefore, such systems are generally computed using a different method, the density functional theory (DFT). The essence of the DFT method is the determination of a molecule’s GS energy by the electron density,  $\rho$ , instead of solving the Schrödinger equation for all individual electronic wavefunctions. This in turn transformed the problem of approximating all the wavefunctions of particles into a problem of modelling the electron density dependent on 3 spatial coordinates ( $x$ ,  $y$  and  $z$ ). This is largely based on the Thomas-Fermi method, which was first validated by Hohenberg and Kohn in 1964, through the Hohenberg-Kohn (HK) existence theorem confirming the possibility of expressing the GS energy as a functional of the GS electron density,  $\rho$ :<sup>35</sup>

$$E[\rho] = T[\rho] + V_{ee}[\rho] + \int \rho(\mathbf{r})v(\mathbf{r})d\mathbf{r} \quad (2.34)$$

where  $T[\rho]$  and  $V_{ee}[\rho]$  are the kinetic and electron-electron potential energy functionals respectively;  $\rho(\mathbf{r})$  is the density function depending on the coordinate of electron  $\mathbf{r}$ ; and  $v(\mathbf{r})$  is the external potential that accounts for nuclei-electron and nuclei-nuclei and other nuclear specific energies. While this provided the basis for solving GS energy using the Thomas-Fermi method, approximation techniques were not elucidated in the reported work. In the year following the publication of the HK theorem, Kohn and Sham then established the first approximation technique,<sup>36</sup> which is very similar to the Hartree-Fock method. Firstly, the many-body system is separated into the ‘non-interacting’ density functions of individual electrons, akin to the expression in Equation (2.14), but replacing the wavefunctions with density

functions. It then follows procedures similar to HF-SCF and represents the ‘reference function’ as the Slater determinant of density spin orbitals, akin to Equations (2.17) and (2.18). As with the HF-SCF method, this approximation requires the correction for the lack of electron correlations, the Kohn-Sham (KS) method therefore introduced the basis for all subsequent approximation methods, in the following form:

$$E[\rho] = T_{ks}[\rho] + V_{ks}[\rho] + E_{ne}[\rho] + E_{xc}[\rho] \quad (2.35)$$

where  $T_{ks}$  and  $V_{ks}$  are the reference functional for  $T$  and  $V_{ee}$  from Equation (2.34);  $E_{ne}[\rho]$  accounts for the electron-nuclei potential energy; and  $E_{xc}[\rho]$  is the exchange-correlation energy correction. These two theorems are now considered the foundation for DFT and are usually jointly referred to as the Hohenberg-Kohn-Sham (HKS) theory, and for his contribution to this significant work, Kohn was awarded a Nobel prize in 1998. Similar to the HF-SCF, the basic forms of HKS do not account for the ES electronic configurations. However, an avenue for ES computation was provided in 1984 by Runge and Gross,<sup>37</sup> in the form of time dependent density functional theorem (TD-DFT). These two methods are now amongst the most widely employed techniques in the field of computational chemistry, and was utilised to provide qualitative understanding of the systems investigated in Chapters 3 and 5. Subsequent development on DFT then largely revolves around the improvements of  $E_{xc}[\rho]$  approximation as well as TD-DFT implementations. Generally speaking, these improvements follow similar methodologies as the higher level methods based on HF-SCF discussed (CASSCF, MPN and ADC( $N$ ) *etc.*) and vary greatly. As such, these will not be elaborated in this work, but the sources of methods utilised are provided in specific chapters for readers.

In general, for systems consisting of small numbers of atoms that require significant insights to the photodynamics (Chapter 3), HF-SCF based methods (MP2 and ADC(2)) were utilised for the potential energy surface calculations, while the more computational intensive molecular dynamics calculations were performed with DFT based methods. For systems with much greater number atoms (Chapter 5), only DFT calculations could be performed due to the prohibitive computational costs associated with MP2 calculations.

## References

- [1] J. P. Patterson, A. M. Sanchez, N. Petzetakis, T. P. Smart, T. H. Epps, III, I. Portman, N. R. Wilson and R. K. O’Reilly, *Soft Matter*, 2012, **8**, 3322–3328.

- [2] C. Würth, M. Grabolle, J. Pauli, M. Spieles and U. Resch-Genger, *Nat. Protocols*, 2013, **8**, 1535–1550.
- [3] A. N. Fletcher, *Photochem. Photobiol.*, 1969, **9**, 439–444.
- [4] K. Suzuki, A. Kobayashi, S. Kaneko, K. Takehira, T. Yoshihara, H. Ishida, Y. Shiina, S. Oishi and S. Tobita, *Phys. Chem. Chem. Phys.*, 2009, **11**, 9850–9860.
- [5] J. N. Miller, in *Standards in Fluorescence Spectrometry*, Chapman and Hall, 1981, pp. 49–67.
- [6] J. A. Gardecki and M. Maroncelli, *Appl. Spectrosc.*, 1998, **52**, 1179–1189.
- [7] H. Du, R.-C. A. Fuh, J. Li, L. A. Corkan and J. S. Lindsey, *Photochem. Photobiol.*, 1998, **68**, 141–142.
- [8] J. M. Dixon, M. Taniguchi and J. S. Lindsey, *Photochem. Photobiol.*, 2005, **81**, 212–213.
- [9] J. Lindsey and coworkers, *PhotochemCAD*, 2009, <http://www.photochemcad.com/pages/chemcad/chem-home.html>.
- [10] P. R. Bevington and D. K. Robinson, *Data Reduction and Error Analysis for the Physical Sciences*, McGraw Hill, 2nd edn., 1992.
- [11] S. E. Greenough, M. D. Horbury, J. O. F. Thompson, G. M. Roberts, T. N. V. Karsili, B. Marchetti, D. Townsend and V. G. Stavros, *Phys. Chem. Chem. Phys.*, 2014, **16**, 16187–16195.
- [12] S. E. Greenough, G. M. Roberts, N. A. Smith, M. D. Horbury, R. G. McKinlay, J. M. Zurek, M. J. Paterson, P. J. Sadler and V. G. Stavros, *Phys. Chem. Chem. Phys.*, 2014, **16**, 19141–19155.
- [13] M. Staniforth, J. D. Young, D. R. Cole, T. N. V. Karsili, M. N. R. Ashfold and V. G. Stavros, *J. Phys. Chem. A*, 2014, **118**, 10909–10918.
- [14] M. P. Grubb, A. J. Orr-Ewing and M. N. R. Ashfold, *Rev. Sci. Instrum.*, 2014, **85**, 064104.
- [15] L. Spörkel, G. Cui, A. Koslowski and W. Thiel, *J. Phys. Chem. A*, 2014, **118**, 152–157.
- [16] F. H. Westheimer, *Chem. Rev.*, 1961, **61**, 265–273.

- [17] C. G. Swain, E. C. Stivers, J. F. Reuwer and L. J. Schaad, *J. Am. Chem. Soc.*, 1958, **80**, 5885–5893.
- [18] M. A. Drezdson, *The manipulation of air-sensitive compounds*, John Wiley & Sons, 1986.
- [19] M. D. Horbury, L. A. Baker, W.-D. Quan, J. D. Young, M. Staniforth, S. E. Greenough and V. G. Stavros, *J. Phys. Chem. A*, 2015, **119**, 11989–11996.
- [20] A. S. Chatterley, C. W. West, V. G. Stavros and J. R. R. Verlet, *Chem. Sci.*, 2014, **5**, 3963–3975.
- [21] L. A. Baker, M. D. Horbury, S. E. Greenough, F. Allais, P. S. Walsh, S. Habershon and V. G. Stavros, *J. Phys. Chem. Lett.*, 2016, **7**, 56–61.
- [22] L. A. Baker, M. D. Horbury, S. E. Greenough, P. M. Coulter, T. N. V. Karsili, G. M. Roberts, A. J. Orr-Ewing, M. N. R. Ashfold and V. G. Stavros, *J. Phys. Chem. Lett.*, 2015, **6**, 1363–1368.
- [23] J. R. Lakowicz, *Principles of Fluorescence Spectroscopy*, Springer Science+Business Media, 3rd edn., 2006.
- [24] P. W. Atkins and R. S. Friedman, *Molecular Quantum Mechanics*, Oxford University Press, 5th edn., 2011.
- [25] J. G. Hill, *Int. J. Quantum Chem.*, 2013, **113**, 21–34.
- [26] C. Møller and M. S. Plesset, *Phys. Rev.*, 1934, **46**, 618–622.
- [27] J. Schirmer, *Phys. Rev. A*, 1982, **26**, 2395–2416.
- [28] A. B. Trofimov and J. Schirmer, *J. Phys. B*, 1995, **28**, 2299.
- [29] P. H. P. Harbach, M. Wormit and A. Dreuw, *J. Chem. Phys.*, 2014, **141**, 064113.
- [30] *TURBOMOLE V6.2 2010, a development of University of Karlsruhe and Forschungszentrum Karlsruhe GmbH, 1989-2007, TURBOMOLE GmbH, since 2007; available from <http://www.turbomole.com>.*
- [31] R. Ahlrichs, M. Bär, M. Häser, H. Horn and C. Kölmel, *Chem. Phys. Lett.*, 1989, **162**, 165–169.
- [32] F. Furche, R. Ahlrichs, C. Hättig, W. Klopper, M. Sierka and F. Weigend, *WIREs: Comp. Mol. Sci.*, 2014, **4**, 91–100.

- [33] A. Dreuw and M. Wormit, *WIREs Comput. Mol. Sci.*, 2015, **5**, 82–95.
- [34] Y. Shao, L. F. Molnar, Y. Jung, J. Kussmann, C. Ochsenfeld, S. T. Brown, A. T. Gilbert, L. V. Slipchenko, S. V. Levchenko, D. P. O’Neill, R. A. DiStasio Jr, R. C. Lochan, T. Wang, G. J. Beran, N. A. Besley, J. M. Herbert, C. Yeh Lin, T. Van Voorhis, S. Hung Chien, A. Sodt, R. P. Steele, V. A. Rassolov, P. E. Maslen, P. P. Korambath, R. D. Adamson, B. Austin, J. Baker, E. F. C. Byrd, H. Dachsel, R. J. Doerksen, A. Dreuw, B. D. Dunietz, A. D. Dutoi, T. R. Furlani, S. R. Gwaltney, A. Heyden, S. Hirata, C.-P. Hsu, G. Kedziora, R. Z. Khalliulin, P. Klunzinger, A. M. Lee, M. S. Lee, W. Liang, I. Lotan, N. Nair, B. Peters, E. I. Proynov, P. A. Pieniazek, Y. Min Rhee, J. Ritchie, E. Rosta, C. David Sherrill, A. C. Simmonett, J. E. Subotnik, H. Lee Woodcock III, W. Zhang, A. T. Bell, A. K. Chakraborty, D. M. Chipman, F. J. Keil, A. Warshel, W. J. Hehre, H. F. Schaefer III, J. Kong, A. I. Krylov, P. M. W. Gill and M. Head-Gordon, *Phys. Chem. Chem. Phys.*, 2006, **8**, 3172–3191.
- [35] P. Hohenberg and W. Kohn, *Phys. Rev.*, 1964, **136**, B864–B871.
- [36] W. Kohn and L. J. Sham, *Phys. Rev.*, 1965, **140**, A1133–A1138.
- [37] E. Runge and E. K. U. Gross, *Phys. Rev. Lett.*, 1984, **52**, 997–1000.

## Chapter 3

# Unravelling the photodynamics of a mono-amino-maleimide (MAM) fluorophore

As discussed in Section 1.5, the previously unexplained quenching of MAM fluorescence in protic solvents could limit its potential as a photosensitiser. Therefore, it is important to determine the mechanisms behind the fluorescence quenching and whether these processes could be alleviated to facilitate their role as upstream photosensitisers in aqueous media, or alternatively, exploited to introduce additional photoexcitation energy transfer or relaxation pathways for the light harvesting complex mimic. Furthermore, the synthesis of these MAM compounds is relatively simple, and their small sizes make the photophysical characterisations more approachable. Therefore, the investigation of maleimide based chromophore could serve as the first explorative step into the respective fields of chemistry that are essential for achieving the aim presented in Section 1.5.4 for the current thesis.

### 3.1 Introduction

Although the current thesis revolves around the utilisation of the MAM fluorophores as a photosensitiser for porphyrin in the overall vision of the thesis work which is to create light harvesting complex (LHC) mimics, they also possess strong application potential as a fluorescence probe. Indeed, one of the most utilised tools in industry and the scientific community is that of the fluorescent probes, ranging in applications from the macroscale such as contamination detection in water treatment to the micro-scale such as sub-cellular imaging. In particular, fluorescent dyes had

been traditionally applied through immunostaining to visualise protein distribution in cells, a destructive technique that renders live cell imaging infeasible. Such limitations were lifted since the discovery of green fluorescent proteins (GFPs).<sup>1</sup> Thanks to the ease of GFP integration in the form of protein fusion, a non-destructive technique with unmatched specificity, GFPs are by far the most utilised fluorophores in bio-imaging applications. Since the discovery of GFP, tremendous progress has been made in the field of *in vitro* live cell imaging, especially over the past two decades.<sup>2-4</sup> The role of fluorescent dyes has since evolved to be utilised for applications in the visualisation of biological molecules beyond the capability of GFP techniques, such as ions, metabolites or unusual inter-cellular aggregates.<sup>5-7</sup>

In recent years, methods for incorporation of non-canonical amino acids (ncAA) with highly modifiable functionalities into living organisms have matured greatly.<sup>8-10</sup> Furthermore, the concerted effort by the light microscopy community to push and break the diffraction limit produced techniques achieving spatial resolution of up to 10-30 nm.<sup>11-14</sup> These two advancements in their respective fields may lead to a new evolution of *in vitro* intracellular imaging technologies. Thus, the small size and the environmental sensing capability of the reported MAM fluorophores in conjunction with these techniques could help improve upon the two inherent limitations of GFPs: i) the size of GFPs may alter the intracellular activities of smaller proteins, hence observations may not be the accurate representation of the proteins under study;<sup>2</sup> and ii) their emission profiles do not change in response to their environment.<sup>4</sup> Furthermore, the maleimide based fluorophores have already been demonstrated as a viable self-reported functional handle, which was utilised to identify and localise micelle internalisation in live cells in the work by Robin and co-workers.<sup>15</sup> Together with their ease of synthesis, usually involving inexpensive materials,<sup>16</sup> they have the strong potential to be a very versatile tools for bio-imaging applications, and, more importantly for the current thesis work, as a photosensitiser that could potentially change its role when environment changes were present.

Therefore, the unravelling of the photodynamics of MAM would not only help determine the feasibility of this class of chromophore as photosensitiser for light harvesting applications, but also provide significant insights for the design rules of creating MAM based fluorophores for other applications. In the current chapter, the general synthesis of MAM through existing methods of maleimide modifications was detailed. This was followed by the experimental studies of the photodynamics of a simple variant of MAM fluorophore with the combination of static absorption/fluorescence spectroscopy and femtosecond transient electronic absorption spec-

trospecty (TEAS) performed in a non-polar, polar aprotic, and polar protic solvent. These results were complemented with insights from *ab initio* trajectory-based surface hopping molecular dynamics (MD) as well as electronic structure calculations, based around some of the methodologies discussed in Chapter 2, Section 2.8. These combined experimental and theoretical approach presented herein provided a close to complete structure-dynamics-function description of this molecule, serving as a basic guide for future designs of functional MAMs.

## 3.2 Maleimide modifications

A general rule for deciphering any photodynamical processes of a system is to start with the simplest molecule possible. More specifically, in order to minimise computational cost, the number of atoms should be kept to a minimum for the systems under investigation. As such, the model system was based on three basic forms of maleimide molecules, whose structures are shown in Figure 3.1.

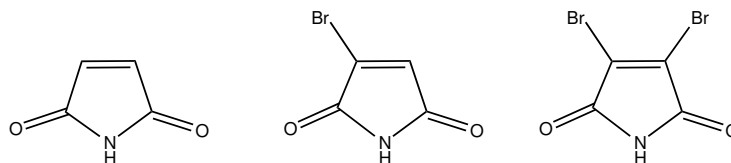


Figure 3.1: Chemical structures of unmodified maleimide (left) and the two modifiable version: monobromo-maleimide (MBM, middle) and dibromo-maleimide (right).

Of the 3 maleimides shown in Figure 3.1, the brominated versions can be easily modified. However, in the interest of simplicity and computational cost (discussed in Section 2.8), the monobromo-maleimide (3-bromo-1*H*-pyrrole-2,5-dione, henceforth referred to as MBM) variant was chosen as the starting material. As mentioned, the efficient synthesis of this compound from the unmodified maleimide was readily available from the literature, with a reported overall yield of *ca.* 22%, which was relatively simple to follow.<sup>17</sup> The synthesis conditions are shown in Figure 3.2.<sup>17</sup>

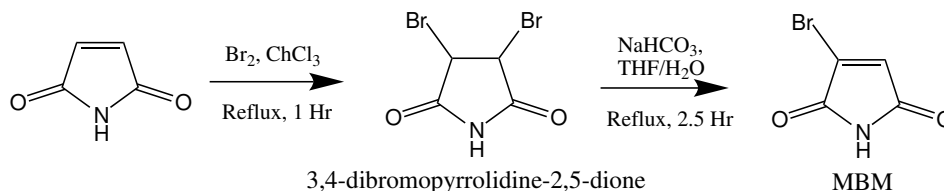


Figure 3.2: Synthesis of MBM, as reported by Vanel *et al.*<sup>17</sup>

Unfortunately, the exact reported work up procedures, in the present thesis work, only resulted in approximately half of the reported yield on the best attempts. Therefore, some modifications to the method were tested. For the first step, the most successful modification involved the rapid cooling of the solution in a dry ice–acetone bath upon completion (*cf.* slow cooling to room temperature in reported method). Upon complete precipitation of the crude intermediate product, the resulting solution was then filtered and washed with ice cold chloroform until a clear filtrate was obtained. This slight modification resulted in an improvement of the yield of the first step reaction from the literature reported yield of 49% to 80%. Furthermore, the same yields were obtained for syntheses with up to 5 g of starting material (51.5 mmol). For the second step, the modifications involved the removal of tetrahydrofuran (THF) solvent *in vacuo* prior to extraction with diethyl ether (Et<sub>2</sub>O) (*cf.* extraction with ethyl acetate without removal of THF in the reported work up). The Et<sub>2</sub>O extract was then washed and dried as reported. The yield of the second step was improved from the reported yield of 45% to 69%, and was reproducible for up to 2.5 g of the starting 3,4-dibromopyrrolidine-2,5-dione (9.73 mmol). The overall yield was therefore improved from 22% to 55% with these modifications.

The MBM can then be modified with a functionalised primary/secondary amine, in the presence of a base, to produce a mono-amino maleimide (MAM) compound. Depending on the strength of the base utilised, modification could be specific to the bromide site or at both the NH and bromide sites. A typical modification reaction using either sodium acetate (NaOAc) or sodium bicarbonate (NaHCO<sub>3</sub>), is illustrated in Figure 3.3 as a simple demonstration.

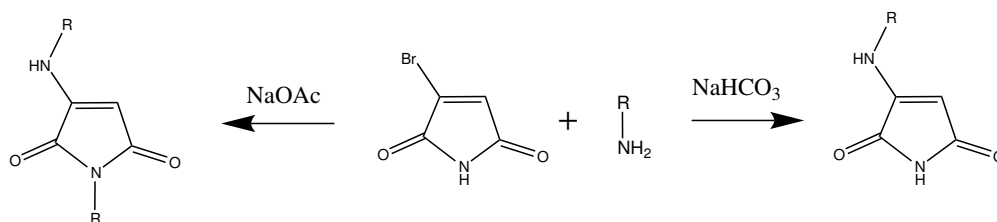


Figure 3.3: The two bases used for the modification of MBM, giving bromide site specific or simultaneous Br and NH site modifications.

More specifically, in the presence of a weak base such as sodium bicarbonate, the MBM could be selectively functionalised at the bromide site *via* an S<sub>N</sub>1 reaction, illustrated in Figure 3.4.

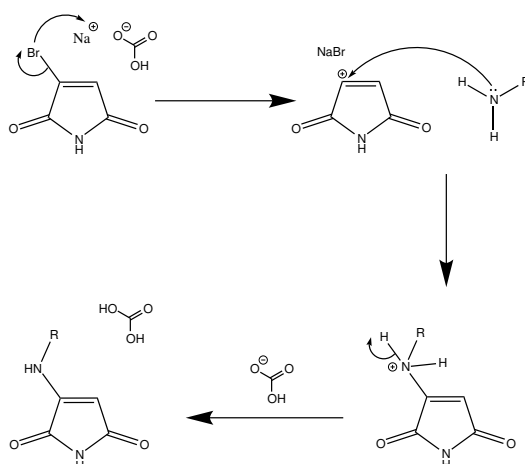


Figure 3.4:  $S_N1$  reaction mechanism of MBM for the functionalisation of MBM at the bromide site.

In the presence of a stronger base capable of deprotonating the functionalised amine, such as sodium acetate, further functionalisation at the amide site could occur *via* the ring-opening-ring-closing reaction, illustrated in Figure 3.5.

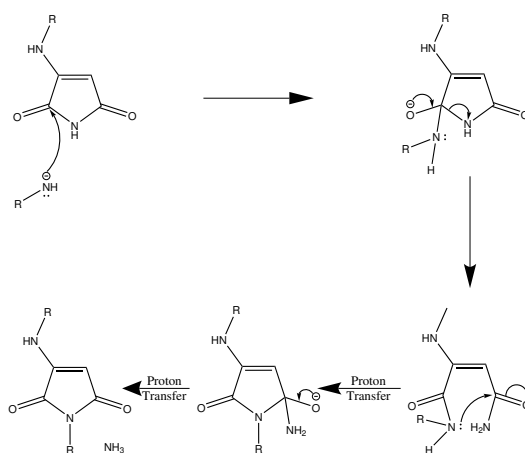


Figure 3.5: Ring-opening-ring-closing reaction mechanism of MBM for the functionalisation of MBM at the amide site.

Considering that the number of atoms in the system should be kept to a minimum, a single substitution at the Br site was preferred. However, the resulting compound was insoluble in non-polar solvents, especially cyclohexane (*c*-hexane), the quintessential starting solvent for condensed phase photochemical studies. Therefore, the best compromise between simplicity and solubility of the desired compound was the functionalisation of both Br and NH sites with a simple alkyl chain in the presence of NaOAc. A system with a methyl chain (NM-MAM) was chosen for the TEAS experiment, as its solubility in *c*-hexane was sufficient for obtaining

appreciable signal in the TEAS experiments ( $\sim 1$  m $\Delta$ OD, where OD denotes optical density, with saturated solution). The synthetic conditions for the synthesis of NM-MAM are shown in Figure 3.6.

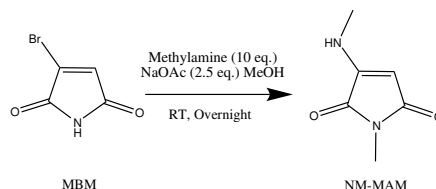


Figure 3.6: Synthetic scheme of 1-methyl-3-(methylamino)-1*H*-pyrrole-2,5-dione (NM-MAM)

More specifically, MBM (1 equivalent) and NaOAc (2.5 eq.) were first dissolved in methanol (MeOH) and stirred for *ca.* 10 minutes. To the stirring solution, 10 eq. of methylamine was then added. The reaction turned greenish yellow immediately and pure yellow as the reaction progressed. The solution was then left to stir overnight. Upon completion of the reaction, the MeOH was removed *in vacuo*, and the crude product was extracted with CH<sub>2</sub>Cl<sub>2</sub> and washed with water (3 $\times$ ) and brine (1 $\times$ ) and dried over MgSO<sub>4</sub>. The CH<sub>2</sub>Cl<sub>2</sub> was then reduced *in vacuo*, the residual solution was then directly loaded onto the silica column (CH<sub>2</sub>Cl<sub>2</sub>  $\rightarrow$  0.5% MeOH in CH<sub>2</sub>Cl<sub>2</sub>). In most cases, the product was the yellow band that moves down the column, whereas the major yellow/orange by-product tended to stick to the silica column. This made the extraction process relatively straight forward by simply collecting the front running yellow band, obtaining yellow solid product upon removal of solvent *in vacuo*. Successful synthesis can be confirmed by the two N-methyl peaks appearing on the <sup>1</sup>H NMR spectrum at 2.92 and 2.98 ppm (3H), along with the singular proton (=C-H) from the starting maleimide at 4.82 ppm. Characterisation data for NM-MAM are presented in Section 3.8.

However, the best yield achieved with this synthetic method was rather disappointing at *ca.* 20%. This might be due to formation of by-products from the final ring-closing steps illustrated in Figure 3.5. On the one hand, isolation of the desired product was easily achieved due to the affinity of by-product to the silica column. On the other hand, the aforementioned affinity also rendered the recovery of by-products difficult for the analysis of their chemical nature. However, these by-products likely arise from the reaction condition for the functionalisation at the amide site. Therefore, for future designs, an N-functionalised MBM as the starting material may improve the overall yield by avoiding the use of the stronger base required for the simultaneous functionalisation of both the bromide and the amide site of MBM. However, as mentioned in Section 3.1, the primary objective of the current chapter

of the thesis work was to unravel the previously unexplained mechanisms causing the fluorescence quenching of MAM fluorophores in protic solvents. Furthermore, the starting material MBM can be easily synthesised in large quantities, which in turn provided sufficient amount of MAM to achieve this objective. Thus, the optimisation of producing the N-functionalised MBM starting materials is beyond the scope of the current thesis and are not discussed further.

### 3.3 Static spectroscopy characterisation of NM-MAM

Prior to the investigation into the ultrafast photodynamics of the current NM-MAM, the confirmation of fluorescence quenching in the presence of protic solvents were required for the NM-MAM to be comparable to previously reported maleimide based fluorophores.<sup>15;16</sup> Therefore, standard static spectroscopic measurements were performed. Firstly, the ultraviolet-visible (UV-Vis) absorption of NM-MAM, solvated in non-polar (c-hexane), polar aprotic (acetonitrile, hence forth referred to MeCN) and polar protic (MeOH, and deuterated methanol, MeO- $d_4$ ) solvents were investigated. The normalised UV-Vis spectra collected are shown in Figure 3.7.

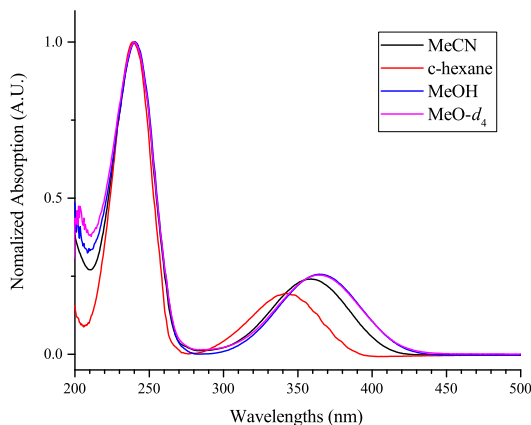


Figure 3.7: Normalised UV-Vis spectra of NM-MAM in all solvents studied. MeCN–acetonitrile; c-hexane–cyclohexane; MeOH–methanol; and MeO- $d_4$ –deuterated methanol. Spectra are normalised such that the absorption maxima covering the spectral region of 230–260 nm equal 1.

Briefly, two major absorption bands were observed for the NM-MAM solvated in all solvent systems. The higher energy band, with a maximum at *ca.* 240 nm, showed very little variation between the solvent systems. The lower energy band however, showed much greater sensitivity towards solvent polarity, with the maximum shifting from *ca.* 345 nm in c-hexane to *ca.* 365 nm in MeOH and MeO- $d_4$ . Of the two absorption bands, the lower energy band will be the focus of the current studies as the feature likely involves a single lowest excited state, thus simplifying

the subsequent photodynamics interpretations and quantum mechanical calculations. Furthermore, applications exploiting the wavelength corresponding to higher energy band (240 nm) is relatively limited due to the low irradiance content at the far UV region ( $< 280$  nm), as shown in Figure 1.1, as well as their overlap with the absorption of biological molecules such as the DNA base pairs.

To determine whether the fluorescence of the NM-MAM under study demonstrate similar quenching behaviour as reported maleimide fluorophores, fluorescence quantum yield ( $\phi_f$ ) measurements were also performed with the method described in Section 2.6.1. These measurements showed fluorescence quenching in protic solvent in the current NM-MAM molecule, similar to the previously reported MAM.<sup>15;16</sup> When solvated in the aprotic solvents, relatively high  $\phi_f$ s were observed:  $38 \pm 2\%$  in n-hexane (non-polar aprotic) and  $30 \pm 1.5\%$  in MeCN (polar aprotic). Upon solvation in the protic solvent MeOH, the  $\phi_f$  suffered a significant drop to a mere  $1.6 \pm 0.1\%$ . The  $\phi_f$  in MeO- $d_4$  was slightly higher at  $2.5 \pm 0.2\%$ , the reason for observed higher  $\phi_f$  in MeO- $d_4$  and the inclusion of measurements in this deuterated solvent would be discussed in the latter parts of the current chapter. Furthermore, the emission maxima showed similar degree of red-shifting when solvated in c-hexane, MeCN and MeOH/- $d_4$ . Although it is not uncommon for emission to shift due to solvent polarity, this energy gap may suggest the emissions originate from two, yet to be identified excited states (ES). The normalised fluorescence spectra for NM-MAM solvated in c-hexane, MeCN and MeO- $d_4$  are shown in Figure 3.8. The spectrum for NM-MAM in MeO- $d_4$  showed an almost identical spectral profile to NM-MAM in MeOH, but

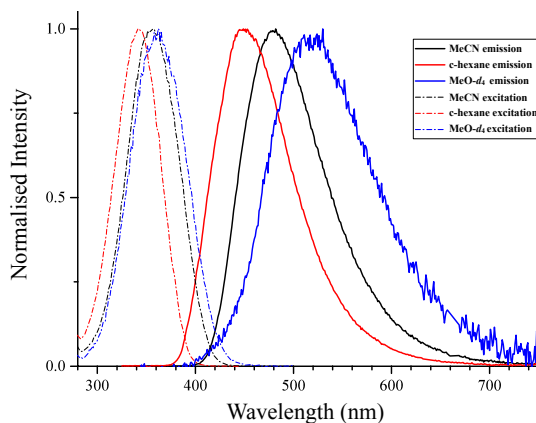


Figure 3.8: Normalised fluorescence spectra of NM-MAM in solvents studied. MeCN–acetonitrile; c-hexane–cyclohexane; and MeO- $d_4$ –deuterated methanol. The collected spectra were first corrected using the method described in Section 2.6.2, which were then normalised to the maxima of each spectra. The signal to noise ratio in MeO- $d_4$  was much lower due to the low  $\phi_f$ , hence the observed noise.

with an increase in signal. It was therefore presented in place of NM-MAM solvated in MeOH.

Based on the static spectroscopic characterisations presented, the fluorescence quantum yield of NM-MAM was within the range of previously studied MAM fluorophores (*ca.* 10–59% in dioxane),<sup>16</sup> and more importantly, similar fluorescence quenching in the presence of protic solvent were observed ( $\leq 2.6\%$  in literature).<sup>16</sup> Therefore, the photophysical processes uncovered in the current chapter, presented in proceeding sections, should be applicable to future designs of MAM fluorophores.

### 3.4 TEAS of NM-MAM in various solvents

TEAS experiments were performed on NM-MAM in all the solvents mentioned in Section 3.3, namely, c-hexane, MeCN, MeOH and MeO-*d*<sub>4</sub>. In similar order to the discussions of static spectroscopic properties, the transient absorption spectra (TAS) obtained with NM-MAM solvated in c-hexane and MeCN were examined first, shown in Figure 3.9.

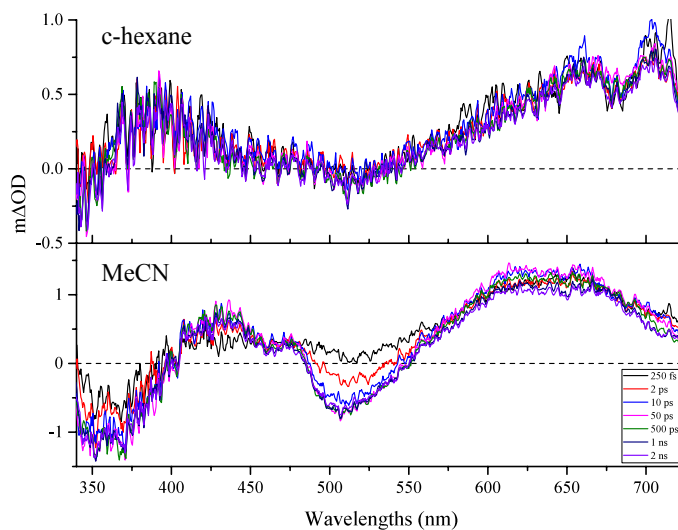


Figure 3.9: TAS for NM-MAM in: cyclohexane (c-hexane, saturated at  $<1$  mM) excited at 345 nm (top); and acetonitrile (MeCN, 8 mM) excited at 360 nm (bottom). The author note that due to the poor solubility of NM-MAM in c-hexane, the signals obtained were much lower than other TAS collected, hence the increased observed noise.

As shown in Figure 3.9 (top), TAS of NM-MAM in c-hexane showed two clear positive absorption features, which was assigned to excited state absorption (ESA). The first was a relatively narrow and weak feature centred at  $\sim 390$  nm, whilst the second, a broader and more intense feature, spans the wavelength range  $\sim 600$ – $725$

nm. Between these ESA features, a weak negative absorption signal was also evident. Such negative signals (that appear at probe wavelengths remote from the absorption maximum) were plausibly assigned to stimulated emission (SE). In addition, a negative absorption signal could be observed close to the pump wavelength ( $<350$  nm), this is a clear indication of ground state bleach (GSB). The spectral features described show no significant evolution across the 2 ns temporal window of our experiment, which was clearly apparent as individual TAS from across the time points presented almost overlap one another. This observation is consistent with population of a relatively long lived excited state (beyond 2 ns), most likely the strongly absorbing  $S_1$  ( $1^1\pi\pi^*$ ) state.

Upon examining the TAS profile of NM-MAM solvated in MeCN (Figure 3.9, bottom), significant differences were immediately apparent when compared to that obtained from the NM-MAM solvated in c-hexane. Firstly, two broad ESA features were observed, centred at  $\sim 440$  nm and  $\sim 640$  nm (*cf.*  $\sim 390$  nm and  $\sim 600$ – $725$  nm in c-hexane). Secondly, the SE feature at  $\sim 515$  nm appears to grow in over the period between 250 fs and 10 ps. Finally, the GSB feature appeared centred at  $\sim 360$  nm was consistent with the UV-Vis measurement and showed no discernible evolution passed 10 ps, in a similar manner to that observed in c-hexane. This then leads to the inspection of the TAS obtained for NM-MAM in MeOH and MeO- $d_4$ , presented for selected pump-probe time delays in Figure 3.10.

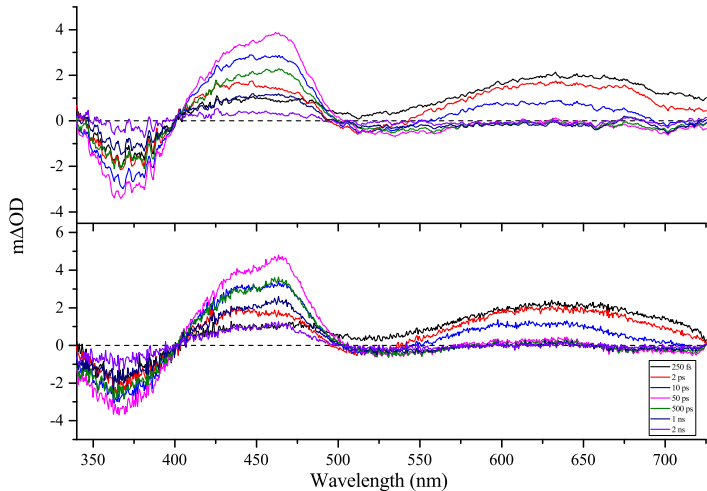


Figure 3.10: TAS of TAS for NM-MAM in: methanol (MeOH, top) and deuterated methanol (MeO- $d_4$ , bottom) both excited at 365 nm (10 mM).

As can be seen in Figure 3.10, the TAS obtained from MeOH and MeO- $d_4$  demonstrated marked differences from those obtained with c-hexane and MeCN solutions. In particular, the TAS features observed during the initial evolution (sub-

ps) were near identical to that from the MeCN solution, with ESA features at  $\sim 450$  nm and  $\sim 640$  nm superimposed with SE at  $\sim 530$  nm and GSB at  $\sim 365$  nm. The ESA feature at  $\sim 640$  nm then decayed concurrently with the growth at  $\sim 450$  nm. The latter of the two features then decays to almost the baseline of the TAS by 2 ns. In order to gain quantitative insight into the photodynamic processes observed, the global fitting procedure described in Section 2.7.3 was performed on the TAS, with the decay associated spectra (DAS) of all TAS of interest shown in Figure 3.11. The DAS provided visual insights towards the interpretation of the time constants for the dynamical processes in operation (see below), where the flow of excited state populations are identified when a positive and negative feature appear concurrently in a DAS associated with a particular time constant. These could arise from either a change in electronic state, through processes such as internal conversion (IC) and intersystem crossing (ISC), or relaxation within a single electronically excited state, through the process of intermolecular vibrational energy transfer (IET), as discussed in Section 1.2.2, Chapter 1.<sup>18;19</sup>

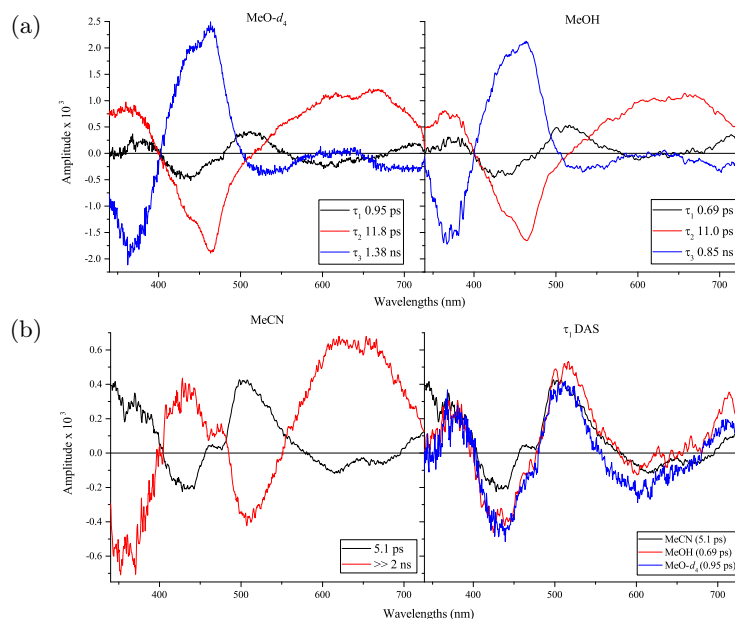


Figure 3.11: DAS obtained from global fitting the TAS of NM-MAM solvated in: (a) MeO- $d_4$  (left) and MeOH (right); (b) MeCN ( $\lambda_{pu}=360$  nm, left), and the DAS associated to  $\tau_1$  for each system (right). Method for global fitting TAS was described in Section 2.7.3.

For the TAS obtained from c-hexane, a single exponential with a time constant beyond the 2 ns temporal window was extracted. This is in accord with the relatively high 38%  $\phi_f$  measured, as expected from  $S_1$  state emission. The DAS shows essentially identical features as the TAS (Figure 3.9, top), hence it is not pre-

sented. For the MeCN solution, two processes were extracted. One at the early time with a time constant of  $\sim 5$  ps, in which the ESA features (at  $\sim 440$  and  $\sim 650$  nm) narrowed and grew in positive intensity slightly, this was accompanied with the SE and GSB features broadening and growing in negative intensity (Figure 3.11b, left, black line). This was then followed by a process beyond the temporal window of 2 ns, showing unchanged TAS features (Figure 3.11b, left, red line). The latter of the processes is in accord to the 30%  $\phi_f$  retained in MeCN. Finally, for the MeOH and MeO- $d_4$  system, three processes were extracted for both. The first component was fitted with a lifetime of  $\sim 0.7$  ps, which showed a spectral profile similar to the 5 ps component of MeCN, as demonstrated by the near overlap of DAS associated with  $\tau_1$  for the three systems (see Figure 3.11b, right). The DAS for the second,  $\sim 11$  ps component correlates strongly to the concurrent decay and growth of ESAs at  $\sim 640$  nm and  $\sim 450$  nm, respectively. This was then followed by the final  $\sim 850$  and  $\sim 1380$  ps components, in MeOH and MeO- $d_4$  respectively, leading to a near complete baseline recovery by 2 ns in the TAS. This greatly reduced lifetime is consistent with the significant reduction of  $\phi_f$  to 1.6% in MeOH. All time constants associated with the processes described and  $\phi_f$ s for each solvated system studied are listed in Table 3.1.

Table 3.1: Fluorescence quantum yields measured and extracted time constants from global fitting the TAS of NM-MAM in all solvents studied. The fitting for MeOH and MeO- $d_4$  were performed with an additional  $\gg 2$  ns component as a benchmark, but showed no appreciable difference in the results. As such, the photodynamics were considered well described by the presented time constants.

Solvent	$\phi_f$	$\tau_1$	$\tau_2$	$\tau_3$
c-hexane	$38 \pm 2\%$	$\gg 2$ ns	-	-
MeCN	$30 \pm 1\%$	$5.1 \pm 2.5$ ps	$\gg 2$ ns	-
MeOH	$1.6 \pm 0.1\%$	$688 \pm 282$ fs	$11 \pm 1.7$ ps	$845 \pm 105$ ps
MeO- $d_4$	$2.5 \pm 0.2\%$	945 fs	$11.8 \pm 2$ ps	$1380 \pm 170$ ps

With these observations, it was clear that, the photodynamic processes observed in MeOH and MeO- $d_4$  could not be rationalised by intuition alone. Therefore, *ab initio* quantum mechanical calculations (QMC) with NM-MAM and explicit MeOH molecules were performed by Dr. Tolga Karsili at Technische Universität München to gain further insight. The results are discussed in the following section.

### 3.5 QMC of NM-MAM

To gain a qualitative mechanistic insight into the excited states dynamics of NM-MAM, non-adiabatic surface hopping molecular dynamics (QMMD) simulations were first employed. These were performed using a locally developed version of Newton-

X,<sup>20;21</sup> on a system consisting of NM-MAM in a cluster of three MeOH solvent molecules (the minimum required to describe all dominant chromophore-solvent hydrogen-bonding interactions). The ground state equilibrium geometry and associated harmonic normal mode wavenumbers were obtained with the Gaussian 09 software package (G09),<sup>22</sup> using Density Functional Theory (DFT) utilising the Becke 3-parameter Lee-Yang-Parr (B3LYP) functional, which was developed based on the methods described in Section 2.8.3 (Chapter 2), and a 6-31G Pople basis set.<sup>23</sup> An ensemble of 50 trajectories was created by sampling a Wigner distribution based on the ground state harmonic normal mode eigenvectors with the Newton-X software.<sup>20;21</sup> The nuclear degrees of freedom were driven by integrating Newton’s classical equations of motion in time steps of 0.5 fs. The electronic coordinates were instead driven by integrating the semi-classical time-dependent Schrödinger equation using Butcher’s fifth-order Runge-Kutta method in time steps of 0.025 fs. As proposed by Granucci,<sup>24;25</sup> a decoherence correction of  $0.1 E_h$  was used. All trajectories were initiated on  $S_1$  and terminated when the  $S_0$ - $S_1$  energy gap fell below 0.1 eV, which were assumed to have relaxed from the higher excited state to the ground state. Trajectories that did not fulfil this termination criteria were propagated to a maximum time of 1 ps. At each time step, energies and gradients were obtained in real time using DFT/B3LYP/6-31G – precluding the necessity to compute a reduced dimensional potential energy (PE) surface. These DFT calculations were also undertaken using the G09 software package.<sup>22</sup> The trajectories showed that the  $S_1$  locally excited (LE) state coupled to a charge transfer (CT) state that contained the electronic configuration  $2p_y(\text{O}_{\text{MeOH}})^1 \pi^*(\text{NM-MAM})^1$  and was reactive with respect to proton transfer (PT) from MeOH to the carbonyl group of the maleimide. These manifested in the form of MeOH proton migration towards the carbonyl group of NM-MAM, a representative geometric progression of NM-MAM over the course of QMMD simulation is shown in Figure 3.12.

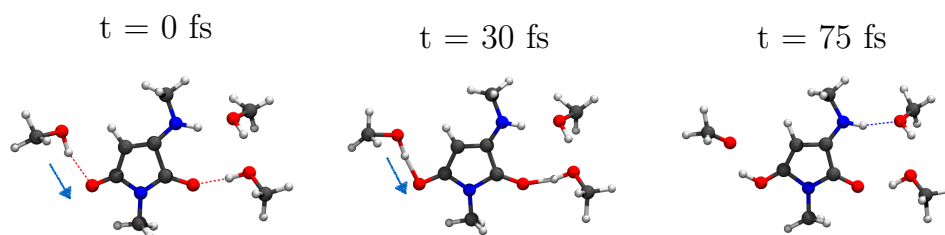


Figure 3.12: Representative geometry of NM-MAM over the course of QMMD simulations, arrows indicate movement of the hydroxyl proton from MeOH.

This process showed very rapid rate of completion, as the majority of the tra-

jectories ( $\sim 90\%$ ) were completed by 80 fs. This was demonstrated by the population remaining in the  $S_1$  excited state, presented in Figure 3.13.

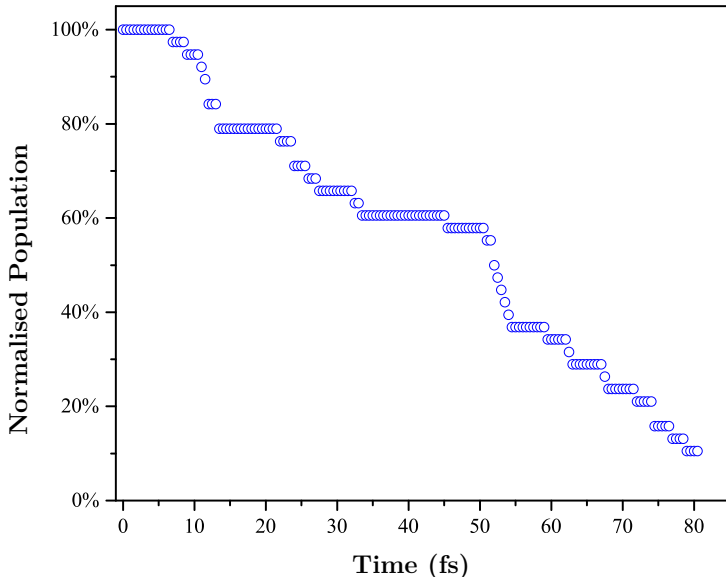


Figure 3.13: The decay of populations remaining in the  $S_1$  excited state over the course of the QMMD simulation. Data are presented as percentage of total trajectories run.

However, it is important to note that the relatively small size of the basis set, coupled with a functional that was not parameterised for long-range correlations, could only (at best) return a qualitative picture of the topography of the potential energy (PE) surface. That said, the present MD simulations were only obtained in order to provide a qualitative insight on the dominate reaction paths. As such, guided by the returned trajectories, relaxed potential energy cuts (PECs) were constructed along the  $R_{O-H}$  stretch dimension of MeOH (the path along which represents intermolecular PT from MeOH to NM-MAM) using state-of-the-art electronic structure theory, using the Turbomole computation package.<sup>26–28</sup> The ground state equilibrium geometry of NM-MAM in the same cluster of three MeOH molecules was re-optimised using the Møller-Plesset second-order perturbation theory (MP2), as briefly described in Section 2.8.2 (Chapter 2), coupled to a cc-pVDZ basis set. Since all trajectories deactivated  $S_1$  by motion along a solvent to solute proton transfer coordinate (Figure 3.12),  $S_1$  relaxed PE scans were undertaken at the second-order algebraic diagrammatic construction (ADC(2)) (see work by Drew and Wormit for detailed description of computation methodologies)<sup>29</sup> using the  $R_{O-H}$  coordinate on a single MeOH as the driving coordinate. The corresponding  $S_0$  energies at a particular  $S_1$  relaxed geometry were computed using MP2/cc-pVDZ. These calculations were undertaken using, once again, the Turbomole software package.<sup>28</sup> The returned

PECs are given in Figure 3.14.

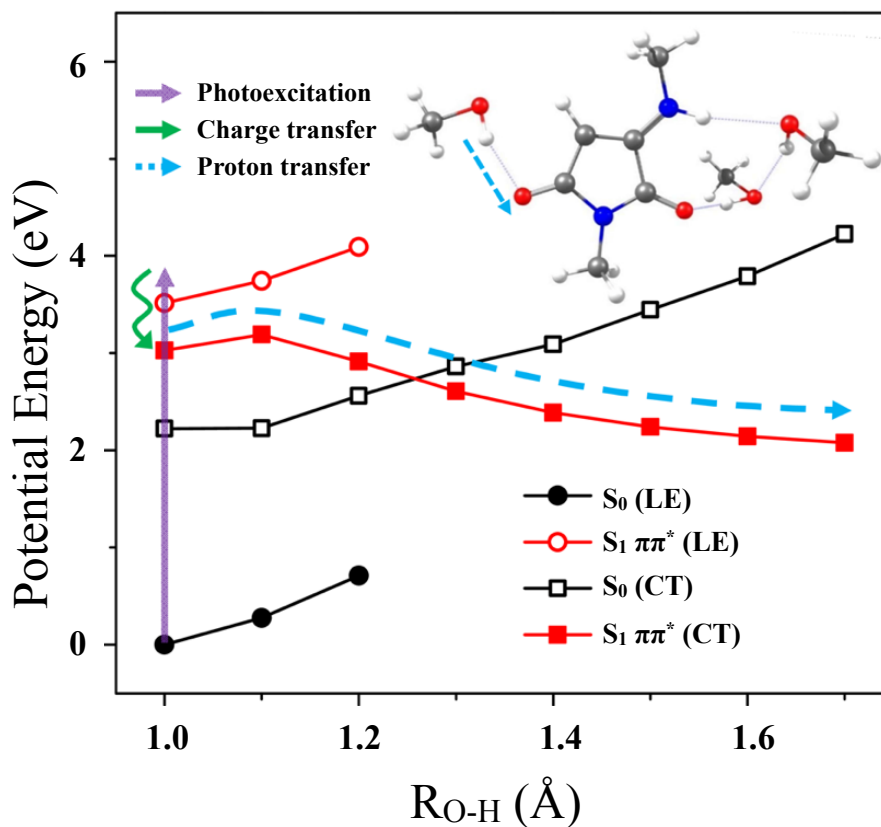


Figure 3.14: PECs of NM-MAM along the OH(Me) coordinate of the  $S_0$  (black) and  $S_1$  (red) states for the locally excited (LE, circles) and charge transfer (CT, squares) configurations. For each point,  $R_{O-H}$  (inset, blue arrow) was fixed and the rest of the geometry allowed to relax. Solid points indicate the state that was optimised for geometry relaxation.

As can be seen in Figure 3.14, the PECs confirmed that the relaxed  $S_1$ (CT) state contains a labile path with respect to proton transfer from MeOH to NM-MAM (blue dashed arrow, Figure 3.14). This stability in the relaxed  $S_1$ (CT) profile can be understood on electronic grounds: the CT state contained a charge-separation that was neutralised by proton transfer. However, it should be noted that the relaxed  $S_1$ (CT) profile contains a local minimum at short  $R_{O-H}$  which could trap population at near threshold excitations (green curved arrow, Figure 3.14). The above described calculations implied that electron driven proton transfer (EDPT) was a viable non-radiative relaxation pathway for NN-MAM in MeOH solution, thus the observed fluorescence quenching. Although MD calculations and associated electronic structure calculations of NN-MAM in MeCN were not performed, the electron withdrawing CN group in MeCN was likely to stabilise a CT state containing the electronic configuration  $\pi(\text{CN})^1 \pi^*(\text{NM-MAM})^1$ , analogous to that of MeOH. However, charge

recombination was unlikely to occur in the MeCN solution due to the absence of a labile proton donor.

The CT and EDPT processes can be more intuitively visualised as the movement of electron ‘holes’ between the solvent and NM-MAM molecules, as illustrated in Figure 3.15.

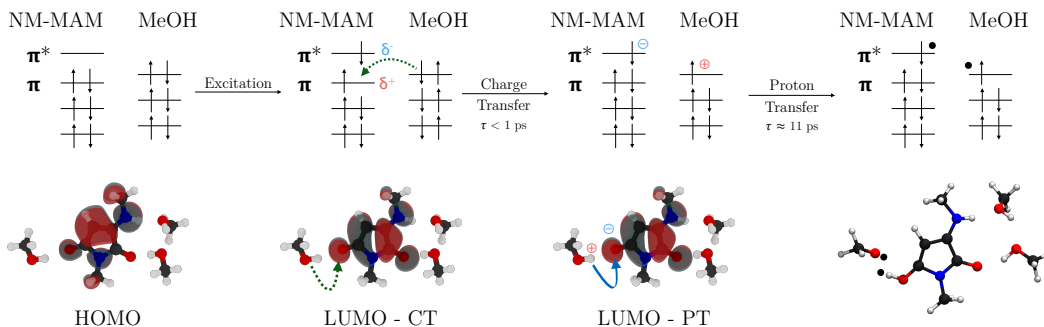


Figure 3.15: Illustration of EDPT mechanism for NM-MAM solvated in MeOH. The molecular orbitals (HOMO and LUMO) were generated with the G09 package,<sup>22</sup> and were rendered with VMD.<sup>30</sup> The bonding orbital diagrams are presented to visualise the location of electron hole. Electronic movement is indicated by the green dashed arrow (LUMO–CT) and proton movement is indicated by the blue solid arrow (LUMO–PT). Mechanism of the EDPT process is detailed in the main text.

With reference to Figure 3.15, upon photoexcitation of the NM-MAM in MeOH, an excited state of  $\pi\pi^*$  was generated. This in turn introduced a slight delocalisation of charge density (Figure 3.15, LUMO–CT, second from the left), which was filled by the migration of an electron from a nearby MeOH solvent molecule. This then resulted in two charge separated species, namely the  $\text{NM-MAM}^\ominus$  and  $\text{MeOH}^\oplus$ . The proton from the  $\text{MeOH}^\oplus$  species then follows the charge difference (Figure 3.15, LUMO–PT, second from the right). Upon the completion of this proton transfer process, the charge in both species was neutralised and took the form of a neutral bi-radical species (final step in Figure 3.15).

Based on all the observations presented thus far, a potential mechanism for the fluorescence quenching observed may be elucidated, with the discussion presented in the proceeding section.

### 3.6 Overall interpretation of photodynamics of MAM

With the insights provided by the theoretical data, it could be postulated that the marked difference in the observed TAS between the non-polar solutions (c-hexane) and polar solutions (MeCN, MeOH and MeO- $d_4$ ) may be understood in terms of a CT state being accessed in the latter. Together with the marked resemblance

between the TAS of MeOH and MeCN during short time delays ( $\Delta t < 500$  fs), such a state was highly likely to be accessed in both cases. Finally, the DAS for the  $\tau_1$  component in MeCN and MeOH are near identical (Figure 3.11b, right). As EDPT was unlikely to occur in MeCN, this component was therefore assigned to  $\tau_1$  in both polar solvents to  $S_1(\text{LE}) \rightarrow S_1(\text{CT})$  internal conversion. The slow time constant in MeCN, as compared to the sub 1 ps lifetime in MeOH, could then be attributed to the weaker interaction between MeCN and NM-MAM, due to the lack of H bonding (*cf.* MeOH and NM-MAM). While the Stokes shifts observed in the UV-Vis absorption measurements indicated a further change of state occurring in MeOH, the PECs in Figure 3.14 would suggest that it was unlikely this emission occurs after EDPT, as the  $^1\pi\pi^*(\text{CT})$  state now becomes the lowest energy state. Therefore, the fluorescence of NM-MAM in MeOH may originate from population trapped *via* vibrational cooling in the  $S_1(\text{CT})$  local minimum present at short  $R_{\text{O-H}}$  ( $\sim 1$  Å, Figure 3.14). The low  $\phi_f$  of this state was then likely a result of the poor Franck-Condon (FC) factors between  $S_1(\text{CT})$  and  $S_0$ , as well as the greatly reduced lifetime of  $S_1$ . Extending the former of these two factors to NM-MAM in MeCN, the relatively high  $\phi_f$  of 30% in MeCN was surprising but can be understood by considering the effect of  $\pi$  stacking between NM-MAM and MeCN, which is not present in MeOH. This  $\pi$  stacking likely led to an increased FC overlap between the participating orbitals that gave rise to the CT state (albeit, still reduced compared to a locally excited  $\pi\pi^*$  state). Furthermore, the long-lived nature of the  $S_1(\text{CT})$  observed may suggest that a larger barrier for the internal conversion of  $S_1(\text{CT}) \rightarrow S_0(\text{CT})$ , hence trapping the populations in the  $S_1(\text{CT})$  state, leading to the relatively high  $\phi_f$  observed.

The calculations performed suggest the CT state was accessed in  $<100$  fs in MeOH, rather than the  $\sim 0.7$  ps observed. However, the QMCs were performed using only three discrete MeOH molecules, at 0 K, effectively ‘freezing’ the molecules in their lowest energy geometry. This geometry may be similar to a previous study on Coumarin 102 (C102) with low concentration of donating solvent in a mixed solvent system, where the rate of CT was significantly increased compared to that observed in bulk solvent.<sup>31</sup> This was attributed to the perturbations to solute/solvent interactions induced by the long chains of H bonds.<sup>31</sup> As such, the slower rate observed may be attributed to the TEAS experimental conditions, which were conducted with bulk solvent at ambient temperature, similar to the previous study on C102.<sup>31</sup>

Given that  $\tau_1$  observed in the TAS of MeOH was most likely attributed to the  $S_1(\text{LE}) \rightarrow S_1(\text{CT})$  IC, the EDPT process was therefore most plausibly captured by the second time constant of  $\sim 11$  ps. This process showed a far more structured and dramatic change in the ESA features than  $\tau_1$ . These significant changes in

the spectral profile were consistent with a proton transfer, as inter/intramolecular H-atom transfer often results in a large perturbation to the excited state energy landscape.<sup>32;33</sup>  $\tau_2$  then likely corresponds to the excited state population progressing out of the local potential minimum predicted at short  $R_{O-H}$  distances in  $S_1(CT)$  and along the reactive  $R_{O-H}$  coordinate resulting in EDPT.

Finally, a third process was evident in MeOH which appeared as a decay of the final ESA and SE, coupled with the recovery of the GSB over  $\tau_3 = 850$  ps. The absence of any long-term component, the near complete recovery of the GSB, and decay of the ESA signal, suggested that no significant photoproduct was formed, and that NM-MAM returns to  $S_0$ . This strongly suggests that the final process must involve a back proton transfer (NM-MAM-to-solvent), *i.e.* a reforming of the starting molecule at the  $S_0/CT$  state crossing at  $R_{O-H} \sim 1.25$  Å (Figure 3.14). The relatively long lifetime of this final process, coupled with the presence of the carbonyl groups on maleimide, suggest that this was likely mediated by intersystem crossing (ISC) followed by proton recombination of the solvent once the wavepacket is on the triplet surface.<sup>34;35</sup>

This then leads to the discussion of the results from MeO- $d_4$  solutions. As discussed in Section 2.7.2 (Chapter 2), these experiments could provide insights of the EDPT by determining the presence of any kinetic isotope effects (KIE). In general, the KIE caused by the deuteration of a single proton site should result in a change in lifetime proportional to the ratio of the reduced masses, *i.e.*  $\sqrt{2}$  or  $\sim 1.4$ .<sup>36-38</sup> Unsurprisingly, the TAS and the extracted DAS of MeOH and MeO- $d_4$  showed near identical spectral features (Figure 3.10). No firm conclusions could be drawn from  $\tau_1$  or  $\tau_2$  (Table 3.1), due to the relatively large error of the fits, which was likely due to their relatively small contribution to the overall ESA evolution (see Section 3.8.2). However previous theoretical work had suggested a range of KIE for ‘double well’ proton transfers of  $\sim 1.0$ – $1.8$ .<sup>39</sup> Furthermore, the very shallow nature of the local minimum at  $R_{O-H} = 1$  Å (Figure 3.14) would not necessarily lead to a tunneling process being involved in EDPT, resulting in a KIE of  $\sim 1.4$ . However, the KIE observed for  $\tau_3$  with a value of  $\sim 1.6$  could be interpreted with confidence. This strongly indicates that the motion of a single proton originating from the solvent was involved. The recovery of the baseline in the MeOH/- $d_4$  TAS also indicates that back proton transfer to the solvent molecules occurred, confirming that the initial EDPT must be attributable to the earlier dynamical processes,  $\tau_1$  or  $\tau_2$ , with the latter process being the most likely candidate. Based on these overall interpretations, we can now construct an overall photorelaxation mechanism for NM-MAM in the solvents studied, illustrated in Figure 3.16.

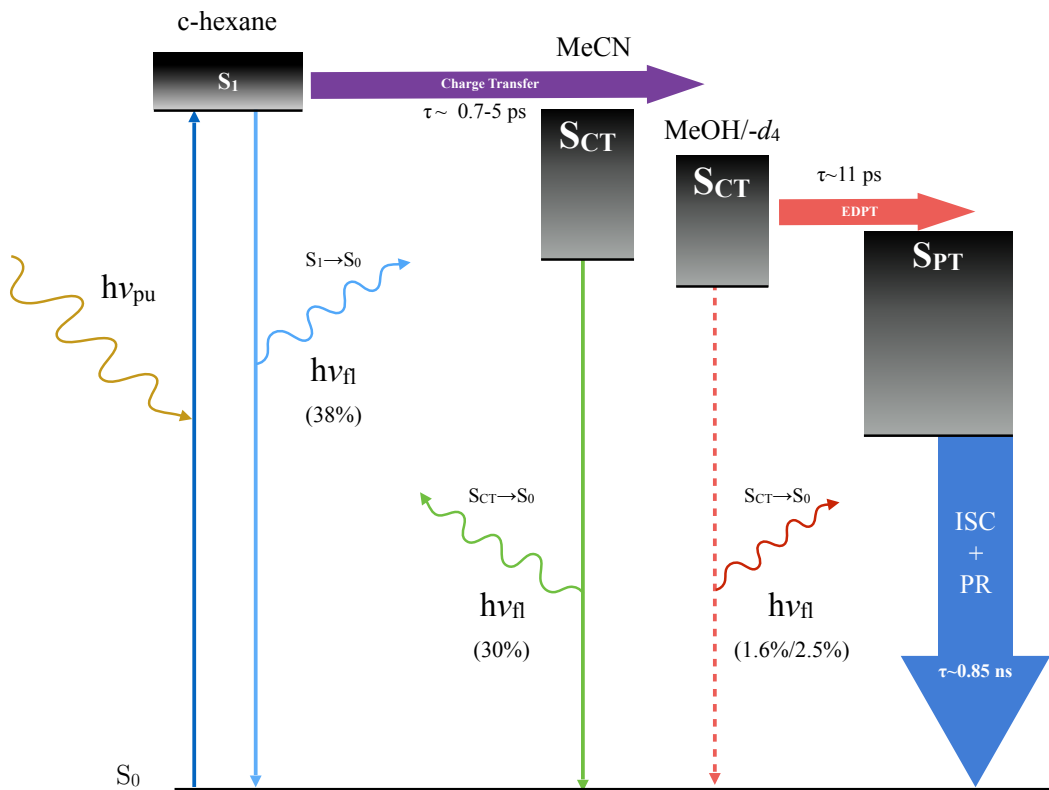


Figure 3.16: Graphical summary of proposed photorelaxation pathways, where:  $h\nu_{pu}$  – photo excitation;  $h\nu_f$  – fluorescence emission;  $S_{CT}$  – charge transferred state; EDPT – electron driven proton transfer;  $S_{PT}$  – proton transferred state; ISC – intersystem crossing; PR – proton recombination. The CT state is accessible in MeCN, MeOH and MeO- $d_4$  but not in c-hexane. The EDPT pathway is only accessible in MeOH and MeO- $d_4$ . The  $\phi_f$  arising from each state are given below the corresponding arrows.

With reference to Figure 3.16, the NM-MAM undergoes the following photorelaxation pathways upon photoexcitation: i) in non-polar c-hexane, the photoexcited  $S_1$  state relaxes *via* fluorescence (likely in competition with IC and/or ISC given non-unity  $\phi_f$ ) back to the ground state in  $\gg 2$  ns; ii) a CT pathway was introduced by polar aprotic solvents, MeCN in this case, which was accessed in  $\sim 5$  ps, the ES population was then likely trapped in the  $S_1(CT)$  state, which returns to  $S_0$  *via* fluorescence in competition with IC/ISC in  $\gg 2$  ns; iii) in protic MeOH CT occurs in  $\sim 0.7$  ps. This CT state then undergoes EDPT ( $\sim 11$  ps), thus quenching fluorescence, and finally back proton transfer to the MeO $\cdot$  radical occurs mediated *via* ISC ( $\sim 850$  ps).

### 3.7 Conclusion

With the evidence presented, the previously unknown process behind the fluores-

cence quenching of the current NM-MAM systems in protic solvents has now been identified as the result of EDPT, making the MAM based fluorophores an unreliable upstream photosensitiser in the presence of protic solvents. However, as mentioned in Section 1.5.1, non-polar fragments could be introduced into a block copolymer, which could offer protection from protic solvents at the cost of increased design complication. However, for the project goal of improving light harvesting applications, as proposed in Section 1.5.2 (Chapter 1), the EDPT could be considered a function of the maleimide based chromophore in addition to the role as a photosensitiser for porphyrin based light harvesting complex mimics. In particular, the specificity of the EDPT pathway towards protic small molecules could be exploited to perform the role as a photosensitiser with photoprotective functionalities in the design of future light harvesting devices. As an example, a small responsive molecule capable of switching to a protonated form when the system was under stress could employ the EDPT as a mechanism for alternative photorelaxation when under excess irradiation. Furthermore, as similar fluorescence quenching was also observed in the thiol-substituted maleimide systems,<sup>40–42</sup> it is likely that the same mechanisms apply to the thiol substituted maleimide based fluorophores. The EDPT pathway could therefore be exploited to complement the recently reported disulfide bridged C<sub>3</sub>N<sub>3</sub>S<sub>4</sub> polymer for light-driven water splitting applications.<sup>43</sup> Last, but not least, as evidenced in the large Stoke shifts between the three solvents, if appreciable  $\phi_f$  in protic solvents were achieved, the MAM based chromophores could prove to be a very powerful environment sensing fluorescence probe. One example would be the sensing of surrounding peptide chains (*e.g.* charged, non-polar, polar), which as mentioned in Section 3.1, was beyond the capability of GFPs, whose chromophore resides in the core of the protein complex and hence protected from solvent environments.

In conclusion, significant insight into the photophysical properties of the maleimide based fluorophores was gained, in the form of the uncovered EDPT mechanism. On the one hand, the EDPT rendered the design of a reliable photosynthesiser for a porphyrin based light harvesting complex mimic a challenging task. On the other hand, the application potential of the maleimide based chromophores were expanded thanks to the EDPT pathway. Therefore, future rational designs incorporating the knowledge gained could yield a wide range of maleimide based chromophores capable of providing additional functionalities to those presented in Section 1.5.2., Chapter 1.

## 3.8 Experimental data

### 3.8.1 NM-MAM synthesis

**MBM** (352 mg, 2 mmol, 1 eq.) and NaOAc (410 mg, 5 mmol, 2.5 eq.) was dissolved in 10 mL methanol. The solution was left to stir for *ca.* 5 minutes, methylamine (10 mmol, 5 mL of 2 M solution in methanol) was then added and stirred overnight (*ca.* 15 hours). Methanol was then reduced *in vacuo*, the crude yellow mixture was redissolved with CH<sub>2</sub>Cl<sub>2</sub> (100 mL) and washed with water (3×100 mL) then brine (150 mL) and dried over MgSO<sub>4</sub>. CH<sub>2</sub>Cl<sub>2</sub> was then reduced *in vacuo* and the residue was loaded directly onto silica gel and purified by column chromatography (0.5% MeOH in CH<sub>2</sub>Cl<sub>2</sub>), collecting the front running yellow band, yielding product as dark yellow/orange solid (56 mg, 20%). IR (neat,  $\lambda_{\text{max}}$ , cm<sup>-1</sup>): 3339 (m), 3115 (w), 2931 (w), 1756 (w), 1695 (m), 1635 (s); <sup>1</sup>H NMR (CDCl<sub>3</sub>, 400 MHz, ppm)  $\delta$ =2.92 (d, <sup>3</sup>J<sub>H-H</sub>=5 Hz, 3H), 2.98 (s, 3H), 4.82 (s, 1H), 5.34 (br, 1H); <sup>13</sup>C NMR (CDCl<sub>3</sub>, 100 MHz, ppm)  $\delta$ =23.4, 30.5, 84.2; HR-MS (MaXis) *m/z* found 163.0473, calc. 163.0478 ([C<sub>6</sub>H<sub>8</sub>O<sub>4</sub>+Na]<sup>+</sup>, 100%).

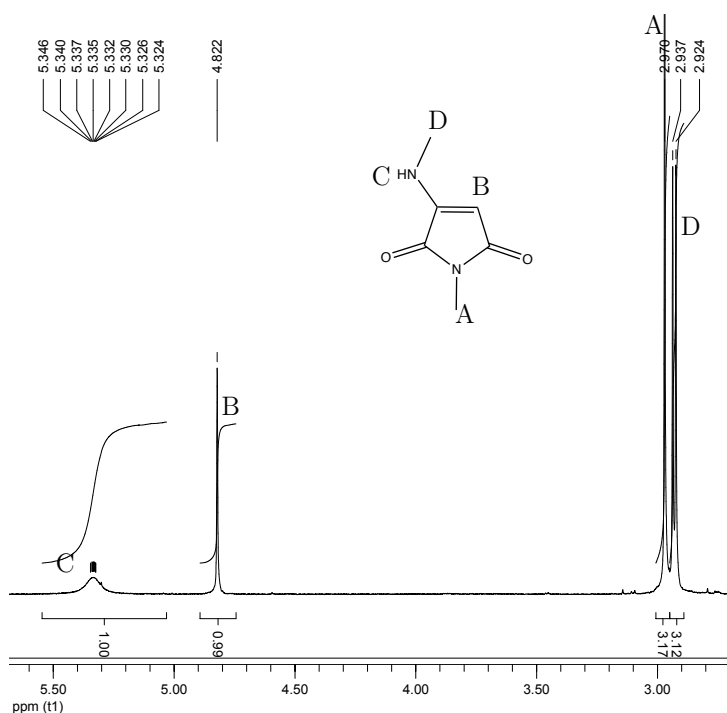


Figure 3.17: <sup>1</sup>H NMR spectrum of NM-MAM (CDCl<sub>3</sub>, 400 MHz)

### 3.8.2 Global fitting

Representative fits for selected traces TAS obtained from the TEAS experiment with NM-MAM in MeOH are shown in Figure 3.18. As is evident, the dynamics were nicely captured by the 3 exponentials given in Table 3.1.

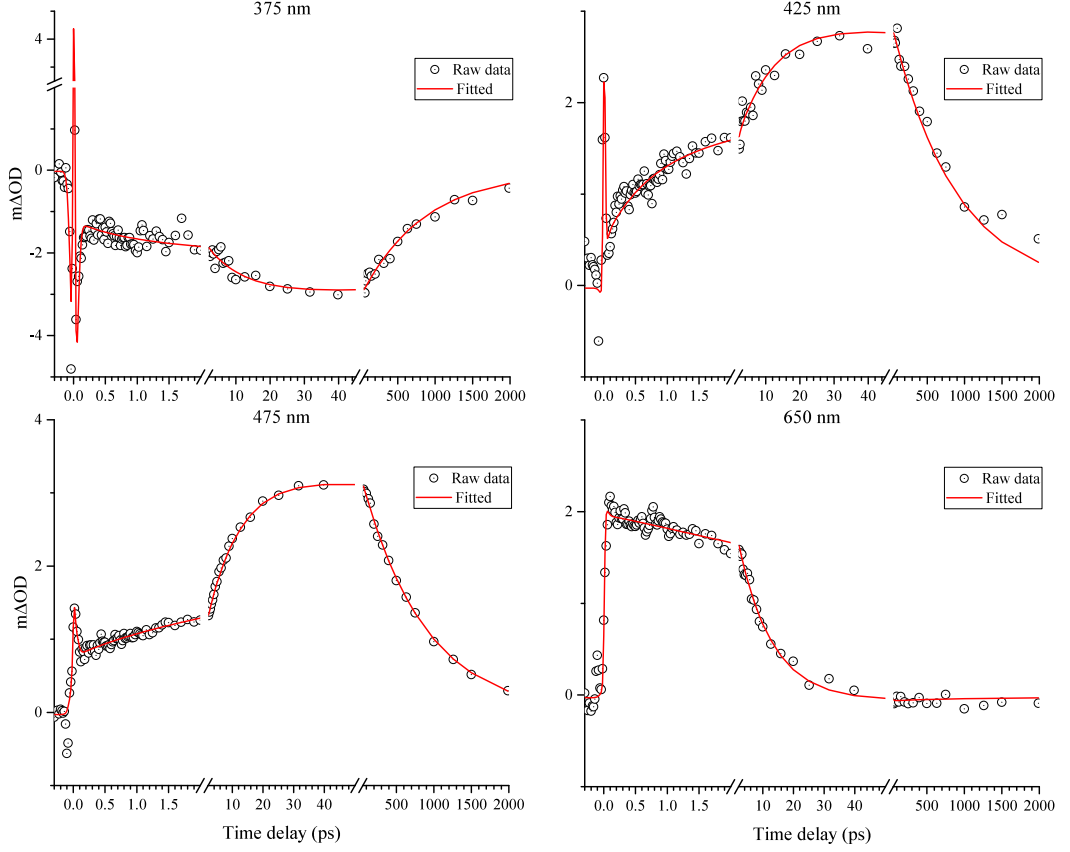


Figure 3.18: Representative fits over the transient absorption spectra of NM-MAM in methanol. The probe wavelengths are given at the top of each trace.

The  $\frac{\chi^2}{\chi_{min}^2}$  for all time-constants of NM-MAM in MeOH, MeO- $d_4$  and MeCN are shown in Figure 3.19. While the uncertainty for  $\tau_2$  and  $\tau_3$  can be obtained with confidence, it was not possible for  $\tau_1$ , which was unbounded for MeO- $d_4$  and only reached the 95% confidence interval on the shorter edge (timescale) for MeOH. Thus the error for  $\tau_1$  for MeOH was reported as the deviation towards the shorter time scale and was not reported for MeO- $d_4$ .

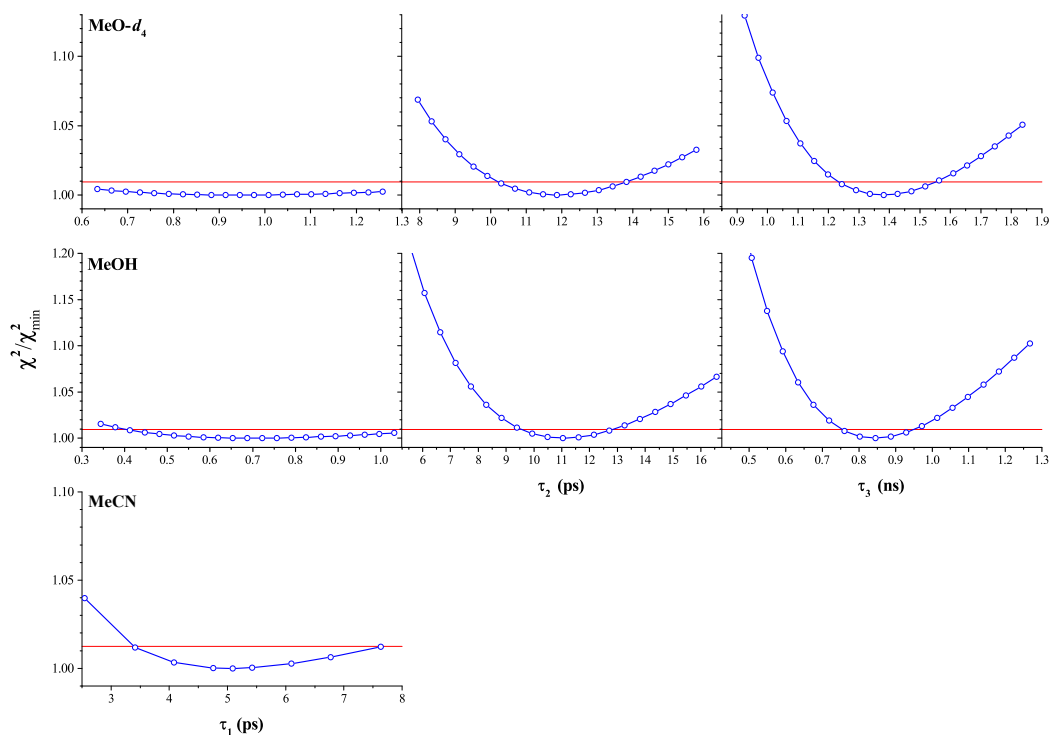


Figure 3.19:  $\frac{\chi^2}{\chi_{min}^2}$  for time constants extracted from TAS NM-MAM in MeOH, MeO- $d_4$  and MeCN. The horizontal lines indicate the 95% levels.

## References

- [1] A. B. Cubitt, R. Heim, S. R. Adams, A. E. Boyd, L. A. Gross and R. Y. Tsien, *Trends Biochem. Sci.*, 1995, **20**, 448–455.
- [2] O. Emanuelsson, S. Brunak and G. von Heijne, *Nat. Protocols*, 2007, **2**, 953–971.
- [3] J. Tavare, L. Fletcher and G. Welsh, *J. Endocrinol.*, 2001, **170**, 297–306.
- [4] F. Brandizzi, M. Fricker and C. Hawes, *Nat. Rev. Mol. Cell Biol.*, 2002, **3**, 520–530.
- [5] H. M. Kim and B. R. Cho, *Acc. Chem. Res.*, 2009, **42**, 863–872.
- [6] A. Sahari, T. T. Ruckh, R. Hutchings and H. A. Clark, *Anal. Chem.*, 2015, **87**, 10684–10687.
- [7] R. E. Combs-Bachmann, J. N. Johnson, D. Vytla, A. M. Hussey, M. L. Kilfoil and J. J. Chambers, *J. Neurochem.*, 2015, **133**, 320–329.

- [8] A. Dumas, L. Lercher, C. D. Spicer and B. G. Davis, *Chem. Sci.*, 2015, **6**, 50–69.
- [9] L. Wang and P. G. Schultz, *Angew. Chem. Int. Ed.*, 2005, **44**, 34–66.
- [10] D. Moatsou, J. Li, A. Ranji, A. Pitto-Barry, I. Ntai, M. C. Jewett and R. K. O'Reilly, *Bioconjugate Chem.*, 2015, **26**, 1890–1899.
- [11] S. W. Hell, *Science*, 2007, **316**, 1153–1158.
- [12] A. M. Sydor, K. J. Czymmek, E. M. Puchner and V. Mennella, *Trends Cell Bio.*, 2015, **25**, 730–748.
- [13] S. W. Hell, S. J. Sahl, M. Bates, X. Zhuang, R. Heintzmann, M. J. Booth, J. Bewersdorf, G. Shtengel, H. Hess, P. Tinnefeld, A. Honigmann, S. Jakobs, I. Testa, L. Cognet, B. Lounis, H. Ewers, S. J. Davis, C. Eggeling, D. Klenerman, K. I. Willig, G. Vicidomini, M. Castello, A. Diaspro and T. Cordes, *J. Phys. D: Appl. Phys.*, 2015, **48**, 443001.
- [14] S. Hell, *Nature Biotech.*, 2003, **21**, 1347–1355.
- [15] M. P. Robin, P. Wilson, A. B. Mabire, J. K. Kiviahio, J. E. Raymond, D. M. Haddleton and R. K. O'Reilly, *J. Am. Chem. Soc.*, 2013, **135**, 2875–2878.
- [16] A. B. Mabire, M. P. Robin, W.-D. Quan, H. Willcock, V. G. Stavros and R. K. O'Reilly, *Chem. Commun.*, 2015, **51**, 9733–9736.
- [17] R. Vanel, F. Berthiol, B. Bessi eres, C. Einhorn and J. Einhorn, *Synlett*, 2011, **2011**, 1293–1295.
- [18] A. S. Chatterley, C. W. West, V. G. Stavros and J. R. R. Verlet, *Chem. Sci.*, 2014, **5**, 3963–3975.
- [19] C. R. S. Mooney, D. A. Horke, A. S. Chatterley, A. Simperler, H. H. Fielding and J. R. R. Verlet, *Chem. Sci.*, 2013, **4**, 921–927.
- [20] M. Barbatti, M. Ruckebauer, F. Plasser, J. Pittner, G. Granucci, M. Persico and H. Lischka, *WIREs: Comp. Mol. Sci.*, 2014, **4**, 26–33.
- [21] M. Barbatti, G. Granucci, M. Persico, M. Ruckebauer, M. Vazdar, M. Eckert-Maksi c and H. Lischka, *J. Photochem. Photobiol. A*, 2007, **190**, 228–240.
- [22] M. J. Frisch, G. W. Trucks, H. B. Schlegel, G. E. Scuseria, M. A. Robb, J. R. Cheeseman, G. Scalmani, V. Barone, B. Mennucci, G. A. Petersson, H. Nakatsuji, M. Caricato, X. Li, H. P. Hratchian, A. F. Izmaylov, J. Bloino, G. Zheng,

- J. L. Sonnenberg, M. Hada, M. Ehara, K. Toyota, R. Fukuda, J. Hasegawa, M. Ishida, T. Nakajima, Y. Honda, O. Kitao, H. Nakai, T. Vreven, J. A. Montgomery, Jr., J. E. Peralta, F. Ogliaro, M. Bearpark, J. J. Heyd, E. Brothers, K. N. Kudin, V. N. Staroverov, R. Kobayashi, J. Normand, K. Raghavachari, A. Rendell, J. C. Burant, S. S. Iyengar, J. Tomasi, M. Cossi, N. Rega, J. M. Millam, M. Klene, J. E. Knox, J. B. Cross, V. Bakken, C. Adamo, J. Jaramillo, R. Gomperts, R. E. Stratmann, O. Yazyev, A. J. Austin, R. Cammi, C. Pomelli, J. W. Ochterski, R. L. Martin, K. Morokuma, V. G. Zakrzewski, G. A. Voth, P. Salvador, J. J. Dannenberg, S. Dapprich, A. D. Daniels, Ö. Farkas, J. B. Foresman, J. V. Ortiz, J. Cioslowski and D. J. Fox, *Gaussian 09 Revision D.01*, Gaussian Inc. Wallingford CT 2009.
- [23] A. D. Becke, *J. Chem. Phys.*, 1993, **98**, 5648–5652.
- [24] G. Granucci, M. Persico and A. Zocante, *J. Chem. Phys.*, 2010, **133**, 134111.
- [25] G. Granucci and M. Persico, *J. Chem. Phys.*, 2007, **126**, 134114.
- [26] *TURBOMOLE V6.2 2010, a development of University of Karlsruhe and Forschungszentrum Karlsruhe GmbH, 1989-2007, TURBOMOLE GmbH, since 2007; available from <http://www.turbomole.com>.*
- [27] R. Ahlrichs, M. Bär, M. Häser, H. Horn and C. Kölmel, *Chem. Phys. Lett.*, 1989, **162**, 165–169.
- [28] F. Furche, R. Ahlrichs, C. Hättig, W. Klopper, M. Sierka and F. Weigend, *WIREs: Comp. Mol. Sci.*, 2014, **4**, 91–100.
- [29] A. Dreuw and M. Wormit, *WIREs Comput. Mol. Sci.*, 2015, **5**, 82–95.
- [30] W. Humphrey, A. Dalke and K. Schulten, *J. Mol. Graphics*, 1996, **14**, 33–38.
- [31] N. Barman, D. Singha and K. Sahu, *Phys. Chem. Chem. Phys.*, 2014, **16**, 6159–6166.
- [32] X. Huang, B. J. Braams and J. M. Bowman, *J. Chem. Phys.*, 2005, **122**, 44308–44308.
- [33] S. Hayashi and I. Ohmine, *J. Phys. Chem. B*, 2000, **104**, 10678–10691.
- [34] X. Liu, A. L. Sobolewski, R. Borrelli and W. Domcke, *Phys. Chem. Chem. Phys.*, 2013, **15**, 5957–5966.

- [35] T. N. V. Karsili, D. Tuna, J. Ehrmaier and W. Domcke, *Phys. Chem. Chem. Phys.*, 2015, **17**, 32183–32193.
- [36] L. Spörkel, G. Cui, A. Koslowski and W. Thiel, *J. Phys. Chem. A*, 2014, **118**, 152–157.
- [37] F. H. Westheimer, *Chem. Rev.*, 1961, **61**, 265–273.
- [38] C. G. Swain, E. C. Stivers, J. F. Reuwer and L. J. Schaad, *J. Am. Chem. Soc.*, 1958, **80**, 5885–5893.
- [39] R. Cukier, *J. Phys. Chem.*, 1994, **98**, 2377–2381.
- [40] M. Moser, T. Behnke, C. Hamers-Allin, K. Klein-Hartwig, J. Falkenhagen and U. Resch-Genger, *Anal. Chem.*, 2015, **87**, 9376–9383.
- [41] K. Ortmayr, M. Schwaiger, S. Hann and G. Koellensperger, *Analyst*, 2015, **140**, 7687–7695.
- [42] S. Waichman, C. You, O. Beutel, M. Bhagawati and J. Piehler, *Anal. Chem.*, 2011, **83**, 501–508.
- [43] Z. Zhang, J. Long, L. Yang, W. Chen, W. Dai, X. Fu and X. Wang, *Chem. Sci.*, 2011, **2**, 1826–1830.

## Chapter 4

# The construction and photophysical characterisation of self-ordering porphyrin assemblies

As discussed in Section 1.5.4, Chapter 1, a key aspect of the current thesis work was the investigation into the feasibility of a porphyrin based light harvesting complex mimic capable of self-assembly in aqueous media. This involved the selection of synthetic techniques for the robust production of these systems, as well as the characterisation of the morphology of the resulting assemblies. Furthermore, the effects of these assembly conditions on the energy transfer processes of the porphyrins used were examined with both static and ultrafast spectroscopic techniques.

### 4.1 Introduction

As discussed in Sections 1.4.3 and 1.4.4, Chapter 1, the synthetic chemistry community have already produced a number of highly sophisticated and elegant multiporphyrin assemblies in recent years.<sup>1–5</sup> However, most, if not all, of these reported assemblies required the conjugations between the porphyrin subunits. Although these methods have produced robust synthetic mimics of biological light harvesting complexes (LHCs), this type of direct conjugation between chromophores is not utilised by natural LHCs.<sup>6–9</sup> The spatial arrangement by non-covalent intermolecular interactions are utilised in a number of functional protein complexes such as haemoglobin and ferritin, with the LHCs being one of the most sophisticated examples. However, large aggregated and cross-linked systems are also commonly utilised in biology for functions such as mechanical movements (actin filaments), photopro-

tection (melanin) and structural support (cross-linked cellulose and pectin). As such, there might be merits in creating multi-chromophoric assemblies *without* the use of direct inter-chromophore conjugations. Furthermore, as mentioned in Section 1.5, the synthetic techniques employed for creating these state-of-the-art biomimics are generally highly challenging, which limit their accessibility.

Interestingly, there already exist, in a handful of studies, amphiphilic polymeric systems that incorporate various functionalised porphyrins. These porphyrin-polymer conjugates have been utilised in a range of applications such as photodynamic therapy (PDT),<sup>10–12</sup> cell-imaging,<sup>13;14</sup> initiators for complex polymers<sup>15</sup> and simple proof-of-concept experiments for potential self-assembly methodologies.<sup>16;17</sup> Importantly for the present work, the ultrafast dynamics of assembled systems have not been well investigated. This is largely due to their application-oriented design, which in general only exploit the static photochemical properties of the porphyrin chromophores. However, ultrafast dynamics of chromophores is a determinant of light energy harvesting efficiency.<sup>18–28</sup> It is therefore crucial to understand the effects of such aggregation processes on the ultrafast photodynamics of individual chromophores to facilitate rational designs of LHC mimics based on similar self-assembly methods.

Thus, in the current chapter, the synthetic methods of creating a platform utilising simple solvophobic interactions to produce a self-assembled system containing the porphyrin chromophore was explored. Furthermore, whenever possible, simple syntheses with minimal steps required were employed. This was followed by the determination of assembly conditions without the use of direct conjugation between chromophores as well as the effect of these conditions on the photophysical properties of the chosen chromophores.

## 4.2 Choice and synthesis of components

For the synthesis of the various components of the system of interest, there are numerous methodologies readily reported.<sup>3;4;13;14;29–41</sup> However, the reported approaches are often low yielding and synthetically challenging. Therefore, the chosen synthetic schemes of each components will be discussed briefly in the current section. However, in the interest of brevity, the full scope of reaction conditions screened were not discussed within the current chapter. Instead, the most effective reported methods are described. The synthetic procedures presented herein should serve as techniques that were found to be the most robust and simple to follow.

### 4.2.1 Azide functionalised polymer

The proof-of-concept design of the system was based on a polymer-porphyrin conjugate with a hydrophilic and a hydrophobic portion. For the hydrophilic part, as discussed in Section 1.5.1, a water-soluble polymer containing functional groups that allow for efficient conjugation to the porphyrin unit would be selected. According to the work on DNA-polymer conjugation by Wilks *et al.*,<sup>42</sup> which investigated the conjugation between synthetic polymer and functionalised DNA strands, the most effective chemistry has been identified as the copper(I)-catalysed azide-alkyne cycloaddition (CuAAC) click reaction. Therefore, this reaction was chosen for the conjugation of polymer and porphyrin for the current thesis work. The reaction generally involves the formation of a 5-membered ring between an azide and an alkyne functional group,<sup>43–45</sup> in the case of current project, from the polymer and the porphyrin, respectively. This then leads to the choice of polymer, in the previous work by Wilks *et al.*, two water soluble polymers were identified as the most robust for the functionalisation with the conjugation handle: poly-*N*-isopropylacrylamide (pNIPAM) and poly-*N,N*-dimethylacrylamide (pDMA).<sup>42</sup> In the case of pNIPAM, it has been shown to be thermally responsive and has been utilised in a number of applications exploiting this property.<sup>46</sup> However, as the current thesis serves as the proof-of-concept experiment, in attempting to develop the assembly vehicle for future LHC mimics, pDMA was chosen for its simplicity to reduce the factors affecting the assembly.

Amongst existing controlled radical polymerisation techniques,<sup>47</sup> reversible addition-fragmentation chain transfer (RAFT) is one of the more versatile methods available.<sup>48;49</sup> One of the most attractive features of RAFT is its utilisation of a chain transfer agent (CTA), which not only facilitates control over the polydispersity of polymerisation, but also provides two modifiable sites,  $\alpha$  and  $\omega$ , as shown in Figure 4.1.

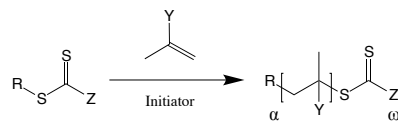


Figure 4.1: General polymerisation with RAFT using a CTA. The CTA is presented in the general form, where the two modification sites,  $\alpha$  and  $\omega$ , are shown on the final polymer (right hand side).

With reference to Figure 4.1, the  $\alpha$  site of the CTA can be modified both prior or post polymerisation. The  $\omega$  site on the opposite end of the CTA however should only be modified post polymerisation, as the chain transfer efficiency is usually determined by the chemical properties of the  $\omega$  site. Based on the work by Wilks *et al.*,

the best results of conjugation was achieved with an azide functionalised polymer.<sup>42</sup> However, polymerisation with an azide functionalised CTA ( $\alpha$  site) resulted in loss of the azide functional group.<sup>42</sup> Therefore, the CTA was first functionalised with pentafluorophenyl acetate (PFP) group at the  $\alpha$  site, which could then be replaced with an azide functionalised amine. Furthermore, the  $\omega$  site of the reported CTA was a long (12 C) alkyl chain. While in most polymers, the relative size of this chain tends not to affect the overall assembly, for the current project, the only hydrophobic component of the final product was the porphyrin, which is much smaller in size than those found in most amphiphilic block copolymers.<sup>34–38</sup> The presence of this alkyl chain might affect the final assembly pattern more so in the current system than those reported. Therefore, the removal of this alkyl chain was required post polymerisation to avoid the affect of a second hydrophobic component in the assembly.

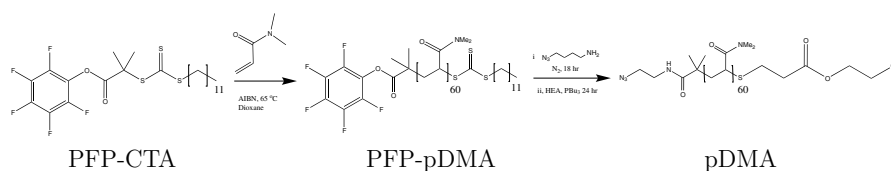


Figure 4.2: Synthetic scheme of azide functionalised pDMA. AIBN–azobisisobutyronitrile; HEA–2-hydroxyethyl acrylate; PBu<sub>3</sub>–tributylphosphine. Detailed procedures are given in Section 4.7.

The azide functionalised pDMA for the current thesis work was synthesised following the RAFT polymerisation conditions as previously reported,<sup>42</sup> with slight modifications.<sup>50</sup> The synthetic scheme is shown in Figure 4.2. In the work by Wilks *et al.*,<sup>42</sup> the pDMA was synthesised in three steps. First, dimethylacrylamide monomers were polymerised with RAFT, using a PFP functionalised chain transfer agent (PFP-CTA), synthesised according to methods developed by Godula *et al.*<sup>51</sup> The trithiocarbonate end group of resulting PFP functionalised pDMA (PFP-pDMA) was then removed by heating in the presence of excess azobisisobutyronitrile (AIBN). The intermediate pDMA was subsequently functionalised with 3-azidopropan-amine. However, the second, trithiocarbonate end group removal step requires very high dilution of the initial product due to potential inter-pDMA coupling, making the synthesis of pDMA at gram scale quantities challenging. Interestingly, as the amine is also reactive to the trithiocarbonate, this property was exploited by Doncom *et al.* to perform both the functionalisation at the  $\alpha$  end and the removal of the  $\omega$  end of the final polymer in the same reaction.<sup>50</sup> Therefore, the two-step one-pot end group removal and functionalisation method reported by Doncom *et al.* was tested and proved to be successful.<sup>50</sup>

Briefly, instead of separating the two final steps of the aforementioned method,

they were combined by introducing an excess quantity of 3-azidopropan-amine (5 equivalent) to a solution of PFP-pDMA. Firstly, the PFP activated ester (at the  $\alpha$  site) was substituted by 3-azidopropan-amine. Secondly, a free thiol (SH) was left at the trithiolcarbonate end ( $\omega$  site, Figure 4.1) following the aminolysis reaction with the excess amine present. The reaction was then left to stir for 24 hours prior to the addition of the reducing agent tributylphosphine and the monomer 2-hydroxyethyl acrylate (HEA). The tributylphosphine served to reduce the possible disulfide bridges formed during the previous reaction step, thus allowing the Michael addition reaction between the free thiol and the acrylate monomer, which replaced the hydrophobic alkyl chain from the starting CTA with the hydrophilic HEA monomer. 18.2 M $\Omega$ ·cm water ( $3\times$  starting volume of THF) was then added to the reaction after 24 hours, with the pDMA purified by dialysis against 18.2 M $\Omega$ ·cm water. The water was then removed *via* lyophilisation, recovering the desired pDMA. The successful removal of the CS<sub>3</sub> end groups are usually indicated by the reduction of absorption at 309 nm. The azide functionalisation could then be confirmed by the presence of infra-red (IR) absorption at *ca.* 2160-2120 cm<sup>-1</sup> (see Figure 4.6). The synthetic scheme and conditions of pDMA with these modifications are shown in Figure 4.2

With the above modifications, the number of synthesis steps required for the production of the final pDMA was reduced, and the methods presented were relatively straight forward. Unfortunately, the reaction conditions were still sensitive to contaminants: oxygen in the polymerisation step and water in the functionalisation step. However, the presented modifications allowed the synthesis to be scaled to multi-gram quantities. Therefore, although the simplicity in synthetic methods could still be improved, they were sufficient for the aim of the current project. This then leads to the discussion on the synthesis of alkyne functionalised porphyrin, which has been traditionally considered a relatively challenging synthesis.

#### 4.2.2 Alkyne functionalised porphyrin

As discussed in Section 1.4.2 (Chapter 1), the functionalisation of all 4 *meso* sites of the porphyrin with identical functional groups could be achieved with the Lindsey method using a functionalised aldehyde and pyrrole as starting materials.<sup>29-33</sup> However, in an attempt to keep the number of functionalisation sites to minimum (similar to chlorophyll A and B, see Section 1.4.2), two options were explored. First was the functionalisation of a single *meso*-site. This was performed using the Lindsey method with pyrrole, benzaldehyde and 4-(3-hydroxy-3-methylbut-1-ynyl) benzaldehyde (1), synthesised according to procedures by Stulz and coworkers,<sup>31</sup> at 4:3:1 molar ratio, catalysed with 1 mol% trifluoroacetic acid, and subsequently oxidised

with 2,3-dichloro-5,6-dicyano-1,4-benzoquinone (DDQ). Although this method successfully produced the desired mono-*meso* alkyne functionalised porphyrin, due to the statistical nature of the reaction, a mixture of porphyrin with various number of functionalised *meso* sites were present in the crude reaction. Therefore, the purification of the desired product was relatively challenging, which resulted in the disappointing yield of 1.5%. Coupled with the requirement of high dilution to minimise the formation of undesired poly-pyrrole, this method was limited to the production scale of <20 mg per reaction. As such, the mono-*meso* alkyne functionalised porphyrins were deemed unsuitable for the current thesis work. Therefore the step-wise synthesis of *para*-di-*meso* alkyne functionalisation of porphyrin (Zn-dPP) was explored. This could be considered a compromise between minimising the number of functional sites and ease of synthesis. The overall synthetic scheme and conditions are shown in Figure 4.3, with detailed synthetic procedures given in Section 4.7.1.

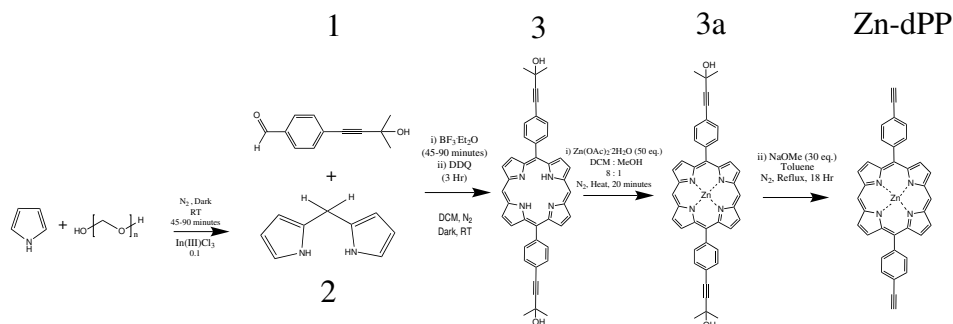


Figure 4.3: Synthetic scheme of Zn-dPP. DCM—dichloromethane;  $\text{BF}_3 \cdot \text{Et}_2\text{O}$ —boron trifluoride diethyl etherate; DDQ—2,3-dichloro-5,6-dicyano-1,4-benzoquinone; NaOMe—sodium methoxide. Detailed procedures are given in Section 4.7.

In this synthetic method, the cyclisation of poly-pyrrole, as depicted in Figure 1.16 (Section 1.4.1, Chapter 1), was separated into two reactions, with the first being the dimerisation of pyrrole with formaldehyde (steps 1–8 in Figure 1.16). The resultant dipyrrolemethane was then first isolated and subsequently cyclised with the protected alkyne functionalised aldehyde and oxidised forming the desired porphyrin (final 3 steps in Figure 1.16), followed by metallation of the porphyrin and deprotection of the alkyne moiety. Briefly, with reference to Figure 4.3, the most complex part of the syntheses were the two initial steps, first the synthesis of dipyrrolemethane (2), this was then followed by the coupling of two dipyrrolemethane with compound 1, yielding the freebase di-*meso* functionalised porphyrin (3). Of all the methods screened from previous literature, the most efficient one for compound 2 was reported by Laha *et al.*<sup>30</sup> In this reported procedure, pyrrole was utilised as solvent, thus in huge excess (up to 300 eq.) to the functionalised aldehyde. The reaction was then

catalysed with a soft Lewis acid,  $\text{InCl}_3$  at 10 mol%. The completed reaction was then quenched with excess  $\text{NaOH}$  (to  $\text{InCl}_3$ ). The purification of the final product was relatively simple involving first removing the  $\text{InCl}_3$  and base through filtration, followed by recovery of excess pyrrole under high vacuum (0.5 mbar starting at 20 °C and gradually heating to 35 °C). The resulting crude product (greenish in colour) was then easily purified with flash column chromatography (silica,  $\text{CH}_2\text{Cl}_2$ ) as the green impurity did not migrate over the silica bed. The  $\text{CH}_2\text{Cl}_2$  was then reduced *in vacuo* and pure product was recovered as greyish white solid by precipitation into hexane. This method was relatively simple, especially the purification, although the final yield was a disappointing 39%. The scalability of this particular method, however, means that gram scale of the material could be produced per reaction. The second step of the synthesis followed the general Lindsay method, with slight modifications: compounds 1 and 2 were dissolved in  $\text{CH}_2\text{Cl}_2$  at 1:1 molar ratio, catalysed by boron trifluoride diethyl etherate ( $\text{BF}_3\cdot\text{Et}_2\text{O}$ , 0.6 eq.), subsequently oxidised by DDQ twice (the second oxidation was conducted in toluene, and was heated to reflux over 3 hours). The lack of scrambling (formation of *cis-meso* functionalised porphyrin by-products) were confirmed by the single N-H  $^1\text{H}$  NMR peak at -3.14 (see Section 4.7.1, Figure 4.17). These slight modifications improved the yield significantly from 1.5% (for the mono-*meso* functionalised porphyrin) to 16%.

Although it was still considered a low yielding synthesis (*ca.* 6% overall yield from pyrrole), *ca.* 200-300 mg of the desired compound 3 could be produced per reaction. This resulted in sufficient quantities of material for all subsequent reactions: the Zn metallation of 3 was simply performed by slightly heating a solution of 3 in the presence of excess  $\text{Zn(II)}$  acetate dihydrate, a single filtration step to remove  $\text{Zn(II)}$  acetate dihydrate gave 3a at 94% yield upon removal of solvent *in vacuo*. The deprotection of the alkyne functional group was then achieved by refluxing a toluene solution of 3a under inert atmosphere in the presence of sodium methoxide ( $\text{NaOMe}$ ) overnight. Upon completion of the reaction and the removal of solvent *in vacuo*, the standard extraction, wash and drying over  $\text{MgSO}_4$  procedures in  $\text{CH}_2\text{Cl}_2$  was then followed (see Section 4.7 for detail). The  $\text{CH}_2\text{Cl}_2$  was then reduced *in vacuo* and the resulting crude solution was loaded directly onto a silica column with a short activated basic aluminium oxide patch ( $\text{CH}_2\text{Cl}_2 \rightarrow 0.5\%$  methanol in  $\text{CH}_2\text{Cl}_2$ ). Removal of the eluent solvent *in vacuo* afforded pinkish-purple solid product (Zn-dPP) with 90% yield. The successful deprotection could be determined by the concurrent loss of  $^1\text{H}$  NMR peak of 12H at 1.79 ppm (from the protecting group of 3a) and appearance of 2H peak at 3.35 ppm (from the terminal alkyne proton of Zn-dPP).

As can be seen from the above description of the synthetic procedures for Zn-dPP, the stepwise synthesis could still prove to be challenging, especially for the initial steps. However, as long as reasonable quantity of compound 3 or similar functionalised porphyrin could be produced with minimal synthetic steps, the subsequent modifications could be easily achieved. For the current thesis work, the overall low yield of 6% was mitigated by the ease of synthesising the preceding intermediate compound (2) in gram scale quantities. As such, the ultimate goal of developing a high yielding synthetic scheme of Zn-dPP (>50%), for the purpose of reducing production cost, was not fully achieved. However the synthetic methods presented herein strike a good balance between practical ease and overall quantities of the desired product. Furthermore, the multi-step nature of this synthetic condition allowed the removal of trace impurity of the crude compound 3 from the second step of reaction after each of the subsequent synthetic steps with a reduced penalty to the final yield compared to that of the mono-functionalised porphyrin previously discussed. With the syntheses of the two building blocks established, we will now proceed to discuss the final step of the production of the polymer to porphyrin conjugate system desired.

### 4.2.3 Conjugation of pDMA to Zn-dPP

As mentioned in Section 4.2.1, the most efficient method reported by Wilks *et al.*<sup>42</sup> for the conjugation between a synthetic polymer with a functionalised DNA was the copper(I)-catalysed azide-alkyne cycloaddition (CuAAC) click reaction. This would therefore, naturally, be the first condition to be explored. The reaction conditions are illustrated in Figure 4.4.

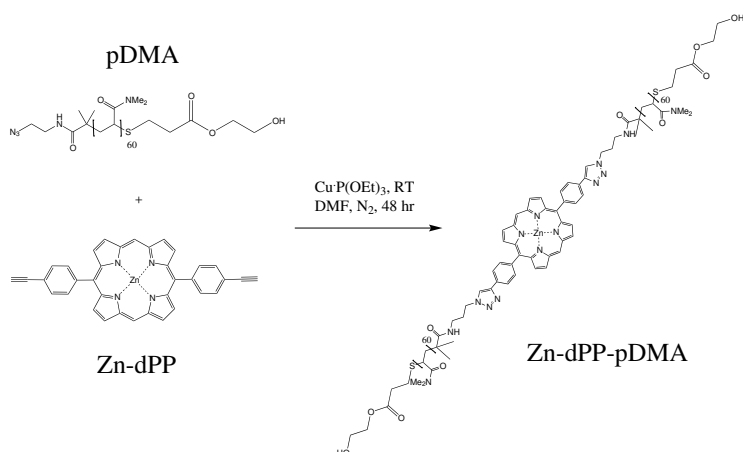


Figure 4.4: Reaction scheme of Zn-dPP to pDMA conjugation. DMF–*N,N*dimethylformamide. Detailed procedures are given in Section 4.7.

In contrast to the synthesis of Zn-dPP, the conjugation *via* CuAAC was highly efficient, resulting in *ca.* 80% final yield of the desired Zn-dPP to pDMA conjugate (Zn-dPP-pDMA), hence no screening of reported methods was required. The reaction was conducted by stirring a solution of *N,N*-dimethylformamide (DMF) with the two starting materials, Zn-dPP and pDMA (1:2.5 molar ratio) in the presence of  $\text{Cu}\cdot\text{P}(\text{OEt})_3$  (2.5 eq.) under inert atmosphere at ambient temperature (*ca.* 25°C). The reaction was monitored by thin layer chromatography (TLC), with  $\text{CH}_2\text{Cl}_2$  as the running solvent: the Zn-dPP would migrate along the TLC plate, whereas the conjugated product would not. Upon complete conjugation of the Zn-dPP (usually 24 hours), determined by TLC, the reaction was left to proceed for an additional 24 hours to ensure the maximum number of Zn-dPP with both alkyne functional groups conjugated. The resulting solution was then dialysed against 18.2 M $\Omega$ -cm water to remove the DMF and some of the Cu(I) catalyst. The water was then removed *via* lyophilisation. An additional preparatory size-exclusion chromatography (prep-SEC) column was performed with the collected material (redissolved in dioxane) to remove the remaining catalyst and unreacted pDMA. As the product was strongly coloured, the prep-SEC was relatively simple by collecting the front running purple/red band while discarding the pinkish ‘smear’ that followed. The dioxane was then removed *via* lyophilisation. As a qualitative confirmation of conjugation at both alkyne terminals of the Zn-dPP, size exclusion chromatography (SEC) traces of the starting pDMA (refractive index) and the Zn-dPP-pDMA product (absorption at 415 nm, corresponding to the Soret-band of Zn-dPP) were collected, shown in Figure 4.5.

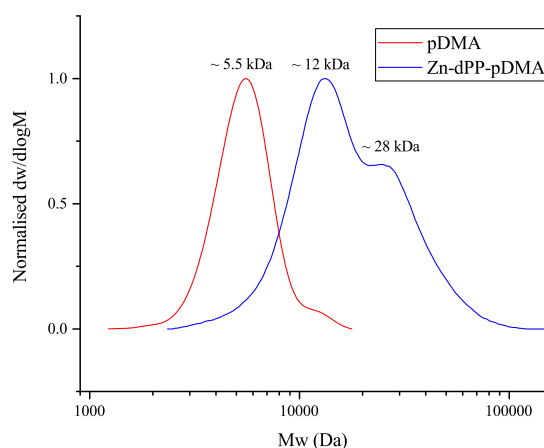


Figure 4.5: SEC of polymers in DMF with LiBr.

As evidenced in Figure 4.6, the final Zn-dPP-pDMA was found to be approximately double the molecular weight when compared to the starting pDMA. It is

worth noting that, the anomalous shoulder at approximately double the molecular weight ( $M_w \approx 28$  kDa), which was attributed to the dimer of Zn-dPP-pDMA, was also observed, in accord with previously reported porphyrin-polymer conjugate systems.<sup>16</sup> The successful conjugation was further confirmed by the loss of the infrared (IR) peaks associated with the azide functional group from pDMA and the alkyne terminal from Zn-dPP. This is best illustrated by the comparison of IR spectrum with all preceding compounds, as shown in Figure 4.6.

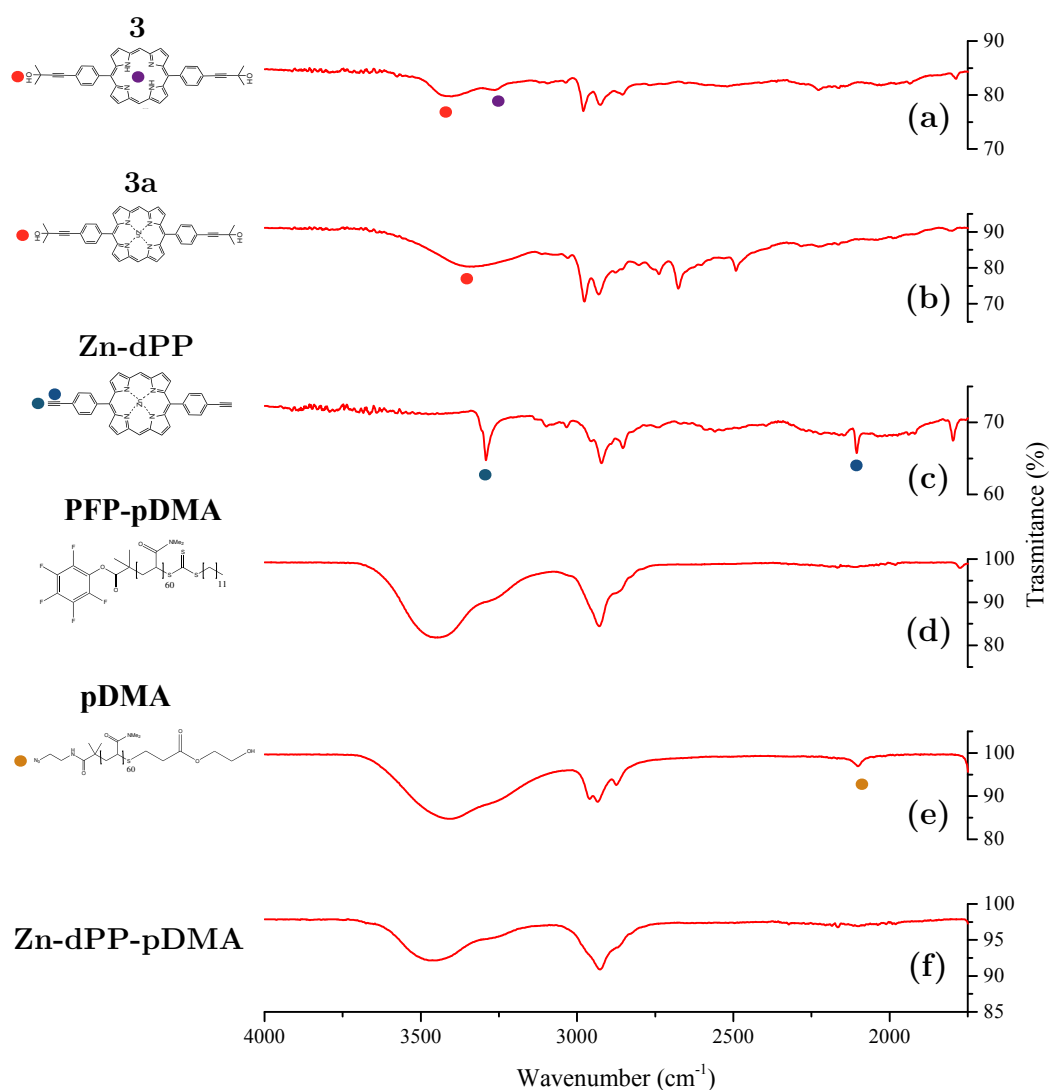


Figure 4.6: IR spectrum of the starting and final products. Regions of interest are highlighted by dots of corresponding colours and are discussed in detail in the main text.

In particular, with reference to Figure 4.6 for the synthesis of Zn-dPP, the metallation of compound 3 resulted in the loss of signal associated with the NH

stretch in 3a (Figure 4.6a, purple dots). The deprotection of the alkyne was indicated by the concurrent loss of OH stretch from compound 3a (Figure 4.6a and b, red dots) and the appearance of sharp terminal alkyne C–H and C≡C feature in Zn-dPP (Figure 4.6c, blue dots). The azide functionalisation of PFP-pDMA was indicated by the appearance of the signal associated with the azide functional group in pDMA (Figure 4.6e, orange dots). Finally, the conjugated Zn-dPP-pDMA showed the loss of both the terminal alkyne CH (blue dots) and azide (orange dots) feature (Figure 4.6f).

In summary, the overall synthesis of the desired Zn-dPP-pDMA still required multiple synthetic steps, and some steps were much more challenging than the highly scalable 3-step synthesis of NM-MAM fluorophore studied in Chapter 3. However, the majority of the synthetic methods were relatively simple, and generally high yielding. Furthermore, the only low yielding step, namely the synthesis of compound 3, was somewhat mitigated by the scalable nature of the synthesis of the preceding compound 2. Coupled with the ease of subsequent synthetic procedures, the aim of identifying a robust and scalable overall synthesis of a porphyrin containing building block for future assembly applications, as discussed in Section 1.5.4 (Chapter 1), was largely achieved. With the sufficient supply of these building blocks, their assembly behaviour in the aqueous environment was investigated.

### 4.3 Macro-assembly morphology characterisation of Zn-dPP-pDMA in aqueous media

Upon successful synthesis of the Zn-dPP-pDMA, they were assembled in aqueous media by the solvent switch method, as described in Section 2.3, with the final concentration of  $3 \text{ mg}\cdot\text{mL}^{-1}$ . Briefly, the starting solution of Zn-dPP-pDMA in dioxane at  $6 \text{ mg}\cdot\text{mL}^{-1}$  was sonicated for 30 minutes to minimise  $\pi$  stacking between the porphyrin cores. The starting solution should be clear with a deep pinkish-purple colour. An equal volume  $18.2 \text{ M}\Omega\cdot\text{cm}$  water was then slowly added at  $0.6 \text{ mL}\cdot\text{min}^{-1}$  and was left to stir overnight, at which point, the solution would turn slightly cloudy, indicating particle formation, with little change in colour. The mixed solution was then dialysed against  $18.2 \text{ M}\Omega\cdot\text{cm}$  water to remove the remaining dioxane. Upon complete removal of dioxane (minimum 6 water changes), the solution would show a very slight change in colour to appear pinkish-red. Upon completion of the solvent switch procedure, the macro assembly patterns was then characterised. Due to the much lower hydrophobic volume of the porphyrin core compared to the hydrophilic arm of pDMA, formation of small micelles were expected.<sup>36</sup> However, after a series

of characterisation experiments, the observations strongly suggested that these assemblies took the form of large polymersomes. These will be discussed briefly in this section.

#### 4.3.1 Multi-angle laser light scattering characterisations

To determine the morphologies of the assembled system, they were first analysed with static and dynamic light scattering (SLS and DLS, respectively) experiments. Initially, the results were inconsistent between measurements, with radii ranging from *ca.* 50 nm to micron scale. As these measurements were taken with samples of identical preparation method and concentrations ( $0.5 \text{ mg}\cdot\text{mL}^{-1}$ ), we first attributed these to the strong absorption of the Zn-dPP cores affecting the readings. However, as the instrument used a 632 nm laser, it was outside the absorption range of Zn-dPP. We therefore examined our procedures more carefully, and identified the only inconsistency in our sample preparation methodology, which was the filtering of the samples prior to measurements, to remove potential contamination from dusts. Therefore, a series of measurements were conducted for filtered samples using filters of 0.22 and 0.45  $\mu\text{m}$  pore sizes, as well as unfiltered systems. The samples were prepared by first passing the stock solution at  $3 \text{ mg}\cdot\text{mL}^{-1}$  through the membrane filters with appropriate pore sizes, followed by dilution to a final concentration of  $0.5 \text{ mg}\cdot\text{mL}^{-1}$ . The radius of gyration ( $R_g$ ) and hydrodynamic radius ( $R_h$ ) as well as the  $R_g/R_h$  ratio of each measurements are summarised in Table 4.1.

Table 4.1: Fitted radii of filtrated assembled Zn-dPP-pDMA systems.

<b>Filter pore-sizes</b>	$R_g/\text{nm}$	$R_h/\text{nm}$	$R_g/R_h$
<b>220 nm</b>	$55 \pm 6$	$34 \pm 3$	1.6
<b>450 nm</b>	$136 \pm 14$	$86 \pm 9$	1.6
<b>Unfiltered</b>	$420 \pm 42$	$190 \pm 19$	2.4

As shown in Table 4.1, all radii of gyration ( $R_g$ ) were approximately a quarter of the filter pore-sizes. This strongly suggested that the assembled systems underwent rearrangement upon filtration. The  $R_g/R_h$  of 1.6 (filtered) and 2.4 (unfiltered) suggested that the systems under study were either elongated or of irregular formation undergoing fusion/fission rearrangement.<sup>52</sup>

#### 4.3.2 UV-Vis absorption of filtrated samples

Since the unfiltered sample seemed to adopt highly irregular morphology, we measured the ultraviolet-visible (UV-Vis) spectrum of the filtrated and unfiltered samples to investigate whether Zn-dPP were present in the observed large particles.

The filtration process seemed to have removed a rather large amount of the Zn-dPP chromophores from the assembled systems. The Soret peak was reduced by *ca.* 40% and 50% post filtration, through 0.45 and 0.22  $\mu\text{m}$  pores respectively. The UV-Vis spectra of these measurements are shown in Figure 4.7.

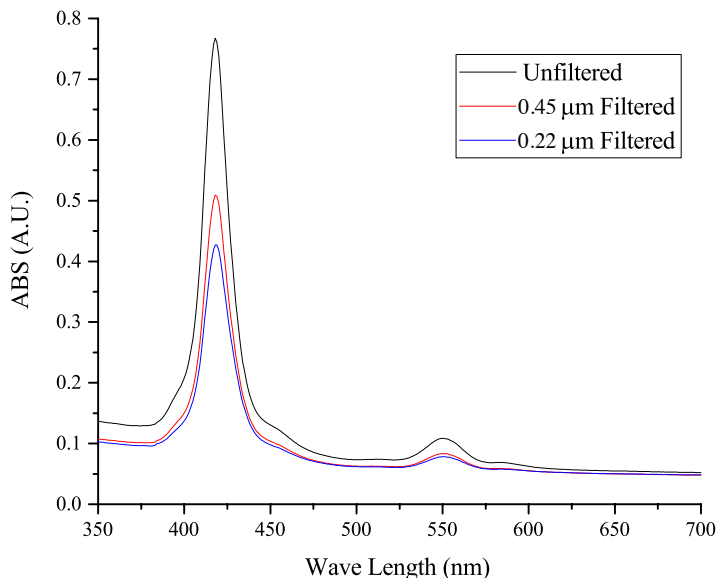


Figure 4.7: UV-Vis absorption spectrum of filtrated samples. Samples were assembled in conditions detailed in Section 4.3 and are diluted from  $3 \text{ mg}\cdot\text{mL}^{-1}$  to  $0.5 \text{ mg}\cdot\text{mL}^{-1}$  prior to filtration and measurements.

To rule out the possible loss due to the chromophores sticking to the filter membrane, a test measurement with dioxane solution prior to addition of  $18.2 \text{ M}\Omega\cdot\text{cm}$  water filtered through the  $0.22 \mu\text{m}$  filters resulted in 2.5% decrease at the Q-band region (data not shown). As such, the loss of up to 50% of samples was unlikely the results of materials sticking to the filter membranes, hence indicating that the Zn-dPP chromophores of Zn-dPP-pDMA were indeed part of the large aggregates and were removed in the filtration process.

#### 4.3.3 Transmission electron microscopy (TEM) studies

We then observed the filtered samples under dry state transmission electron microscopy (TEM) (see Section 2.5, Chapter 2 for sample preparation methods and instrument settings). In agreement to our filtrated SLS/DLS studies, the size of the observed particles were roughly half the diameter of the filter pore-sizes. These are shown in Figures 4.8 and 4.9.

As observed in these filtrated samples, even though some large spherical struc-

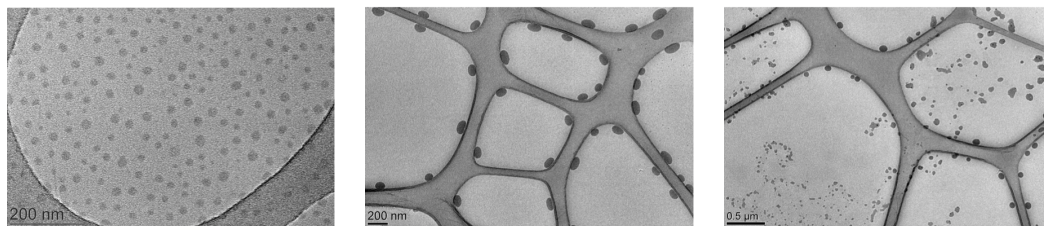


Figure 4.8: TEM images of Zn-dPP-pDMA assemblies filtered through 0.22  $\mu\text{m}$  pores on GO coated grids.

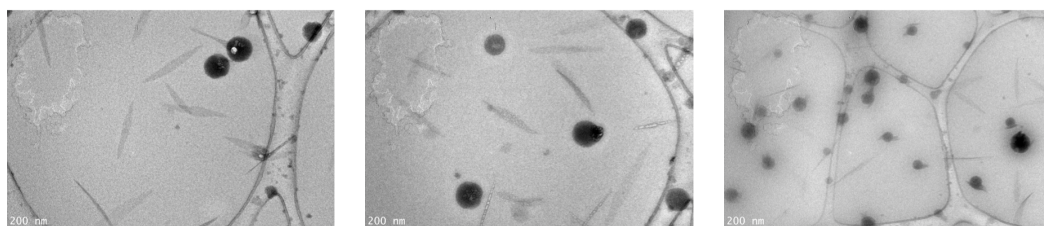


Figure 4.9: TEM images of Zn-dPP-pDMA assemblies filtered through 0.45  $\mu\text{m}$  pores on GO coated grids.

tures remained, the overall assemblies were damaged during the filtration processes, evidenced by the small circular fragments (0.22  $\mu\text{m}$  filtered, Figure 4.8) and needle like structures (0.45  $\mu\text{m}$  filtered, Figure 4.9). This, together with the SLS/DLS data (Section 4.3.1), strongly suggests that the assembled structures were extremely sensitive to shear forces applied during the filtration processes. Therefore, the unfiltered samples were observed under cryogenic transmission electronic microscopy (cryo-TEM) to determine the their morphology, these are shown in Figure 4.10.

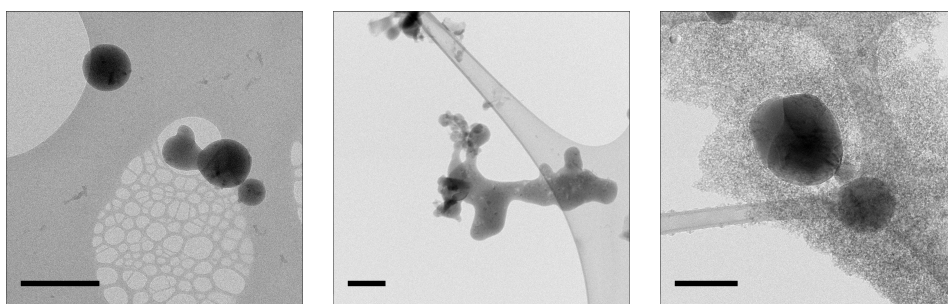


Figure 4.10: Cryo-TEM of unfiltered Zn-dPP-pDMA assemblies on uncoated grids.

With reference to Figure 4.10, the cryo-TEM showed coexistence of both vesicular polymersomes with spherical (Figure 4.10, left) and ellipsoid morphologies (Figure 4.10, centre). The irregular structures observed (Figure 4.10, centre and

right) suggested that the morphology of the assemblies were likely unstable and were undergoing both fusion and fission processes, similar to other reported polymer-based vesicles.<sup>53</sup> These observations were also in good agreement with the SLS/DLS characterisations.

#### 4.3.4 Overall interpretation

Based on all the presented data and observations, the most plausible assembly patterns the Zn-dPP-pDMA adopt in water were vesicular structures, this postulation was further supported by their visualisations under cryo-TEM. The cartoon representations of these processes Zn-dPP-pDMA assemblies are presented in Figure 4.11.

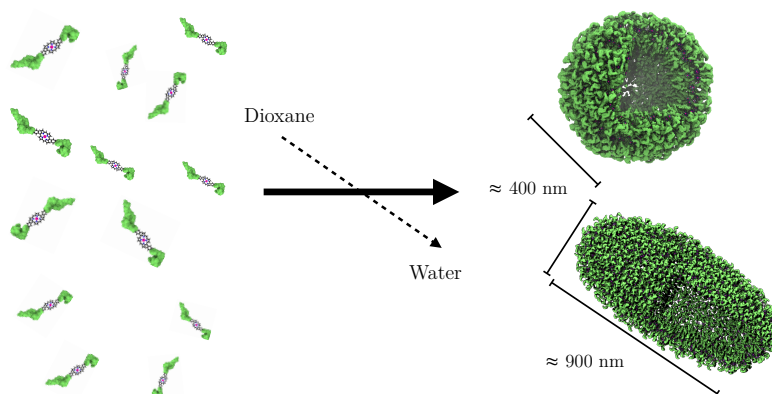


Figure 4.11: Cartoon representation of the unfiltered Zn-dPP-pDMA assembly.

While it was difficult to determine the exact dynamic formation patterns of these structures, the assemblies likely started as spherical structures, which then underwent fusion rearrangements upon collisions with one another. The larger ellipsoid vesicles then elongated further, leading to the fission process.<sup>53</sup> Furthermore, the series of filtration studies clearly showed that, not only were these assemblies highly sensitive to external forces, they also contained the Zn-dPP chromophores of the Zn-dPP-pDMA conjugate. Therefore, all photochemical experiments of these assemblies were performed with fresh, unfiltered samples as those observed under cryo-TEM (Figure 4.10).

With some appreciations of the macro assembly pattern of the system under study, the effects of such aggregations on the photodynamics of Zn-dPP were then investigated, documented in the proceeding sections.

## 4.4 Static spectroscopic characteristics

In the current section, the static spectroscopic property of the assembled Zn-dPP-pDMA system was investigated, with references to the observations of Zn-dPP and Zn-dPP-pDMA solvated in dioxane. The UV-Vis absorption spectrum of all the systems are presented in Figure 4.12

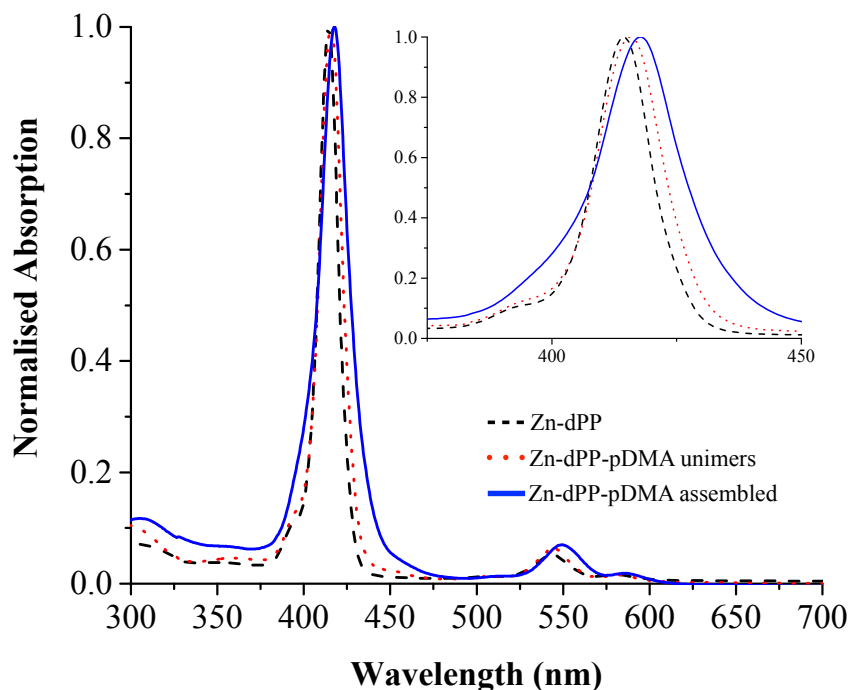


Figure 4.12: Normalised UV-Vis spectrum of Zn-dPP (black, dashed line), Zn-dPP-pDMA unimers in dioxane (red, dotted line) and Zn-dPP-pDMA assembled in water (blue, solid line). Inset shows zoomed-in Soret-band of each system.

Interestingly, although extensive aggregation of Zn-dPP-pDMA in the assembly were indicated by the characterisation data presented in the preceding section, the spectral features evidenced in the UV-Vis spectrum of Zn-dPP were largely retained in the assembled system (Figure 4.12). However, differences were apparent, which warrant discussion. Firstly, the Soret-band ( $\sim 414\text{-}420\text{ nm}$ ,  $S_2 \leftarrow S_0$ ) and Q-band ( $\sim 500\text{-}625\text{ nm}$ ,  $S_1 \leftarrow S_0$ ) were red-shifted by *ca.* 5 nm. Secondly, a slight broadening of the Soret band was evident. Lastly, there was a modest increase in Q-band relative to Soret-band intensities. These subtle changes closely resembled that of a recently reported Mg(II)bisporphyrin system, in which the  $\text{Mg} \cdots \text{Mg}$  nonbonding distance was determined to be *ca.* 6.5-7.5 Å.<sup>54</sup> This lack of significant alteration of spectroscopic property upon assembly was further demonstrated by their static fluorescence spectra, presented in Figure 4.13.

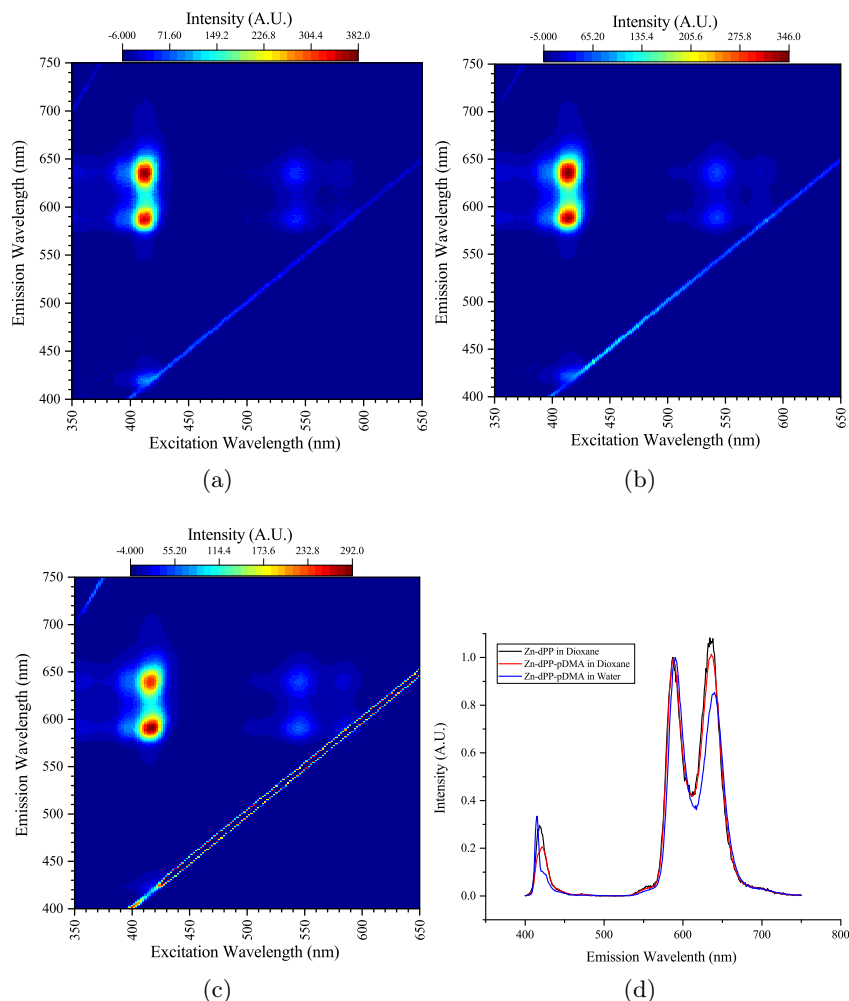


Figure 4.13: Static fluorescence heat map of (a), Zn-dPP, 57  $\mu\text{M}$  in dioxane; (b), Zn-dPP-pDMA, 0.25  $\text{mg}\cdot\text{mL}^{-1}$  (19.2  $\mu\text{M}$ ) in dioxane; (c), Zn-dPP assembled as described in Section 4.3, diluted from 3  $\text{mg}\cdot\text{mL}^{-1}$  to 0.33  $\text{mg}\cdot\text{mL}^{-1}$  (25.6  $\mu\text{M}$ ) in 18.2  $\text{M}\Omega\cdot\text{cm}$  water; and (d), selected emission spectra with excitation at 414 nm from (a)–(c). Spectra (a)–(c) were recorded with identical settings. Signals greater than the maximum fluorescence intensity (arising from instrument scattering) were all set to 0 for clarity. Spectra presented in (d) was normalised such that the intensity of Q(0,0) centred at *ca.* 590 nm were equal to 1 for clarity.

As shown in Figure 4.13, the systems under study demonstrated similar features to those previously reported for Zn-*meso*-tetraphenyl-porphyrins.<sup>55–58</sup> In particular, modest emissions corresponding to  $\text{S}_2 \rightarrow \text{S}_0$  at *ca.* 420 nm could be observed in both Zn-dPP and Zn-dPP-pDMA solvated in dioxane (Figures 4.13a and 4.13b); in the assembled system however, this feature appeared to be relatively weakened, which may suggest a slightly reduced  $\text{S}_2$  excited state life-time as a result of the conjugation to pDMA (Figure 4.13c). Emissions from the  $\text{S}_1 \rightarrow \text{S}_0$  (*ca.* 570–670 nm)

showed the typical dual band features arising from the relaxation of  $S_1$  into the two Franck-Condon active vibrational mode (FCAM) in the ground state:  $Q(0,0)$  centred at *ca.* 590 nm and  $Q(0,1)$  centred at *ca.* 640 nm, where the number of quanta of the dominant FCAM in the excited state and ground state are given in parentheses respectively. The fully solvated systems demonstrated almost identical ratio between the  $Q(0,0)$  and  $Q(0,1)$  peaks, similar to measurements in previous studies.<sup>55–57</sup> However, a notable difference could be observed in the assembled system (Figure 4.13c): the ratio between these peaks were altered in the assembled system, with the  $Q(0,1)$  showing reduced intensity relative to the  $Q(0,0)$  peak. This observation may indicate differences in the geometries of the porphyrin in the  $S^1$  and  $S^0$  states were introduced by conjugation to pDMA and upon assembly, leading to differences in the Franck-Condon factors. Although vibrational frequency calculations would provide a more refined explanation of this difference this was beyond the scope of the present thesis work, and was therefore not attempted. It is important to note that, as demonstrated in the emission spectrum of the Zn-dPP-pDMA assembled in water (Figure 4.13d, blue trace), the peaks associated with scattering of excitation was present and was not possible to be removed. In conjunction to the scattering observed in the UV-Vis spectrum (Figure 4.12), the quantum yield measurements using the methods described in Section 2.6.1 was not feasible and were therefore not attempted.

Taking the above observations together: the near identical fluorescence spectrum of all the present systems, the absence of dramatic spectral shifts in the UV-Vis spectrum (as seen in reported dimers and ordered aggregates)<sup>59;60</sup> and evident lack of excimer induced splitting, which usually manifest in the form of intense absorption bands in addition to the Soret and Q-bands of porphyrin<sup>61–69</sup> led to the postulation that, although the  $\pi\pi$  interaction between chromophores were present and likely the driving force for the current assembly, extensive interchromophoric interactions leading to the formation of excimers was prevented. This was very likely the result of the repulsive interactions between the polymer chains.<sup>36;37</sup> It is important to note that, due to the dynamic nature of these assemblies, exact determination of interchromophoric arrangement was, to the author’s best knowledge, not likely to be achievable by standard characterisation techniques. Therefore, these spectral properties, when compared to other systems with well defined crystal structures, served to infer the interactions between the Zn-dPP cores, and are by no means definitive. This then leads to the investigation of the ultrafast photodynamics of these systems to determine if additional ultrafast photophysical processes were introduced by the self-assembly process.

## 4.5 Effects of assembly on the ultrafast photodynamics of Zn-dPP-pDMA

After having established the general chromophore arrangement, the excited state dynamics of the three systems (Zn-dPP, Zn-dPP-pDMA unimers solvated in dioxane; and Zn-dPP-pDMA assembled in 18.2 M $\Omega$ -cm water) were determined, using ultrafast transient electronic absorption spectroscopy (TEAS) following photoexcitation to the  $S_2$  state with 400 nm radiation. The transient absorption spectra (TAS) obtained from these experiments are presented in Figure 4.14.

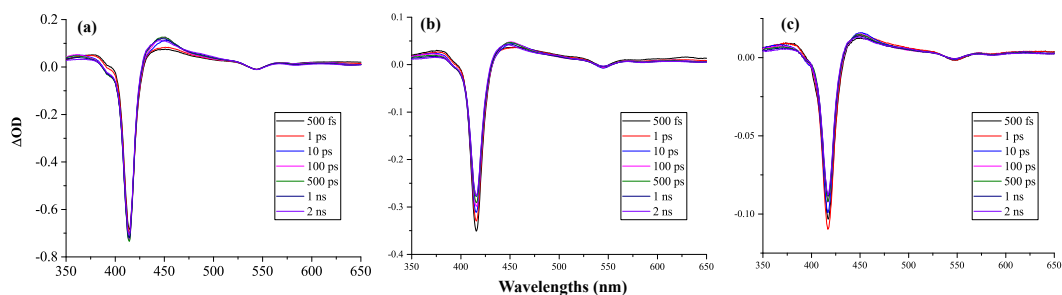


Figure 4.14: TAS of (a), Zn-dPP dissolved in dioxane ; (b), Zn-dPP-pDMA (3 mg·mL<sup>-1</sup>, 250  $\mu$ M) solvated in dioxane; and (c), Zn-dPP-pDMA (3 mg·mL<sup>-1</sup>, 250  $\mu$ M) assembled in water. All TAS are recorded following excitation to  $S_2$  state with 400 nm pump pulse (frequency doubled from 800 nm fundamental with BBO crystal, 3 mJ·cm<sup>-2</sup>, 0.5 mm sample pathlength).

The simple molecule Zn-dPP was first examined, in which the TAS showed two dominate features: the large ground state bleach (GSB) in the Soret region (*ca.* 416 nm, Figure 4.14a) and the excited state absorption (ESA) shoulders (*ca.* 450 nm). Global fitting the TAS (see Section 2.7.3 for detail)<sup>70–72</sup> revealed two ultrafast processes: internal conversion (IC) of  $S_2 \rightarrow S_1$  ( $\tau_{IC} \approx 1$  ps) and intermolecular vibrational energy transfer (IET) between the Zn-dPP  $S_1$  excited state and the dioxane solvent bath ( $\tau_{IET} \approx 21.8$  ps). These time constants and corresponding processes were comparable to the previously studied model Zn-tetraphenyl-porphyrin (Zn-tPP) reported by Zewail and co-workers.<sup>55</sup> It is worth noting that in addition to these two extracted time-constants, there was a time-constant that extends beyond the temporal window of the TEAS measurements (2 ns) which, in accord with previous interpretation and experiments conducted by Zewail and co-workers,<sup>55</sup> was most plausibly attributed to intersystem crossing (ISC) of  $S_1 \rightarrow T_n$  ( $\tau_{ISC}$ ) in keeping with the longer lived dynamics observed (as briefly discussed in Section 1.2.2, Chapter 1). The decay associated spectra (DAS) from the global fitting procedure associated with the described processes are shown in Figure 4.15. It is worth noting that, due

to the very large signal intensities associated with instrument response attained at time zero, which extended to  $\sim 150$  fs, this signal was excluded from the global fits (as discussed in Section 2.7.3).

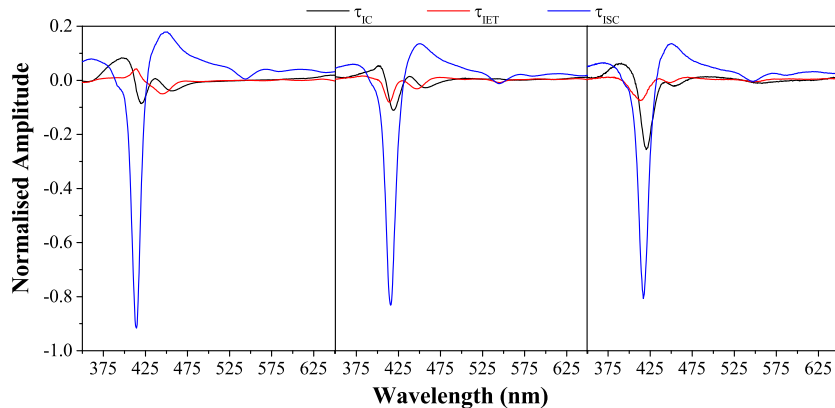


Figure 4.15: DAS of Zn-dPP (left), Zn-dPP-pDMA unimers (middle) fully solvated in dioxane and Zn-dPP-pDMA assembled in water (right). Time scale of each processes are discussed in main text and are listed in Table 4.2. Amplitudes were normalised such that the sum of amplitudes at 416 nm equal to minus one. Error determined by methods described in Section 2.7.4

Interestingly, almost identical features were observed in the TAS of the functionalised systems, with the only observable difference being the observed red-shift of the GSB feature for the Zn-dPP-pDMA assembled in water (Figure 4.14c), in a similar fashion to the Soret-band from the UV-Vis spectrum ( $\sim 5$  nm, Figure 4.12). Furthermore, these were fitted with almost identical time constants (Figure 4.15) and the DAS (Figure 4.15) revealed no discernible differences in their features. Of these,  $\tau_{IC}$  showed insignificant variations, whilst slightly faster  $\tau_{IET}$  could be observed in the assembled system ( $\sim 15.2$  ps *cf.*  $\sim 20.3$  ps in dioxane). Previous studies on Zn-tPP have demonstrated that the IET of Zn-tPP was sensitive to surrounding solvent bath, increasing from  $\sim 12$  ps when solvated in benzene to  $\sim 38$  ps in  $\text{CH}_2\text{Cl}_2$ .<sup>55</sup> This was explained in terms of vibrational frequency ( $\nu_v$ ) match between the instantaneous normal modes (INM) of its surrounding solvent bath and the Franck-Condon active mode (FCAM) of the photo-excited Zn-tPP in the works by Zewail *et al.*<sup>55;73</sup> Therefore, the difference in  $\tau_{IET}$  observed in the current study might suggest that the  $\nu_v$  match between the FCAM of the photoexcited Zn-dPP and the INM of its surrounding molecules might be different between the fully solvated and assembled systems. However, the differences were within the 95% confidence interval of each other (see Table 4.2 and Section 4.7), which makes this supposition tentative. The final ISC process demonstrated no discernible difference within the temporal window of our experiments with DAS features bearing marked resemblance (Table 4.2 and

Figure 4.15). The extracted time constants for all systems are listed in Table 4.2

Table 4.2: Global fitted time constants of each system studied ( $\tau_n$ ).

System Studied	$\tau_{IC}$	$\tau_{IET}$	$\tau_{ISC}$
Zn-dPP solvated in dioxane	$1.0 \pm 0.3$ ps	$21.8 \pm 8$ ps	$\gg 2$ ns
Zn-dPP-pDMA solvated in dioxane	$1.0 \pm 0.3$ ps	$20.3 \pm 8$ ps	$\gg 2$ ns
Zn-dPP-pDMA assembled in water	$0.8 \pm 0.3$ ps	$15.2 \pm 6$ ps	$\gg 2$ ns

## 4.6 Conclusion

In conclusion, the aim of producing a basic system of solvated and aggregated porphyrin molecules assembled *via* solvophobicity interactions, as discussed in Section 1.5.4 (Chapter 1), was achieved. The photodynamic studies presented demonstrated that the individual Zn-dPP molecules, interestingly, retained their overall photochemical properties following the addition of a large polymer chain (pDMA), and even following assemblies into macromolecular vesicles. The fact that the addition of such a large polymer has very little effect on the photochemical properties of the porphyrin adds credence to the ‘bottom-up’ approach towards understanding the photochemistry and photophysics of complex biological systems.<sup>74–78</sup> Furthermore, the lack of variation in their photochemical properties may allow the full exploitation of individual pigment characteristics. Coupled with the relatively simple synthetic methodologies involved in their production, these types of polymer-chromophore conjugates could be opportune building blocks for more complex biomimetic light harvesting systems, such those proposed in Section 1.5.3, Chapter 1, with the potential of adoption by a wider area of research. Therefore, the next natural step was to determine whether this proof-of-concept study could facilitate further modular designs of photo-active biomimetic arrays, without the need of complex covalent conjugation between differing chromophores.

## 4.7 Experimental

### 4.7.1 Synthetic procedures and characterisation data

RAFT polymerisation of dimethylacrylamide (PFP-pDMA,  $M_n(^1\text{NMR}) = 6.2$  kDa,  $M_n(\text{SEC}) \approx 5.8$  kDa,  $M_w(\text{SEC}) \approx 6.3$  kDa,  $D_M \approx 1.09$ ) with PFP-CTA was performed as previously reported.<sup>42</sup>

## Dipyrrolemethane (2)

Dipyrrolemethane (2) was synthesised based on procedure described by Laha *et al.*<sup>30</sup> A suspension of paraformaldehyde (649 mg, 21.6 mmol, 1 eq.) in pyrrole (300 mL, 4.26 mol, 200 eq.) was placed in a 500-mL two-necked round-bottomed-flask. The mixture was degassed with N<sub>2</sub> for 20-30 minutes before heating to 55°C until clear solution was obtained. InCl<sub>3</sub> (478 mg, 2.16 mmol, 0.1 eq.) was then added. The reaction mixture was stirred at 55°C for 2.5 hrs before quenching with NaOH (2.6 g, 64.8 mmol, 3 eq.). Insoluble InCl<sub>3</sub> and NaOH was filtered out of the reaction mixture. Excess pyrrole was recovered by distillation under vacuum (0.5 mbar) at room temperature (RT). Hexane (25 mL) was added to the crude oil and evaporated three times to yield greenish grey solid. The green solid was re-dissolved in CH<sub>2</sub>Cl<sub>2</sub> and purified by column chromatography (silica, CH<sub>2</sub>Cl<sub>2</sub>). Solvent of the collected fraction was reduced *in vacuo* and precipitated in 500 mL of hexane. This afforded greyish-white powder (1.22 g, 8.3 mmol, 39%). <sup>1</sup>H NMR (CDCl<sub>3</sub>, 400 MHz, ppm)  $\delta$  = 3.96 (s, 2 H), 6.03 (m, 2 H), 6.15 (q, <sup>3</sup>J<sub>H-H</sub> = 2.9 Hz, 2 H), 6.64 (m, 2 H), 7.81 (br s, 2 H). Other characterisation data was found to be in accordance with the literature.<sup>30</sup>

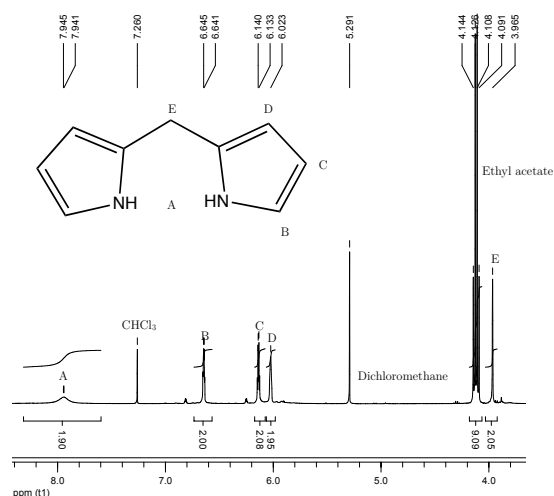


Figure 4.16: <sup>1</sup>H NMR spectrum of 2 in CDCl<sub>3</sub>

## 4,4'-(porphyrin-5,15-diylbis(4,1-phenylene))bis(2-methylbut-3-yn-2-ol) (3)

Compounds 1 (1.411 g, 7.5 mmol, 1 eq.) and 2 (1.096 g, 7.5 mmol, 1 eq.) were dissolved in 750 mL of CH<sub>2</sub>Cl<sub>2</sub>. The solution was purged with dry N<sub>2</sub> for 45 minutes before adding BF<sub>3</sub>·Et<sub>2</sub>O (600  $\mu$ L, 4.5 mmol, 0.6 eq.). The solution was protected

from light. After stirring the solution for 45 minutes at RT, 2,3-dichloro-5,6-dicyano-1,4-benzoquinone (DDQ, 1.532 g, 6.75 mmol, 0.9 eq.) was added to the reaction. The reaction was stirred for one hour and the crude mixture was filtered through a neutral aluminium oxide patch (7.5 cm) and washed with 5% methanol in CH<sub>2</sub>Cl<sub>2</sub> until the eluent was colourless. The crude product was dried *in vacuo* and re-dissolved in 150 mL of toluene. A fresh batch of DDQ (1.702 g, 7.5 mmol, 1 eq.) was added and the mixture was heated to reflux for 3 hrs. The crude reaction was passed through a neutral aluminium oxide patch again before being purified by flash chromatography (silica, neutralised with 1% triethylamine, 5% ethylacetate in CH<sub>2</sub>Cl<sub>2</sub>→10% EtOAc in CH<sub>2</sub>Cl<sub>2</sub>), yielding purple solid products (334 mg, 0.53 mmol, 16%). <sup>1</sup>H NMR (CDCl<sub>3</sub>, 400 MHz, ppm)  $\delta$  = -3.14 (br, 2H), 1.79 (s, 12H), 7.87 (d, <sup>3</sup>J<sub>H-H</sub> = 8 Hz, 4H); 8.21 (d, <sup>3</sup>J<sub>H-H</sub> = 8 Hz, 4H), 9.05 (d, <sup>3</sup>J<sub>H-H</sub> = 5 Hz, 4H), 9.40 (d, <sup>3</sup>J<sub>H-H</sub> = 5 Hz, 4H), 10.32 (s, 2H); <sup>13</sup>C NMR (CDCl<sub>3</sub>, 400 MHz, ppm)  $\delta$  = 31.4, 130.3, 130.3, 131.9, 134.8; HR-MS (MaXis) m/z found 627.2733, calc. 627.2755 ([C<sub>42</sub>H<sub>34</sub>N<sub>4</sub>O<sub>2</sub>+H]<sup>+</sup>, 100%).

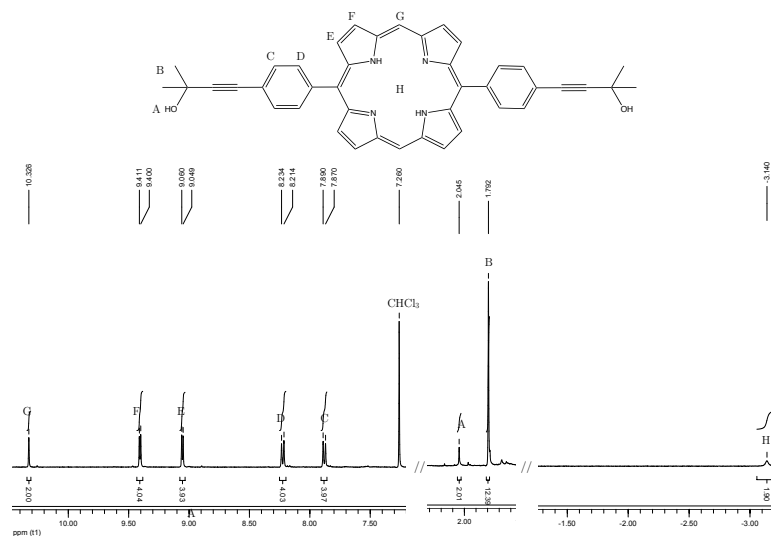


Figure 4.17: <sup>1</sup>H NMR spectrum of 3 in CDCl<sub>3</sub>

### Zn-4,4'-(porphyrin-5,15-diylbis(4,1-phenylene))bis(2-methylbut-3-yn-2-ol) (3a)

Zn(II) acetate dihydrate (1.756 g, 8 mmol, 50 eq.) and compound 3 (10 mg, 16  $\mu$ mol, 1 eq.) were dissolved in 9 mL methanol/CH<sub>2</sub>Cl<sub>2</sub> (1 : 8), degassed with N<sub>2</sub> for 20 minutes. The solution was then heated to 35 °C for 20 minutes. The mixture was then dried *in vacuo* and dissolved in 2 mL CH<sub>2</sub>Cl<sub>2</sub>, filtered to remove excess Zn(II) acetate dihydrate. Solvent was removed under reduced pressure, affording

pinkish-purple solid products (10.4 mg, 14.4  $\mu\text{mol}$ , 94%).  $^1\text{H}$  NMR ( $\text{CDCl}_3$ , 400 MHz, ppm)  $\delta$  = 1.79 (s, 12H), 7.87 (d,  $^3J_{\text{H-H}}$  = 8 Hz, 4H), 8.21 (d,  $^3J_{\text{H-H}}$  = 8 Hz, 4H), 9.05 (d,  $^3J_{\text{H-H}}$  = 4 Hz, 4H), 9.41 (d,  $^3J_{\text{H-H}}$  = 4 Hz, 4H), 10.34 (s, 2H);  $^{13}\text{C}$  NMR ( $\text{CDCl}_3$ , 400 MHz, ppm)  $\delta$  = 33.6, 129.2, 129.8, 131.7, 134.7; HR-MS (MaXis)  $m/z$  found 711.1694, calc. 711.1709 ( $[\text{C}_{42}\text{H}_{32}\text{N}_4\text{O}_2+\text{Na}]^+$ , 100%).

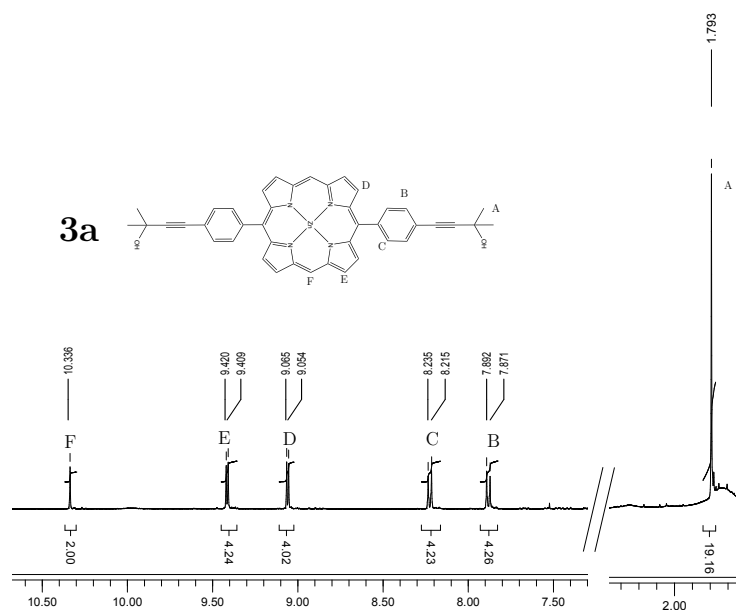


Figure 4.18:  $^1\text{H}$  NMR spectrum of 3a in  $\text{CDCl}_3$

### Zn-5,15-bis(4-ethynylphenyl)-porphyrin (Zn-dPP)

$\text{NaOMe}$  (24 mg, 432 mmol, 30 eq.) and compound 3a (10.4 mg, 14.4  $\mu\text{mol}$ , 1 eq.) were dissolved in 15 mL of toluene, degassed with  $\text{N}_2$  for 20 minutes before heating to reflux (125°C). The reaction was left over night. Solvent was removed *in vacuo*, crude product was extracted with 20 mL  $\text{CH}_2\text{Cl}_2$ , washed with water ( $3 \times 100$  mL) then brine ( $2 \times 100$  mL) and dried with  $\text{MgSO}_4$ . Basic alumina was added to the filtered solution, dried *in vacuo* before loading onto the column (neutralised silica with short aluminium oxide plug, eluent:  $\text{CH}_2\text{Cl}_2 \rightarrow 0.5\%$  methanol in  $\text{CH}_2\text{Cl}_2$ ). This afforded pinkish-purple solid products (7.4 mg, 13.0  $\mu\text{mol}$ , 90%).  $^1\text{H}$  NMR ( $\text{CDCl}_3$ , 400 MHz, ppm)  $\delta$  = 3.35 (s, 2H), 7.93 (d,  $^3J_{\text{H-H}}$  = 8 Hz, 4H), 8.23 (d,  $^3J_{\text{H-H}}$  = 8 Hz, 4H), 9.12 (d,  $^3J_{\text{H-H}}$  = 5 Hz, 4H), 9.46 (d,  $^3J_{\text{H-H}}$  = 4 Hz, 4H), 10.36 (s, 2 H), -3.14 (broad, 2 H);  $^{13}\text{C}$  NMR ( $\text{CDCl}_3$ , 400 MHz, ppm)  $\delta$  = 130.5, 132.1, 132.3, 134.6.

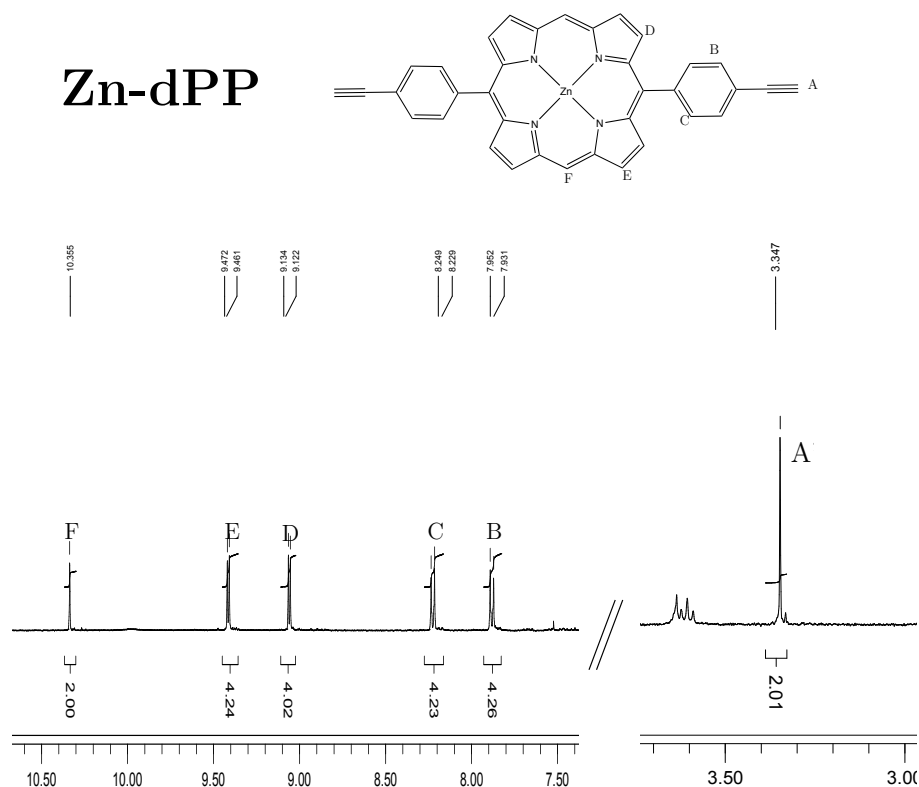


Figure 4.19: <sup>1</sup>H NMR of Zn-dPP in CDCl<sub>3</sub>.

### Azido-amine-poly(DMA)<sub>60</sub>-thiol-HEA (pDMA)

PFP-pDMA (1.5 g, 0.25 mmol, 1 eq.) and 3-azidopropan-amine (75 mg, 0.75 mmol, 5 eq.) were dissolved in dry THF, 30 mL and 1 mL, respectively, in separate oven-dried ampoules and degassed by three freeze-pump-thaw (FPT) cycles. The 3-azidopropan-1-amine solution was then added to the polymer solution *via* cannular transfer under dry N<sub>2</sub>. The solution turned from dark yellow in colour to a clear-pale yellow-green colour after being stirred at RT for 24 hrs. Neat 2-hydroxyethyl acrylate (2.9 g, 25 mmol, 100 eq.) and PBu<sub>3</sub> (1.011 g, 5 mmol, 20 eq.) were placed in separate oven-dried ampoules and degassed by three FPT cycles and added to the clear reaction solution *via* cannula transfer under dry N<sub>2</sub>. The final mixture was stirred at RT for 24 hrs. 100 mL of 18.2 MΩ·cm water was added to the mixture, turning the solution from pale yellow to a cloudy-white colour. The resulting solution was dialysed against water using dialysis tubing with 3.5k MWCO over a minimum of 6 water changes to remove excess starting material. The water was removed by lyophilisation, recovering the polymer in quantitative yield.  $M_n(^1\text{NMR})=5.6$  kDa,  $M_n(\text{SEC})=5.5$  kDa,  $M_w(\text{SEC})=7.0$  kDa  $D_M\approx 1.28$

### Zn-5,15-bis(4-(1-poly(DMA)<sub>60</sub>-1H-1,2,3-triazole-4-yl)phenyl)-porphyrin (Zn-dPP-pDMA)

Polymer pDMA (800 mg, 133  $\mu$ mol, 2.5 eq.), Zn-dPP (30.4 mg, 66.7  $\mu$ mol, 1 eq.) and Cu-P(OEt)<sub>3</sub> (48 mg, 133  $\mu$ mol, 2.5 eq.) were dissolved in 15 mL of DMF. The solution was purged with dry N<sub>2</sub> for 30 minutes then stirred under N<sub>2</sub> at RT for 48 hrs. 50 mL of 18.2 M $\Omega$ ·cm water was then added to the reaction and dialysed against 18.2 M $\Omega$ ·cm water using dialysis tubing with 6-8k MWCO over 6 water changes. The water was removed by lyophilisation. The resulting polymers were redissolved in minimal amount of HPLC-grade 1,4-dioxane and sonicated before purification by prep-SEC in dioxane, collecting the reddish-purple band. The dioxane was removed by lyophilisation yielding the final pinkish-red Zn-dPP-pDMA (676 mg, 52  $\mu$ mol, 78%).

#### 4.7.2 Global fitting of TAS

The full width at half maximum of the instrument response for the TEAS experiments was measured to be  $\sim$ 150 fs (determined through solvent only transients, data not shown). Representative fitted traces at 416 nm of the experimental data are shown in Figure 4.20.

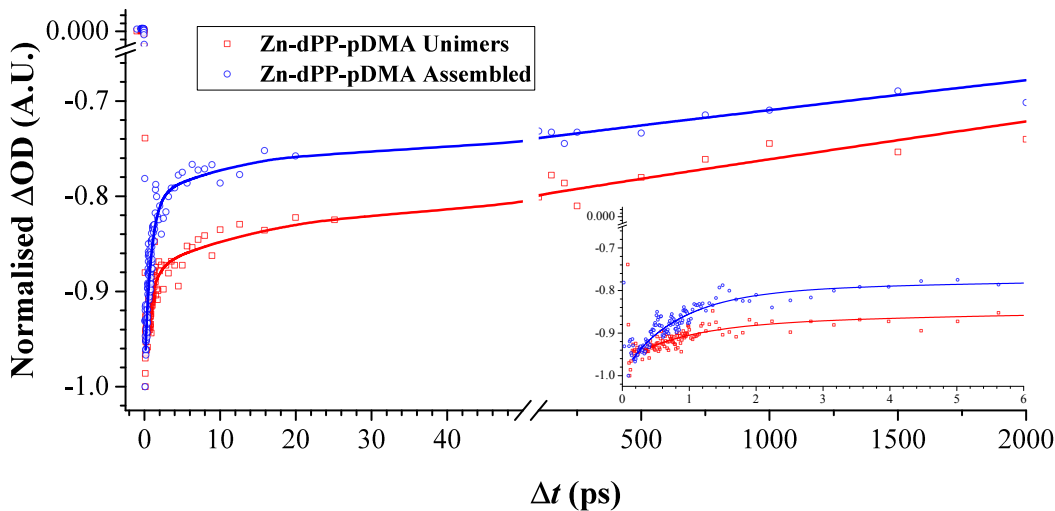


Figure 4.20: Normalised experimental data and the global fitted trace of Zn-dPP-pDMA both fully solvated in dioxane (Unimers) and assembled in water (Assembled), integrated at 416 nm. The traces were normalised such that the minima of the GSB = -1.

## Lifetime uncertainties of global fitting

The 95% confidence interval on the lifetimes determined from global fitting the TAS obtained from TEAS experiments was determined by the SPA method described in Section 2.7.4. Due to the dominant long time delay dynamics, the confidence level of  $\tau_{2/\text{IET}}$  extending to longer time delays is over estimated by our algorithm. We therefore quoted the error of  $\tau_{2/\text{IET}}$  as the distance from the origin to the furthest point towards  $\tau_{1/\text{IC}}$  in Table 4.2. The 95% confidence level for each of the systems is highlighted by the bold black lines shown in Figure 4.21.

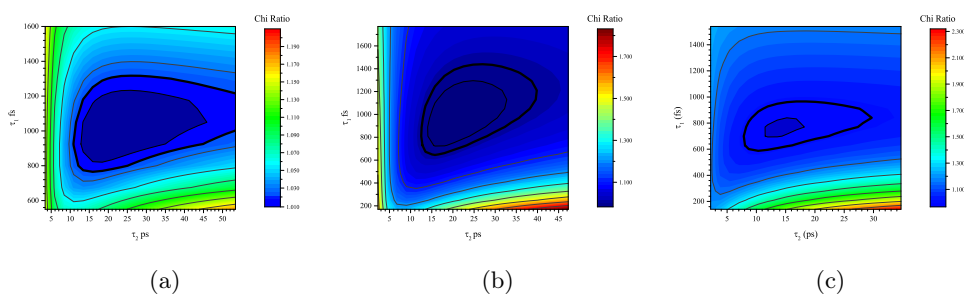


Figure 4.21: Chi ratio ( $\chi^2(\tau_{1/\text{IC}}, \tau_{2/\text{IET}})/\chi^2_{\text{min}}$ ) for  $\tau_{1/\text{IC}}$ ,  $\tau_{2/\text{IET}}$  of (a), Zn-dPP solvated in dioxane; (b), Zn-dPP-pDMA solvated in dioxane; and (c), Zn-dPP-pDMA assembled in 18.2 MΩ·cm. 95% confidence interval is indicated by bold black contour.

## References

- [1] S.-P. Wang, Y.-F. Shen, B.-Y. Zhu, J. Wu and S. Li, *Chem. Commun.*, 2016, **52**, 10205–10216.
- [2] J. Yang, M.-C. Yoon, H. Yoo, P. Kim and D. Kim, *Chem. Soc. Rev.*, 2012, **41**, 4808–4826.
- [3] N. Aratani, D. Kim and A. Osuka, *Acc. Chem. Res.*, 2009, **42**, 1922–1934.
- [4] F. Durola, V. Heitz, F. Reviriego, C. Roche, J.-P. Sauvage, A. Sour and Y. Trolez, *Acc. Chem. Res.*, 2014, **47**, 633–645.
- [5] Y. Nakamura, N. Aratani and A. Osuka, *Chem. Soc. Rev.*, 2007, **36**, 831–845.
- [6] M. Suga, F. Akita, K. Hirata, G. Ueno, H. Murakami, Y. Nakajima, T. Shimizu, K. Yamashita, M. Yamamoto, H. Ago *et al.*, *Nature*, 2015, **517**, 99–103.
- [7] L. Dall’Osto, M. Bressan and R. Bassi, *BBA-Bioenergetics*, 2015, **1847**, 861–871.

- [8] L.-X. Shi, M. Hall, C. Funk and W. P. Schröder, *BBA–Bioenergetics*, 2012, **1817**, 13–25.
- [9] Y. Umena, K. Kawakami, J.-R. Shen and N. Kamiya, *Nature*, 2011, **473**, 55–60.
- [10] F. Li and K. Na, *Biomacromolecules*, 2011, **12**, 1724–1730.
- [11] L. Xu, L. Liu, F. Liu, H. Cai and W. Zhang, *Polym. Chem.*, 2015, **6**, 2945–2954.
- [12] X.-H. Dai, H. Jin, M.-H. Cai, H. Wang, Z.-P. Zhou, J.-M. Pan, X.-H. Wang, Y.-S. Yan, D.-M. Liu and L. Sun, *React. Funct. Polym.*, 2015, **89**, 9–17.
- [13] E. Huynh, J. F. Lovell, B. L. Helfield, M. Jeon, C. Kim, D. E. Goertz, B. C. Wilson and G. Zheng, *J. Am. Chem. Soc.*, 2012, **134**, 16464–16467.
- [14] T. V. Duncan, P. P. Ghoroghchian, I. V. Rubtsov, D. A. Hammer and M. J. Therien, *J. Am. Chem. Soc.*, 2008, **130**, 9773–9784.
- [15] L. R. H. High, S. J. Holder and H. V. Penfold, *Macromolecules*, 2007, **40**, 7157–7165.
- [16] D. A. Roberts, M. J. Crossley and S. Perrier, *Polym. Chem.*, 2014, **5**, 4016–4021.
- [17] D. A. Roberts, T. W. Schmidt, M. J. Crossley and S. Perrier, *Chem. Eur. J.*, 2013, **19**, 12759–12770.
- [18] L. Valkunas, J. Chmeliov, G. Trinkunas, C. D. P. Duffy, R. van Grondelle and A. V. Ruban, *J. Phys. Chem. B*, 2011, **115**, 9252–9260.
- [19] J. Martiskainen, R. Kananavičius, J. Linnanto, H. Lehtivuori, M. Keränen, V. Aumanen, N. Tkachenko and J. Korppi-Tommola, *Photosyn. Res.*, 2011, **107**, 195–207.
- [20] N. Nelson and W. Junge, *Annu. Rev. Biochem.*, 2015, **84**, 659–683.
- [21] J. M. Anna, G. D. Scholes and R. van Grondelle, *BioScience*, 2014, **64**, 14–25.
- [22] R. Moca, S. R. Meech and I. A. Heisler, *J. Phys. Chem. B*, 2015, **119**, 8623–8630.
- [23] D. I. G. Bennett, K. Amarnath and G. R. Fleming, *J. Am. Chem. Soc.*, 2013, **135**, 9164–9173.
- [24] H. Liu, H. Zhang, D. M. Niedzwiedzki, M. Prado, G. He, M. L. Gross and R. E. Blankenship, *Science*, 2013, **342**, 1104–1107.

- [25] G. Schlau-Cohen, J. M. Dawlaty and G. Fleming, *IEEE J. Sel. Top. Quantum Electron.*, 2012, **18**, 283–295.
- [26] M. Ballottari, M. J. P. Alcocer, C. D’Andrea, D. Viola, T. K. Ahn, A. Petrozza, D. Polli, G. R. Fleming, G. Cerullo and R. Bassi, *Proc. Natl. Acad. Sci. U.S.A.*, 2014, **111**, E2431–E2438.
- [27] G. S. Engel, T. R. Calhoun, E. L. Read, T.-K. Ahn, T. Mancal, Y.-C. Cheng, R. E. Blankenship and G. R. Fleming, *Nature*, 2007, **446**, 782–786.
- [28] V. Sundström, T. Pullerits and R. van Grondelle, *J. Phys. Chem. B*, 1999, **103**, 2327–2346.
- [29] B. J. Littler, M. A. Miller, C.-H. Hung, R. W. Wagner, D. F. O’Shea, P. D. Boyle and J. S. Lindsey, *J. Org. Chem.*, 1999, **64**, 1391–1396.
- [30] J. K. Laha, S. Dhanalekshmi, M. Taniguchi, A. Ambroise and J. S. Lindsey, *Org. Process Res. Dev.*, 2003, **7**, 799–812.
- [31] E. Stulz, S. M. Scott, Y.-F. Ng, A. D. Bond, S. J. Teat, S. L. Darling, N. Feeder and J. K. M. Sanders, *Inorg. Chem.*, 2003, **42**, 6564–6574.
- [32] P. D. Rao, S. Dhanalekshmi, B. J. Littler and J. S. Lindsey, *J. Org. Chem.*, 2000, **65**, 7323–7344.
- [33] M. O. Senge, *Chem. Commun.*, 2011, **47**, 1943–1960.
- [34] Y. Mai and A. Eisenberg, *Chem. Soc. Rev.*, 2012, **41**, 5969–5985.
- [35] H.-A. Klok and S. Lecommandoux, *Adv. Mater.*, 2001, **13**, 1217–1229.
- [36] A. Blanazs, S. P. Armes and A. J. Ryan, *Macromol. Rapid Commun.*, 2009, **30**, 267–277.
- [37] M. Stefik, S. Guldin, S. Vignolini, U. Wiesner and U. Steiner, *Chem. Soc. Rev.*, 2015, **44**, 5076–5091.
- [38] R. K. O’Reilly, C. J. Hawker and K. L. Wooley, *Chem. Soc. Rev.*, 2006, **35**, 1068–1083.
- [39] R. E. Blankenship, D. M. Tiede, J. Barber, G. W. Brudvig, G. Fleming, M. Ghirardi, M. R. Gunner, W. Junge, D. M. Kramer, A. Melis, T. A. Moore, C. C. Moser, D. G. Nocera, A. J. Nozik, D. R. Ort, W. W. Parson, R. C. Prince and R. T. Sayre, *Science*, 2011, **332**, 805–809.

- [40] Q. Yan, Z. Luo, K. Cai, Y. Ma and D. Zhao, *Chem. Soc. Rev.*, 2014, 4199–4221.
- [41] Y. Yamamoto, G. Zhang, W. Jin, T. Fukushima, N. Ishii, A. Saeki, S. Seki, S. Tagawa, T. Minari, K. Tsukagoshi and T. Aida, *Proc. Natl. Acad. Sci. U.S.A.*, 2009, **106**, 21051–21056.
- [42] T. R. Wilks, J. Bath, J. W. de Vries, J. E. Raymond, A. Herrmann, A. J. Turberfield and R. K. O'Reilly, *ACS Nano*, 2013, **7**, 8561–8572.
- [43] V. V. Rostovtsev, L. G. Green, V. V. Fokin and K. B. Sharpless, *Angew. Chem. Int. Ed.*, 2002, **41**, 2596–2599.
- [44] C. W. Tornøe, C. Christensen and M. Meldal, *J. Org. Chem.*, 2002, **67**, 3057–3064.
- [45] H. C. Kolb, M. Finn and K. B. Sharpless, *Angewandte Chemie International Edition*, 2001, **40**, 2004–2021.
- [46] M. A. C. Stuart, W. T. Huck, J. Genzer, M. Müller, C. Ober, M. Stamm, G. B. Sukhorukov, I. Szleifer, V. V. Tsukruk, M. Urban *et al.*, *Nat. Mater.*, 2010, **9**, 101–113.
- [47] W. A. Braunecker and K. Matyjaszewski, *Prog. Polym. Sci.*, 2007, **32**, 93 – 146.
- [48] G. Moad, E. Rizzardo and S. H. Thang, *Acc. Chem. Res.*, 2008, **41**, 1133–1142.
- [49] H. Willcock and R. K. O'Reilly, *Polym. Chem.*, 2010, **1**, 149–157.
- [50] K. E. B. Doncom, C. F. Hansell, P. Theato and R. K. O'Reilly, *Polym. Chem.*, 2012, **3**, 3007–3015.
- [51] K. Godula, D. Rabuka, K. Nam and C. Bertozzi, *Angew. Chem. Int. Ed.*, 2009, **48**, 4973–4976.
- [52] J. P. Patterson, M. P. Robin, C. Chassenieux, O. Colombani and R. K. O'Reilly, *Chem. Soc. Rev.*, 2014, **43**, 2412–2425.
- [53] D. E. Discher and A. Eisenberg, *Science*, 2002, **297**, 967–973.
- [54] S. A. Iqbal, A. Dhamija and S. P. Rath, *Chem. Commun.*, 2015, **51**, 14107–14110.
- [55] H.-Z. Yu, J. S. Baskin and A. H. Zewail, *J. Phys. Chem. A*, 2002, **106**, 9845–9854.

- [56] P. G. Seybold and M. Gouterman, *J. Mol. Spectrosc.*, 1969, **31**, 1–13.
- [57] D. J. Quimby and F. R. Longo, *J. Am. Chem. Soc.*, 1975, **97**, 5111–5117.
- [58] R. Humphry-Baker and K. Kalyanasundaram, *J. Photochem.*, 1985, **31**, 105–112.
- [59] I.-W. Hwang, M. Park, T. K. Ahn, Z. S. Yoon, D. M. Ko, D. Kim, F. Ito, Y. Ishibashi, S. R. Khan, Y. Nagasawa, H. Miyasaka, C. Ikeda, R. Takahashi, K. Ogawa, A. Satake and Y. Kobuke, *Chem. Eur. J.*, 2005, **11**, 3753–3761.
- [60] S. Verma, A. Ghosh, A. Das and H. N. Ghosh, *J. Phys. Chem. B*, 2010, **114**, 8327–8334.
- [61] T. van der Boom, R. T. Hayes, Y. Zhao, P. J. Bushard, E. A. Weiss and M. R. Wasielewski, *J. Am. Chem. Soc.*, 2002, **124**, 9582–9590.
- [62] T. Park, J. S. Shin, S. W. Han, J.-K. Son and S. K. Kim, *J. Phys. Chem. B*, 2004, **108**, 17106–17111.
- [63] M. Takeuchi, S. Tanaka and S. Shinkai, *Chem. Commun.*, 2005, 5539–5541.
- [64] M. Morisue, Y. Hoshino, K. Shimizu, M. Shimizu and Y. Kuroda, *Chem. Sci.*, 2015, **6**, 6199–6206.
- [65] J. Wang, Y. Zhong, L. Wang, N. Zhang, R. Cao, K. Bian, L. Alarid, R. E. Haddad, F. Bai and H. Fan, *Nano Lett.*, 2016, **16**, 6523–6528.
- [66] J. J. Piet, P. N. Taylor, H. L. Anderson, A. Osuka and J. M. Warman, *J. Am. Chem. Soc.*, 2000, **122**, 1749–1757.
- [67] A. Osuka and H. Shimidzu, *Angew. Chem. Int. Ed.*, 1997, **36**, 135–137.
- [68] T. Nagata, A. Osuka and K. Maruyama, *J. Am. Chem. Soc.*, 1990, **112**, 3054–3059.
- [69] M. Kasha, H. Rawls and M. Ashrafel-Bayoumi, *Pure Appl. Chem.*, 1965, **11**, 371–392.
- [70] A. S. Chatterley, C. W. West, V. G. Stavros and J. R. R. Verlet, *Chem. Sci.*, 2014, **5**, 3963–3975.
- [71] L. A. Baker, M. D. Horbury, S. E. Greenough, P. M. Coulter, T. N. V. Karsili, G. M. Roberts, A. J. Orr-Ewing, M. N. R. Ashfold and V. G. Stavros, *J. Phys. Chem. Lett.*, 2015, **6**, 1363–1368.

- [72] J. R. Lakowicz, *Principles of Fluorescence Spectroscopy*, Springer Science+Business Media, 3rd edn., 2006.
- [73] R. M. Stratt and M. Maroncelli, *J. Phys. Chem.*, 1996, **100**, 12981–12996.
- [74] G. M. Roberts and V. G. Stavros, *Chem. Sci.*, 2014, **5**, 1698–1722.
- [75] M. Staniforth and V. G. Stavros, *Proc. R. Soc. A*, 2013, **469**,.
- [76] J. R. R. Verlet, *Chem. Soc. Rev.*, 2008, **37**, 505–517.
- [77] S. J. Harris, D. Murdock, Y. Zhang, T. A. A. Oliver, M. P. Grubb, A. J. Orr-Ewing, G. M. Greetham, I. P. Clark, M. Towrie, S. E. Bradforth and M. N. R. Ashfold, *Phys. Chem. Chem. Phys.*, 2013, **15**, 6567–6582.
- [78] P.-Y. Cheng, J. S. Baskin and A. H. Zewail, *Proc. Natl. Acad. Sci. U.S.A.*, 2006, **103**, 10570–10576.

## Chapter 5

# Construction of the push-pull self-assembled multichromophoric system

As mentioned in Section 1.5, Chapter 1, the vision of the current thesis work was the development of a flexible alternative towards the creation of a biological light harvesting complex (LHC) synthetic mimic. The vehicle for achieving this goal was established in Chapter 4. However, a fundamental property of natural LHCs is the incorporation of a reaction centre within the multi-chromophore arrays. Therefore, in an effort to further improve the applicability of the system studied in Chapter 4, a pseudo reaction centre was selected and introduced to this platform. Their co-assembly conditions and subsequent photophysical properties are discussed in the present chapter.

### 5.1 Introduction

As discussed in Section 1.3.1, one of the most evolutionarily conserved structural features of biological LHCs is the arrangement of chromophores around their reaction centres.<sup>1-4</sup> This is considered the key trait facilitating their abilities to trap and channel light energy into the reaction centres on ultrafast time scales.<sup>5-17</sup> Therefore, a functional mimic of LHC would require the association of light harvesting chromophores around some form of reaction centre. As mentioned in Section 1.4, multi-porphyrin arrays with a guest core similar to a reaction centre have been demonstrated in the literature, most notably works by Kobuke *et al.*<sup>18</sup> and Anderson *et al.*<sup>19</sup> However, as mentioned, the reported materials were not water soluble, and

the assemblies were therefore performed in organic solvents, rather than aqueous media. Furthermore, the reported systems all required varying degrees of direct inter-chromophore conjugations, which were not utilised in biological LHCs. In contrast to these reported assemblies, the Zn-porphyrin-poly-*N,N*dimethylacrylamide (Zn-dPP-pDMA) system described in Chapter 4 was capable of self-assembly in aqueous media, *without* the need of direction conjugation between the porphyrin chromophores. Furthermore, the photochemical properties, both static and ultrafast, of the active chromophore, Zn-porphyrin (Zn-dPP), were largely retained, likely a result of the repulsive interaction between polymer arms counteracting Zn-dPP's stacking tendency. Therefore, exploration into the potential prospective of such a system in producing functional multi-component LHC mimics was explored. Thus, the hexadentate template (T), a hexaarylbenzene (HAB) variant instrumental for the synthesis of porphyrin nano-rings demonstrated by Anderson *et al.*,<sup>20–22</sup> was chosen as the pseudo reaction centre for this investigation. The chemical structure of T is shown in Figure 5.1.

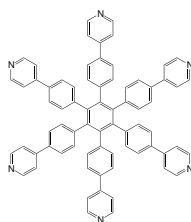


Figure 5.1: Chemical structure of hexadentate, T.

In the current chapter, the ideal conditions for the two components, Zn-dPP-pDMA and T, could co-assembled was determined. Upon establishing this, their photophysical properties was investigated. It is postulated that these experiments would provide a good insight into the application potential of the platform described in the present thesis, laying the foundations for future work into designing efficient synthetic LHC mimics, in keeping with the vision laid out in this thesis (as discussed in Section 1.5, Chapter 1).

## 5.2 Assembly conditions determination and characterisation

### 5.2.1 T:Zn-dPP-pDMA molar ratio

While the ligand binding properties between the molecule T to Zn-dPP had been thoroughly explored by Anderson and co-workers,<sup>22</sup> it was not clear whether such

conditions could be applied to the assembly of the system under current investigation. Therefore, a series of assemblies with varying molar ratio of T:Zn-dPP-pDMA were performed, with the final concentration of Zn-dPP-pDMA fixed at  $1.5 \text{ mg}\cdot\text{mL}^{-1}$  (*ca.*  $115 \text{ }\mu\text{M}$ ). As the purpose of these experiments was the determination of the degree of coordination between the Zn metal centre of Zn-dPP-pDMA and the N donor from the pyridyl functional group of T, they were conducted with the small volume of 3 mL. All assemblies were performed using the solvent switch method described in Section 2.3 using tetrahydrofuran (THF) as the starting organic solvent. Briefly, the quantity of Zn-dPP-pDMA and T listed in Table 5.1 were dissolved in 1.5 mL of THF and sonicated for *ca.* 30 minutes. 1.5 mL of  $18.2 \text{ M}\Omega\cdot\text{cm}$  water was then added to the stirring solution drop wise *via* peristaltic pump at 0.6 mL per minute. The resulting mixture was dialysed against  $18.2 \text{ M}\Omega\cdot\text{cm}$  water to slowly remove the remaining THF. The successful coordination was then determined by the spectral shift of the Soret-band of Zn-dPP-pDMA, as these have been commonly observed in reported systems upon coordination of an N-donor ligand to Zn(II)-porphyrin variants.<sup>23–26</sup> Therefore, the ultraviolet-visible (UV-Vis) absorption spectra of these assembly conditions were recorded as shown in Figure 5.2.

Table 5.1: Quantity of T and Zn-dPP-pDMA in the preliminary molar ratio screening measurements, as well as volumes of  $1 \text{ mg}\cdot\text{mL}^{-1}$  stock solution of T for the desired final volume of 3 mL.

Zn-dPP-pDMA:T Molar ratio as shown in legend of Figure 5.2	Zn-dPP-pDMA (mole equivalent)	T (mole equivalent)	$1 \text{ mg}\cdot\text{mL}^{-1}$ T Stock
6:1	4.5 mg (6)	0.05 mg (1)	50 $\mu\text{L}$
3:1	4.5 mg (3)	0.1 mg (1)	0.1 mL
1:1	4.5 mg (1)	0.3 mg (1)	0.3 mL
1:2	4.5 mg (1)	0.6 mg (2)	0.6 mL
1:3	4.5 mg (1)	0.9 mg (2)	0.9 mL
1:4	4.5 mg (1)	1.2 mg (2)	1.2 mL

Interestingly, as shown in Figure 5.2, as the molar concentration of T increased in the assembly, the red-shift of the Zn-dPP Soret-band became more pronounced. However, further increasing the concentration of T beyond the concentration of Zn-dPP-pDMA only resulted in the broadening of the Soret-band. This strongly indicated that the solvent switch method was capable of driving the coordination between the N donor of T with the Zn centre of Zn-dPP-pDMA; this will be henceforth referred to as T-N $\cdots$ Zn-dPP-pDMA for brevity. Furthermore, at higher molar concentration of T, the UV-Vis absorption at *ca.* 275 nm, attributed to the absorption of T, overwhelmed that of the Zn-dPP’s Soret-band. Taking these preliminary results into consideration, a 1:1 molar ratio was likely to afford the maximum

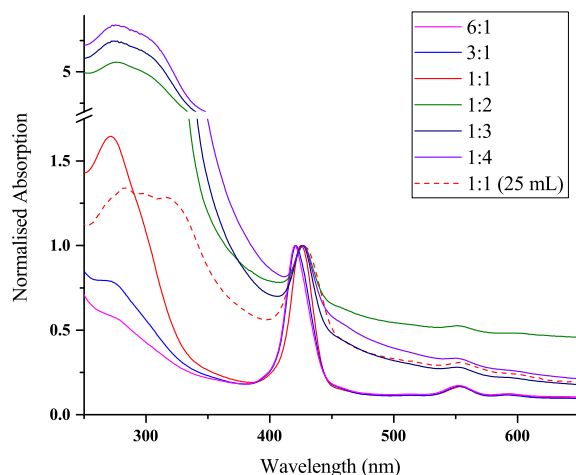


Figure 5.2: Normalised UV-Vis spectra of assemblies with different molar ratios between Zn-dPP-pDMA:T (given in the same order in legend). All spectra were normalised such that the maxima at the Soret-band (410–435 nm) equals one. The assembly at 1:1 with total volume of 25 mL (red, dashed line) was assembled at doubled the concentration.

degree of T-N $\cdots$ Zn-dPP-pDMA achievable.

Upon establishing the T:Zn-dPP-pDMA molar ratio for the system under study, the assembly was performed in higher volume for further characterisation and experiments. The resultant UV-Vis spectrum of the assembly (dashed, red trace, Figure 5.2) showed rather interesting variations from the preliminary testing: i) the Soret-band of Zn-dPP was further red-shifted and broadened; ii) a new population of T with an absorption local maximum at *ca.* 330 nm was clearly present along with a reduction of the absorption maximum at *ca.* 275 nm. These variations were likely the result of a number of changes in assembly conditions. Firstly, the final concentration of both components were doubled from the initial preliminary study ( $3\text{ mg}\cdot\text{mL}^{-1}$  *cf.*  $1.5\text{ mg}\cdot\text{mL}^{-1}$  in the preliminary study, red solid trace in Figure 5.2) in order to obtain reasonable signal in the subsequent transient electronic absorption spectroscopy (TEAS) experiment. Hence, the higher concentration ( $3\text{ mg}\cdot\text{mL}^{-1}$  *vs.*  $1.5\text{ mg}\cdot\text{mL}^{-1}$ ) might facilitate T-N $\cdots$ Zn-dPP-pDMA coordination, likely due to increased chance of the two components coming within coordination proximity. Secondly, the total volume of the assembly was increased from 3 mL to 25 mL. While the drop-wise addition of water were both performed at the same flow rate (slowest allowed by the instrument), each water droplet would contribute to a much smaller total volume change in the 12.5 mL initial volume of THF (*cf.* 1.5 mL for the preliminary screening). Thus, this increase in total volume allowed smaller steps in conformation changes to the assembly between addition of water. Thirdly, the time required for the equilibration between water and the THF content in the solu-

tion for the dialysis step would likely be increased, as a result of the larger volume of initial THF; therefore more population of the two components could reach the conformation/localisation favourable for the T-N $\cdots$ Zn-dPP-pDMA coordination. It was therefore postulated that these smaller incremental changes in volume, together with the increased time allowed for reaching the equilibrium during the assembly process resulted in a higher population of T-N $\cdots$ Zn-dPP-pDMA, manifested in the form of the pronounced UV-Vis absorption peak at *ca.* 330 nm and the slight increase in red-shift and broadening of the Zn-dPP Soret-band.

To further infer the micro-organisation of the chromophores, the observed spectral shifts in the UV-Vis spectra were inspected with reference to the building blocks as well as the mono-chromophoric assembly of Zn-dPP-pDMA in the following section.

### 5.2.2 UV-Vis spectra analysis

The normalised UV-Vis spectrum of the Zn-dPP-pDMA+T assemblies along with the reference systems, Zn-dPP (in THF), T (in THF), Zn-dPP-pDMA+T in THF, and Zn-dPP-pDMA assembled in water (from Chapter 4) are shown in Figure 5.3

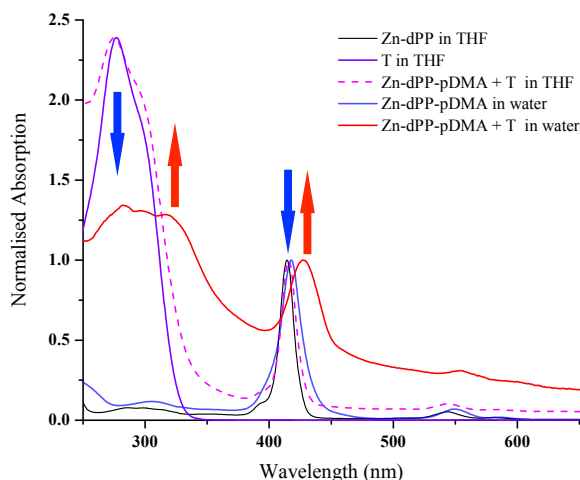


Figure 5.3: UV-Vis absorption spectra of Zn-dPP (black, solid line), T (purple, solid line) and Zn-dPP-pDMA+T (magenta, dashed line) solvated in THF; Zn-dPP-pDMA (blue, solid line, from Chapter 4), and Zn-dPP-pDMA+T assembled in water (red, solid line). All spectra were normalised to the peak of the Soret-band (*ca.* 414-432 nm), with the exception of T, which was normalised such that the maxima equals that of Zn-dPP-pDMA+T in THF. Red and blue arrows indicate increase and reduction in spectral features upon assembly.

As evidenced from Figure 5.3, in comparison to the previous assembled Zn-dPP-pDMA system (from Chapter 4), clear spectral shifts could be observed in the UV-Vis spectrum of the assembled Zn-dPP-pDMA+T. Firstly, the Soret-band

( $\sim 414\text{--}420\text{ nm}$ ,  $S_2 \leftarrow S_0$ ) was significantly broadened and red-shifted by *ca.* 15 nm. Secondly, when comparing the spectra of Zn-dPP-pDMA+T solvated in THF and the assembled form, there was a reduction of absorption in the region corresponding to T at *ca.* 278 nm (likely photoexcitation of  $S_n \leftarrow S_0$  in T, henceforth referred to as  $S_n^T \leftarrow S_0^T$ ). This reduction was accompanied by the appearance of a new absorption feature at *ca.* 330 nm. Interestingly, there was a lack of excimer induced splitting arising from reported Zn-dPP dimers and ordered aggregates, which would manifest in the form of intense absorption peaks or large degree of broadening.<sup>27–34</sup> This observation, which was similar to that observed for the assembly of Zn-dPP-pDMA, suggested that the formation of excimer was again prevented, with the assembly largely driven by the  $\pi\pi$  interaction of the Zn-dPP-pDMA and their metal to N donor interaction with T. Therefore, these observed differences could imply the T-N $\cdots$ Zn-dPP-pDMA coordination, according to the literature.<sup>23–26</sup> However, as T is a relatively large molecule with extensive  $\pi$  orbitals, these spectral shifts could also be attributed to  $\pi$  stacking between Zn-dPP-pDMA and T. Therefore, in order to ascertain that the spectral shifts observed were mainly attributed to the N-donor to metal coordination capability of the pyridyl functional group of T in the current assemblies, we introduced a variant of T with the pyridyl subunit replaced with phenyl (T-Phe). The Zn-dPP-pDMA and T-Phe was assembled with the identical 1:1 condition as previously described. UV-Vis spectra of the fully solvated (in THF) and assembled system, as well as the chemical structure of T-Phe are shown in Figure 5.4.

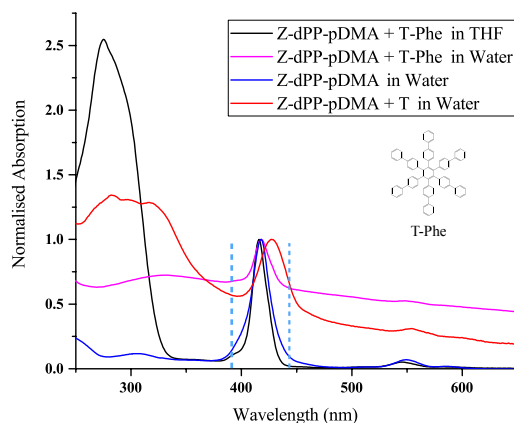


Figure 5.4: Normalised UV-Vis spectra of fully solvated (black) and assembled (magenta) Zn-dPP-pDMA+T-Phe; UV-Vis spectra of the assembled Zn-dPP-pDMA (blue) from Chapter 4 and Zn-dPP-pDMA+T under study (red) are also included for comparison. All spectra were normalised such that the maximum at the Soret-band (410–435 nm) equals one. The blue dashed lines indicate the width of Zn-dPP Soret-band of the assembled Zn-dPP-pDMA+T-Phe, as the broadening was exaggerated due to the elevated baseline. Inset shows the chemical structure of T-Phe

As shown in Figure 5.4, the co-assembly of Zn-dPP-pDMA with T-Phe showed similar spectral shifts of Soret-band as the Zn-dPP-pDMA assembly from Chapter 4, with their respective maxima almost overlapping one another in the normalised UV-Vis spectra. Although the broadening of the Soret-band seemed to be greater, they were in fact, again, very similar (indicated by the blue dashed lines in Figure 5.4) and was obscured by the elevated baseline of the Zn-dPP-pDMA+T-Phe assembly. More importantly, the T-Phe absorption peak at *ca.* 280 nm was significantly reduced and red-shifted, along with the aforementioned elevation of scattering baseline. Furthermore, the solution, upon preparation, was extremely cloudy with visible particulate formation; these observations strongly suggested that significant aggregation of the T-Phe molecules was present in water. It was therefore proposed that only a very small population of T-Phe was incorporated into the Zn-dPP core of the Zn-dPP-pDMA+T-Phe assembly, with the majority of T-Phe forming the visible particulates in the final solution.

### 5.2.3 Dry-state transmission electron microscopy observations and overall assembly interpretation

Observation of the resulting Zn-dPP-pDMA+T assemblies under dry-state transmission electron microscopy (TEM, Figure 5.5), revealed large aggregates with diameters ranging from 100–800 nm, similar to the Zn-dPP-pDMA system from Chapter 4. However, the structures observed were highly irregular, consisting of a number of different morphologies. As such, unlike the mono-chromophoric Zn-dPP-pDMA assemblies, no conclusion could be drawn on the nature of these nanostructures by the observation of TEM.

However, when taking all the observations from the preceding characterisations into account, there was clearly a certain degree of T-N $\cdots$ Zn-dPP-pDMA coordination. Furthermore, when assembled with T-Phe, the spectral shifts were not present, and loss of T-Phe in the final assemblies was apparent (inferred by UV-Vis measurements), likely due to the lack of the N-donor from the pyridyl group of T. It was therefore postulated that the pyridyl functional group played a significant role in the observed spectral shifts of the Zn-dPP-pDMA Soret-band under the aforementioned assembly conditions. This was further supported by the minimal incorporation of T-Phe into the final assembly in the absence of an N-donor. The requirement of an N-donor (or potentially any metal-coordinating group) could be exploited for future design of a functional reaction centre with different arms for selective site-specific interactions.

Based on these discussions, it was tentatively postulated that, the assembled

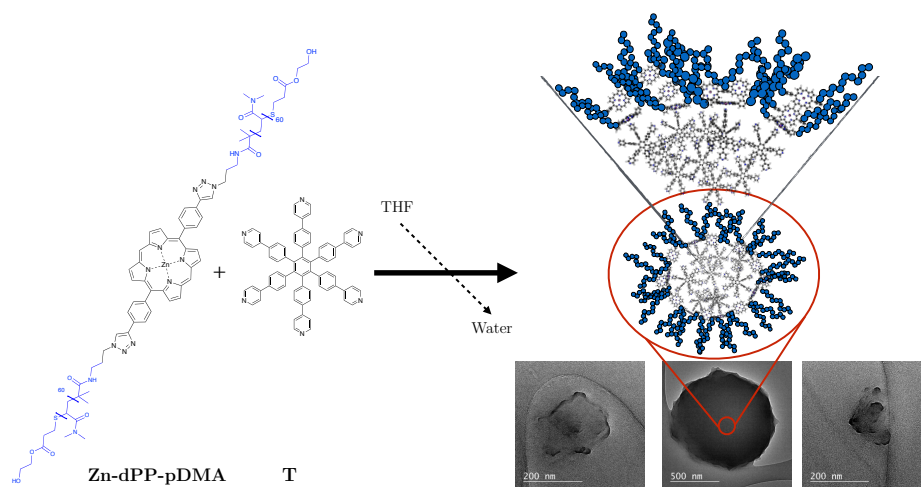


Figure 5.5: Schematic of the solvent switch assembly method (left), their observation under dry-state TEM (bottom right) and the cartoon representation of the possible micro-arrangements of chromophores in ‘micro-pockets’ form (top right). The poly-dimethylacrylamide arms are drawn as blue interlinking circles for visual clarity.

system under study mainly consisted of micro-pockets of  $T-N \cdots Zn-dPP-pDMA$  coordinated complexes, with a small population of self-aggregated  $T$  trapped within. Based on the observations from the UV-Vis experiments, the majority, if not all of  $Zn-dPP$  chromophores were likely coordinated to the  $T$ . Furthermore, based on previous studies on similar pyridyl to  $Zn$ -porphyrin variants,<sup>35–39</sup> the coordination of two pyridyl ligands by a single  $Zn$ -porphyrin had been shown to be relatively rare, thus unlikely to be present in the system under study. Therefore, the observed large aggregates were likely formed with such pockets interconnected by weak  $\pi\pi$  interactions between the  $Zn-dPP$  chromophores coordinated to  $T$ . A cartoon representation of the proposed micro-pockets is shown in Figure 5.5. It is important to note that, while the cartoon presents the micro-assembly as circular in arrangement, it is unlikely to be the case in actuality, and the circular representation was only selected for the ease of visualisation.

In summary, although a definitive chromophoric arrangement could not be obtained for the current assemblies due to their irregular morphologies, a qualitative picture was drawn by inference from the presented data and the literature. With these insights, we now proceed to investigate the photodynamics of the  $Zn-dPP-pDMA+T$  assemblies.

### 5.3 TEAS experiments

Following the characterisation of the assembly morphologies, the excited state dynamics of the assembled Zn-dPP-pDMA+T system was investigated, with reference to Zn-dPP, T solvated in THF and the Zn-dPP-pDMA assembled system (from Chapter 4) in water. The TEAS were recorded following photoexcitation to the Zn-dPP  $S_2$ , and T  $S_n^T$  states with 420 nm and 320 nm radiation (pump wavelength,  $\lambda_{pu}$ ) respectively. The excitation wavelength of 420 nm (for Zn-dPP  $S_2$ ) was chosen due to the significant red-shift observed in the assembled Zn-dPP-pDMA+T system under study, leading to significant reduction in the absorption at 400 nm (utilised in Chapter 4); and the 320 nm photoexcitation of T was chosen in an effort to photoexcite both the new population at 330 nm and the population of fully solvated T, making the experiment applicable to both the assembled and fully solvated systems. The transient absorption spectra (TAS) collected from the TEAS are presented in Figure 5.6.

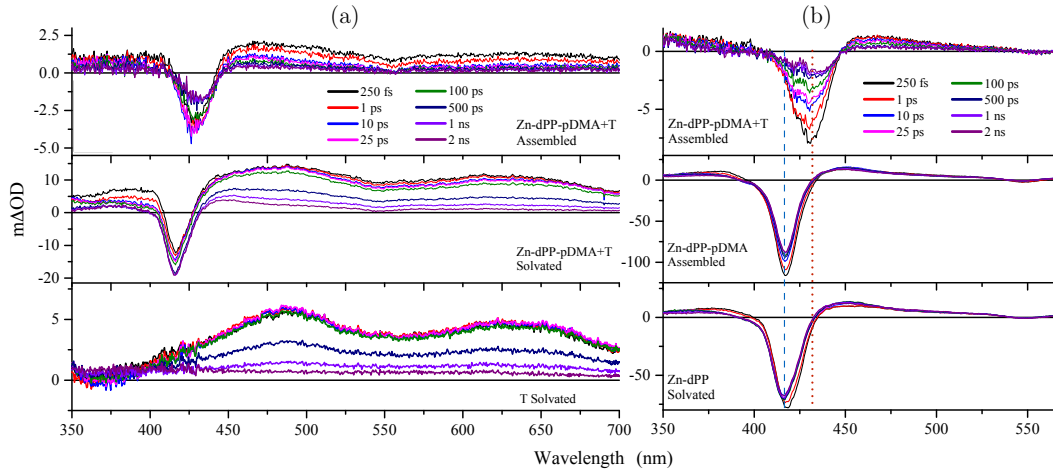


Figure 5.6: TAS of systems studied in the current chapter. (a) TAS of Zn-dPP-pDMA+T (top) assembled in water, Zn-dPP-pDMA+T (middle) and T (bottom) solvated in THF, collected following photoexcitation at 320 nm; (b) TAS of Zn-dPP-pDMA+T (top), Zn-dPP-pDMA (middle) assembled in water and Zn-dPP (bottom) solvated in THF, collected following photoexcitation at 420 nm. The red dotted line and blue dashed line highlight the different wavelengths corresponding to the minimum of GSB in each system.

Firstly, the TAS of Zn-dPP (Figure 5.6b, bottom) was examined, which showed features indistinguishable from those observed in Chapter 4 (upon photoexcitation at 400 nm). Briefly, two dominant features were apparent in the TAS: the ground state bleach (GSB) at the Soret region (*ca.* 416 nm) and the excited state absorption shoulders (ESA, *ca.* 450 nm). Global fitting of the TAS revealed the three well established processes (as discussed in Section 4.5, Chapter 4),<sup>40</sup> namely,

the internal conversion (IC) of  $S_2 \rightarrow S_1$  ( $\tau_1 \approx 1$  ps) and intermolecular vibrational energy transfer (IET) between  $S_1$  and surrounding solvent molecules ( $\tau_2 \approx 20$  ps), followed by intersystem crossing (ISC) of  $S_1 \rightarrow T_n$  extending beyond the 2 ns temporal window of our experiment ( $\tau_3 \gg 2$  ns). Since the Zn-dPP-pDMA system had been shown to exhibit identical excited state dynamics as Zn-dPP when fully solvated in Chapter 4, it is not discussed in the present chapter.

This was followed by the examination of the TAS of T solvated in THF ( $\lambda_{pu} = 320$  nm, Figure 5.6a, bottom). Two broad ESA features centred at *ca.* 480 nm and *ca.* 640 nm were observed, likely arising from a strongly absorbing  $S_1^T$  excited state; these were accompanied with a small negative feature at *ca.* 360 nm, which was likely attributed to stimulated emission. Global fitting the TAS revealed two processes, where  $\tau_1 \approx 830$  ps, and  $\tau_2 \gg 2$  ns. The nature of this process will be elucidated in conjunction of quantum mechanical calculations (QMCs) results in the subsequent section. The fitted time constants for all systems under discussion are presented in Table 5.2.

Table 5.2: Global fitted time constants of each system studied ( $\tau_n$ ).  $\lambda_{pu}$  - excitation wavelength.

System Studied (Solvent, $\lambda_{pu}$ )	$\tau_1$	$\tau_2$	$\tau_3$	$\tau_4$
T (THF, 320 nm)	830 $\pm$ 200 ps	$\gg 2$ ns	-	-
Zn-dPP-pDMA+T (THF, 320 nm)	420 $\pm$ 80 ps	$\gg 2$ ns	-	-
Zn-dPP (THF, 420 nm)	1.0 $\pm$ 0.2 ps	20 $\pm$ 10 ps	$\gg 2$ ns	-
Zn-dPP-pDMA (water, 400 nm)	0.8 $\pm$ 0.3 ps	15.2 $\pm$ 6 ps	$\gg 2$ ns	-
Zn-dPP-pDMA+T (water, 320 nm)	0.27 $\pm$ 0.1 ps	3 ps $\pm$ 1.6 ps	131 $\pm$ 60 ps	$\gg 2$ ns
Zn-dPP-pDMA+T (water, 420 nm)	0.33 $\pm$ 0.1 ps	25 $\pm$ 16 ps	340 $\pm$ 170 ps	$\gg 2$ ns

The TAS of the mixed Zn-dPP-pDMA+T systems was then examined by first comparing the TAS of Zn-dPP-pDMA+T solvated in THF (Figure 5.6a, middle) and assembled in water (Figure 5.6a, top), both collected upon photoexcitation at 320 nm. On the one hand, the TAS of both system shared similar ESA features and closely resembled the summation of TAS of Zn-dPP and T. On the other hand, global fitting the respective TAS revealed differences in relaxation processes between the two systems. For the TAS of fully solvated Zn-dPP-pDMA+T, fitting with 2 exponentials was sufficient, where the first,  $\tau_1 \approx 420$  ps, was likely a convolution between the 830 ps component of T in THF and the IET process of Zn-dPP in THF;

and the second,  $\tau_2 \gg 2$  ns corresponding to the convoluted  $S_1 \rightarrow T_n$  ISC of Zn-dPP and T. In contrast, global fitting the TAS of the assembled system required two additional exponentials to sufficiently model the spectrum, with  $\tau_1 \approx 0.3$  ps and  $\tau_2 \approx 3$  ps, followed by a slightly longer lived process ( $\tau_3 \approx 130$  ps) and finally ISC ( $\tau_4 \gg 2$  ns). The decay associated spectra (DAS) extracted from global fitting of all the TAS obtained from the TEAS experiments are shown in Figure 5.7.

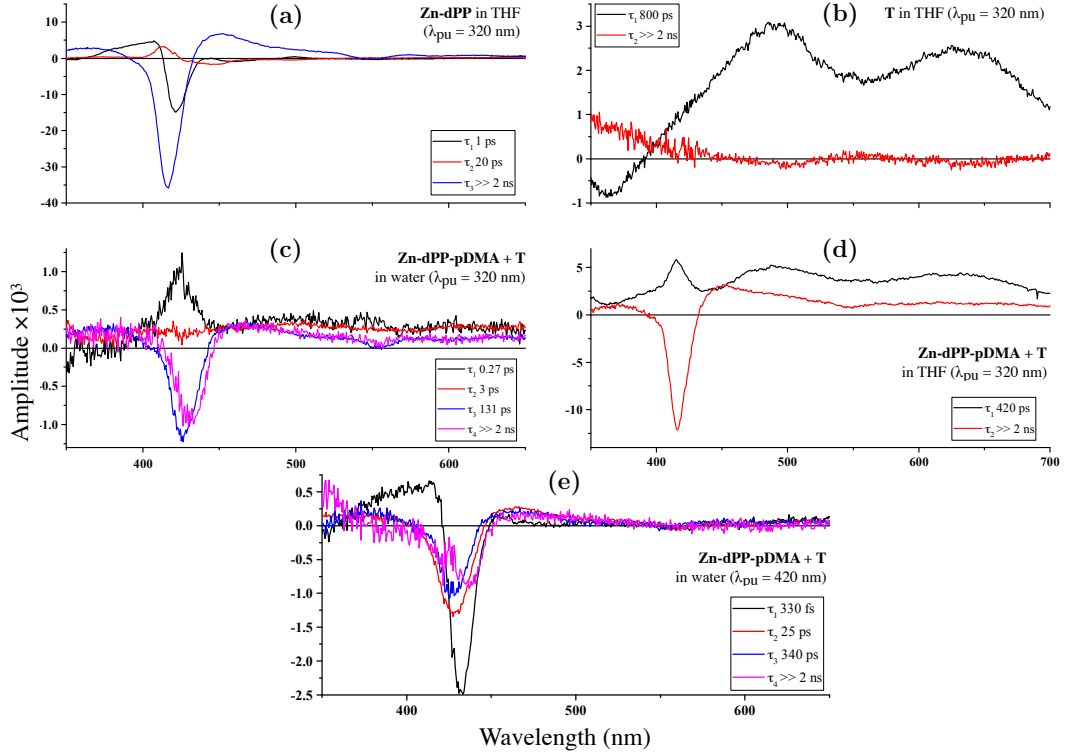


Figure 5.7: DAS of all systems presented in Section 5.3. Time constants ( $\tau_n$ ) are listed in Table 5.2.

By comparison of the TAS collected with the assembled Zn-dPP-pDMA+T (Figure 5.6b, top,  $\lambda_{pu} = 420$  nm) and Zn-dPP-pDMA (Figure 5.6b, middle  $\lambda_{pu} = 400$  nm), two notable differences were observed: i) a clear red-shift of the Soret-band GSB minima was observed, in-line with the static UV-Vis measurements (Figure 5.3); and ii) significant recovery of the GSB was observed within the temporal window of 2 ns. Similar to the TAS of the assembled Zn-dPP-pDMA+T collected with 320 nm  $\lambda_{pu}$ , 4 exponentials were required to fully describe the TAS, with time constants comparable to processes from isolated Zn-dPP and T:  $\tau_1 \approx 0.3$  ps (Zn-dPP IC),  $\tau_2 \approx 25$  ps (Zn-dPP IET),  $\tau_3 \approx 340$  ps and  $\tau_4 \gg 2$  ns (Zn-dPP and T ISC). Taking these observations together, two remarks could be made about the dynamics in the T-N...Zn-dPP-pDMA coordinated complex following excitation at 420 nm. Firstly,

the timescale for ultrafast processes ( $< 1$  ps) decreased relative to isolated Zn-dPP (Table 5.2 and Figure 5.7). Second, there was significant GSB recovery associated with the 25 ps time-constant, as was evident from the TAS (Figure 5.6) and the DAS (Figure 5.7e, red trace). This was in stark contrast to the Zn-dPP-pDMA assemblies in Chapter 4, where the excited state dynamics for a similar time-constant (15.2 ps) were attributed to IET, with little observable GSB recovery associated (Figure 5.7a, red trace). Furthermore, the process associated with the 340 ps time constant could not be explained by the reported photodynamic processes of porphyrins.<sup>40</sup> These suggested that additional relaxation pathways for the excited states of both Zn-dPP and T were present in these assembled systems.

With the additional processes extracted with the global fitting process, especially the sub-ps to ps extracted from the TAS of the assembled Zn-dPP-pDMA+T, they were difficult to interpret without some qualitative insight to, at least, their molecular orbital (MO) configurations. Therefore, *ab initio* quantum mechanical calculations (QMCs) were performed by Mr. Lewis Baker to provide some preliminary insights into the extracted processes in these systems.

## 5.4 QMCs on the T-N $\cdots$ Zn-dPP-pDMA coordinated complex

To aid the qualitative interpretations of processes extracted from the global fitting of the TAS, QMCs on the Zn-dPP, T and a single T-N $\cdots$ Zn-dPP-pDMA coordinated Zn-dPP-pDMA+T complex were performed using the Turbomole program,<sup>41–43</sup> using density functional theory (DFT) and its time-dependent variant (TD-DFT)<sup>44,45</sup> with the B-P86 functional (developed based on the DFT methods described in Section 2.8.3, Chapter 2),<sup>46,47</sup> the def2-SV(P) basis set,<sup>48</sup> and the ‘M4’ quadrature scheme.<sup>49</sup> Where applicable, resolution of the identity and multipole accelerated resolution of the identity approximations with default auxiliary basis sets were employed, and geometry optimisations used a loose ( $10^{-4}$  Hartree) SCF convergence criterion.<sup>50–52</sup> It is important to note that, as discussed in Section 2.8, Chapter 2, the DFT based computational methods were chosen due to their reasonable computation cost when dealing with systems of similar size to those investigated in the present chapter. Furthermore, while the simulation of the full assembly could provide more accurate quantitative description of observations from the TEAS experiments, the aim of QMC was only for qualitative identification of *plausible* dynamical processes, which were much more computationally tractable. Therefore, an endeavour to fully describe the assembled system computationally is beyond the scope of the current

thesis work. The results from these calculations will be discussed herein.

#### 5.4.1 Individual components

QMCs were first performed on the two key photoactive components of the system under study, namely Zn-dPP and T. The molecular orbitals (MO) of interests, highest occupied molecular orbitals (HOMO) HOMO and HOMO-1 and lowest unoccupied molecular orbitals (LUMO) LUMO and LUMO+1, of the two systems are shown in Figure 5.8.

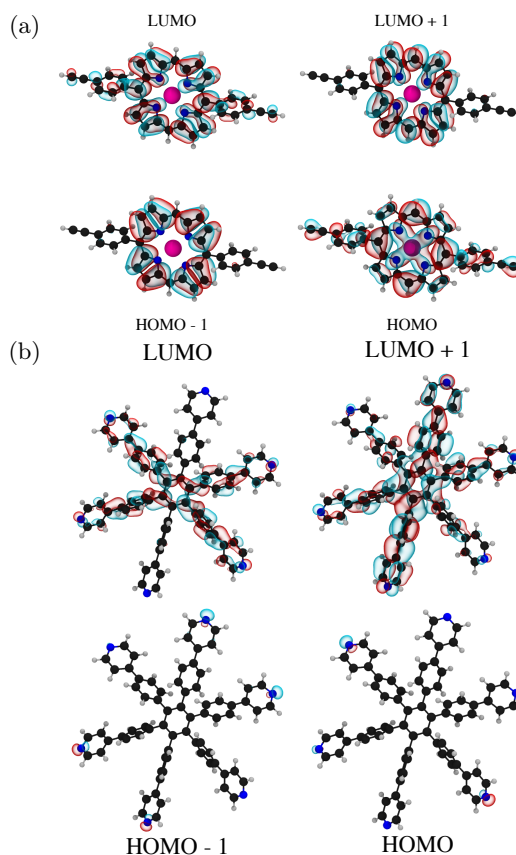


Figure 5.8: Frontier molecular orbitals of Zn-dPP (a) and T (b).

As shown in Figure 5.8, the localisation of HOMOs and LUMOs of both individual components are in good agreement with previous studies of similar model systems. In particular, the MOs of Zn-dPP (Figure 5.8a) are in good agreement with the well established Gouterman four-orbital theory.<sup>53</sup> The HOMOs and LUMOs of T (Figure 5.8b) are very similar to the 4-phenylpyridine (4-PPY) small molecule, analogous to an individual arm of T. More specifically, the two HOMOs of T are both non-bonding (n) orbitals, whilst the two LUMOs are  $\pi$  orbitals. These electronic

configurations suggest that the singlet states of T are likely similar to that of 4-PPY, which were identified as  $^1n\pi^*$  in nature.<sup>54–56</sup> These qualitative results thus provided some insights to their photochemical properties, and will be discussed in conjunction with the observations from TAS.

#### 5.4.2 T-N...Zn-dPP-pDMA coordinated complex

In order to aid the interpretation of observed photodynamics of the assembled system, QMCs were performed on the T-N...Zn-dPP-pDMA coordinated complex. The frontier MOs of interests are depicted in Figure 5.9.

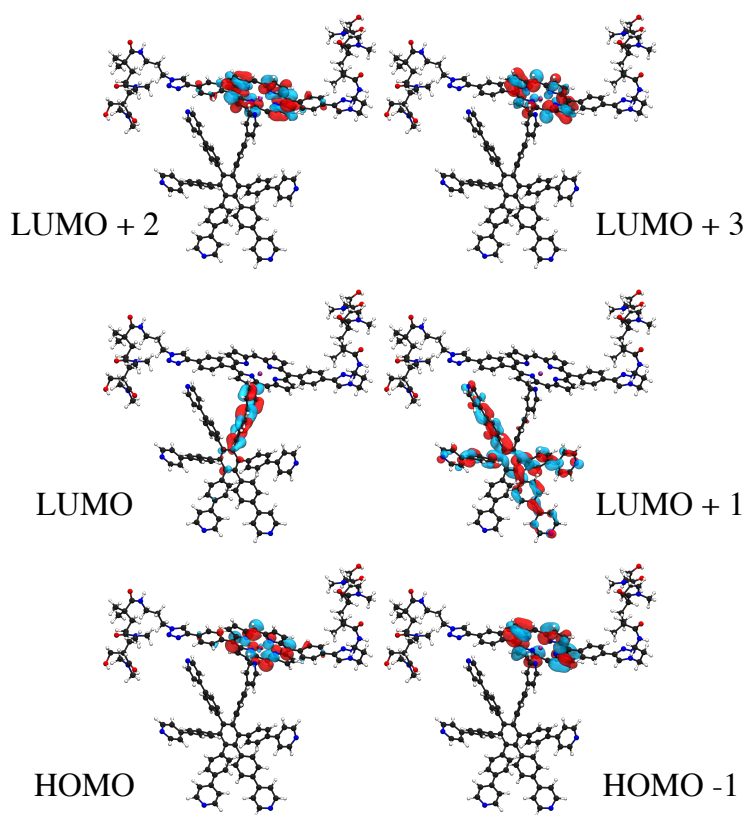


Figure 5.9: Frontier MOs of interest for the T-N...Zn-dPP-pDMA coordinated complexes.

As can be seen in Figure 5.9, the HOMOs and LUMOs of the T-N...Zn-dPP-pDMA coordinated complex are mainly localised around the Zn-dPP ring and the arms of T. Interestingly, the HOMO of the complex showed a mixture of the Zn-dPP  $\pi$  and the T  $n$  orbitals. As such, both the  $^1n\pi^*$  (excitation of T) and  $^1\pi\pi^*$  (excitation of Zn-dPP) singlet excited state should be accessible either by direct photoexcitation or *via* IC from a higher lying state. Furthermore, direct transfer of electron density

between Zn-dPP and T is likely feasible for the excited states of the present electronic configurations. The TD-DFT calculations provided some qualitative insights into the likelihood of such transfer occurring *via* direct photoexcitation. We note that, of the 15 singlet excited states calculated, only the excited states with oscillator strengths greater than  $1 \times 10^{-4}$  were considered, and the assignment of  $S_n$  starts from the lowest energy state of these excited states of interest, with  $S_1$  also being the lowest energy excited state calculated, hence likely corresponds to the lowest energy Zn-dPP Q-band. The properties of these excited states are listed in Table 5.3.

Table 5.3: Excited states of interest and their oscillator strengths from the TD-DFT calculations. The orbital transitions contribution indicate the probability of given transition when the system is photoexcited to a particular excited state.

excited states	Orbital transitions (contribution)	Oscillator Strengths
$S_1$	LUMO $\leftarrow$ HOMO (80%) LUMO+2 $\leftarrow$ HOMO (17%)	$0.79 \times 10^{-3}$
$S_2$	LUMO+1 $\leftarrow$ HOMO (32%) LUMO+2 $\leftarrow$ HOMO-1 (23%) LUMO+2 $\leftarrow$ HOMO (20%)	$0.91 \times 10^{-2}$
$S_3$	LUMO+2 $\leftarrow$ HOMO (34%) LUMO+1 $\leftarrow$ HOMO (24%) LUMO+1 $\leftarrow$ HOMO-1 (21%)	$0.73 \times 10^{-2}$

When considering both the MO localisation (Figure 5.9) and their involvement in the excited states of interest (Table 5.3), it can be concluded that the virtual orbitals localised on T (LUMO and LUMO+1) were largely accessed from the HOMO, a mixture of the Zn-dPP  $\pi$  with T-N $\cdots$ Zn-dPP-pDMA (localised on Zn-dPP and N) orbitals. As a result of the above, it was postulated that: i), the direct photoexcitations most likely resulted in the T  $^1n\pi^*$  excited states species instead of a charge separated (CS) complex, generated through direct orbital delocalisation of T(n) $\rightarrow$ Zn-dPP( $\pi^*$ ) or Zn-dPP( $\pi$ ) $\rightarrow$ T( $\pi^*$ ) transitions; and ii), upon photoexcitation of Zn-dPP (LUMO+2 $\leftarrow$ HOMO/HOMO-1), the electron density may be transferred, or ‘pushed’, into the lower lying LUMO and LUMO+1, generating a CS complex. As no further downstream electron acceptor was present in the system under study, this difference in electron density would likely be ‘pulled’ back to the Zn-dPP, returning the complex to its ground state.

## 5.5 Photorelaxation pathways of systems under study

With all the observations presented, the potential photorelaxation mechanisms for systems studied thus far may be elucidated and discussed.

The discussion shall begin with the photodynamics of the pseudo reaction centre T. Based on the QMC results, these showed that the HOMOs and LUMOs are localised around the arms of T (Figure 5.8b), which is analogous to the simple 4PPY molecule. It was therefore postulated that the  $S_1$  excited state of T underwent similar photorelaxation pathways to 4PPY, which has been very well characterised in previous studies,<sup>54–56</sup> in the form of two concurrent processes: i) IC of  $S_1^T(^1n\pi^*) \rightarrow S_0^T$  ( $\tau \approx 830$  ps); and ii) ISC of  $S_1^T(^1n\pi^*) \rightarrow T_n^T(^3\pi\pi^*)$ . The latter process was then followed by ISC of  $T_1^T \rightarrow S_0^T$  beyond 2 ns. It is worth noting that, the rate of the preferred IC pathway of 4PPY has been shown to be dependent on the vibronic coupling between the  $^1n\pi^*$  and the ground state, and was sensitive to both steric hindrance and interactions with the non-bonding orbital (n) of 4PPY from its environment (such as solvent molecules). It was therefore postulated that the slower IC in the current system ( $\sim 830$  ps *cf.*  $\sim 22$ – $100$  ps of 4PPY)<sup>54</sup> was likely the result of steric hindrance introduced by close proximity of the neighbouring 4PPY arms.

This then leads to the discussion of the assembled Zn-dPP-pDMA+T. From the QMC results, the LUMOs of T (LUMO and LUMO +1) are sandwiched between the HOMOs (HOMO and HOMO-1) and LUMOs (LUMO+2 and LUMO+3) of Zn-dPP-pDMA, similar to a recent study on smaller systems of Zn(II)-porphyrin axially coordinated to pyridyl units.<sup>23</sup> Furthermore, TD-DFT calculations suggested that direct photoexcitation of  $LUMO_T \leftarrow HOMO_{Zn-dPP}$  was possible. However, the excited states of T-N $\cdots$ Zn-dPP-pDMA are much more likely to be a mixture of transitions, hence this CS state is likely accessed through IC from other locally excited states. More importantly, such electronic MO configuration implicates the potential of a ‘push-pull’ process: where photoexcited molecules first push the electron density to the ligand, generating a CS complex. This excess electron density is then pulled back, returning the complex back to the GS, similar to some reported systems in the literature.<sup>57;58</sup> However, it is highly unlikely that the latter, pull process could facilitate the return to GS on a sub-ps time scale. Therefore, we tentatively propose that upon photoexcitation, the Zn-dPP chromophore first relaxed *via* the push process ( $Zn-dPP(\pi^*) \rightarrow T(\pi^*)$ ), generating a CS complex, concurrently with the intramolecular IC of Zn-dPP  $S_2 \rightarrow S_1$ ; in the case of T (where  $\lambda_{pu}=320$  nm), only the push relaxation pathway ( $T(\pi^*) \rightarrow Zn-dPP(\pi^*)$ ) was available and this was likely captured by  $\tau_1$ . As the time scales for  $\tau_1$  observed in both cases were near identical ( $\sim 0.27$  and  $\sim 0.33$  ps), it was postulate that the slightly quicker time constant compared to those of the fully solvated Zn-dPP and assembled Zn-dPP-pDMA ( $\sim 1$  and  $\sim 0.8$  ps, respectively) reflected the slight differences between the rates of the push and IC processes.

Additionally, as the T-N...Zn-dPP-pDMA coordinated complexes relaxed into the GS, they could serve as an energy sink for the neighbouring photoexcited molecules, which could then relax back to their respective GS *via* intermolecular excited energy transfer (EET). This EET pathway is likely a mixture of the two mechanisms described in Section 1.3.2, namely Förster type incoherent energy transfer (FIET),<sup>59;60</sup> and coherent phonon-induced relaxation (CPIR) between exciton levels.<sup>61</sup> However, CPIR is unlikely as it requires strong coupling between chromophores, and tends not to persist beyond 1 ps in solution, even for the highly optimised structures of biological LHCs.<sup>15;61</sup> It was therefore tentatively postulated that FIET was the predominant mechanism for our current system under study, where the degree of coupling between chromophores being the determinant for the rate of such process. Therefore, upon the completion of the initial push and IC processes, the T-N...Zn-dPP-pDMA on the CS state then relaxed back to their respective GS *via* the pull process, this in turn facilitated the aforementioned intermolecular EET, which was likely captured by  $\tau_2$  of the Zn-dPP-pDMA+T assemblies. In the case of T ( $\lambda_{pu} = 320$  nm), this process proceeded at a rather rapid time scale ( $\tau_2 \approx 3$  ps). As no IET was observed in the TAS of fully solvated T, this likely reflects the rate at which the pull processes occurred concurrently with EET as well as the stronger coupling between the T molecules. In the case where the Zn-dPP chromophore was photoexcited, the rate of EET was likely determined by IET, suggested by the similar time scale of  $\tau_2$  extracted from the three TAS collected upon excitation at the Soret-bands (400 and 420 nm). The 131–340 ps relaxation time scale (depending on photoexcitation wavelength) was then likely  $S_1 \rightarrow S_0$  IC of T-N...Zn-dPP-pDMA coordinated complexes relaxed into vibronic modes unfavourable for undergoing the push-pull processes *via* IET. The final time constant ( $\gg 2$  ns) then likely captured the ISC ( $S_1 \rightarrow T_n$ ) of Zn-dPP chromophores in Zn-dPP-pDMA outside the effective EET range of the T-N...Zn-dPP-pDMA complex.

Based on all the presented observations and discussions, the following photodynamical processes was postulated for the assembled Zn-dPP-pDMA+T: i) upon photoexcitation to the excited state, the T-N...Zn-dPP-pDMA coordinated complex quickly underwent the push process, transferring the excited energy to a CS state ( $\tau \approx 0.3$  ps) concurrently with the Zn-dPP  $S_2 \rightarrow S_1$  (upon photoexcitation at 420 nm); ii) the CS state then relaxed to the GS *via* the pull process, which then acted as an excited energy sink for the neighbouring photo-excited chromophores (Zn-dPP-pDMA and T), hence facilitating intermolecular EET, predominantly FIET, the rate of which were likely determined by both the coupling between chromophores (T) and IET of Zn-dPP-pDMA; iii) the population of T-N...Zn-dPP-pDMA complex relaxed

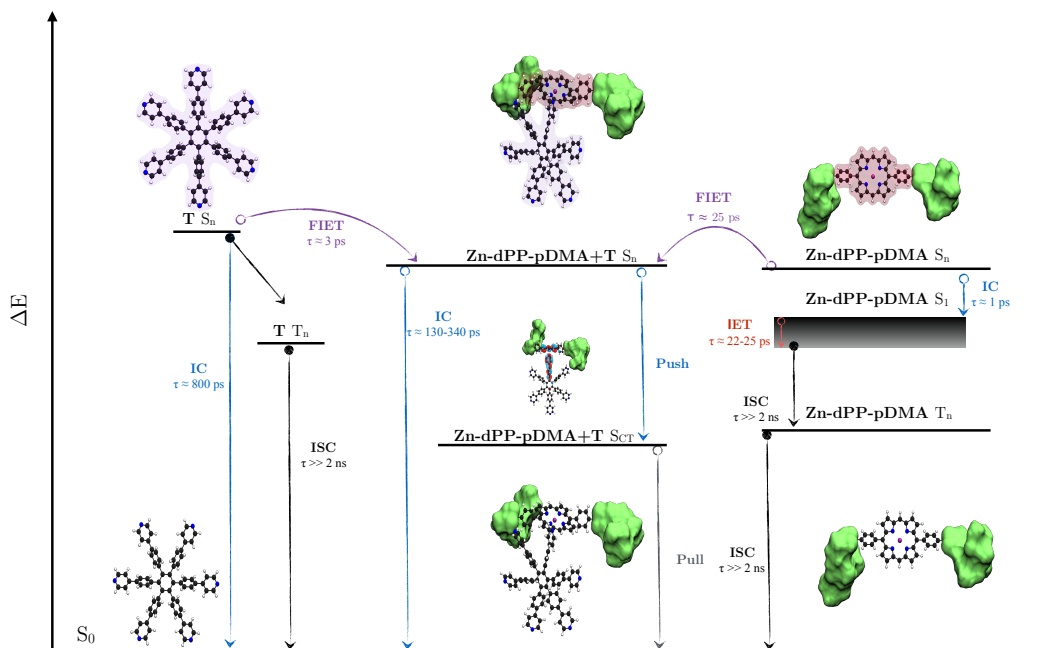


Figure 5.10: Illustration of proposed relaxation dynamics of Zn-dPP-pDMA+T assemblies. IC, internal conversion; IET - intermolecular vibrational energy transfer; FIET - Förster type incoherent energy transfer; ISC - intersystem crossing. The push process likely occurs within 0.33-1 ps, while the pull process likely occurs concomitantly with FIET.

into vibronic modes unfavourable for the push-pull process then returned to the GS *via* IC of  $S_1 \rightarrow S_0$  (131–340 ps); and iv) the Zn-dPP chromophore of Zn-dPP-pDMA outside the effective EET range then underwent ISC of  $S_1 \rightarrow T_n$ , similar to the Zn-dPP based systems studied in Chapter 4. A simple illustration of these processes are presented in Figure 5.10.

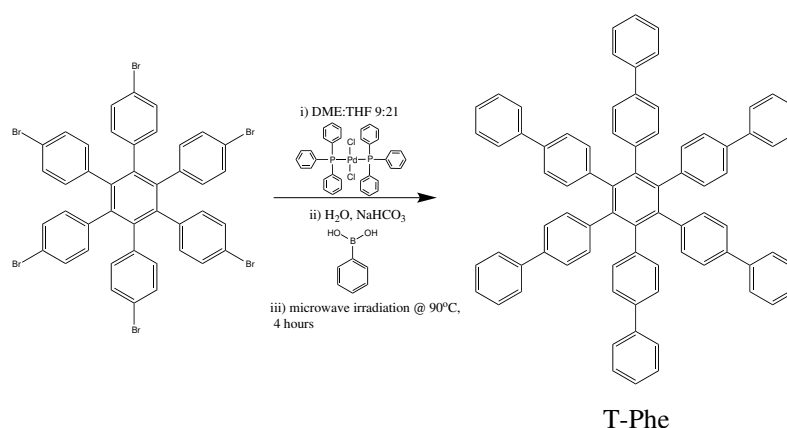
## 5.6 Conclusion

In summary, the attempt to explore the feasibility of utilising the platform established from Chapter 4 had shown moderate success. On the one hand, the morphologies of the final assembly were highly irregular, thus the methodology employed, so far, has yet to produce controlled  $T\text{-N}\cdots\text{Zn-dPP-pDMA}$  coordinating complexes. On the other hand, the assembly method was very simplistic, and could be performed with relative ease. Furthermore, the experimental observations suggest that a push-pull relaxation pathway for the chromophores could be introduced by simply assembling the system in the presence of an N-donor ligand. Interestingly, this new pathway seems to facilitate the relaxation of neighbouring chromophores *via* FIET. Perhaps more importantly, each photo-active component in the system exhibited in-

dependent rate of such EET. This, together with the fact that the ‘arms’ of the model HAB (T) seems to be the determinant of its photodynamics, such EET mechanism could be fine tuned and exploited by simply ‘switching’ the reaction centres with different functional arms. Coupled with the recent large scale synthesis of uncommon HABs demonstrated by Jux and co-workers,<sup>62</sup> screening of various reaction centres could be achieved with relatively high throughput. Thus, considering the current system as a proof-of-concept vehicle for the creation of a functional synthetic biological LHC mimic, the goals set out at the start of the present thesis (as discussed in Section 1.5.4, Chapter 1) were mostly achieved.

## 5.7 Experimental

### Hexadentate-phenyl (T-Phe) synthesis



T-Phe was synthesised using a similar procedure for T as reported by Anderson and co workers,<sup>22</sup> with microwave radiation as a heat source (hence shorter reaction time) and phenylboronic acid in place of 4-Pyridinylboronic acid: hexa-(4-bromophenyl)benzene (100 mg, 99  $\mu\text{mol}$ )<sup>63</sup> and dichlorobis(triphenylphosphine)-palladium(II) (10.0 mg, 14.3  $\mu\text{mol}$ ) was dissolved in 3 mL of dimethyleneglycol and THF (3:7) inside a microwave reaction tube. Two separate solutions of  $\text{NaHCO}_3$  (150 mg, 1.79 mmol) in 1.2 mL of water and phenylboronic acid in 1 mL of THF was added to the mixture. The suspension was then degassed by purging under argon for 20 minutes, and sealed. The suspension was stirred for one minute before heating to  $90^\circ\text{C}$  for 4 hours. The resulting mixture was then added to 150 mL of  $\text{CH}_2\text{Cl}_2$ , washed with water ( $3 \times 200$  mL) then brine (150 mL) and dried over  $\text{Mg}_2\text{SO}_4$ . Upon removal of  $\text{CH}_2\text{Cl}_2$  *in vacuo*, the crude product was purified by column chromatography (petroleum ether :  $\text{CH}_2\text{Cl}_2$  10:1  $\rightarrow$  1 : 2), yielding product as white solid

(13 mg, 13%).  $^1\text{H}$  NMR ( $\text{CDCl}_3$ , 300 MHz, ppm)  $\delta$ =6.96 (m, 18H), 7.17 (m, 12H), 7.31 (m, 12H), 7.42 (m, 12H); IR (neat,  $\lambda_{\text{max}}$ ,  $\text{cm}^{-1}$ ): 2970 (m). MALDI/TOF MS (Superflex Extreme)  $m/z$  found 1013.414, calc. 1013.412 ( $[\text{C}_{78}\text{H}_{54}+\text{Na}]^+$ , 100%).

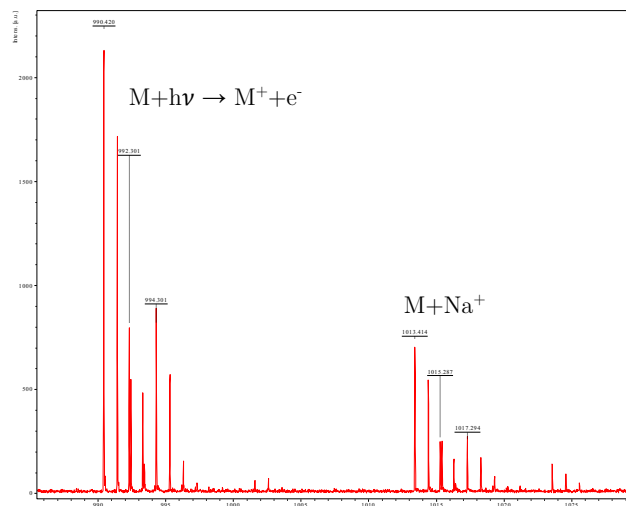


Figure 5.11: MALDI/TOF spectrum of T-Phe. The two ionised species are labelled next to the associated peaks.

### 5.7.1 Global fitting

As mentioned in Section 5.3, 4 exponentials were required to fully describe the TAS of the assembled systems these are illustrated by the comparison between fits with 3 and 4 exponentials, with TAS collected with TEAS performed upon photoexcitation of both 320 nm and 420 nm, shown in Figure 5.12 and Figure 5.13 respectively.

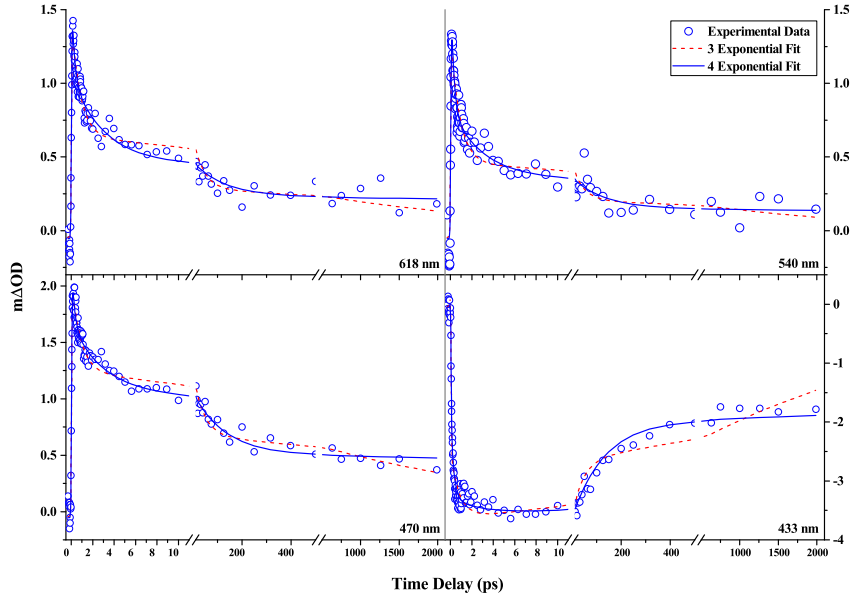


Figure 5.12: Selected fitted traces with 3 and 4 exponentials, upon 320 nm photoexcitation. Probe wavelengths are indicated on corresponding traces.

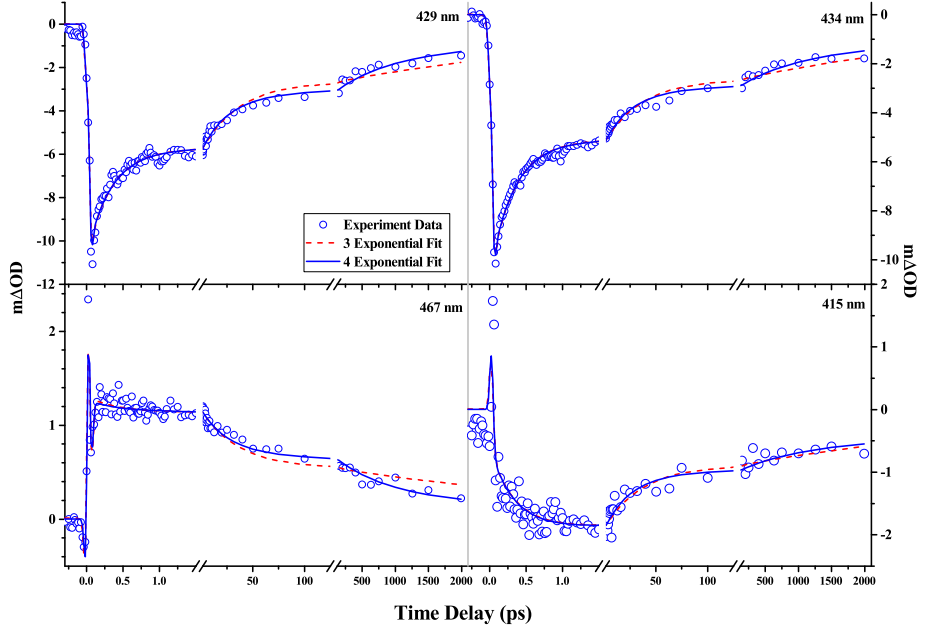


Figure 5.13: Selected fitted traces with 3 and 4 exponentials, upon 420 nm photoexcitation. Probe wavelengths are indicated on corresponding traces.

Uncertainties at the 95% level were assigned to the determined lifetimes using an asymptotic standard error (ASE) technique described in Section 2.7.4.<sup>64;65</sup> The  $\frac{\chi^2}{\chi_{min}^2}$  for all studied systems are shown in Figure 5.14. We note that, for the time

constants attributed to IET of Zn-dPP ( $\tau_2$ ) and of Zn-dPP-pDMA+T assembled in water ( $\tau_3$ ) were unbounded on the longer edge (timescale). Thus the errors for these two time constants quoted in Table 5.2 were reported as the deviation towards the shorter time scale.

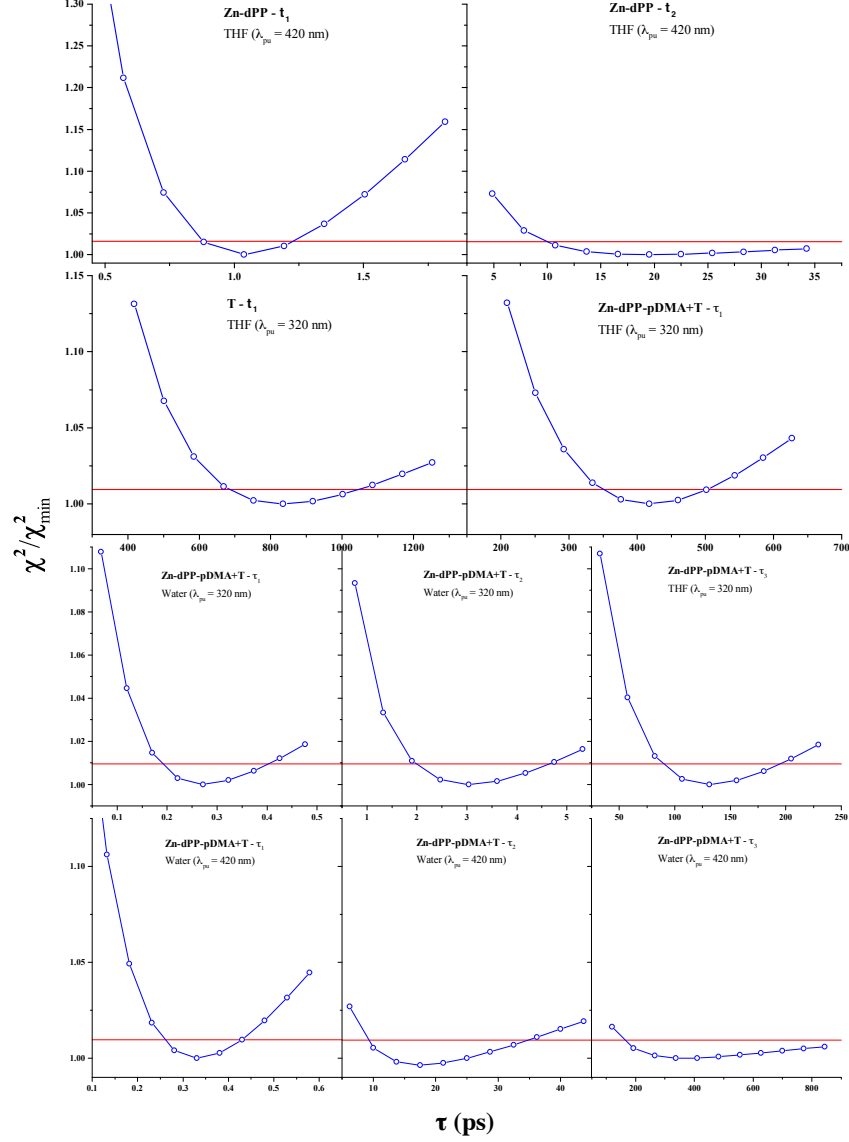


Figure 5.14:  $\frac{\chi^2}{\chi_{min}^2}$  for all time constants fitted for each systems. The red horizontal lines indicate the 95% levels.

## References

- [1] M. Suga, F. Akita, K. Hirata, G. Ueno, H. Murakami, Y. Nakajima, T. Shimizu, K. Yamashita, M. Yamamoto, H. Ago *et al.*, *Nature*, 2015, **517**, 99–103.
- [2] L. Dall’Osto, M. Bressan and R. Bassi, *BBA-Bioenergetics*, 2015, **1847**, 861–871.
- [3] L.-X. Shi, M. Hall, C. Funk and W. P. Schröder, *BBA-Bioenergetics*, 2012, **1817**, 13–25.
- [4] Y. Umena, K. Kawakami, J.-R. Shen and N. Kamiya, *Nature*, 2011, **473**, 55–60.
- [5] B. F. Milne, C. Kjær, J. Houmøller, M. H. Stockett, Y. Toker, A. Rubio and S. B. Nielsen, *Angew. Chem. Int. Ed.*, 2016, **55**, 6248–6251.
- [6] X. Qin, M. Suga, T. Kuang and J.-R. Shen, *Science*, 2015, **348**, 989–995.
- [7] J. Martiskainen, R. Kananavičius, J. Linnanto, H. Lehtivuori, M. Keränen, V. Aumanen, N. Tkachenko and J. Korppi-Tommola, *Photosyn. Res.*, 2011, **107**, 195–207.
- [8] N. Nelson and W. Junge, *Annu. Rev. Biochem.*, 2015, **84**, 659–683.
- [9] J. M. Anna, G. D. Scholes and R. van Grondelle, *BioScience*, 2014, **64**, 14–25.
- [10] R. Moca, S. R. Meech and I. A. Heisler, *J. Phys. Chem. B*, 2015, **119**, 8623–8630.
- [11] D. I. G. Bennett, K. Amarnath and G. R. Fleming, *J. Am. Chem. Soc.*, 2013, **135**, 9164–9173.
- [12] H. Liu, H. Zhang, D. M. Niedzwiedzki, M. Prado, G. He, M. L. Gross and R. E. Blankenship, *Science*, 2013, **342**, 1104–1107.
- [13] G. Schlau-Cohen, J. M. Dawlaty and G. Fleming, *IEEE J. Sel. Top. Quantum Electron.*, 2012, **18**, 283–295.
- [14] M. Ballottari, M. J. P. Alcocer, C. D’Andrea, D. Viola, T. K. Ahn, A. Petrozza, D. Polli, G. R. Fleming, G. Cerullo and R. Bassi, *Proc. Natl. Acad. Sci. U.S.A.*, 2014, **111**, E2431–E2438.
- [15] G. S. Engel, T. R. Calhoun, E. L. Read, T.-K. Ahn, T. Mancal, Y.-C. Cheng, R. E. Blankenship and G. R. Fleming, *Nature*, 2007, **446**, 782–786.

- [16] E. Collini, C. Y. Wong, K. E. Wilk, P. M. G. Curmi, P. Brumer and G. D. Scholes, *Nature*, 2010, **463**, 644–647.
- [17] G. Trinkunas, J. L. Herek, T. Polívka, V. Sundström and T. Pullerits, *Phys. Rev. Lett.*, 2001, **86**, 4167–4170.
- [18] Y. Kuramochi, A. Satake and Y. Kobuke, *J. Am. Chem. Soc.*, 2004, **126**, 8668–8669.
- [19] S. A. Rousseaux, J. Q. Gong, R. Haver, B. Odell, T. D. Claridge, L. M. Herz and H. L. Anderson, *J. Am. Chem. Soc.*, 2015, **137**, 12713–12718.
- [20] S. Liu, D. V. Kondratuk, S. A. L. Rousseaux, G. Gil-Ramírez, M. C. O’Sullivan, J. Cremers, T. D. W. Claridge and H. L. Anderson, *Angew. Chem. Int. Ed.*, 2015, **54**, 5355–5359.
- [21] D. V. Kondratuk, L. M. Perdigão, A. M. Esmail, J. N. O’Shea, P. H. Beton and H. L. Anderson, *Nat. Chem.*, 2015, **7**, 317–322.
- [22] M. Hoffmann, J. Kärnbratt, M.-H. Chang, L. M. Herz, B. Albinsson and H. L. Anderson, *Angew. Chem. Int. Ed.*, 2008, **47**, 4993–4996.
- [23] J.-X. Zhang, F.-M. Han, J.-C. Liu, R.-Z. Li and N.-Z. Jin, *Tetrahedron Lett.*, 2016, **57**, 1867–1872.
- [24] E. M. Finnigan, R. Rein, N. Solladié, K. Dahms, D. C. Götz, G. Bringmann and M. O. Senge, *Tetrahedron*, 2011, **67**, 1126–1134.
- [25] C. C. Mak, N. Bampos and J. K. M. Sanders, *Angew. Chem. Int. Ed.*, 1998, **37**, 3020–3023.
- [26] C. A. Hunter, M. N. Meah and J. K. M. Sanders, *J. Am. Chem. Soc.*, 1990, **112**, 5773–5780.
- [27] T. van der Boom, R. T. Hayes, Y. Zhao, P. J. Bushard, E. A. Weiss and M. R. Wasielewski, *J. Am. Chem. Soc.*, 2002, **124**, 9582–9590.
- [28] T. Park, J. S. Shin, S. W. Han, J.-K. Son and S. K. Kim, *J. Phys. Chem. B*, 2004, **108**, 17106–17111.
- [29] M. Takeuchi, S. Tanaka and S. Shinkai, *Chem. Commun.*, 2005, 5539–5541.
- [30] M. Morisue, Y. Hoshino, K. Shimizu, M. Shimizu and Y. Kuroda, *Chem. Sci.*, 2015, **6**, 6199–6206.

- [31] J. Wang, Y. Zhong, L. Wang, N. Zhang, R. Cao, K. Bian, L. Alarid, R. E. Haddad, F. Bai and H. Fan, *Nano Lett.*, 2016, **16**, 6523–6528.
- [32] M. Kasha, H. Rawls and M. Ashrafel-Bayoumi, *Pure Appl. Chem.*, 1965, **11**, 371–392.
- [33] I.-W. Hwang, M. Park, T. K. Ahn, Z. S. Yoon, D. M. Ko, D. Kim, F. Ito, Y. Ishibashi, S. R. Khan, Y. Nagasawa, H. Miyasaka, C. Ikeda, R. Takahashi, K. Ogawa, A. Satake and Y. Kobuke, *Chem. Eur. J.*, 2005, **11**, 3753–3761.
- [34] S. Verma, A. Ghosh, A. Das and H. N. Ghosh, *J. Phys. Chem. B*, 2010, **114**, 8327–8334.
- [35] L. Favereau, A. Cnossen, J. B. Kelber, J. Q. Gong, R. M. Oetterli, J. Cremers, L. M. Herz and H. L. Anderson, *J. Am. Chem. Soc.*, 2015, **137**, 14256–14259.
- [36] I. Tabushi, S. Kugimiya, M. G. Kinnaird and T. Sasaki, *J. Am. Chem. Soc.*, 1985, **107**, 4192–4199.
- [37] R. J. Abraham, P. Leighton and J. K. M. Sanders, *J. Am. Chem. Soc.*, 1985, **107**, 3472–3478.
- [38] A. Satake and Y. Kobuke, *Tetrahedron*, 2005, **61**, 13 – 41.
- [39] I. Beletskaya, V. S. Tyurin, A. Y. Tsivadze, R. Guilard and C. Stern, *Chem. Rev.*, 2009, **109**, 1659–1713.
- [40] H.-Z. Yu, J. S. Baskin and A. H. Zewail, *J. Phys. Chem. A*, 2002, **106**, 9845–9854.
- [41] *TURBOMOLE V6.2 2010, a development of University of Karlsruhe and Forschungszentrum Karlsruhe GmbH, 1989-2007, TURBOMOLE GmbH, since 2007; available from <http://www.turbomole.com>.*
- [42] M. Von Arnim and R. Ahlrichs, *J. Comput. Chem.*, 1998, **19**, 1746–1757.
- [43] R. Ahlrichs, M. Bär, M. Häser, H. Horn and C. Kölmel, *Chem. Phys. Lett.*, 1989, **162**, 165–169.
- [44] R. Bauernschmitt, M. Häser, O. Treutler and R. Ahlrichs, *Chem. Phys. Lett.*, 1997, **264**, 573–578.
- [45] R. Bauernschmitt and R. Ahlrichs, *Chem. Phys. Lett.*, 1996, **256**, 454–464.

- [46] A. D. Becke, *Phys. Rev. A*, 1988, **38**, 3098–3100.
- [47] J. P. Perdew, *Phys. Rev. B*, 1986, **33**, 8822–8824.
- [48] F. Weigend and R. Ahlrichs, *Phys. Chem. Chem. Phys.*, 2005, **7**, 3297–3305.
- [49] O. Treutler and R. Ahlrichs, *J. Chem. Phys.*, 1995, **102**, 346–354.
- [50] K. Eichkorn, O. Treutler, H. Öhm, M. Häser and R. Ahlrichs, *Chem. Phys. Lett.*, 1995, **240**, 283–290.
- [51] K. Eichkorn, F. Weigend, O. Treutler and R. Ahlrichs, *Theor. Chem. Acc.*, 1997, **97**, 119–124.
- [52] M. Sierka, A. Hogekamp and R. Ahlrichs, *J. Chem. Phys.*, 2003, **118**, 9136–9148.
- [53] M. Gouterman, *J. Mol. Spectrosc.*, 1961, **6**, 138–163.
- [54] G. Buntinx, R. Naskrecki, C. Didierjean and O. Poizat, *J. Phys. Chem. A*, 1997, **101**, 8768–8777.
- [55] A. Sarkar and S. Chakravorti, *J. Lumin.*, 1995, **65**, 163–168.
- [56] J. Kubin and A. Testa, *J. Photochem. Photobiol. A*, 1994, **83**, 91–96.
- [57] P. D. Zoon, I. H. M. van Stokkum, M. Parent, O. Mongin, M. Blanchard-Desce and A. M. Brouwer, *Phys. Chem. Chem. Phys.*, 2010, **12**, 2706–2715.
- [58] X. Wang, G. Brisard, D. Fortin, P.-L. Karsenti and P. D. Harvey, *Macromolecules*, 2015, **48**, 7024–7038.
- [59] V. I. Novoderezhkin, *Biochem. (Mosc.) Suppl. Ser. A Membr. Cell Biol.*, 2012, **6**, 314–319.
- [60] T. Förster, *Discuss. Faraday Soc.*, 1959, **27**, 7–17.
- [61] P. Vasa and D. Mathur, in *Ultrafast Quantum Mechanical Processes in Plants*, Springer International Publishing, Cham, 2016, pp. 123–144.
- [62] D. Lungerich, D. Reger, H. Hölzel, R. Riedel, M. M. J. C. Martin, F. Hampel and N. Jux, *Angew. Chem. Int. Ed.*, 2016, **55**, 5602–5605.
- [63] R. Rathore, C. L. Burns, and M. I. Deselnicu, *Org. Lett.*, 2001, **3**, 2887–2890.

- [64] L. A. Baker, M. D. Horbury, S. E. Greenough, F. Allais, P. S. Walsh, S. Habershon and V. G. Stavros, *J. Phys. Chem. Lett.*, 2016, **7**, 56–61.
- [65] J. R. Lakowicz, *Principles of Fluorescence Spectroscopy*, Springer Science+Business Media, 3rd edn., 2006.

## Chapter 6

# Summary and future prospect

In summary, the current thesis work aimed to contribute towards the development of a novel biological light harvesting complex (LHC) synthetic mimic, discussed throughout Chapter 1. In particular, as discussed in Section 1.5.4, the current thesis served as the first step towards achieving this goal by determining the viability of the proposed systems studied as building blocks for the future construction of functional biological LHC mimics. Subsequent characterisations and experimental findings suggested the potential of these systems for the proposed applications.

In particular, the fluorescence quenching of the maleimide based fluorophores in protic solvents has been a phenomenon that was exploited in a number of applications, but never understood.<sup>1;2</sup> However, for the utilisation of the maleimide based fluorophores as a robust and reliable photosensitiser expanding the spectral coverage of a porphyrin containing light harvesting system, the investigation of this phenomenon was required. Therefore, in Chapter 3, the photochemical process responsible for this quenching was potentially identified, using a small monoamino maleimide (MAM), as electron driven proton transfer (EDPT). Although this discovered pathway may limit the potential as a photosensitiser for the maleimide based chromophore, it could also lead to further functionalities for the proposed light harvesting application, such as additional photo-protection pathways or photo-induced hydrogen generation applications. Thus, manipulations of EDPT based on this knowledge may result in a number of functional handles based on this class of chromophores.

Chapter 4 then documented the attempt to develop a porphyrin containing self-assembled system, which consisted of the screening and selection of accessible and robust synthetic methodologies, and the photophysical characterisation of the resulting material. From this work, a simple self-ordering Zn-porphyrin-poly-*N,N*-

dimethylacrylamide (Zn-dPP-pDMA) was produced. Not only was this material able to assemble into large nanostructures without the utilisation of an inter-chromophoric covalent linkage, the photophysical properties of the porphyrin chromophore were also largely retained despite the  $\pi$  stacking tendency of porphyrin. This may be the result of a fortuitous balance between the  $\pi$  stacking tendency of porphyrin and the repulsion between the polymer arms. With these interesting properties, further investigation into their potential for the proposed goal was warranted.

Therefore, a pseudo reaction centre, the hexadentate template utilised in a number of works by Anderson *et al.*,<sup>3-5</sup> a hexaarylbenzene (HAB) variant with six pyridyl N-donor sites (T), was introduced to the assembly as documented in Chapter 5. Interestingly, the addition of this template induced appreciable changes to the photodynamics of the assembled materials. In particular, with the qualitative insights provided by the electronic structure calculations, a push-pull relaxation pathway seems to be facilitated by the coordination between the porphyrin Zn metal centre and the N-donor of the template. This then allowed the porphyrin chromophores to relax to the ground state at a much more rapid rate than when assembled in the absence of this template. These results suggest that it was indeed possible to use the methods described in Chapter 4 to create a multi-chromophoric system without the need of direct covalent inter-chromophore conjugations. Unfortunately, the dynamic nature of these assemblies rendered their exact chromophoric arrangement extremely difficult to determine (as were the overall relaxation dynamics). Furthermore, as the observed nanostructures exhibited highly irregular morphologies, it is likely that the metal to ligand coordination processes was not very well controlled. Therefore, future research on these class of material should focus on the determination of the assembly conditions that facilitate the controlled coordination between different classes of chromophores.

Based on the findings of the current thesis, the systems studied could be applied towards the construction of the novel LHC mimics by the step wise addition and combination of functional components. As these are best illustrated with specific examples, two proposed methods for their utilisation for future development towards functional systems are presented in the proceeding sections.

## 6.1 Exploitation of maleimide based chromophore for water splitting applications

The first method of producing the system proposed in Section 1.5 could be considered the exploitation of the combined systems studied in chapters 3 (maleimide based



polymerisation of  $C_3S_3N_3$  monomers and their thiol-functionalisation of the bromo-maleimide monomers. The final assembly would therefore be partially soluble in aqueous media. If this approach proves to be successful, it would have a number of advantage over the poly- $C_3S_3N_3$  system: i) the reported polymer was not soluble in water,<sup>6</sup> as such, the surface area in contact with water, provided water molecules could migrate through the corona, would be greatly enhanced; ii) the spectral coverage of the proposed system would be much greater thanks to the presence of two additional chromophores; and iii) the reported system was only capable of partial water splitting,<sup>6</sup> although this is only speculation, the addition of the maleimide EDPT capability may increase the likelihood of achieving complete water splitting.

However, it is worth noting that, the water splitting process in biological LHCs requires a regenerative electron acceptor, *e.g.* plastoquinone in the processes described in Section 1.3.<sup>8</sup> As such, for the proposed system to achieve total water splitting, further exploration into methods for the incorporation of a similar electron acceptor may be required.

## 6.2 Introduction of true RC to Zn-dPP-pDMA assemblies

The second approach towards generating a functional self-assembly synthetic mimic of biological LHCs could be considered the improvement over the system discussed in Chapter 5. In particular, the hexadentate template (T) will be swapped with a different HAB variant with reactive functional arms, with the porphyrin-polymer serving as both photosensitiser and structural support. This could be the more realistic of the two approaches proposed, thanks to the recently reported large scale synthesis of HAB with a number of different functional sites by Jux *et al.*<sup>9</sup> The potential variations shown in this reported work is illustrated in Figure 6.2.<sup>9</sup>

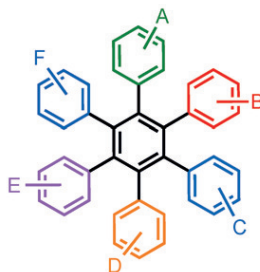


Figure 6.2: General structure of HAB variants demonstrated by Jux *et al.*<sup>9</sup> Where A–F are sites that could be modified with select functional groups independently based on the synthesis demonstrated.

As shown in Figure 6.2, all of the 6 sites could be independently selected based on the reported synthesis method. Further more, the impressive gram scale production of these potential ‘true’ RCs could be achieved.<sup>9</sup> As such, after the small scale screening of these HAB variants for the most effective synthetic RCs, these could be then be produced with the large scale methods described. As an example of a functional RC, one of the six arms will be the identical 4-phenylpyridine (4PPY) demonstrated in Chapter 5. The arm directly opposite to it would then be the reactive arm, which could take the form of either a catalytic complex or the maleimide based water splitting core. The most enticing design would then introduce two different arms capable of forming complementary ligand binding pairs similar to DNA base-pairs to the arms directly adjacent to this reactive arm. This would then facilitate the formation of a ring-like structure between these RCs. Finally, the remaining arms could be decorated by functional groups such as the maleimide based fluorophore, serving as photosensitiser to the overall system. This proposed assembly is presented in Figure 6.3.

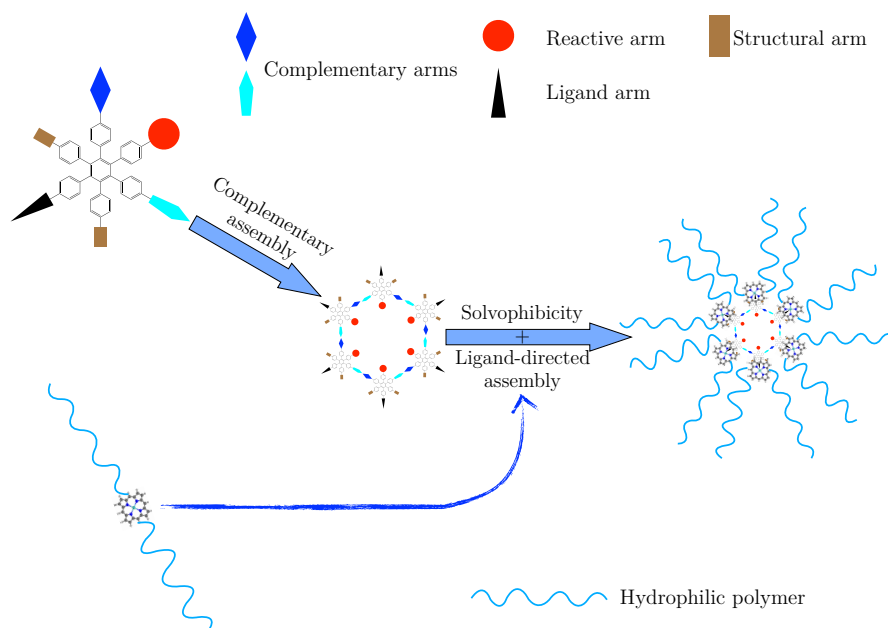


Figure 6.3: Assemblies of proposed approach expanding on the T-N...Zn-dPP-pDMA assembled system.

With reference to Figure 6.3, the proposed method of constructing a natural LHC mimic with a true RC can be postulated. Firstly, as aforementioned, the complementary arms will assemble into the most energetically stable form in a water miscible solvent. In a well designed system, this should adopt in a cyclic

arrangement, thanks to the angles induced by their placements on the HAB. The Zn-dPP-pDMA dissolved in the same organic solvent would then be introduced to the pre-assembled RCs. The solution of this mixture then undergoes the solvent switch procedures as described in Section 2.3, leading to the final formation of the assembly with the RC coordinated with the Zn-dPP chromophores. With this design, the uncontrolled aggregation of T observed in Chapter 5 may be mitigated by the controlled arrangement directed by the complimentary arms on the envisaged HAB RC. Therefore, the vesicular morphology observed in Chapter 4 could likely be preserved. This class of nanostructures could prove to be a very strong candidate for creating live cell mimics, in which the cyclic RC could perform similar tasks of LHC, such as generating a proton gradient across the polymersome membrane. Thus, this could be a platform for future designs of functional synthetic mimics of biological systems, especially photosynthetic organisms. Alternatively, the reactive arm of the HAB variant could be designed to anchor onto a semiconducting substrate, serving as a flexible assembly for applications such as dye sensitised solar cells.

As shown in the two presented examples of furthering the application potential of systems studied in the current thesis, the facile nature of their assembly and modification could provide a number of avenues for the exploration into future applications. Therefore, it is hoped that the works described could provide an accessible alternative for future LHC mimic designs utilising these simple assembly methods, thus the means for further exploitation of solar energy.

## References

- [1] A. B. Mabire, M. P. Robin, W.-D. Quan, H. Willcock, V. G. Stavros and R. K. O'Reilly, *Chem. Commun.*, 2015, **51**, 9733–9736.
- [2] M. P. Robin, P. Wilson, A. B. Mabire, J. K. Kiviaho, J. E. Raymond, D. M. Haddleton and R. K. O'Reilly, *J. Am. Chem. Soc.*, 2013, **135**, 2875–2878.
- [3] M. Hoffmann, J. Kärnbratt, M.-H. Chang, L. M. Herz, B. Albinsson and H. L. Anderson, *Angew. Chem. Int. Ed.*, 2008, **47**, 4993–4996.
- [4] J. K. Sprafke, B. Odell, T. D. W. Claridge and H. L. Anderson, *Angew. Chem. Int. Ed.*, 2011, **50**, 5572–5575.
- [5] S. A. Rousseaux, J. Q. Gong, R. Haver, B. Odell, T. D. Claridge, L. M. Herz and H. L. Anderson, *J. Am. Chem. Soc.*, 2015, **137**, 12713–12718.

- [6] Z. Zhang, J. Long, L. Yang, W. Chen, W. Dai, X. Fu and X. Wang, *Chem. Sci.*, 2011, **2**, 1826–1830.
- [7] M. A. Gauthier, M. I. Gibson and H.-A. Klok, *Angew. Chem. Int. Ed.*, 2009, **48**, 48–58.
- [8] F. M. Harold, *The Vital Force: A study of Bioenergetics*, W.H. Freeman, 1987.
- [9] D. Langerich, D. Reger, H. Hölzel, R. Riedel, M. M. J. C. Martin, F. Hampel and N. Jux, *Angew. Chem. Int. Ed.*, 2016, **55**, 5602–5605.